Copyright is owned by the Author of the thesis. Permission is given for a copy to be downloaded by an individual for the purpose of research and private study only. The thesis may not be reproduced elsewhere without the permission of the Author.

ATOMIZATION OF FRUIT JUICE WITH FIBRES AS DRYING AID: NOZZLE

A thesis presented in partial fulfilment of the requirements for the degree of

Doctor of Philosophy

in

Chemical and Process Engineering

at Massey University, Palmerston North, New Zealand.

Siti Nadjiha Mohd Rozali

2019

ABSTRACT

Spray drying of fruit juices is desirable as it produces dry powders which extend the shelf-life, reduce storage and transport costs, and produce a free-flowing powder which makes it easier to blend as an ingredient. Commercially, maltodextrin is added to the juices as a drying aid to increase the efficiency of the spray drying process. In this project, pomace fibres were investigated as an alternative drying aid. The main attraction of pomace fibres as a drying aid is the pomace fibres are originally derived from the fruits itself. This study explores the rheological behaviour of juice-fibre suspensions inside the spraying device, specifically the nozzle, to ensure high efficiency powder production by enabling atomization of the mixtures. This study also sought to determine the type of nozzle and operating conditions for efficient atomization of the juice-fibre suspensions inside the spray dryer.

Flow-fields inside a nozzle consists of shear and extensional flows. Previous studies on the shear rheology of fibre suspensions revealed the addition of fibres creates a non-Newtonian shear-thinning liquid. The studies on extensional rheology of fibre suspensions, however, were absent. It is widely known the atomization of liquids with both shear and extensional resistances, require additional energy for atomization when compared to Newtonian liquids or viscous non-Newtonian liquids of a similar intrinsic viscosity.

In this work, four types of fibres with different aspect ratios were investigated. Some of the significant and notable methods achieved during the study include 1) the use of capillary viscometer to examine the shear rheology of fibre suspensions at shear rates up to 20 000 s^{-1}, which represents the calculated shear rate experienced during atomization, 2) the building of a portable capillary breakup extensional rheometer to accurately characterize the extensional rheology of the fibre suspensions at high extensional strain rates and 3) the use of flash photography technique to capture the atomization patterns. Important findings from this work include:

- Fibre suspension is a non-Newtonian shear thinning liquid with shear viscosity dependents on the fibre aspect ratio. The shear thinning behaviour continued until the shear rate of 25 000 s^{-1} and a plateau occurred at 25 000 s^{-1} shear rate. The plateau is independent of the fibre aspect ratio.

- The fibre suspension exhibited extensional resistance. The extensional rheological properties of the fibre suspensions were dependent on fibre aspect ratio. When comparing between the shear and extensional rheology of a specific fibre suspension, the transient extensional viscosity, η_E^+ of the fibre suspension was relatively greater than its corresponding shear viscosity.
- The entrance pressure drop into the nozzle was significantly increased with the addition of fibre. This made the use of a pressure nozzle inefficient. It was advised by personal discussion with industry experts that rotary atomizers usually fail in atomizing extensional liquids, so its application was not explored in this study.
- Spray visualization showed the extensional resistance of the fibre suspensions significantly affected the atomization behaviour and pattern (droplet size distribution) by forming filament structures connecting successive droplets together. This pattern was absent in Newtonian atomization.
- Successful atomization of fibre suspensions was achieved by using a two-fluid nozzle at high atomizing air velocities and at air-to-liquid ratio above 0.25. At an atomizing air velocity of 150 m/s, the atomization performance is dependent on the fibre aspect ratio, but this effect was reduced at higher atomizing air velocities. At the highest tested atomizing air velocity of 240 m/s, all fibre suspensions yielded a volume-based average droplet size, D(v,50), of 200 – 250 μm.
- Using a two-fluid nozzle at high atomizing air velocities, the droplets sizes of the fibre suspensions insignificantly reduced when the temperature of the inlet fibre suspensions was increased. No change was observed to the atomization performance when an ultrasonic mechanism was added to the two-fluid nozzle as an attempt to improve the atomization performance.
- A method of predicting the atomization performance of a given two-fluid nozzle from its dimensionless numbers, for actual spray dryer applications, was demonstrated and the results showed that the two-fluid nozzle can be used inside a spray dryer if the air-to-liquid ratio exceeds 0.25.

Overall, the methodology used in this thesis provides a systemic means of investigating the suitability of an atomization method for the spraying of a non-Newtonian fluid with extensional rheological properties.

ACKNOWLEDGEMENTS

A PhD is a rollercoaster ride of success and failure. This journey is never completed alone. There are many people who deserve to be thanked for the part they have played along the way.

Firstly, thanks to my primary supervisor, Professor Tony Paterson, for your guidance and support. Thank you for always challenging my ideas, I was able to grow as an independent thinker through this PhD journey. Also, thanks to Dr. Jason Hindmarsh, my co-supervisor, for the enthusiasm and encouragement that you have given me. I truly appreciate your guidance and knowledge that you have shared with me. I would like to acknowledge my co-supervisor, Dr. Lee Huffman, for the words of encouragement and the valuable insights that you have given me. I would like to thank the Ministry for Business, Innovation and Employment (MBIE) New Zealand for the funding provided through Food Industry Enabling Technologies (FIET) program that has enabled this project to proceed.

Thanks to the staff in the School of Food and Advanced Technology, especially John Edwards, Ian Thomas, Anthony Wade, Ann-Marie Jackson, Glenda Rosoman, John Pedley and Hannah Vale. I truly appreciate the sincere advices, knowledge, lab assistance and time that all of you have given me. I feel very grateful to have had the opportunities to learn a lot of things while working with all of you. Also, thanks to the other postgraduate students who helped me survive the process, especially Aiman, Jolin, Sebastian, Meghan and Marzie.

I am indebted to my family and friends for the support throughout my PhD journey. I certainly could not have done it without all of you. Special thanks to my husband; Aiman Jamsari, my parents; Mohd Rozali Idris and Marshita Dahlui, my siblings and all my friends for the love, support and encouragement.

TABLE OF CONTENTS

LIST OF FIGURES

LIST OF TABLES

NOMENCLATURE

μ_0	Newtonian shear viscosity or zero-shear viscosity (Pa.s)
μ_{app}	apparent shear viscosity (Pa.s)
μ	shear viscosity (Pa.s)
η_E^+	transient extensional viscosity (Pa.s)
ε	Hencky strain
$\dot{\varepsilon}$	extensional/strain rate
$\dot{\gamma}$	shear rate (s^{-1})
σ	surface tension (mN/m)
ρ	density (kg/m^3)
θ	contact angle (°)
$\emptyset$	volume fraction of fibre suspensions
$\emptyset_C$	critical volume fraction based on fittings
$\emptyset_{C,actual}$	actual critical volume fraction based on pumping
$\emptyset_{C,f}$	theoretical critical volume fraction for fibres, rods or elongated particles
$[\eta]$	intrinsic viscosity
A	constant in Arrhenius equation
C	correlation coefficient
$\langle d \rangle_{VE}$	number average droplet sizes for viscoelastic liquid, D(n,50)
D	tube diameter (µm)
D_f	fibre diameter (µm)

De	Deborah number
D_J	orifice or jet diameter (mm)
D_{mid}	mid-plane diameter of a filament (mm)
D_0	initial filament mid-point diameter in extensional rheometer test (mm)
$D(t)$	filament mid-point diameter in the extensional rheometer test, at a specific time (mm)
D_P	piston diameter (mm)
E_a	activation energy for viscous flow (kJ/mol)
E_Y	Young's modulus
g	gravitational constant (m/s^2)
H	gap distance between cup and bob in the coaxial cylinder (mm)
h_0	initial separation between upper and lower piston on the portable extensional rheometer (mm)
k	consistency index ($Pa.s^n$)
l_w	wetted length of Wilhelmy plate (m)
L	fibre length (µm)
L_0	initial gap between pistons (mm)
L_f	final gap between pistons (mm)
n	flow index
n_f	number density of fibres ($1/ \mu m^3$)
Oh	Ohnesorge number
P	pressure (Pa)

P_w	Wilhelmy force (mN)
Q_L	liquid flow rate (mL/min)
R	gas constant (kJ/mol.K)
R_0	initial radius of a liquid before stretching on the portable extensional rheometer (mm)
S_{eff}	Effective stiffness of fibres
T	temperature (°C or K if in Kelvin)
Tr	Trouton ratio
τ	stress tensor
τ_{shear}	shear stress (Pa)
τ_r	relaxation time (s)
τ_R	Rayleigh timescale (s)
U_A	velocity of atomizing air (m/s)
U_L	velocity of liquid (m/s)
V	volume (cm^3)
We	Weber number
Re	Reynolds number

LIST OF PUBLICATIONS AND CONFERENCES

Studies completed during candidature have been published or presented in the following communications:

Peer-reviewed papers:

Rozali, S. N., Paterson, A. H., Hindmarsh, J. P., & Huffman, L. M. (2019). Theoretical prediction of atomization performance of fibre suspensions and the effect of feed temperature and air velocity. *Journal of Food Engineering, 269*.

Rozali, S. N., Paterson, A. H., Hindmarsh, J. P., & Huffman, L. M. (2019). Atomization behaviour of juice-fibre suspensions in a two-fluid nozzle. *Journal of Food Engineering, 256*, 53-60.

Rozali, S. N., Paterson, A. H., Hindmarsh, J. P., & Huffman, L. M. (2019). Understanding the shear and extensional properties of pomace-fibre suspensions prior to the spray drying process. *LWT-Food Science and Technology*, *99*, 138-147.

Conferences, symposiums:

Rozali, S. N., Paterson, A. H., Hindmarsh, J. P., & Huffman, L. M. (2019). Atomization of juice-fibre suspensions in a two-fluid nozzle. Oral presentation at 10th International Conference on Food Engineering and Biotechnology 2019, 26th – 29th March, Tokyo, Japan.

Rozali, S. N., Paterson, A. H., Hindmarsh, J. P., & Huffman, L. M. (2018). Atomization of fruit juice. Oral presetation at The New Zealand Institute of Food Science and Technology (NZIFST) Annual Conference 2018, 3rd – 5th July, Hamilton, New Zealand.

Rozali, S. N., Paterson, A. H., Hindmarsh, J. P., & Huffman, L. M. (2017). Characterization of shear and extensional rheology of fibre suspensions and its atomization behaviour. Oral presentation at 19th Annual Conference of ILASS-ASIA (Institute for Liquid Atomization and Spray Systems – ASIA) 2017, 18th – 21st October, Jeju Island, Korea.

Rozali, S. N., Paterson, A. H., Hindmarsh, J. P., & Huffman, L. M. (2017). Characterization of shear and extensional rheology of fibre suspensions. Oral presentation at 3rd International Conference on Rheology and Modelling of Materials 2017, 2nd – 6th October, Miskolc-Lillafured, Hungary.

Rozali, S. N., Paterson, A. H., Hindmarsh, J. P., & Huffman, L. M. (2017). Atomization of fruit juice: Rheology. Oral presentation at Food Industry Enabling Technologies (FIET) Annual Symposium 2017, 14th – 15th June, Palmerston North, New Zealand.

Rozali, S. N., Paterson, A. H., Hindmarsh, J. P., & Huffman, L. M. (2016). Nozzle design for the spray drying of fruit juices: Overview. Oral presentation at Food Industry Enabling Technologies (FIET) Annual Symposium 2016, 21st – 22nd July, Palmerston North, New Zealand.

Chapter 1 Introduction

Spray drying of fruit juice is a problematic industrial process with the aim to increase the shelf life of the juice and ease of food handling. Spray drying of fruit juice requires the addition of a drying aid into the juice to improve the spray drying performance and increase the product yield because the fruit sugars and fruit acids present in the juice cause the dried powders to be sticky. Usually, maltodextrin is used as the drying aid as this increases the glass transition temperature of the amorphous structure formed by the sugar and acid molecules during drying. Cheuyglintase (2009) introduced a new drying aid where they used carrot fibre to enable them to dry apple juice. This idea has been put forward that the pomace from the fruit might also be used as a drying aid to replace the maltodextrin.

Introduction of fibres as a drying aid into the fruit juice creates a clean-labelling juice powder and at the same time maintains a total utilization of the fruit nutrients. The accomplishment of using fibres as a drying aid will attract many food industries in New Zealand and overseas to change into creating clean-labelling products. At the same time, the pomace fibres, which are usually treated as waste, will find a new purpose. These advantages benefit both consumers and suppliers. To accomplish these aims, it will be necessary to understand the overall fluid behaviour of the fruit juice once fibres are added. Fruit juice are simple Newtonian liquids, and many have successfully spray dried fruit juice with various types of drying aid with the main one being maltodextrin.

Spray drying is divided into two major processes; the first stage is the atomization of the liquid into droplets and the second stage is the drying of the droplets into powder. To be able to use the fibres as a drying aid to improve the drying performance, the fibres that are incorporated into the fruit juice must first be successfully atomized. It was realized that the introduction of fibres into the fruit juice would probably change the fruit juice from a simple Newtonian liquid into a liquid with non-Newtonian behaviours. From the literature, the behaviour, or rheology of a liquid, is the key parameter that controls the atomization performance inside a spray dryer. The questions to be addressed by this project are:

A) Is it possible to spray or atomize the fibre suspension from a liquid into droplets?
B) What factors influence the successful atomization from a liquid into droplets?
C) What type of atomization technique, or what type of atomizer can be used to achieve the successful atomization from a liquid into droplets?

D) Is the selected atomization technique or atomizer able to produce droplets as needed by the drying stage?
E) What are the limitations of the findings?

To answer question A, the questions B – D must be investigated first. In order to investigate B, the study will explore the rheology of the fibre suspensions. This includes the study on the shear rheology and extensional rheology of the fibre suspensions. Shear rheology of fibre suspensions has been well-explored and well-explained in the literature, but not in relation to the atomization process. In this thesis, the shear rheology of fibre suspensions will be examined in depth, specifically in relation to the atomization process. Studies on the extensional rheology are very scarce relative to the shear rheology.

Overall, the main aim of the study is to atomize fibre suspensions. This thesis investigates the potential atomization techniques and methods based on a deep understanding and profound analysis of the rheology of the fibre suspensions. To achieve the goal, three hypotheses are proposed:

1. Fibre suspensions exhibit a shear-thinning property with Newtonian plateau limitation.
2. Fibre suspensions exhibit an extensional resistance which might limit nozzle performances.
3. Air-assisted nozzles possibly can atomize fibre suspensions better than other nozzles.

The next Chapter 2 summarizes the findings and limitations based on the current literature that helped in building the hypotheses. The experimental plan in Chapter 3 outlines the detailed methods and equipment that has been developed to answer the hypotheses. Chapters 4 and 5 discuss the shear and extensional rheology of fibre suspensions, respectively. Chapter 6 analyses the atomization performance of fibre suspensions, and Chapter 7 summarizes the conclusions.

Chapter 2 Literature review

This section is divided into four parts. Section 2.1 starts with the basic mechanism of Newtonian atomization. Section 2.2 provides the background information on the rheology of non-Newtonian liquids, which includes the shear and extensional rheology, and Section 2.3 explains the breakup and atomization of the non-Newtonian liquids. Section 2.4 discusses briefly the different types of nozzle in practice nowadays.

2.1 Newtonian breakup

Newtonian fluids exhibit constant viscosity which means the viscosity is independent of shear rate and deformation time. When a bulk of the Newtonian liquid is injected through a nozzle into a gaseous medium or air surrounding (e.g. a liquid jet or sheet into a stationary or co-flowing gas), perturbations will grow on the liquid surface which will then induce disturbances in the liquid and cause the breakup of the bulk liquid into droplets; this initial disintegration process is referred to as primary breakup. This phenomenon is due to the competition between disruptive and cohesive or stabilizing forces, where the former forces overcome the latter (Lefebvre, 1988). The disruptive forces include kinetic energy, friction, gravity, interface shearing, pressure fluctuations and aerodynamic instabilities. Meanwhile, the stabilizing forces within the liquid consist of surface tension and shear viscosity. Secondary breakup occurs when large droplets produced in primary breakup become unstable as they exceed a critical size. Hence, a secondary breakup is often known as the continual disintegration of primary droplets into smaller droplets. Final droplet size distribution in sprays thus is dependent on both primary and secondary breakups.

Rayleigh (1878) is the first that predicted the collapse of a laminar liquid jet when injected into a still gas. By neglecting aerodynamic interactions, Rayleigh concluded that the liquid jet collapses if the wavelength of the surface disturbances, λ, exceeds the jet circumference. After that, many researchers have since conducted extended Rayleigh's analysis by accounting for the effects of liquid viscosity and aerodynamic (relative velocity at the air-liquid interface), together with experimental investigations on the breakup of liquid jets which then contributes to the current well-known series of different disintegration regimes

(Castleman, 1931; Ohnesorge, 1936; Reitz, 1978; Weber, 1931). One of the important analysis proposed by Ohnesorge (1936) suggested the relative importance of inertial, viscous and capillary forces. He classified and plotted an atomization regime according to liquid Reynolds number, *Re* and Ohnesorge number, *Oh* as shown in Equations 2.1 and 2.2, respectively.

$$Re = \frac{\rho_L U_L D_J}{\mu_L} \qquad \text{Equation 2.1}$$

$$Oh = Z = \frac{\mu_L}{\sqrt{\rho_L \sigma_L D_J}} \qquad \text{Equation 2.2}$$

where μ_L (Pa.s) is the liquid shear viscosity, σ_L (N/m) is the liquid surface tension, ρ_L (kg/m^3) is the liquid density, D_J (m) is the orifice or jet diameter and U_L is the liquid velocity (m/s). Reynolds number determines the state of the jet's flow, either laminar or turbulent. In a jet, the *Re* needs to be large; *Re* >> 10^3, in order for the jet to become turbulent near its nozzle (Lasheras et al., 1998). Meanwhile, *Oh* provides a convenient way to determine the relative importance of liquid viscosity and surface tension. It is solely a reflection of the thermophysical properties of the fluid at a given size of nozzle. Typically, low viscosity liquids such as water and aniline, with a jet diameter of 1 mm, would have a very small *Oh* i.e. *Oh* << 1. However, for viscous liquids such as glycerine and oils, the *Oh* can exceed unity.

Reitz (1978) extended Ohnesorge study and concluded that a breakup of a liquid jet in stationary gas could be divided into four regimes, as shown in Figure 2.1, which consists of Rayleigh, first wind-induced, second wind-induced and atomization regimes. Rayleigh breakup regime is marked by the formation of radially symmetric perturbation on the liquid jet surface due to the capillary forces. This is obvious from the image of Regime 1 in Figure 2.1. At this stage, aerodynamic effects are negligible. The jet breakup length and the jet velocity are linearly related. The final droplet sizes are in the order of D_J. With increasing jet velocity thus *Re*, the aerodynamic forces become progressively more important relative to the capillary forces. This occurs during the first wind-induced regimes. At this regime, the liquid jet starts to oscillate about its axis and thus produces a sinuous wave. This is obvious from the image of Regime 2 in Figure 2.1. The sinous wave eventually collapses many jet diameters downstream of the nozzle under the influence of aerodynamic forces. The resultant droplet sizes are comparable to the D_J. In the second wind-induced regime,

at a greater jet velocity, the intensified relative motion between the liquid jet and surrounding gas promotes the development of short-wavelength perturbations when compared to the first wind-induced regime. At this regime, aerodynamic forces start to strip ligaments and droplets directly off the ruffled or disturbed liquid jet. The breakup takes place only several jet diameters downstream of the nozzle. The resultant droplet sizes are much smaller than the D_J. The use of nozzles in any application typically operates in the atomization regime. As shown in Figure 2.1, the atomization regime occurs at significantly high *Re*, which allows the jet to disintegrate almost spontaneously within a short distance from the nozzle exit and to form a conical spray shape with its vertex within the nozzle (Reitz & Bracco, 1986). The atomization regime is marked by a complete and chaotic disintegration of the liquid jet immediately downstream of the nozzle. This is obvious from the image of Regime 4 in Figure 2.1. Compared to the other first three regimes which their underlying mechanisms are well developed and understood, the mechanisms for atomization regime is still inconsistent and unclear (Lefebvre, 1988; Liu, 1999; Reitz & Bracco, 1982). Overall, it is widely accepted that the liquid jet turbulence disrupts the smooth liquid jet surface, thus making it more susceptible to aerodynamic effects. The aerodynamic effects contributed by the relative motion of liquid and gas then breaks the unstable ligaments from the bulk liquid (Lefebvre, 1988; Liu, 1999). It means that the atomization mechanism of a liquid is influenced by the liquid jet turbulence and aerodynamic interaction.

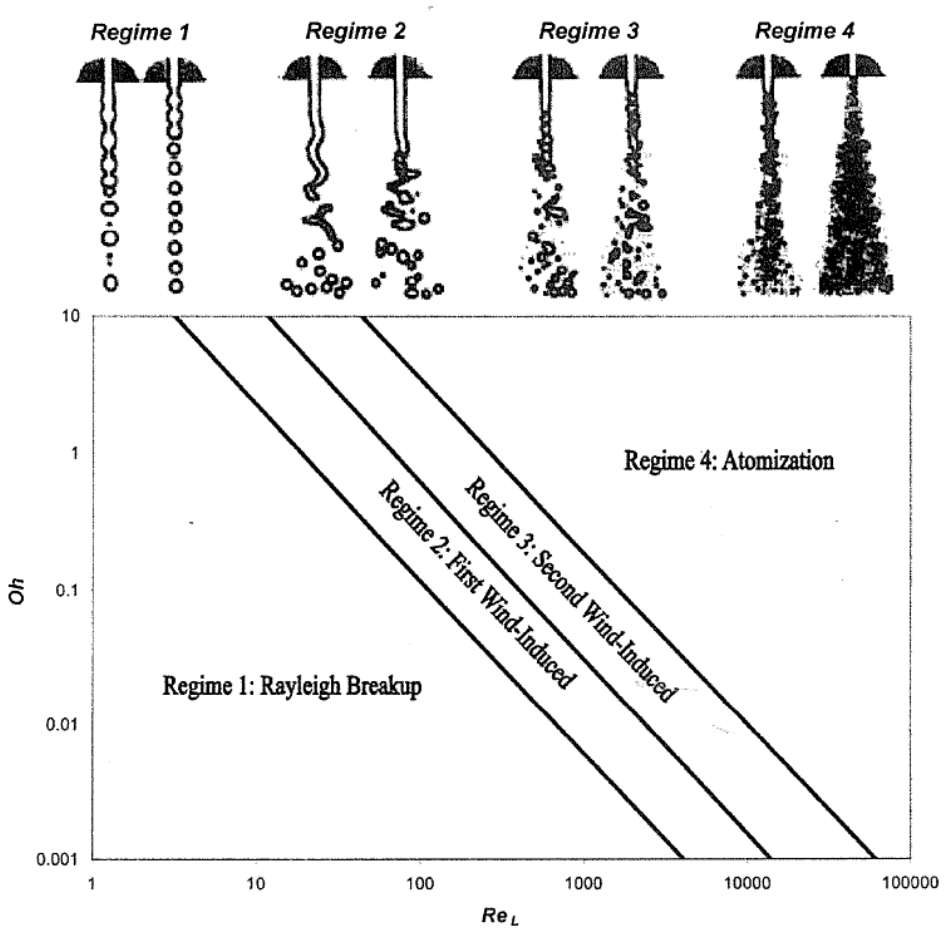

Figure 2.1 Breakup regimes of Newtonian liquid jet proposed by R. D. Reitz (1978) and Ohnesorge (1936). (Regime 1) Rayleigh regime, (Regime 2) first-wind induced regime, (Regime 3) second-wind induced regime and (Regime 4) atomization regime.

Another method for atomization involves the injection of a relatively slow-moving liquid jet into a high-speed co-flowing air or gas jet. This method is often termed twin-fluid atomization. None of the *Re* and *Oh* explains the effects of increasing the relative velocity between the liquid and air. Farago and Chigier (1990) and Lasheras et al. (1998) were the first to be able to demonstrate the importance of the aerodynamic Weber number, *We*, during the two-fluid atomization. Weber number, *We*, as shown in Equation 2.3, is the ratio between the aerodynamic deformation forces exerted on the liquid and the restoring surface tension forces.

$$We = \frac{\rho_L (U_L - U_A)^2 D_J}{\sigma_L} \qquad \text{Equation 2.3}$$

where ρ_L (kg/m^3) is the liquid density, D_J (m) is the orifice or jet diameter, σ_L (N/m) is the liquid surface tension, U_L (m/s) and U_A (m/s) are the liquid and air velocities respectively. Chigier and Farago (1992) have classified four main regimes of the breakup involving water and high-speed air jet through the analysis of high-speed photographs. The regimes were plotted based on *Re* and *We*, as shown in Figure 2.2. The regimes or types of breakup consist of Rayleigh breakup, membrane-type breakup and fibre-type breakup. During the Rayleigh breakup, the liquid jet collapses into droplets without forming any ligaments, membranes or fibres. The resultant droplet size is in the order of the jet diameter. Axisymmetric Rayleigh breakup occurs when $We < 15$ while non-axisymmetric Rayleigh breakup happens when $15 < We < 25$. Axisymmetric Rayleigh breakup produces helical structures, as shown in Figure 2.2, which resembles the first wind-induced regime in Figure 2.1. During both types of Rayleigh breakup, the aerodynamic effects are important with more intense effect during the non-axisymmetric Rayleigh breakup, where the interaction between the jet and surrounding turbulent air structures is obvious from the jet's orientation in Figure 2.2. With increasing air velocity thus, *We*, a membrane-type breakup takes place at $25 < We < 70$. At this regime, the high air velocity flattens the round liquid jet into a sheet or membrane. The aerodynamic interactions produce surface waves. As shown in Figure 2.2, liquid accumulates at the membrane edge that forms a thick frame that bounds a thin internal membrane. The thick frame further collapses into large droplets via the non-axisymmetric Rayleigh breakup while the thin membrane bursts into a multiplicity of smaller droplets. The resultant droplet size is about one order of magnitude smaller than the jet diameter. Finally, at a much greater air velocity where $We > 70$, the aerodynamic forces drag and strip away small-scale ligaments or also known as fibres from the crests or waves formed on the liquid jet. The dragging and stripping quickly detach the fibres from the liquid jet or core. The fibres further collapse into droplets via the Rayleigh mechanism. At this stage, the droplets formed are a few orders magnitude smaller than the jet diameter. The liquid core continues to accelerate under the influence of the high air velocity at a position further downstream of the nozzle and more ligaments and fibres are stripped. Here the droplet sizes are larger than those produced immediately at the nozzle exit.

Various researchers suggested different values for a critical *We* above which the droplet disintegrates. For example, Hanson et al. (1963) recommended a value of 10 while Derby (2010) proposed that $We_{\text{crit}} \geq 4$, specifically for a drop in inkjet printing. Besides that, Hinze (1955) suggested that the value is less than 10 when the flow is turbulent. Based on

Wierzba (1990), various experimental data from the literature show that the critical Weber numbers are scattered over a very wide range from 2.2 to 99.6.

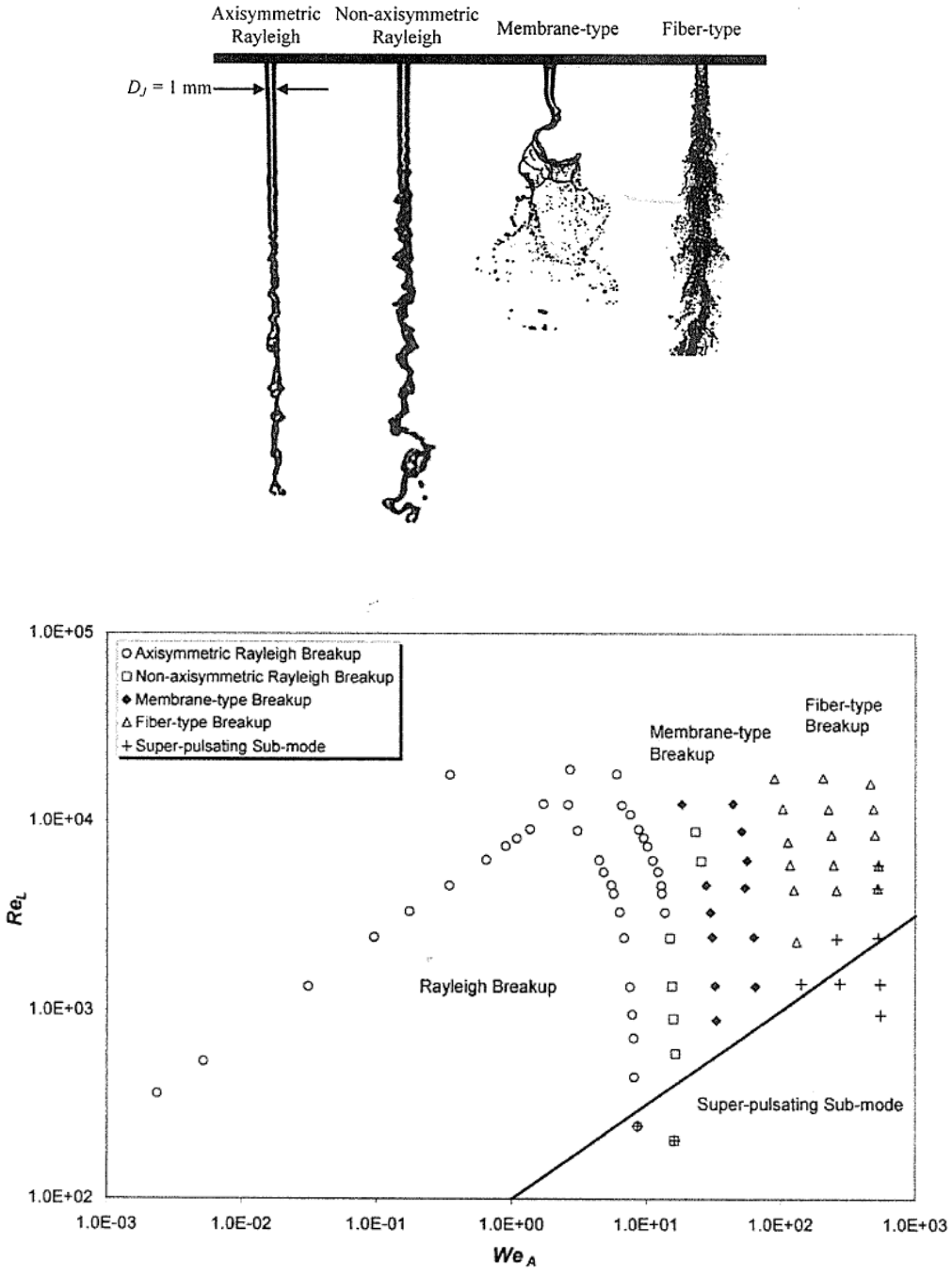

Figure 2.2 Breakup regimes during a twin-fluid atomization that consists of Rayleigh regime, membrane-type regime and fibre-type regime (Chigier & Farago, 1992).

Theoretically, at low or moderate *We*, the jet disintegrates into a bag membrane shape which flattens and breaks up into small droplets. At higher *We*, the surface of the jet tears into liquid fibres or ligaments which produces droplets at the end (Chigier & Farago, 1992; Joseph et al., 1999; Krzeczkowski, 1980; Nicholls & Ranger, 1969; Pilch & Erdman, 1987). The low and high *We* correlate to low and high gas velocities, respectively. Figure 2.3 illustrates the effect of increasing air velocity, thus *We*, which shows that when the jet was exposed to higher air velocities, jet disintegration into ligaments and fibres was more prone to occur.

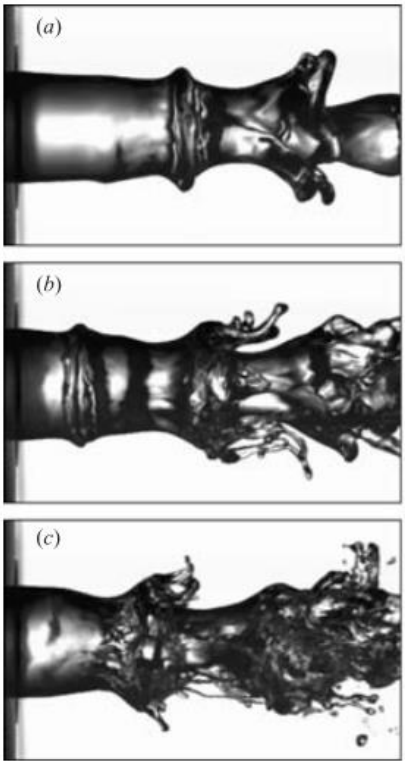

Figure 2.3 Development of instabilities that contribute to jet breakup at different air velocities, U_A (a) 24 m/s, (b) 27 m/s and (c) 32 m/s (Marmottant & Villermaux, 2004).

The rate of stretch and the evolution of diameter of the ligaments at breakup depend strongly on the air velocity, U_A, with higher velocity contributes to shorter ligament length at the breakup and thus faster breakup times, as shown in Figure 2.4 (Marmottant & Villermaux, 2004).

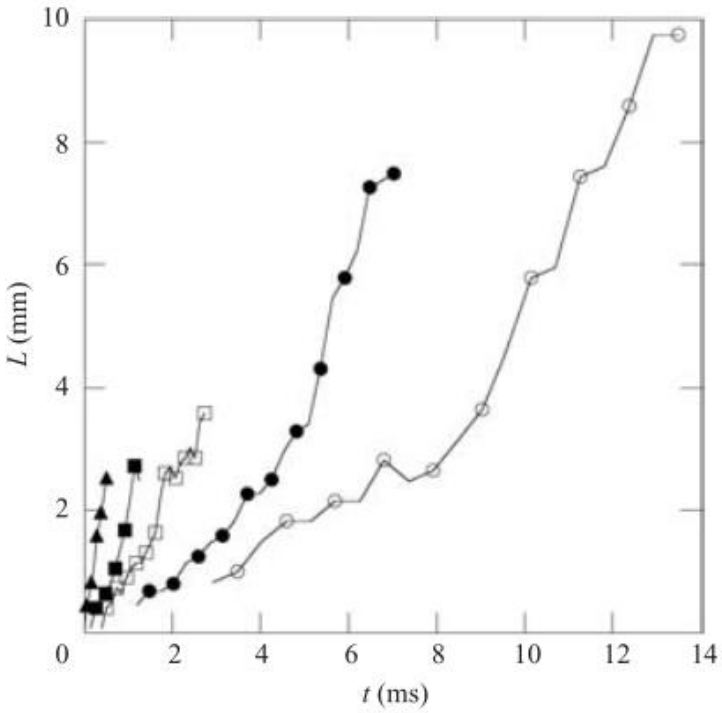

Figure 2.4 Ligament lengths at breakup as a function of time when using water. The end of each curve indicates the breakup. (○) U_A = 25 m/s, (●) U_A = 29 m/s, (□) U_A = 34 m/s (■) U_A = 40 m/s and (▲) U_A = 50 m/s (Marmottant & Villermaux, 2004).

A further example is illustrated in Figure 2.5, which demonstrates that a higher *We* induces atomization of liquids. Figure 2.5 pairs the effect of *We* and *Oh* and proves that a higher viscosity liquid which the *Oh* is closer to unity, requires a greater *We* to achieve the atomization. Based on Figure 2.5(b), water with a constant shear viscosity of 0.98×10^{-3} Pa.s, can be easily atomized at *We* = 153. However, 85% glycerol solution, which has a viscosity in the range of 63×10^{-3} to 78×10^{-3} Pa.s, could not be atomized at *We* = 153. Based on Figure 2.5(c), the glycerol solution can be said to undergo an early stage of atomization at *We* = 640, which is approximately four times greater than the *We* required by water.

Faeth et al. (1995) created a deformation and breakup regimes map which correlates the *We* with *Oh*, based on the available literature results. The regimes illustrated in the map, as shown in Figure 2.6, are mainly independent of liquid viscous forces or $Oh < 1$. It is evident from the map that the transition from deformation to breakup regime requires increasing *We*, supporting the idea of higher velocities needed to achieve atomization. While the map was generated by focusing on non-viscous liquids, however, it shows a few significant features relating to viscous liquids. For example, while the value of *We* required for regime

transitions is relatively low for *Oh* < 0.1, the *We* required is relatively higher and progressively increases when *Oh* > 1. It is unclear whether a large value of *Oh* implies no breakup or simply means that a greater value of *We* is needed. Most existing studies and literature data are limited to insignificant *Oh*; *Oh* < 0.1, which makes it harder to predict the spray behaviour of viscous liquids.

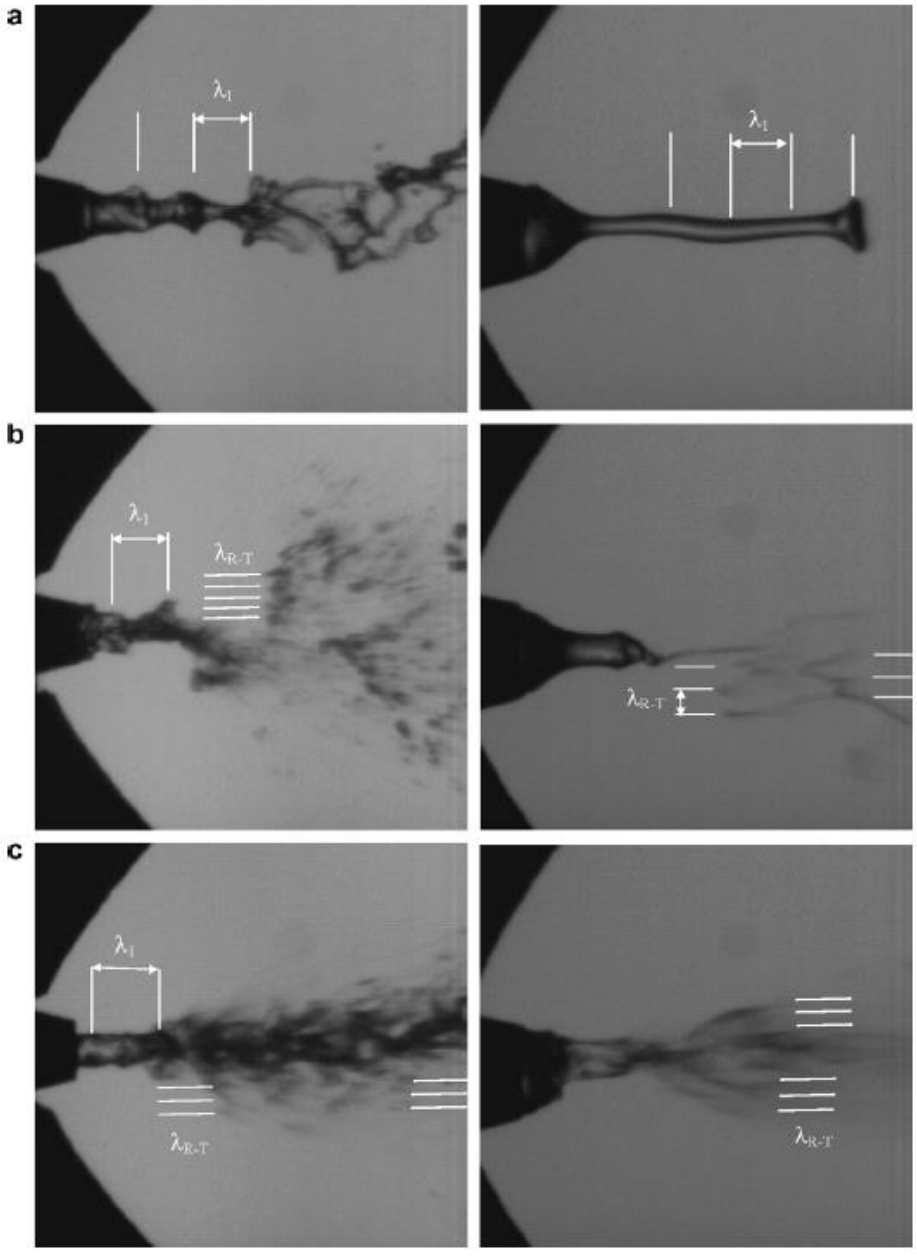

Figure 2.5 Atomization of water (left) and 85% glycerol solution (right) at increasing air velocity. (a) *We* = 60, (b) *We* = 153 and (c) *We* = 640 (Aliseda et al., 2008).

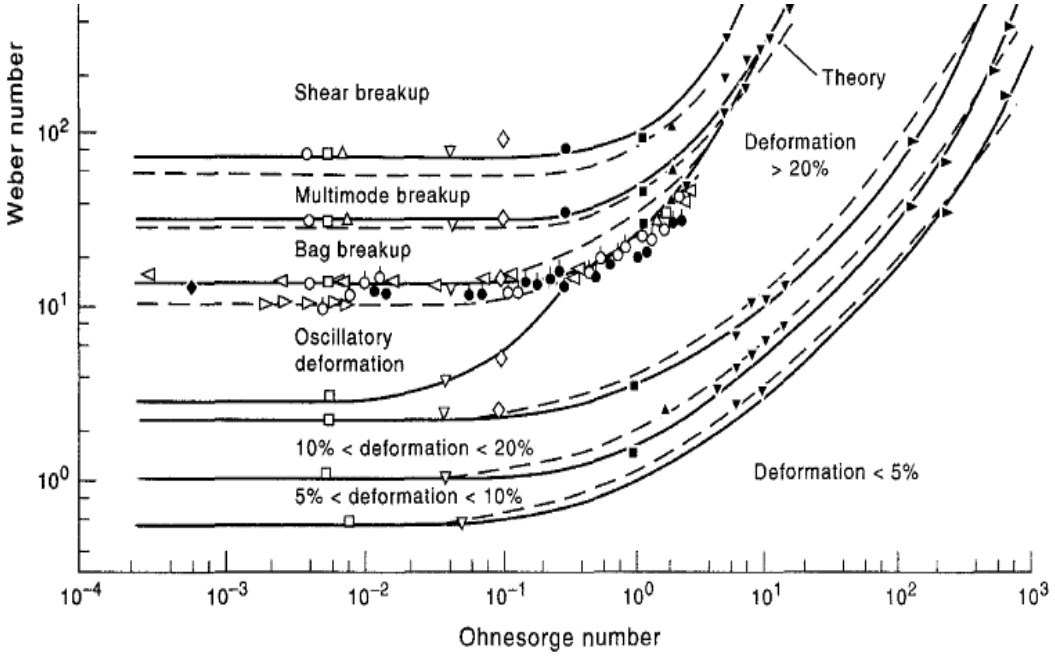

Figure 2.6 Deformation and breakup regimes map designed mainly for non-viscous liquids (Faeth et al., 1995).

In this century, a lot of the focus on jetting and breakup application has been carried out in inkjet printing technology. Generally, inkjet printing is based on a drop-on-demand (DOD). Specifically, it deposits a precise quantity of ink in the form of droplets by applying a short pressure pulse through a nozzle with a diameter of typically between 20 and 50 μm (Le, 1998). The ink meniscus at the end of the nozzle orifice is maintained by surface tension. A piezoelectrically induced pressure wave then propagates against the surface tension of the ink fluid which causes a small droplet to be ejected from the nozzle. Many studies have concentrated on the jetting and breakup performance in inkjet printing (Reis and Derby, 2000; Dong et al., 2006; Jang et al., 2009; Lee et al., 2012). The important parameters affecting the atomization and thus the printability of inkjet fluids are viscosity, density, and surface tension. These fluid properties influence the drop formation mechanism and the subsequent drop size at a given voltage.

2.2 Non-Newtonian rheology

2.2.1 Shear rheology

Rheology is the study of flow and deformation of matter, under the application of shear and normal stress. Non-Newtonian liquids includes dilatant or shear-thickening, pseudoplastic or shear-thinning, Bingham plastic, rheopectic and thixotropic. Shear viscosity of non-Newtonian liquid can increase (dilatant or shear-thickening) or decrease (pseudoplastic or shear-thinning) as the shear rate increases. Meanwhile, at a constant shear rate, rheopectic liquids exhibit an increase in the shear viscosity as a function of time, as opposed to thixotropic liquids (Barnes et al., 1989). These behaviours are shown in the linear plots in Figures 2.7 and 2.8. Unlike Newtonian liquids, the microstructure of non-Newtonian liquids can change under shear, which is why their macroscopic property such as shear viscosity can be affected by deformation. Regardless of the nature of the liquid; either Newtonian or non-Newtonian, the shear viscosity decreases with increasing temperature.

Fitting of mathematical models to the experimental shear flow data such as power-law model, as shown in Equation 2.4, is a relatively straightforward and it contains two parameters which are consistency index, *k* and power-law or flow index, *n*.

$$\tau_{shear} = k \times \dot{\gamma}^{n} \qquad \text{Equation 2.4}$$

where τ_{shear} (Pa) is the shear stress and $\dot{\gamma}$ is the shear rate. $n < 1$ for shear-thinning liquids while $n > 1$ for shear-thickening liquids. As Newtonian liquid is independent of shear rates, the n is always equal to 1. The power-law model is effective in predicting the shear behaviour of most liquids, but limitation exists at high $\dot{\gamma}$ values. For example, for shear-thinning liquids, the predicted shear viscosity decreases indefinitely with increasing $\dot{\gamma}$. This means that the liquids will have an inifinite viscosity at rest and zero viscosity at an infinite $\dot{\gamma}$. However, in reality, the liquids have both maximum and minimum shear viscosity determined by the physical chemistry at the molecular level. This means that the use of the power-law model is effective but valid across certain ranges of $\dot{\gamma}$ only. Unlike the power-law model, another mathematical model, known as Cross fluid model, incorporates the shear viscosity of a liquid at infinite shear rate, as shown in Equation 2.5. The Cross model covers the entire shear rate range.

$$\mu(\dot{\gamma}) = \mu_\infty + \frac{\mu_0 - \mu_\infty}{1+(k\dot{\gamma})^n} \qquad \text{Equation 2.5}$$

where μ (Pa.s) is the shear viscosity, μ_∞ (Pa.s) is the viscosity at infinite shear rate and μ_0 (Pa.s) is the viscosity at zero shear rate.

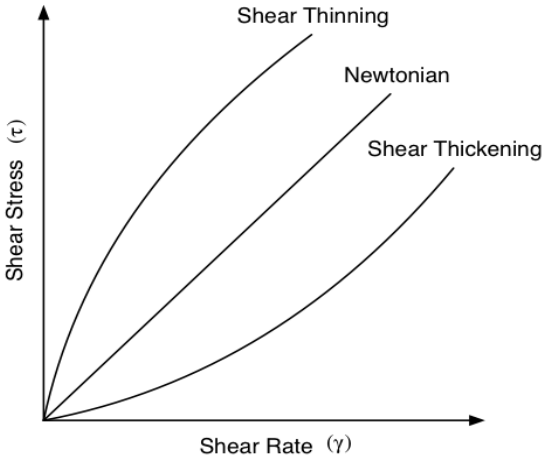

Figure 2.7 Variation of shear stress with shear rate for Newtonian and non-Newtonian liquids.

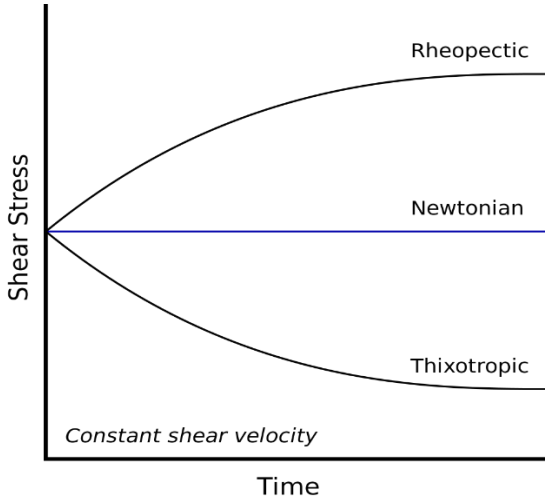

Figure 2.8 Variation of shear viscosity with time (at a constant shear rate) for non-Newtonian liquids.

The effect of volume fraction on shear viscosity is described by Krieger-Dougherty equation as follow:

$$relative\ viscosity,\ \eta_R = \frac{\mu}{\mu_0} = \left(1 - \frac{\emptyset}{\emptyset_C}\right)^{-[\eta]\emptyset_C} \qquad \text{Equation 2.6}$$

where $[\eta]$ is the intrinsic viscosity and equal to 2.5 for spheres, $\emptyset$ is the volume fraction of solid particles, $\emptyset_c$ is the critical volume fraction, μ and μ_0 are the viscosity of suspension and viscosity of medium respectively. There are other proposed relationships between volume fraction and shear viscosity of suspensions as explanied by Stickel and Powell (2005). Krieger-Dougherty equation shows that an increase in volume fraction increases the viscosity of suspensions. This is because, at higher volume fractions, the particles pack tightly together which make it harder for the particles to move freely and further induce particle-particle interactions. This is shown graphically by Hoffman (1972) and reproduced by Stickel and Powell (2005), as shown in Figure 2.9. Many previous authors suggest that it is convenient to assume that concentrated suspensions generally behave like shear-thinning liquids with Newtonian plateau limitation, before the onset of shear-thickening as the shear rates increases (Stickel & Powell, 2005).

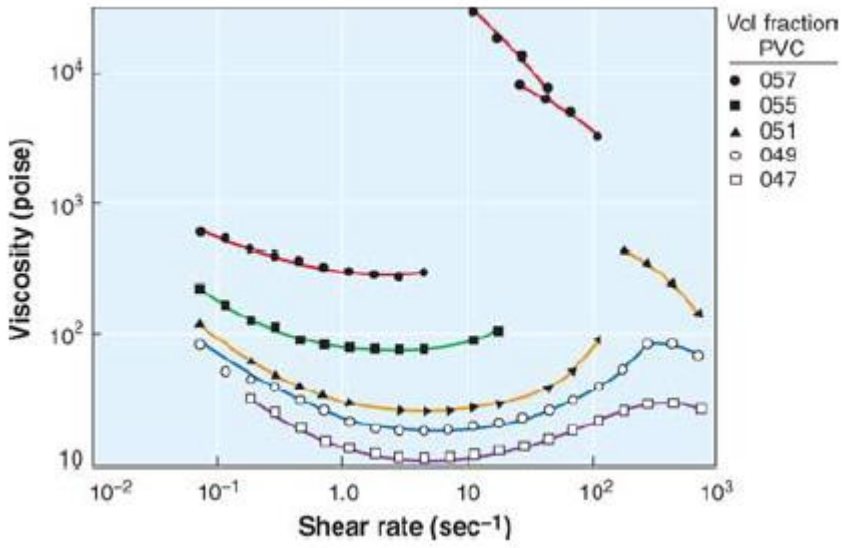

Figure 2.9 Effect of volume fraction on shear viscosity of suspensions (Stickel & Powell, 2005).

$\emptyset_C$ is often used as an adjustable parameter in viscosity models and for monomodel sphere, a range of reported theoretical values varies between 0.524 to 0.740. $\emptyset_C$ increases with size ratio up to about 10:1, which means that a polydisperse system yields lower viscosity values than a monodisperse distribution of either small and large particles. This is because, with

polydisperse sample, small particles can fill the gaps between the closely packed large particles, resulting in a greater allowable maximum volume fraction in the suspension (McGeary, 1961). Krieger-Dougherty equation is also supported by experimental work done by Bibbó (1987) and Djalili-Moghaddam and Toll (2006) specifically on nylon fibres and polyamide 66 fibres, respectively. They prove that viscosity increases with fibre content. Figure 2.10 shows that the highest volume fraction has the highest shear viscosity both at low and high shear rates. Meanwhile, the lowest volume fraction has a lower viscosity. Bibbó (1987) proves that fibre suspensions show a shear-thinning behaviour up to certain shear rates, and behave as Newtonian liquids afterwards due to a plateau limitation. The occurrence of shear-thickening behaviour after the plateau is uncertain.

The proposed relationships between volume fraction and suspensions shear viscosity and the theoretical values for $\emptyset_C$, were all build by considering spherical, or atleast particles with aspect ratio closes to unity. Aspect ratio, α, is the length to diameter of particles. Suspensions of fibres or rods usually have aspect ratio exceeds unity. Fibres, rods or elongated particles will pack differently compared to the spherical particle and thus, contributing to different values of $\emptyset_C$. Fibres have been widely used in composite systems, with predicted $\emptyset_{C,f}$ values between 0.785 and 0.907 (Pan, 1993; Shah et al., 2012). Evans and Gibson (1986) suggested a relationship of $\emptyset_{C,f} = kd/L$, but restricted to aspect ratios above 10 with *k* value of 5.3.

Djalili-Moghaddam and Toll (2006) use polyamide 66 fibres suspended in silicone oil. They use fibres with different length to diameter ratio, from α=39 to α=73. Figure 2.11 indicates that the shear viscosity increases with both volume fraction and aspect ratio. As the aspect ratio increases from 39 to 73 at a similar fibre fraction, the low aspect ratio fibre suspension yields a lower shear viscosity value when compared to the high aspect ratio fibre suspension. The same trend can be observed in Figure 2.12. Figure 2.12 shows that the shear viscosity increases with shorter fibre length. At a constant aspect ratio, longer fibres are made up of larger diameter which makes the absolute size of the fibres fatter than the shorter fibres. Fatter fibre size increases the distance between successive fibres and thus, hindering strong attractive forces between them. This allows the suspension to flow easily compared to the small fibre size.

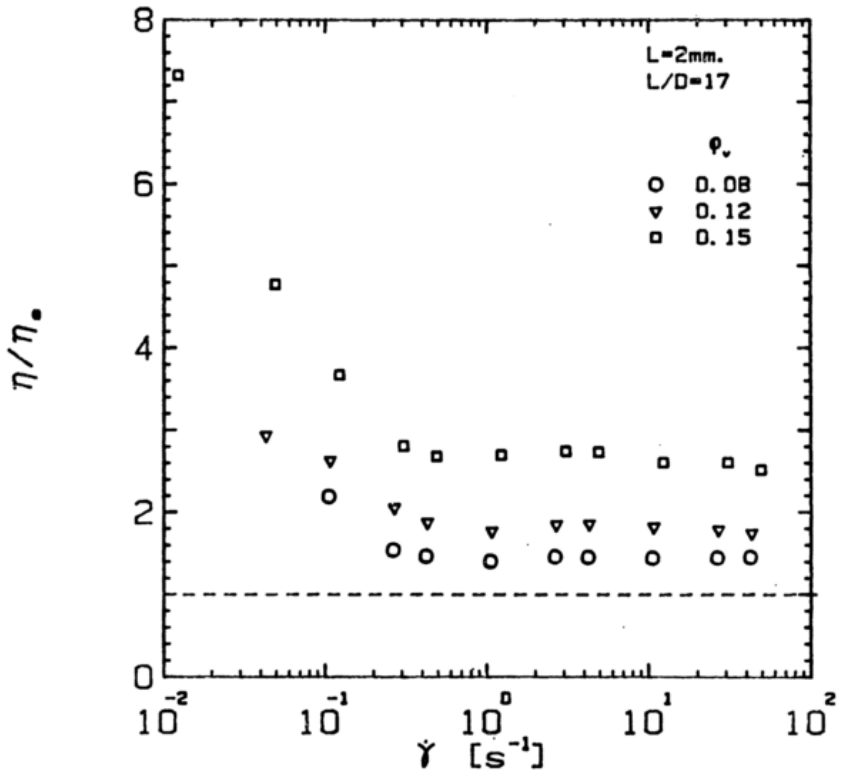

Figure 2.10 Shear viscosity as a function of shear rate at different volume fraction of fibres. (○) ∅ = 0.08, (inverted triangle) ∅ = 0.12 and (□) ∅ = 0.15 (Bibbó, 1987).

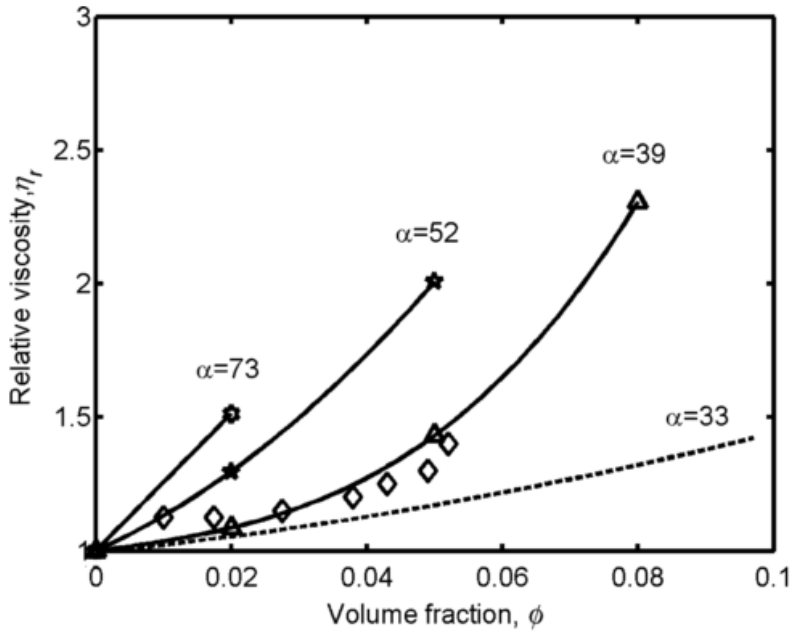

Figure 2.11 Relative viscosity as a function of volume fraction at different fibre aspect ratios (Djalili-Moghaddam & Toll, 2006).

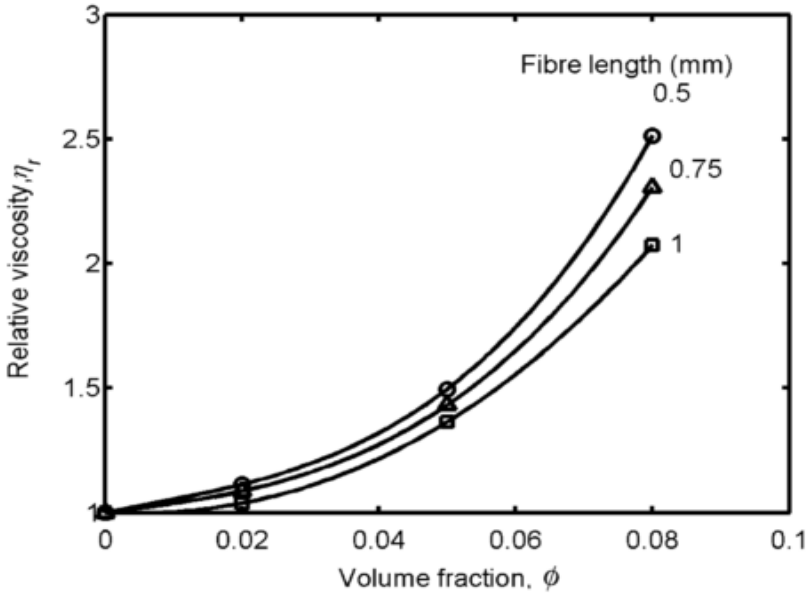

Figure 2.12: Relative viscosity as a function of volume fraction at a similar aspect ratio but different fibre lengths (Djalili-Moghaddam & Toll, 2006).

Many studies on fibre suspensions confirmed the shear thinning behaviour at low shear rates, but very limited knowledge is available on the behaviour of fibre suspension at very high shear rates, as needed in spraying applications. A study performed by Grigelmo-Miguel et al. (1999) proves that peach dietary fibre suspensions up to 20% behave as a pseudoplastic or shear-thinning fluid. Elleuch et al. (2008) shows that date dietary fibre suspensions also act as a shear-thinning fluid. Pulp suspension from hardwood Kraft also shows a shear-thinning behaviour up to 5% fibre fraction (Derakhshandeh et al., 2011). These studies were all conducted at relatively lower shear rates compared to the rates needed in spraying application.

The effects of fibre addition on the shear viscosity of the suspensions are very complex. So far, the factors that affect the suspension viscosity include the particle size and particle size distribution, volume fraction and particle shape which determines the aspect ratio. Other effects such as fibre curvature and fibre flexibility also affect the shear viscosity of the suspensions. Previous studies show that fibre curvature is one of the factors affecting the suspension viscosity (Anczurowski & Mason, 1967; Joung et al., 2002; Nawab & Mason, 1958). A study by Blakeney (1966) on nylon fibres proves that the effect of fibre curvature is significant as the suspension viscosity increases by an order of 10-15% when compared

to the straight fibre suspension. Figure 2.13 below shows the effect of curved fibres on suspension viscosity via a numerical simulation. The results are in agreement with Blakeney (1966), which indicates that curvature in fibres is a significant contributor to the increase in suspension viscosity.

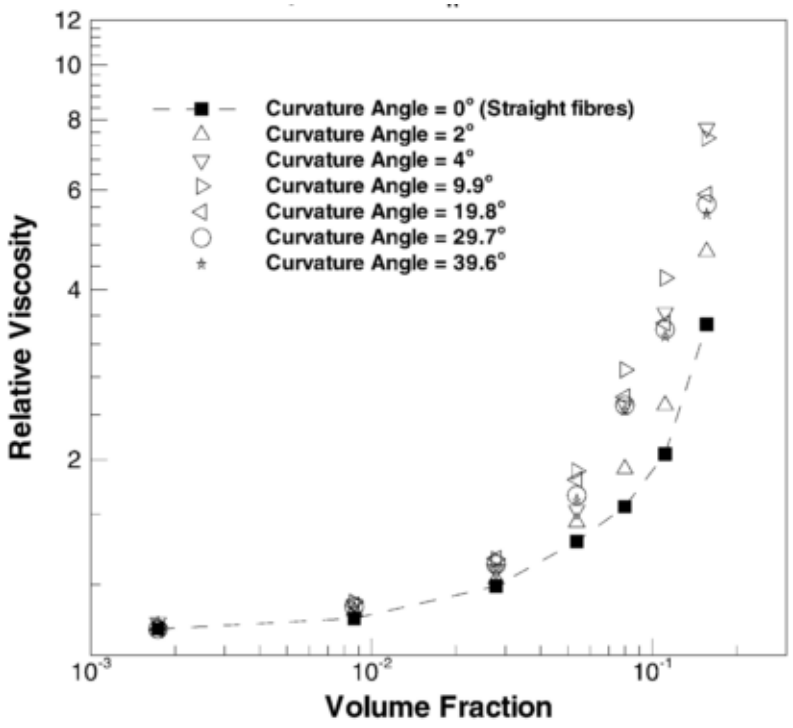

Figure 2.13 The viscosity of fibre suspension across increasing volume fractions, at different fibre curvature angles (Joung et al., 2002).

Based on Figure 2.13, the straight fibres can be seen to have the lowest viscosity at all volume fractions. The effect of fibre curvature on resultant viscosity is more pronounced at higher concentrations. Surprisingly, the highest viscosity is not displayed by the biggest curvature angle. This effect can be seen clearer in Figure 2.14. Based on Figure 2.14, at all volume fractions, the viscosity peak is displayed by the curvature angles in the range 5° < θ_{fibre} < 10°. Surprisingly, beyond 10°, the viscosity of the suspension decreases, although the viscosity is still greater than the viscosity of the straight fibres at 0°. This is in agreement with Andrić et al. (2014). They show that the viscosity decreases after reaching a maximum curvature value because the fibres now become coiled.

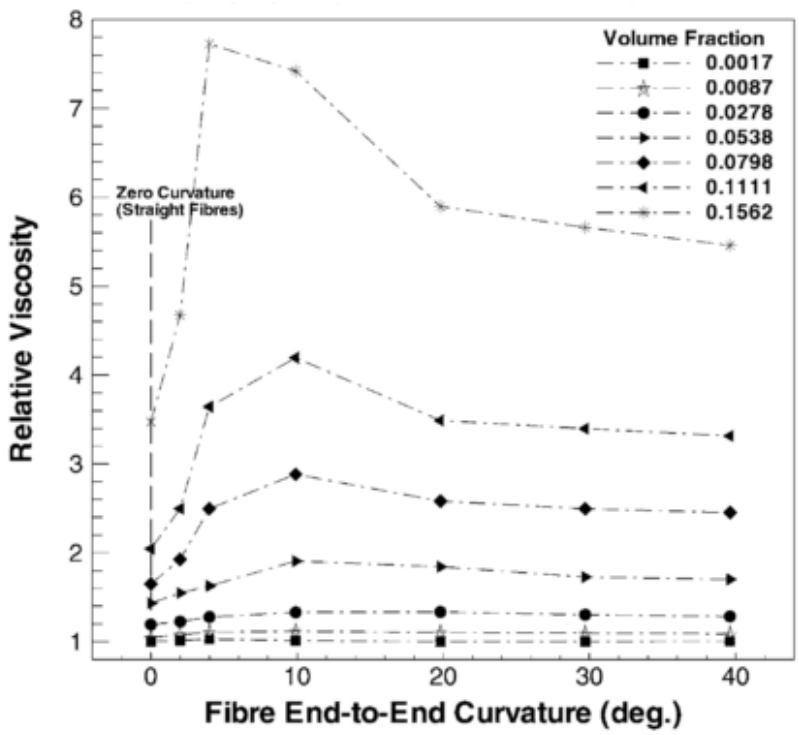

Figure 2.14 The effect of fibre curvature angles on the suspension viscosity (Joung et al., 2002).

Joung et al. (2002) show that the suspension viscosity is sensitive towards the fibre shape imperfections and the curvature effects need to be considered when dealing with fibres. The curvature also contributes to the misalignment of fibres during shear and thus increases the viscosity (Joung et al., 2002). Switzer and Klingenberg (2003) also compared the viscosity of straight and curved fibres. They found that the suspension viscosity of U-shaped fibres is significantly larger than those of the straight fibres. Even a small curvature deviation from a straight line resulted in a significant increase in the viscosity.

Ideal fibres are straight and have rigid physical properties while natural fibres have curves and great flexibility. These curved and flexible fibres have greater viscosity when compared to rigid fibres. According to Joung et al. (2001), the viscosity of concentrated flexible fibre suspensions is 7-10% greater in magnitude than the rigid fibre suspensions. Figure 2.15 shows that fibres with more flexibility exert a greater suspension viscosity. Glass fibres, which is the stiffest material, can be seen to behave quite similarly with rigid fibres. Meanwhile, nylon fibres, which can be categorised as flexible fibres, show a

significant difference in viscosity compared to the rigid fibres. From the graph, at low volume fractions, the effect of fibre flexibility on viscosity becomes negligible.

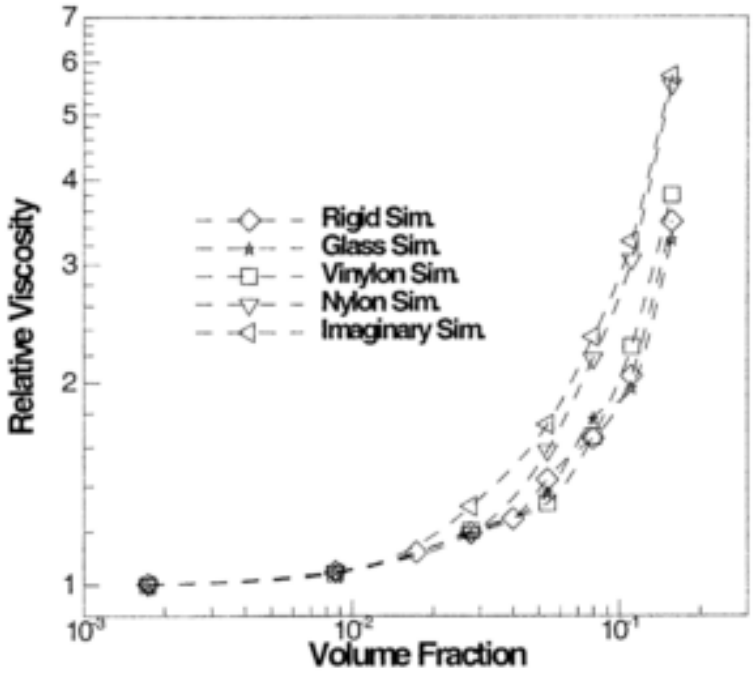

Figure 2.15 Viscosity of flexible fibres compared to rigid fibre at increasing volume fraction (Joung et al., 2001).

A few studies suggest that the flexibility of fibres contributes to a shear-thinning behaviour. This is because, the increase in fibres flexibility results in more configurations of fibres due to bending, which in turn favours the fibre-fibre contacts and thus, the fibre-fibre interactions. These interactions or flocculation create network-like structures with low mobility. However, if the shear rate is further increased, a reversal of the flocculation occurs, where these networks are destroyed and thus, lead to a shear-thinning behaviour (Keshtkar et al., 2010; Schmid et al., 2000).

Yamanoi et al. (2010) propose that the influence of flexibility on suspension viscosity can not be explained without considering other factors. For example, a similar type of two flexible fibre suspensions yield different suspension viscosity depending on the fibre aspect ratio. It means that various studies might propose different relationships between the fibres

flexibility and suspension viscosity, depending on the parameters being considered. Another example, in Andrić et al. (2014) study, they suggest that the shear viscosity decreases with fibre flexibility. However, this relationship is limited to the investigated ranges of fibre bending ratios only.

Effective stiffness, which characterized the relative importance of fibre stiffness, has been proposed by Switzer and Klingenberg (2003), as shown in Equation 2.7. It is used as a criterion for fibre flexibility.

$$S_{eff} = E_Y \pi D^4 / 64 \eta_m \dot{\gamma} L^4 \qquad \text{Equation 2.7}$$

where E_Y (Pa) is the Young modulus of the fibres, η_m (Pa.s) is the viscosity of suspending fluid and $\dot{\gamma}$ (s^{-1}) is the shear rate. As $S_{eff} \rightarrow 0$, the fibres behave like completely flexible threads, whereas for $S_{eff} \rightarrow \infty$, the fibres become rigid. Overall, most of the previous works and authors have shown and agreed that fibre flexibility enhances both viscosity and the storage and loss moduli (Keshtkar et al., 2009; Kitano et al., 1984; Kotsilkova, 1992; Soszynski & Kerekes, 1988).

In atomization, shear viscosity is the major factor that affects the dynamics of jet instabilities as it stabilizes the forces of inertia and thus, delays the breakup of the liquid jet (Agrawal et al., 2013). Meanwhile, surface tension effect is usually insignificant due to the aerodynamic effects (Reitz, 1978; Farago and Chigier, 1990; Lasheras et al., 1998). The shear viscous stress is the major factor that affects the dynamics of jet instabilities and their dynamics only. A study performed by Reitz and Bracco (1982) shows the influence of the liquid viscosity on the resulting jet flow. They vary the proportion of glycerol in water and prove that the instabilities in jet flow are greatly dampened as the viscosity is increased, which results in the formation of a laminar liquid jet instead. Therefore, the position of the primary break shifts further downstream. This phenomenon can also be proved through the calculation of Reynolds number of the liquid jet. A high shear viscosity will lower the Reynolds number (Agrawal et al., 2013). Besides that, Lin and Reitz (1998) show that the increase in liquid viscosity declines the wave growth rate and increases the wavelength of instabilities.

2.2.2 Extensional rheology

Previous section discusses in general the shear rheology of non-Newtonian liquids with a lot of examples given based on fibre suspensions specifically. The shear rheology or behaviour mainly depends on volume fraction, aspect ratio and particle shape. The different types of flow between shear and extensional fluids and their forms of deformations and resistances are illustrated by Steffe (1996), as shown in Figure 2.16. In the presence of extensional flow, some liquids, such as fibre suspensions, can develop extra resistance or tension that cannot be quantified by shear rheology (Ooi & Sridhar, 2004).

Previous studies proved the important role of extensional viscosity in dynamics of liquid breakup (Mansour & Chigier, 1995; McKinley, 2005; Rothstein, 2003), and thus suggesting that both shear and extensional viscosities need to be considered in designing atomization or spraying processes. The extensional flow is present along with the shear flow in the case where a liquid encounters a flow path that includes some degree of convergence or contraction from a larger diameter inlet tube to a fine exit orifice, such as in pipe contraction and in almost all nozzles (Astarita & Greco, 1968). During the breakup and atomization via a nozzle, most of the flow inside and outside of the nozzle is irrotational, except for the flow near the solid boundaries. This means that the liquid will experience extensional flow more often than the shear flow, and thus promotes stretching, based on the sketch in Figure 2.16.

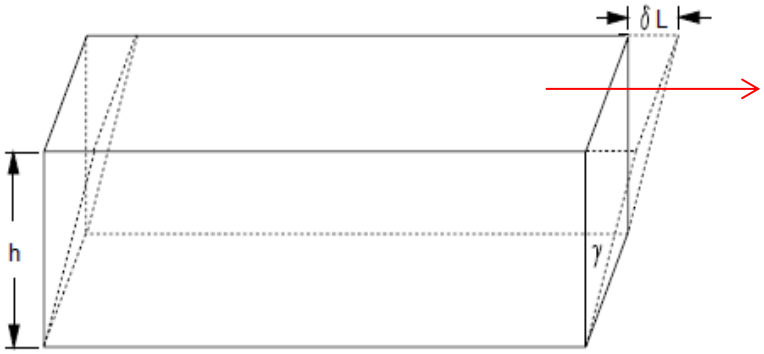

(a) Shear flow

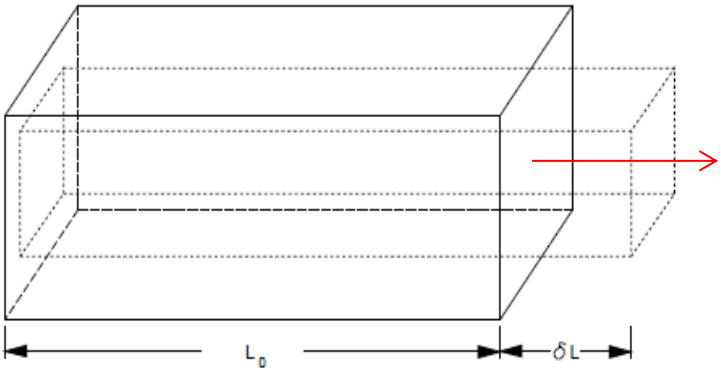

(b) Extensional flow

Figure 2.16 The difference between the shear and extensional flow experienced by a liquid and the resultant deformations occurred to the liquid molecule after the shearing and stretching (Steffe, 1996).

Chhabra (2006) explains the difference between shear stress and normal stress developed in a flowing liquid due to the shear and stretching of the liquid, respectively. In a steady one-dimensional shearing flow of the liquid, the stresses developed are shown in Figure 2.17. The cubic is considered as a liquid which is being sheared by two planes. The unidirectional flow of the liquid makes the y- and z-components of velocity vector zero. From Figure 2.17, during the shearing motion of liquid, there is additional normal stress developed which is P_{xx}, due to the stretching of the liquid along with the shear stress, τ_{yx}, due to the shearing of the liquid. P_{yy} and P_{zz} are zero since the velocity vectors are zero in y- and z-directions. Early theoretical studies on the effects of suspended macromolecules on extensional rheology suggest that the orientation and stretching of suspended particles

or molecules along the extensional flow direction can increase the extensional viscosity or contribute to the greater extensional resistance (Baloch et al., 1994; Batchelor, 1970, 1971).

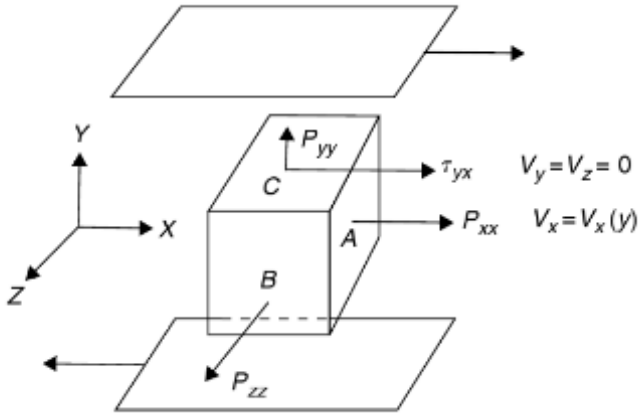

Figure 2.17 Stresses developed in sheared flow of viscoelastic fluid (Chhabra, 2006).

Bird et al. (2007) explain in depth the stress tensors developed by writing a momentum balance over a fixed volume element consists of $\Delta x\, \Delta y\, \Delta z$ through which a fluid is flowing, as shown in Figure 2.18. The momentum balance can be written as Equation 2.8.

$$\begin{bmatrix} rate\ of \\ increase \\ of\ momentum \end{bmatrix} = \begin{bmatrix} rate\ of \\ momentum \\ in \end{bmatrix} - \begin{bmatrix} rate\ of \\ momentum \\ out \end{bmatrix} + \begin{bmatrix} external \\ force\ on \\ the\ fluid \end{bmatrix} \qquad \text{Equation 2.8}$$

By referring to Figure 2.18, the rate at which x-component of momentum enters across the plane at x is $\tau_{xx}|_x\, \Delta y\, \Delta z$ and the rate at which it leaves the plane at $x + \Delta x$ is $\tau_{xx}|_{x+\Delta x}\, \Delta y\, \Delta z$. The rates at which the x-momentum enters and leaves through the planes at y and $y + \Delta y$ are $\tau_{yx}|_y\, \Delta z\, \Delta x$ and $\tau_{yx}|_{y+\Delta y}\, \Delta z\, \Delta x$, respectively. Similarly, the rates at which the x-momentum enters and leaves through the planes at z and $z + \Delta z$ are $\tau_{zx}|_z\, \Delta x\, \Delta y$ and $\tau_{zx}|_{z+\Delta z}\, \Delta x\, \Delta y$, respectively. τ_{xx}, τ_{yx} and τ_{zx} are known as the stress tensors. Addition of all these contributions produced the net rate of addition of x-momentum across all three pairs of planes, as shown in Equation 2.9 below.

$$\Delta y \Delta z(\tau_{xx}|_x - \tau_{xx}|_{x+\Delta x}) + \Delta z \Delta x\left(\tau_{yx}|_y - \tau_{yx}|_{y+\Delta y}\right) + \Delta x \Delta y(\tau_{zx}|_z - \tau_{zx}|_{z+\Delta z})$$

– Equation 2.9

Based on Equation 2.8, the external force on the fluid is typically related to the gravitational force acting on the volume element and the x-component of this force is $\rho g_x \Delta x\, \Delta y\, \Delta z$.

Meanwhile, the rate of increase of momentum in Equation 2.8 can be written as $\Delta x\,\Delta y\,\Delta z\,\delta(\rho v_x)/\delta t$. The final form of x-component of the momentum balance divided by $\Delta x\,\Delta y\,\Delta z$ is shown in Equation 2.10, when the limit is taken as Δx, Δy and Δz go to zero.

$$\frac{\delta}{\delta t}\rho v_x = -\left(\frac{\delta}{\delta x}\tau_{xx} + \frac{\delta}{\delta y}\tau_{yx} + \frac{\delta}{\delta z}\tau_{zx}\right) + \rho g_x \qquad \text{Equation 2.10}$$

Similarly, the equations of momentum balance for y- and z-components can be developed and are as in Equation 2.11 and 2.12, respectively. τ_{xx}, τ_{yx}, τ_{zx}, τ_{yx}, etc., are the nine components of τ, known as the stress tensor.

$$\frac{\delta}{\delta t}\rho v_y = -\left(\frac{\delta}{\delta x}\tau_{xy} + \frac{\delta}{\delta y}\tau_{yy} + \frac{\delta}{\delta z}\tau_{zy}\right) + \rho g_y \qquad \text{Equation 2.11}$$

$$\frac{\delta}{\delta t}\rho v_z = -\left(\frac{\delta}{\delta x}\tau_{xz} + \frac{\delta}{\delta y}\tau_{yz} + \frac{\delta}{\delta z}\tau_{zz}\right) + \rho g_z \qquad \text{Equation 2.12}$$

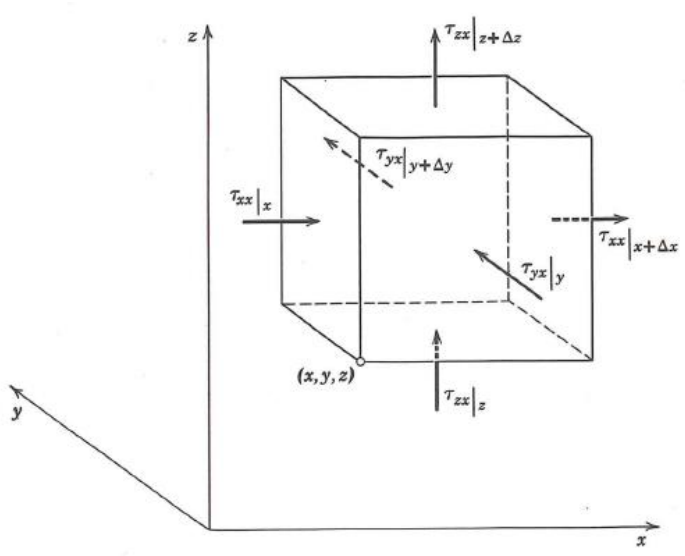

Figure 2.18 Fixed volume element $\Delta x\,\Delta y\,\Delta z$, with six arrows indicating the flux of x-momentum through the planes.

By using vector-tensor notation, Equations 2.10-2.12 can be reproduced and written as in Equation 2.13. ρv_i are the Cartesian components of the vector ρv, which is the momentum per unit volume at a point in the fluid. ρg_i are the components of the vector ρg, which is

the external force per unit volume. The term $-[\nabla \cdot \tau]_i$ is the *i*th component of the vector $-[\nabla \cdot \tau]$.

$$\frac{\delta}{\delta t}\rho v_i = -[\nabla \cdot \tau]_i + \rho g_i \quad i = x, y, z \qquad \text{Equation 2.13}$$

Further explanation on the development of the stress tensors can be found in Bird et al. (2007). Bird et al. (2007) lists out each component of the stress tensor in both rectangular and cylindrical coordinates which are represented by x, y, z and r, θ, z, respectively. Previous studies by Entov and Hinch (1997) and Torres et al. (2014) have described the derivation of simple expressions for extensional behaviour based on the developed stress tensors within a liquid filament and they show the difference between the stress tensors developed during a shear flow. In their derivation and analysis, it is evident that shear and extensional flow result in a completely different deformations and one behaviour could not be predicted by the other behaviour.

Precise measurements of extensional properties such as fluid relaxation time and extensional viscosity are essential for a quantitative study of the extensional rheology. Relaxation time is the characteristic time scale for viscoelastic stress growth in a uniaxial elongational flow (Rodd et al., 2004). There are few well-known methods that can be used to quantify the extensional effects which are Filament Stretching Extensional Rheometer, FiSER™ (Cambridge Polymer Group, Boston), Capillary Breakup Extensional Rheometer, CaBER™ (Cambridge Polymer Group, Boston and Haake) and Cambridge Trimaster (Hallmark et al., 2016). These devices measure the necking of an extensionally-strained fluid filament as a function of time. The CaBER was first developed by McKinley and co-workers at MIT in conjunction with the Cambridge Polymer Group. The CaBER can provide information on elasticity, relaxation time and filament breakup time. Conventional extensional rheometers are heavy, delicate and expensive. There is, therefore, a need for a portable device for measuring the extensional properties. The first lightweight portable extensional rheometer was built by Collett et al. (2015). The portable rheometer works very similarly to the CaBER, by monitoring the dynamics of the breakup of fluid filament following a short, rapid, extensional deformation. One can obtain information about the relaxation time, the extent of elasticity and the breakup time for the fluid. Other methods for studying extensional behaviour include the use of capillry or confined ducts.

Tuladhar and Mackley (2008) show the extensional behavior of diethyl phthalate (DEP) polymer solution with and without polystyrene (PS) as an elasticity enhancer. The DEP alone is a Newtonian liquid while the addition of 5% PS results in a shear-thinning behaviour with significant elastic properties found based on the FiSER™ technique. It means that the DEP/PS suspension is an extensional liquid. From the Tuladhar and Mackley (2008) study, it can be concluded that extensional resistance increases with concentration which agrees with the Calvo and Chigier (1995) study.

During the breakup and atomization via a nozzle, the flow of the liquid is affected by both the shear and extensional rheology of the liquid. Mansour and Chigier (1995) found that the normal stresses developed in viscoelastic materials are much higher than their associated shear stress during a two-fluid atomization. The normal stresses consequently inhibit the breakup. Other studies found that the extensional behaviour of liquids plays an important role in influencing the dynamics of the liquid breakups. For example, it can influence the pressure drop and this affects the atomization or spray ability of the liquids (Chhabra, 2006; Keshavarz et al., 2015; McKinley, 2005; Rothstein, 2003; Thompson & Rothstein, 2007). Thus, it is important to understand both the shear and extensional rheology of liquids before designing the atomization or spraying process. The comparison of extensional and shear viscosity contributions is usually made through the calculation of Trouton ratio, *Tr*, and is defined as in Equation 2.14.

$$Trouton\ ratio, Tr = \eta_E^+ (\dot{\varepsilon})/\mu(\dot{\gamma}) \qquad \text{Equation 2.14}$$

where η_E^+ (Pa.s) is the extensional viscosity at the extensional rate of $\dot{\varepsilon}$ (s^{-1}) and μ (Pa.s) is the steady shear viscosity at the shear rate of $\dot{\gamma}$ (s^{-1}). The standard method implies that $\dot{\gamma} = \dot{\varepsilon}$ but a few authors proposed and suggested that $\dot{\gamma} = \sqrt{3}\dot{\varepsilon}$ should be used to calculate the *Tr* (Jones et al., 1987; Meadows et al., 1995; Viebke et al., 1998). Meanwhile, Bach et al. (2003) defined *Tr* as the apparent extensional viscosity, η_E^+, over zero-shear rate viscosity, μ_0. The *Tr* was theoretically predicted to be 3 for Newtonian fluids, however some studies observed this value experimentally and found the *Tr* to be between 3 – 4.3 (Hermansky and Boger, 1995; Fuller et al., 1987; Eastman et al., 2000, Xu et al., 2005).

2.3 Viscoelastic breakup and atomization

Avaliable literature on viscoelastic breakup can be divided into two categories which are capillary jet breakup and atomization. In contrast to the Newtonian breakup and atomization mechanisms accurately explained in Section 2.1 based on different regimes, a development of any constitutive equation or any relationships between the disruptive and stabilzing forces to predict the breakup and atomization regimes for viscoelastic liquids is absent. Almost all previous works relating to viscoelastic breakup and atomization has been experimental only. There are few attempts in at least correlating the extensional rheology to spray properties especially the droplet size.

The capillary jet breakup in Newtonian liquid, owing to the Rayleigh regimes up until before the atomization regime, has been explained in the previous section. Few researches have tried to include the additional stress contributed by the extensional resistance to show the effect on the breakup of a viscoelastic jet. Chhabra (2006), Mansour and Chigier (1995) and Thompson and Rothstein (2007) suggest that the main feature of the breakup is the disintegration of the jet into streamwise ligaments, which will break into droplets at the end but over a much longer distance compared to Newtonian or inelastic fluids. This phenomenon is unfavorable for spray dryer applications as the atomization regime should start as soon as the liquid jet exits the nozzle. Overall, the elasticity or extensional rheology affects the stability of a jet by delaying the the onset of disturbance growth and enhancing the filament stability in the final stages of breakup owing to the normal stress development due to the extensional flow. As consequences, the jet has longer breakup lengths, fewer satelite drops and more pronounced filament stretching between the ligaments or droplets. Eggers and Villermaux (2008) also examined a jet of water with a small amount of flexible polymer inside. Instead of breaking up according to the Rayleigh regime, adjacent drops remain joined by threads, which grow increasingly thinner, and delaying the breakup significantly. This phenomenon is due to the polymer being stretched in the extensional flow inside the thread and thus deviate from their ideal coiled state. Keshavarz and McKinley (2018) showed that the fragmentation and breakup of viscoelastic liquids when using a rotary atomizer was delayed by nonlinear elastic effects and this leads to broader droplet size distributions.

Some inkjet fluids also exhibit extensional properties. Under suitable conditions, the ejected fluid develops into a single droplet for quality ink-jetting as discussed in the

previous Section 2.1. However, most functional ink materials available nowadays contain polymers that exhibit extensional properties. The ink-jetting performance of such fluids is very unstable with the formation of long filaments, connecting the ejected droplet to the nozzle. A lot of studies have focused on the filament behaviour and its lifetime during the ejection process (Morrison and Harlen, 2010; Hoath et al., 2012; Bienia et al., 2016; Du et al., 2018). They found that for polymer inks, the extensional resistance contributed by the coiled-stretch transition occurred along the polymer chains affected the droplet formation. Specifically, elastic stresses acted to contract the trailing ligament or filament into the main drop before capillary breakup occurred. This elasticity can delay or prevent the break-off of the drop from the ink reservoir within the nozzle. The length and lifetime of the filament influence the positional accuracy and resolution of the printing as well as the printability of the inks. It means that when printing, the addition of a small amount of polymer with extensional properties can significantly affect the breakup of filaments generated and thus change the droplet formation characteristics. The extensional properties of polymer inkjet fluids mainly dependent on the molecular weight of the polymer (Hoath et al., 2012).

In contrast to the study or observation on the capillary breakup of a viscoelastic jet, Mansour and Chigier (1995) did actually atomize viscoelastic liquids using a two-fluid atomization technique. A marked difference in breakup pattern between the viscoelastic liquids and liquids with no elasticity was observed. The resultant droplet sizes were independent of shear viscosity or no correlation was found between the shear viscosity of the viscoelastic liquids and the droplet sizes formed. Although it was not shown in their study, it is suspected that the droplet sizes were influenced and controlled by the extensional viscosity, and that is why no correlation was found between the shear viscosity and the resultant droplet sizes (Mansour and Chigier, 1995).

Atomization of viscoelastic and extensional liquids using conventional hydraulic atomizers or simple pressure nozzles constitutes the remaining bulk of the limited available literature. All the studies show the unsuccessful atomization or ineffective atomization of the liquids when using conventional and pressure nozzles. For example, Thompson and Rothstein (2007) and Stelter et al. (2002) employed flat-fan, pressure-swirl and hollow-cone spray nozzle. They show that the atomization of viscoelastic liquids using conventional and pressure nozzles consists of extended sheet breakup length, increasing mean droplet size and inability to form full conical sheet and fully developed hollow-cone sprays. Other studies by Chao et al. (1984), Johnson et al. (1987), Smolinski et al. (1996), Marano et al.

(1997) and Mun et al. (1999) all utilized different types of viscoelastic fluids to purposely supress jet atomization and anti-misting effect and produce large droplets by using conventional and pressure nozzles.

2.4 Nozzles

2.4.1 Rotary atomization

Rotary atomization is often called centrifugal atomization, where the liquid feed is centrifugally accelerated to a high velocity before exiting into an air-gas atmosphere (Lefebvre, 1988; Masters, 1979). The degree of atomization for this technique depends on the peripheral speed, feed rate, liquid properties and atomizer design. For the liquid to gain the maximum centrifugal energy, the liquid must acquire the peripheral speed of the wheel or disc before discharge. For all types of rotary atomizers, the formation of drops directly at the peripheral edge, as in Figure 2.19, can be achieved only at low feed rates. However, the need for high feed rates is always the case in commercially spray drying process. This, in turn, will result in the formation of ligaments prior to complete atomization as shown in Figure 2.20 (Frost, 1981; Lefebvre, 1988).

Commercially, atomizer wheels are always being used when compared to vaneless discs which can be said to find no application in the current industry (Masters, 1979). For the case of wheel atomization, at low speeds and feed rates, viscous and surface tension forces control the breakup process. At intermediate speeds, liquid ligaments start to form and extend out from the edge of the vane and their disintegration is now controlled by centrifugal forces and only a small amount by gravitational forces. The ligaments are further disintegrated during their flight through the air. As the liquid flow is further increased, high wheel peripheral speeds need to be applied. The liquid disintegration then occurs right at the wheel edge by frictional effects between the air and the liquid surface. This is the direct droplet formation mechanism (Masters, 1979). Different modes of disintegration need to be controlled by different parameters. To get the ideal mode of direct droplet formation, the liquid release velocity from the edge of the wheel needs to be high enough to permit air frictional effects between the liquid-air interfaces. It means that high wheel speeds suitable to the feed rates are necessary.

The breakup and atomization of viscoelastic liquids using a rotary atomizer may not be efficient and successful as suggested by Keshavarz and McKinley (2018). They showed that the fragmentation and breakup of viscoelastic liquids when using a rotary atomizer was delayed by nonlinear elastic effects and this leads to broader droplet size distributions.

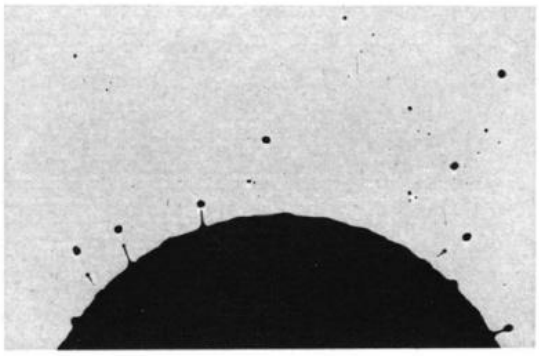

Figure 2.19 Direct drop formation (Frost, 1981)

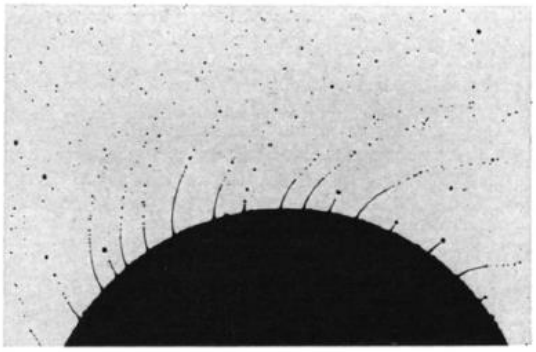

Figure 2.20 Disintegration of ligaments prior to droplets formation (Frost, 1981)

2.4.2 Nozzle atomization

Nozzle atomizers also find broad applications commercially. The function of nozzle atomizers is to accelerate and disintegrate the bulk liquid flow into a spray. The liquid in a nozzle atomizer is disintegrating only if the liquid jet is turbulent enough. The main drawback of the nozzle atomizers includes the inefficient energy transfer during atomization (Masters, 1979). Various types of nozzles have been developed in an attempt to improve the degree of atomization, such as those utilizing either pressure, kinetic or sonic energy. Pressure nozzles, pneumatic nozzles and ultrasonic nozzles all fall into the nozzle atomization category.

2.4.2.1 Centrifugal pressure nozzle

Pressure applied to the liquid within the nozzle forces the liquid out of the orifice at high velocity. Before exiting the nozzle, the high-pressure liquid bulk must flow through an insert such as slotted insert and swirl insert, as shown in Figure 2.21. This arrangement allows the high-pressure liquid to exit the nozzle in the form of conical sheets instead of

thick jets. The formation of conical sheets permits greater energy transfer leading to better atomization. The sheet velocity is constant, but the thickness reduces as the cone develops. However, the sheet length is always invisible during commercial operation due to the direct droplet formation mechanism. Invisibility is due to the high pressures, nozzle velocities and resulting turbulence and frictional effects which all contribute to the very short sheet lengths regardless of a high liquid viscosity (Masters, 1979). Despite the simple operation and requirements of a pressure nozzle, and the wide use in industry, it is important to note that pressure nozzles are unable to atomize very high viscous fluids.

The breakup and atomization of viscoelastic liquids using a pressure nozzle may not be efficient and successful as suggested by Thompson and Rothstein (2007) and Stelter et al. (2002). As an overall, the use of the pressure nozzle mainly supresses jet atomization.

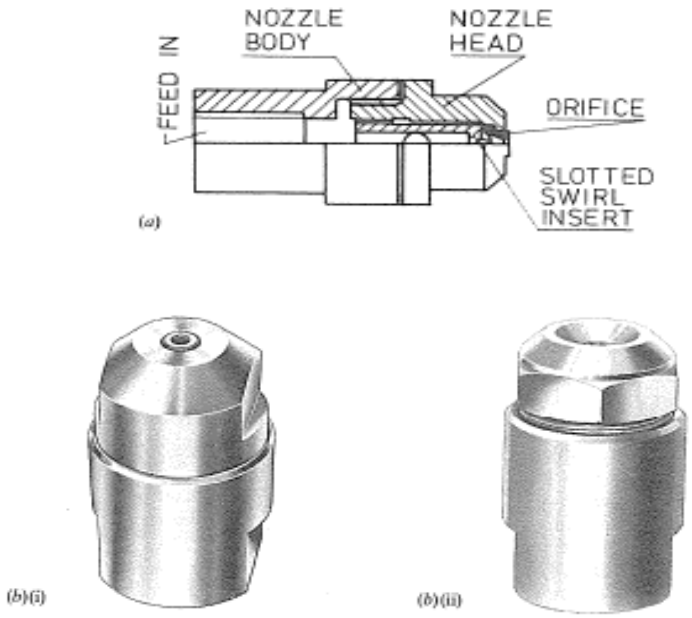

Figure 2.21 Centrifugal pressure nozzles (a) Principal parts (b) Typical nozzles (Masters, 1979)

2.4.2.2 Pneumatic (two-fluid) nozzle

Pneumatic nozzle requires high-velocity gas accelerating and impacting the liquid bulk for liquid disintegration to occur (Mansour & Chigier, 1995). The flow of high-velocity gas or air creates high frictional forces over the liquid surfaces causing the liquid disintegration

into spray droplets. Compared to other types of atomization discussed above, the frictional effects in pneumatic atomization are enhanced by increasing the velocity of the gas instead of the velocity of the moving liquid bulk. According to Masters (1979), a high relative velocity between the liquid and gas must be generated so that the liquid is subjected to optimum frictional conditions. Similar to other atomization, the disintegration involved here can be either the tearing of liquid bulk into ligaments which further break into droplets or the direct formation of droplets as soon as exiting the nozzle.

Pneumatic nozzles have operational flexibility in producing either small or large droplets over a wide range of feed rates and require lower liquid injection pressures for atomization to occur (Mansour & Chigier, 1995; Masters, 1979; Mlkvik et al., 2015). This characteristic differs from the centrifugal pressure nozzles which have a limited capacity range for complete atomization (Masters, 1979). The appealing factor of the two-fluid nozzle is that it can handle both low and high viscous liquids (Masters, 1979; Mlkvik et al., 2015).

The pneumatic nozzles find applications in atomizing highly viscous liquids including slurries, pastes, suspension and corn starches (Mansour & Chigier, 1995). Kufferath et al. (1999) also used a twin-fluid atomizer to atomize a high viscous liquid despite their high energy consumption. A study conducted by Mansour and Chigier (1995) also demonstrated the possibility of using pneumatic nozzles to spray non-Newtonian viscoelastic liquids. This nozzle is also suitable in atomizing dilatant or shear-thickening fluids, which obviously cannot be atomized by pressure nozzles. However, one major drawback of pneumatic nozzles is the requirement of high-cost compressed air (Masters, 1979).

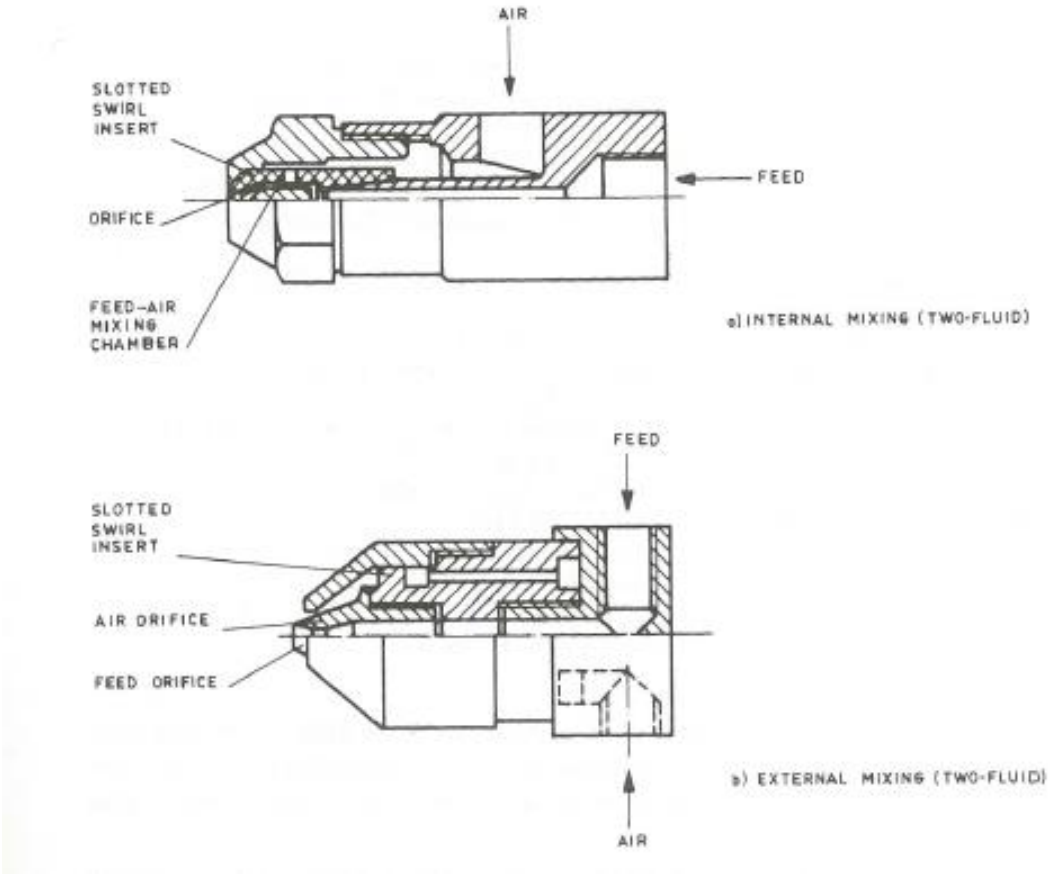

Figure 2.22 Design of pneumatic nozzle head (top) two-fluid internal mixing and (bottom) two-fluid external mixing (Masters, 1979).

2.4.2.3 Ultrasonic atomization

Sonic atomization has started to gain attention as the remaining option as there are increasing numbers of liquids which cannot be atomized successfully by wheels and nozzles. These liquids include non-Newtonian products, highly viscous liquids and liquids with long chain molecular structures. This technique is essential for liquids that require excessive pressures for complete atomization in centrifugal pressure nozzles. Furthermore, ultrasonic atomization is an effective technique for generating small droplets (Barreras et al., 2002).

The different mechanisms of ultrasonic atomization involve the rupture of capillary surface waves and the formation of cavitation bubbles (Barreras et al., 2002; Broniarz-Press et al., 2015; Lang, 1962). However, the interaction between these mechanisms and the conditions or situations in which one could predominate over the other in atomizing the liquid remains

uncertain. Figure 2.23 shows the disintegration of non-Newtonian liquid during ultrasonic inhalation (Broniarz-Press et al., 2015). It shows clearly the atomization mechanism based on capillary waves theory. The continuous application of ultrasonic vibrations makes the capillary waves on the liquid surface unstable. This situation leads to the breakup of the unstable crest waves into droplets. Some droplets can be seen to be connected with ligaments before being completely detached into smaller droplets.

Two different approaches can be applied to generate the droplets (Barreras et al., 2002). One of the methods is to permit the flow of liquid passing across a standing ultrasonic wave. Another approach is to deposit the liquid over an ultrasonic transducer.

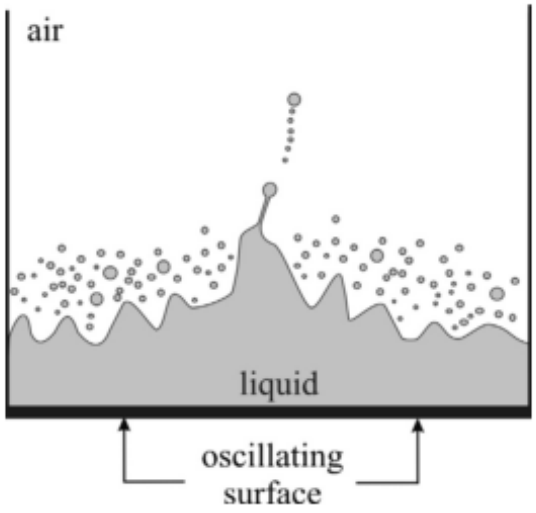

Figure 2.23 The mechanism of atomization of non-Newtonian liquid by ultrasonic inhaler (Broniarz-Press et al., 2015).

2.5 Summary

Over the years, the understanding of the atomization process that occurred during spray drying has been progressing well. A number of previous studies have attempted to characterize and explain the atomization mechanisms starting from dripping to breaking up into smaller micron-size droplets. These findings are being well-utilized up to this date when dealing with atomization or spray drying process. Despite the in-depth and well-

establish mechanisms of the atomization process, they have all been based on Newtonian liquids, or more specifically water. Newtonian liquids behave relatively simple compared to non-Newtonian liquids which allows the use of common nozzles or atomizers to achieve a successful atomization process for the Newtonian liquids. This explains the intensive use of simple pressure nozzles and rotary atomizers for industrial-scale processes. The intensive and demanding use of the simple pressure and rotary atomizers due to the successful applications with Newtonian liquids, possibly contributes to the common approach nowadays, in which these basic nozzles are being used to atomize non-Newtonian liquids. This approach, which is also being practiced by the industry, is regrettably unsuccessful as has shown in several studies mentioned in the literature review.

This dissertation aims to highlight the state of art in which the type of nozzle is being selected after a thorough and in-depth study on the rheology of the non-Newtonian liquid used. Addition of fibres as a drying aid into a fruit juice creates a non-Newtonian liquid, and this finding is well-established in several previous studies. However, these studies have failed to investigate the behaviour or rheology of the fibre suspensions specifically at conditions similar to those inside a nozzle or during atomization. No study has yet been conducted to atomize non-Newtonian fibre suspensions.

The main purposes of this research are to:

1) To first and foremost, characterize the behaviour or rheology of the fibre suspensions. The results of this investigation will assist in determining the limiting factors that affect the atomization performance.
2) To atomize or spray the fibre suspension using selected nozzles. The results from the rheology study will significantly contribute in the decision making for nozzle design. A new nozzle design is not necessary, but it is important to know which type of nozzle is best suited for fibre suspension applications.
3) To study the performance of the selected nozzle by variations in liquid properties and operating conditions. This includes the attempts to improve the atomization or the nozzle performance.
4) To study the possibility of using the selected nozzle for future work i.e. in pilot-scale or industrial-scale trials.

References

Agrawal, K., Sanal, S., Gulati, G., & Kumar, A. (2013). Breakup of Liquid Jets. *International Journal of Emerging Technologies in Computational and Applied Sciences (IJETCAS), 13*, 487-496.

Aliseda, A., Hopfinger, E. J., Lasheras, J. C., Kremer, D., Berchielli, A., & Connolly, E. (2008). Atomization of viscous and non-Newtonian liquids by a coaxial, high-speed gas jet. Experiments and droplet size modeling. *International Journal of Multiphase Flow, 34*, 161-175.

Anczurowski, E., & Mason, S. G. (1967). The kinetics of flowing dispersions. *Journal of Colloid and Interface Science*, *23*(4), 522-532.

Andrić, J., Lindström, S. B., Sasic, S., & Nilsson, H. (2014). Rheological properties of dilute suspensions of rigid and flexible fibers. *Journal of Non-Newtonian Fluid Mechanics, 212*, 36-46.

Bach, A., Rasmussen, H. K., & Hassager, O. (2003). Extensional viscosity for polymer melts measured in the filament stretching rheometer. *Journal of Rheology*, *47*(2), 429-441.

Baloch, A., Townsend, P., & Webster, M. (1994). Extensional effects in flows through contractions with abrupt or rounded corners. *Journal of Non-Newtonian Fluid Mechanics, 54*, 285-302.

Barnes, H. A., Hutton, J. F., & Walters, K. (1989). *An introduction to rheology* (Vol. 3). Elsevier.

Barreras, F., Amaveda, H., & Lozano, A. (2002). Transient high-frequency ultrasonic water atomization. *Experiments in Fluids, 33*, 405-413.

Batchelor, G. (1970). Slender-body theory for particles of arbitrary cross-section in Stokes flow. *Journal of Fluid Mechanics, 44*, 419-440.

Batchelor, G. (1971). The stress generated in a non-dilute suspension of elongated particles by pure straining motion. *Journal of Fluid Mechanics, 46*, 813-829.

Bibbó, M. A. (1987). *Rheology of semiconcentrated fiber suspensions.* Doctoral dissertation, Massachusetts Institute of Technology.

Bienia, M., Lejeune, M., Chambon, M., Baco-Carles, V., Dossou-Yovo, C., Noguera, R., & Rossignol, F. (2016) Inkjet printing of ceramic colloidal suspensions: Filament growth and breakup. *Chemical Engineering Science, 149*, 1-13.

Bird, R. B., Stewart, W. E., & Lightfoot, E. N. (2007). *Transport phenomena.* John Wiley & Sons.

Blakeney, W. R. (1966). The viscosity of suspensions of straight, rigid rods. *Journal of Colloid and Interface Science, 22*, 324-330.

Broniarz-Press, L., Sosnowski, T., Matuszak, M., Ochowiak, M., & Jabłczyńska, K. (2015). The effect of shear and extensional viscosities on atomization of Newtonian and non-Newtonian fluids in ultrasonic inhaler. *International Journal of Pharmaceutics, 485*, 41-49.

Calvo, D., & Chigier, N. (1995). *Measurement of extensional viscosity by the stretching of viscoelastic liquid columns. Quarterly report, April--June, 1995* (No. DOE/PC/92152-T16). Carnegie-Mellon Univ., Pittsburgh, PA (United States). Dept. of Mechanical Engineering.

Castleman, R. A. (1931). *The mechanism of the atomization of liquids*. US Department of Commerce, Bureau of Standards.

Chao, K., Child, C., Grens, E., & Williams, M. (1984). Antimisting action of polymeric additives in jet fuels. *AIChE Journal, 30*, 111-120.

Chhabra, R. P. (2006). *Bubbles, drops, and particles in non-Newtonian fluids.* CRC press.

Chigier, N., & Farago, Z. (1992). Morphological classification of disintegration of round liquid jets in a coaxial air stream. *Atomization and Sprays, 2*.

Collett, C., Ardron, A., Bauer, U., Chapman, G., Chaudan, E., Hallmark, B., . . . Wilson, D. I. (2015). A portable extensional rheometer for measuring the viscoelasticity of pitcher plant and other sticky liquids in the field. *Plant Methods, 11*, 16.

Derakhshandeh, B., Kerekes, R. J., Hatzikiriakos, S. G., & Bennington, C. P. J. (2011). Rheology of pulp fibre suspensions: A critical review. *Chemical Engineering Science, 66*, 3460-3470.

Derby, B. (2010). Inkjet printing of functional and structural materials: fluid property requirements, feature stability, and resolution. *Annual Review of Materials Research, 40*, 395-414.

Djalili-Moghaddam, M., & Toll, S. (2006). Fibre suspension rheology: effect of concentration, aspect ratio and fibre size. *Rheologica Acta, 45*, 315-320.

Dong, H., Carr, W. W., & Morris, J. F. (2006). Visualization of drop-on-demand inkjet: Drop formation and deposition. *Review of Scientific Instruments, 77*(8).

Du, Z., Yu, X., & Han, Y. (2018). Inkjet printing of viscoelastic polymer inks. *Chinese Chemical Letters, 29*(3), 399-404.

Eastman, J. R., Goodwin, J. W., & Howe, A. M. (2000). Extensional viscosity of aqueous solutions of SDS and PVP measured on the rheometrics RFX. *Colloids and Surfaces A: Physicochemical and Engineering Aspects, 161*(2), 329-338.

Eggers, J., & Villermaux, E. (2008). Physics of liquid jets. *Reports on Progress in Physics, 71*, 036601.

Elleuch, M., Besbes, S., Roiseux, O., Blecker, C., Deroanne, C., Drira, N.-E., & Attia, H. (2008). Date flesh: Chemical composition and characteristics of the dietary fibre. *Food Chemistry, 111*, 676-682.

Entov, V. M., & Hinch, E. J. (1997). Effect of a spectrum of relaxation times on the capillary thinning of a filament of elastic liquid. *Journal of Non-Newtonian Fluid Mechanics*, *72*(1), 31-53.

Evans, K., & Gibson, A. (1986). Prediction of the maximum packing fraction achievable in randomly oriented short-fibre composites. *Composites Science and Technology, 25*, 149-162.

Faeth, G., Hsiang, L.-P., & Wu, P.-K. (1995). Structure and breakup properties of sprays. *International Journal of Multiphase Flow, 21*, 99-127.

Farago, Z., & Chigier, N. (1990). Parametric Experiments on Coaxial Airblast Jet Atomization. In *ASME 1990 International Gas Turbine and Aeroengine Congress and Exposition* (V003T06A016-V003T06A016). American Society of Mechanical Engineers.

Frost, A. R. (1981). Rotary atomization in the ligament formation mode. *Journal of Agricultural Engineering Research, 26*, 63-78.

Fuller, G. G., Cathey, C. A., Hubbard, B., & Zebrowski, B. E. (1987). Extensional Viscosity Measurements for Low-Viscosity Fluids. *Journal of Rheology*, *31*(3), 235-249.

Grigelmo-Miguel, N., Ibarz-Ribas, A., & Martín-Belloso, O. (1999). Rheology of peach dietary fibre suspensions. *Journal of Food Engineering, 39*, 91-99.

Hanson, A., Domich, E., & Adams, H. (1963). Shock tube investigation of the breakup of drops by air blasts. *Physics of Fluids, 6*, 1070-1080.

Hermansky, C. G., & Boger, D. V. (1995). Opposing-jet viscometry of fluids with viscosity approaching that of water. *Journal of Non-Newtonian Fluid Mechanics*, *56*(1), 1-14.

Hinze, J. (1955). Fundamentals of the hydrodynamic mechanism of splitting in dispersion processes. *AIChE Journal, 1*, 289-295.

Hoath, S. D., Harlen, O. G., & Hutchings, I. M. (2012). Jetting behaviour of polymer solutions in drop-on-demand inkjet printing. *Journal of Rheology*, *56*(5), 1109-1127.

Hoffman, R. (1972). Discontinuous and dilatant viscosity behavior in concentrated suspensions. I. Observation of a flow instability. *Transactions of the Society of Rheology, 16*, 155-173.

Jang, D., Kim, D., & Moon, J. (2009). Influence of fluid physical properties on ink-jet printability. *Langmuir*, *25*(5), 2629-2635.

Johnson, M. A., Chang §, J., II, E. A. G., & Williams, M. C. (1987). The effect of antimisting additives on flammability of jet fuels. *Chemical Engineering Communications*, *56*, 1-17.

Jones, D. M., Walters, K., & Williams, P. R. (1987). On the extensional viscosity of mobile polymer solutions. *Rheologica Acta*, *26*(1), 20-30.

Joseph, D. D., Belanger, J., & Beavers, G. (1999). Breakup of a liquid drop suddenly exposed to a high-speed airstream. *International Journal of Multiphase Flow*, *25*, 1263-1303.

Joung, C. G., Phan-Thien, N., & Fan, X. J. (2001). Direct simulation of flexible fibers. *Journal of Non-Newtonian Fluid Mechanics*, *99*, 1-36.

Joung, C. G., Phan-Thien, N., & Fan, X. J. (2002). Viscosity of curved fibers in suspension. *Journal of Non-Newtonian Fluid Mechanics*, *102*, 1-17.

Keshavarz, B., & McKinley, G. (2018). Rotary Fragmentation and Atomization of Viscous and Viscoelastic Liquids. *Presented at 71st Annual Meeting of the APS Division of Fluid Dynamics, Bulletin of the American Physical Society*.

Keshavarz, B., Sharma, V., Houze, E. C., Koerner, M. R., Moore, J. R., Cotts, P. M., . . . McKinley, G. H. (2015). Studying the effects of elongational properties on atomization of weakly viscoelastic solutions using Rayleigh Ohnesorge Jetting

Extensional Rheometry (ROJER). *Journal of Non-Newtonian Fluid Mechanics, 222*, 171-189.

Keshtkar, M., Heuzey, M.-C., Carreau, P. J., Rajabian, M., & Dubois, C. (2010). Rheological properties and microstructural evolution of semi-flexible fiber suspensions under shear flow. *Journal of Rheology, 54*, 197-222.

Keshtkar, M., Heuzey, M., & Carreau, P. (2009). Rheological behavior of fiber-filled model suspensions: Effect of fiber flexibility. *Journal of Rheology, 53*, 631-650.

Kitano, T., Kataoka, T., & Nagatsuka, Y. (1984). Dynamic flow properties of vinylon fibre and glass fiber reinforced polyethylene melts. *Rheologica Acta, 23*, 408-416.

Kotsilkova, R. (1992). Dynamic rheological properties of glass fiber suspensions. *Theoretical and Applied Rheology*, 856-858.

Krzeczkowski, S. A. (1980). Measurement of liquid droplet disintegration mechanisms. *International Journal of Multiphase Flow, 6*, 227-239.

Kufferath, A., Wende, B., & Leuckel, W. (1999). Influence of liquid flow conditions on spray characteristics of internal-mixing twin-fluid atomizers. *International Journal of Heat and Fluid Flow, 20*, 513-519.

Lang, R. J. (1962). Ultrasonic atomization of liquids. *The Journal of The Acoustical Society of America, 34*, 6-8.

Lasheras, J., Villermaux, E., & Hopfinger, E. (1998). Break-up and atomization of a round water jet by a high-speed annular air jet. *Journal of Fluid Mechanics, 357*, 351-379.

Le, H. P. (1998). Progress and trends in ink-jet printing technology. *Journal of Imaging Science and Technology*, *42*(1), 49-62.

Lee, M. W., Kang, D. K., Kim, N. Y., Kim, H. Y., James, S. C., & Yoon, S. S. (2012). A study of ejection modes for pulsed-DC electrohydrodynamic inkjet printing. *Journal of Aerosol Science, 46*, 1-6.

Lefebvre, A. (1988). *Atomization and sprays* (Vol. 1040). CRC press.

Lin, S. P., & Reitz, R. D. (1998). Drop and spray formation from a liquid jet. *Annual Review of Fluid Mechanics, 30*, 85-105.

Liu, H. (1999). *Science and Engineering of Droplets: Fundamentals and Applications*. William Andrew.

Mansour, A., & Chigier, N. (1995). Air-blast atomization of non-Newtonian liquids. *Journal of Non-Newtonian Fluid Mechanics, 58*, 161-194.

Marano, R. S., Smolinski, J. M., Manke Jr, C. W., Gulari, E., & Messick, R. L. (1997). Polymer additives as mist suppressants in metal cutting fluids. *Tribology & Lubrication Technology, 53*, 25.

Marmottant, P., & Villermaux, E. (2004). On spray formation. *Journal of Fluid Mechanics, 498*, 73-111.

Masters, K. (1979). Spray drying handbook. *Spray drying handbook.*(Ed. 3).

McGeary, R. (1961). Mechanical packing of spherical particles. *Journal of the American Ceramic Society, 44*, 513-522.

McKinley, G. H. (2005). Visco-elasto-capillary thinning and break-up of complex fluids. HML Report Number 05-P-04.

Meadows, J., Williams, P. A., & Kennedy, J. C. (1995). Comparison of the extensional and shear viscosity characteristics of aqueous hydroxyethyl cellulose solutions. *Macromolecules, 28*(8), 2683-2692.

Mlkvik, M., Stähle, P., Schuchmann, H. P., Gaukel, V., Jedelsky, J., & Jicha, M. (2015). Twin-fluid atomization of viscous liquids: The effect of atomizer construction on breakup process, spray stability and droplet size. *International Journal of Multiphase Flow, 77*, 19-31.

Morrison, N. F., & Harlen, O. G. (2010). Viscoelasticity in inkjet printing. *Rheologica Acta, 49*(6), 619-632.

Mun, R. P., Young, B. W., & Boger, D. V. (1999). Atomisation of dilute polymer solutions in agricultural spray nozzles. *Journal of Non-Newtonian Fluid Mechanics, 83*, 163-178.

Nawab, M. A., & Mason, S. G. (1958). Viscosity of dilute suspensions of thread-like particles. *The Journal of Physical Chemistry, 62*, 1248-1253.

Nicholls, J., & Ranger, A. (1969). Aerodynamic shattering of liquid drops. *AIAA Journal, 7*, 285-290.

Ohnesorge, W. V. (1936). Formation of drops by nozzles and the breakup of liquid jets. *Z. Angew. Math. Mech, 16*, 355-358.

Ooi, Y. W., & Sridhar, T. (2004). Resistance to uniaxial extensional flow of fibre suspensions. *Rheologica Acta, 43*, 223-231.

Pan, N. (1993). Theoretical determination of the optimal fiber volume fraction and fiber-matrix property compatibility of short fiber composites. *Polymer Composites, 14*, 85-93.

Pilch, M., & Erdman, C. (1987). Use of breakup time data and velocity history data to predict the maximum size of stable fragments for acceleration-induced breakup of a liquid drop. *International Journal of Multiphase Flow, 13*, 741-757.

Rayleigh, L. (1878). On the instability of jets. *Proceedings of the London Mathematical Society, 1*, 4-13.

Reis, N., & Derby, B. (2000). Ink jet deposition of ceramic suspensions: Modeling and experiments of droplet formation. *MRS Online Proceedings Library Archive, 625.*

Reitz, R., & Bracco, F. (1982). Mechanism of atomization of a liquid jet. *Physics of Fluids, 25*, 1730-1742.

Reitz, R., & Bracco, F. (1986). Mechanisms of breakup of round liquid jets. *Encyclopedia of Fluid Mechanics, 3*, 233-249.

Reitz, R. D. (1978). *Atomization and other breakup regimes of a liquid jet*. Doctoral dissertation, Princeton University, NJ.

Rodd, L. E., Scott, T. P., Cooper-White, J. J., & McKinley, G. H. (2004). Capillary break-up rheometry of low-viscosity elastic fluids. *Applied Rheology,* HML Report Number 04 – P – 04.

Rothstein, J. P. (2003). Transient extensional rheology of wormlike micelle solutions. *Journal of Rheology, 47*, 1227-1247.

Schmid, C. F., Switzer, L. H., & Klingenberg, D. J. (2000). Simulations of fiber flocculation: Effects of fiber properties and interfiber friction. *Journal of Rheology, 44*, 781-809.

Shah, D. U., Schubel, P. J., Licence, P., & Clifford, M. J. (2012). Determining the minimum, critical and maximum fibre content for twisted yarn reinforced plant fibre composites. *Composites Science and Technology, 72*, 1909-1917.

Smolinski, J. M., Gulari, E., & Manke, C. W. (1996). Atomization of dilute polyisobutylene/mineral oil solutions. *AIChE Journal, 42*, 1201-1212.

Soszynski, R., & Kerekes, R. (1988). Elastic interlocking of nylon fibres suspended in liquid, part 2, process of interlocking. *Nord. Pulp Pap. Res. J, 3*, 180.

Steffe, J. F. (1996). *Rheological methods in food process engineering*. Freeman press.

Stelter, M., Brenn, G., & Durst, F. (2002). The influence of viscoelastic fluid properties on spray formation from flat-fan and pressure-swirl atomizers. *Atomization and Sprays, 12*, 299-327.

Stickel, J. J., & Powell, R. L. (2005). Fluid mechanics and rheology of dense suspensions. *Annu. Rev. Fluid Mech., 37*, 129-149.

Switzer, L. H., & Klingenberg, D. J. (2003). Rheology of sheared flexible fiber suspensions via fiber-level simulations. *Journal of Rheology, 47*, 759-778.

Thompson, J. C., & Rothstein, J. P. (2007). The atomization of viscoelastic fluids in flat-fan and hollow-cone spray nozzles. *Journal of Non-Newtonian Fluid Mechanics, 147*, 11-22.

Torres, M. D., Hallmark, B., Wilson, D. I., & Hilliou, L. (2014). Natural Giesekus fluids: Shear and extensional behavior of food gum solutions in the semidilute regime. *AIChE Journal, 60*(11), 3902-3915.

Tuladhar, T. R., & Mackley, M. R. (2008). Filament stretching rheometry and break-up behaviour of low viscosity polymer solutions and inkjet fluids. *Journal of Non-Newtonian Fluid Mechanics, 148*, 97-108.

Viebke, C., Meadows, J., Kennedy, J. C., & Williams, P. A. (1998). Effect of soluble polymers on the shear and extensional viscosity characteristics of a concentrated latex dispersion. *Langmuir, 14*(7), 1548-1553.

Weber, C. (1931). Disintegration of liquid jets. *Z. Angew. Math. Mech, 11*, 136-159.

Wierzba, A. (1990). Deformation and breakup of liquid drops in a gas stream at nearly critical Weber numbers. *Experiments in Fluids, 9*, 59-64.

Xu, J., Chatterjee, S., Koelling, K. W., Wang, Y., & Bechtel, S. E. (2005). Shear and extensional rheology of carbon nanofiber suspensions. *Rheologica Acta, 44*(6), 537-562.

Yamanoi, M., Maia, J., & Kwak, T. S. (2010). Analysis of rheological properties of fibre suspensions in a Newtonian fluid by direct fibre simulation. Part 2: Flexible fibre suspensions. *Journal of Non-Newtonian Fluid Mechanics, 165,* 1064-1071.

Chapter 3 General materials and method

3.1 Introduction

This chapter describes the materials and methodologies used throughout the study divided into four major sections. Section 3.2 describes the selection of the commercially available fruit juice and food fibres used. Section 3.3 describes the preparation procedure of the fibre suspensions. Section 3.4 explains in depth about the measurements of the physical properties of the fibre particles and fibre suspensions. Lastly, Section 3.5 explains the experimental arrangement and setup during the rheology and atomization studies.

3.2 Selection of materials

A single type of fruit juice was used throughout the study. A range of insoluble fibres with different length and aspect ratios, commonly used in the food industry and available in New Zealand, were selected.

3.2.1 Concentrated apple juice

Concentrated apple juice was used throughout the study for two reasons:

1. Apple fruit or juice is consumed and produced more regularly in New Zealand compared to other types of fruit juices.
2. In the spray drying application, concentrated juice is used as compared to dilute one.

A 60 °Brix (as specified by the supplier) concentrated apple juice supplied by Cedenco Foods (Hawkes Bay, New Zealand) was used. The total solid content of the concentrated apple juice was measured again inside the laboratory using an oven-heating technique. Five samples of the concentrated apple juice were left inside an oven for 24 hours at 105 °C. The mass of the concentrated apple juice before and after the drying was measured. The results are tabulated in Table 3.1. A high-performance liquid chromatography (HPLC)

technique was performed by Sebastian Linnenkugel on a similar concentrated apple juice sample. The components identified in the concentrated apple juice based on the HPLC technique are tabulated in Table 3.2. The amount of each component identified was compared with the average value from 92 commercial apple juice concentrates (Elkins et al., 1996).

Table 3.1: Total solid content of the concentrated apple juice measured using the oven-heating technique.

Concentrated apple juice sample	Total solid content (%)
Sample 1	65.0
Sample 2	64.8
Sample 3	64.5
Sample 4	64.3
Sample 5	64.5

Table 3.2: Solid compound identified in the concentrated apple juice based on high-performance liquid chromatography (HPLC) technique performed by Sebastian Linnenkugel.

Solid compounds	Amount of identified solid compound (%)	
	Concentrated apple juice used in the study	Average of 92 commercial apple juice concentrates
Fructose	68.0	52.8
Glucose	15.0	21.0
Sucrose	14.0	14.4
Sorbitol	2.0	3.5
Citric acid	-	0.1
L-malic acid	1.0	4.0
Total	100	95.7 (The rest was made up of minerals, polyphenolics and amino acids)

3.2.2 Food fibres

Four types of insoluble food fibres commercially available in New Zealand were chosen on the grounds that they differed in length and aspect ratio. These were: Apple Fibre 400-30 (AF 400-30), Wheat Fibre 101 (WF 101), Wheat Fibre 600 (WF 600) all supplied by IMCD New Zealand Limited (Auckland, New Zealand) and citrus fibre supplied by Hawkins Watt (Auckland, New Zealand).

3.2.2.1 Size characterization of the fibres

A light microscopic technique was employed to determine the length distribution of all fibres. All fibre particles were stained with safranin and washed with MilliQ water afterwards. The stained fibres were resuspended in water to ensure a good separation between particles under the microscope. All fibre suspensions were photographed at a suitable magnification using an Olympus BX53 microscope (Tokyo, Japan). Image analysis software, Digimizer (Ostend, Belgium) was used to measure the length and diameter of each fibre. An average of 30 images was analysed for each fibre type. Examples of microscope images of different fibres are shown in Figure 3.1(a-d).

Figure 3.2 shows the length distribution of fibre particles. AF 400-30 and WF 101 fibres had an average length of 30 µm and 50 µm, respectively. Meanwhile, WF 600 and citrus fibres had an average length of 100 µm and 200 µm respectively. Diameter of the fibres did not vary much within and between fibre samples with an average diameter ranging between 10-20 µm. Aspect ratio is the length to diameter of the fibres. All fibres length and aspect ratio are summarized in Table 3.3.

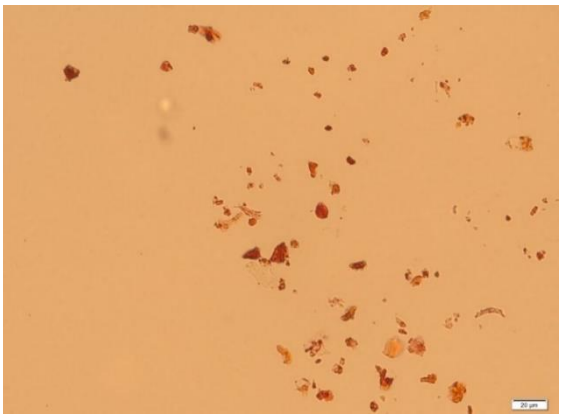

(a) AF 400-30

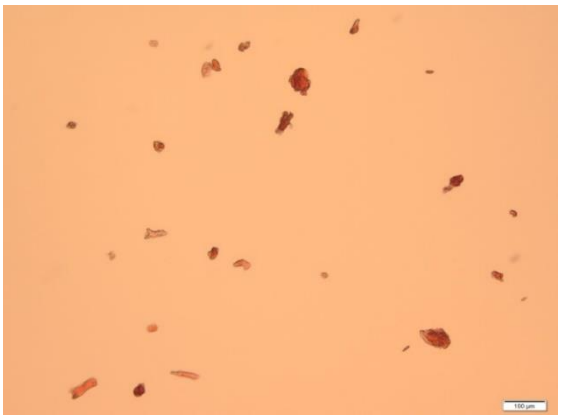

(b) WF 101

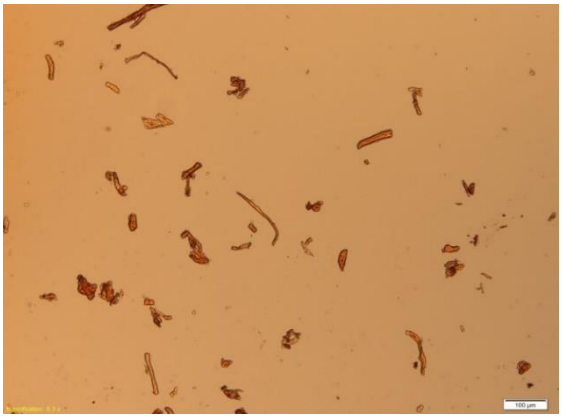

(c) WF 600

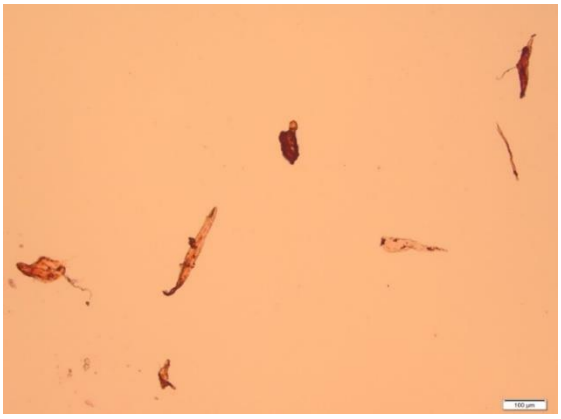

(d) citrus fibre

Figure 3.1 Light microscope image of fibres after staining with safranin (a) AF 400-30 (b) WF 101 (c) WF 600 (d) citrus fibres. The length of the scale bar is (a) 20 µm (b-d) 100 µm.

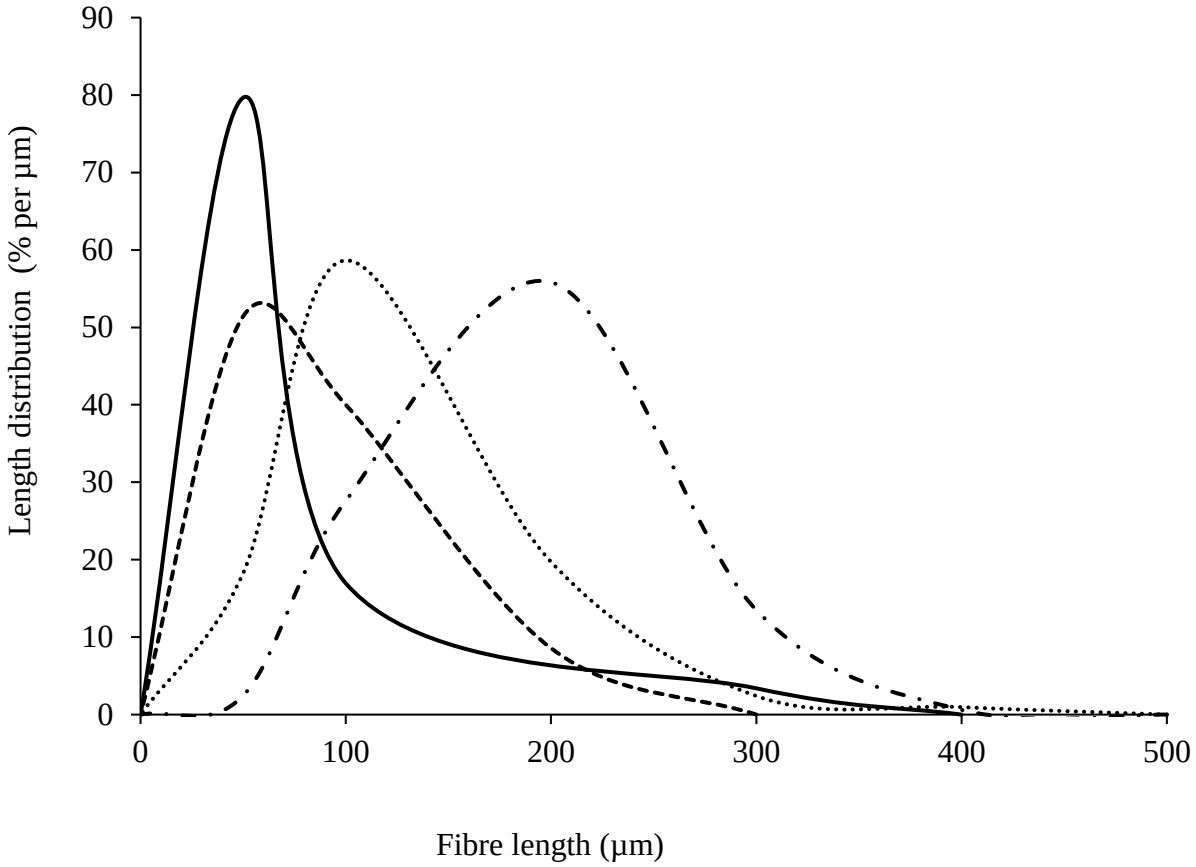

Figure 3.2 Fibre length distribution generated using the combination of Olympus BX53 microscope and Digimizer software. (—) AF 400-30 (---) WF 101 (···) WF 600 (-·-·-) citrus fibres.

Table 3.3: Summary of fibre lengths and its corresponding aspect ratio.

Types of fibres	Supplier	Number-based average fibre length (µm)	Mean aspect ratio
Apple Fibre 400-30 (AF 400-30)	IMCD New Zealand Limited	30	2 – 3
Wheat Fibre 101 (WF 101)	IMCD New Zealand Limited	50	2 – 3
Wheat Fibre 600 (WF 600)	IMCD New Zealand Limited	100	8 – 10
citrus fibre	Hawkins Watt, New Zealand	200	8 – 10

3.3 Test liquid construction

During the early stages of the study where most of the work done involved the characterization of the rheology of the fibre suspensions, different concentrations of fibre suspensions were used. These concentrations ranging between 1.0 wt.% to 10.0 wt.%. During the atomization studies of the fibre suspensions, only 5.0 wt.% of fibre concentration was tested.

Different concentrations of fibre suspensions were prepared by mixing the fibre powders into the 60 °Brix concentrated apple juice at 20 °C and continuously stirred until complete dispersion was achieved. All mixtures were prepared immediately before conducting a test.

3.4 Physical properties of materials

This section describes the measurement methods of the physical properties of the fibres, apple juice and fibre suspensions. The properties explained in this section include the

density and surface tension presented in Section 3.4.1 and 3.4.2 respectively. These properties will affect atomization performance as discussed in the literature review.

3.4.1 Density of apple juice, fibres and fibre suspensions

The bulk density of the apple juice and fibre suspensions were measured based on the mass per volume method. Each solution was poured into a measuring cylinder and the weight was recorded by a weighing scale while the bulk volume was read from the cylinder. Five repeated measurements were performed. The density of the apple juice was 1370 $\pm$ 1.85 kg/m^3 while the average density of the fibre suspensions was 1420 $\pm$ 1.25 kg/m^3. The density of different fibre suspensions at different concentration does not vary much with each other with a maximum difference of 2%.

The density of fibre particles was measured using a helium gas pycnometer, AccuPyc II 1340 V1.09 (Micromeritics, Norcross, USA). The pycnometer measures the volume of porous particles using Archimedes principle of fluid displacement and Boyle-Marriot's law of volume-pressure relationships (Tamari, 2004). The ultrapycnometer with $\sim$ 100 cm^3 blank vessel was calibrated using helium gas under ambient temperature and pressure. The volume of the blank vessel was recorded. After that, the pycnometer was first tested using a calibration ball of 51.1080 cm^3 by placing the ball inside a sample vessel which has the same volume as the blank vessel. These vessels were located side by side. The blank vessel was connected to an air compressor by valve 1 and the sample vessel was connected to the blank vessel by valve 2. The sample vessel with ball inside was then pressurized to a pressure above the ambient condition until a constant pressure was recorded, then pressure was released back to below the ambient condition until a constant pressure was achieved. These processes were controlled by valves 1 and 2. The system returned to ambient pressure afer the gas was released from both vessels. At the end, the pycnometer showed the volume of the ball based on the recorded pressure and volume of the blank and sample vessels by following Boyle-Marriot's law, Equation 3.1.

$$P_1V_1 = P_2V_2 \qquad \text{Equation 3.1}$$

where P (Pa) is the pressure inside the vessel and V (cm^3) is the volume of the vessel. Ten pressure cycles were performed, and the recorded volumes of the calibration ball are tabulated in Table 3.4.

Table 3.4: Experimental measured volume for 51.11 cm^3 calibration ball.

Run	Volume (cm^3)
1	51.08
2	51.08
3	51.10
4	51.11
5	51.11
6	51.11
7	51.11
8	51.11
9	51.10
10	51.11
Average	51.10

Fibres which had been kept in a desiccator overnight were placed into the sample vessel for density measurement. The weight of the fibres was determined beforehand using a weighing scale while the volume was recorded from the pycnometer.

Density of fibre particles = Weight of fibres/Volume of fibres Equation 3.2

Five pressure cycles were performed. The densities of different fibre particles are tabulated in Table 3.5. The densities of all fibre particles shown in Table 3.5 determined by gas pycnometer were less than the reported density of pure cellulose. The absolute density of pure cellulose and pure lignin were reported as 1.59 g/cm^3 (Meredith, 1956) and 1.40 g/cm^3 (Walker, 2006) respectively. WF 101 and WF 600 fibres had the closest densities value to pure cellulose, suggesting that these fibres mostly made up of cellulose. Meanwhile, it is suggested that AF 400-30 and citrus fibres had less cellulose and more lignin content when compared to WF 101 and WF 600 fibres, that contributed to the lower measured density. Besides that, it is also possible that the presence of porosity and impurities resulted in the lower density of AF 400-30 and citrus fibres (Mwaikambo & Ansell, 2001). This behaviour is commonly seen in most plant fibres where the density lies between 1.4 – 1.5 g/cm^3.

Table 3.5: Density of different fibre particles measured using a gas pycnometer.

Run	Density (g/cm^3)			
	AF 400-30	WF 101	WF 600	citrus fibre
1	1.47	1.56	1.57	1.51
2	1.47	1.56	1.57	1.51
3	1.47	1.57	1.57	1.51
4	1.47	1.57	1.56	1.51
5	1.47	1.57	1.56	1.51
Average	1.47	1.57	1.57	1.51

3.4.1.1 Conversion from weight fraction to volume fraction of fibre suspensions

Weight fraction (wt.%) of fibre suspensions is being used throughout the discussion. The conversion from weight fraction to volume fraction (vol.%) was carried out purposely to obtain the maximum volume fraction allowable inside the concentrated apple juice, based on Krieger-Dougherty and Maron-Pierce relations, as shown in Section 4.1.3. For a specific weight of fibres used, the volume of the fibres was acquired based on the density of the fibres found in Table 3.5. A graph that shows the relationship between the weight fraction and its corresponding volume fraction of each type of fibres is shown in Figure 3.3.

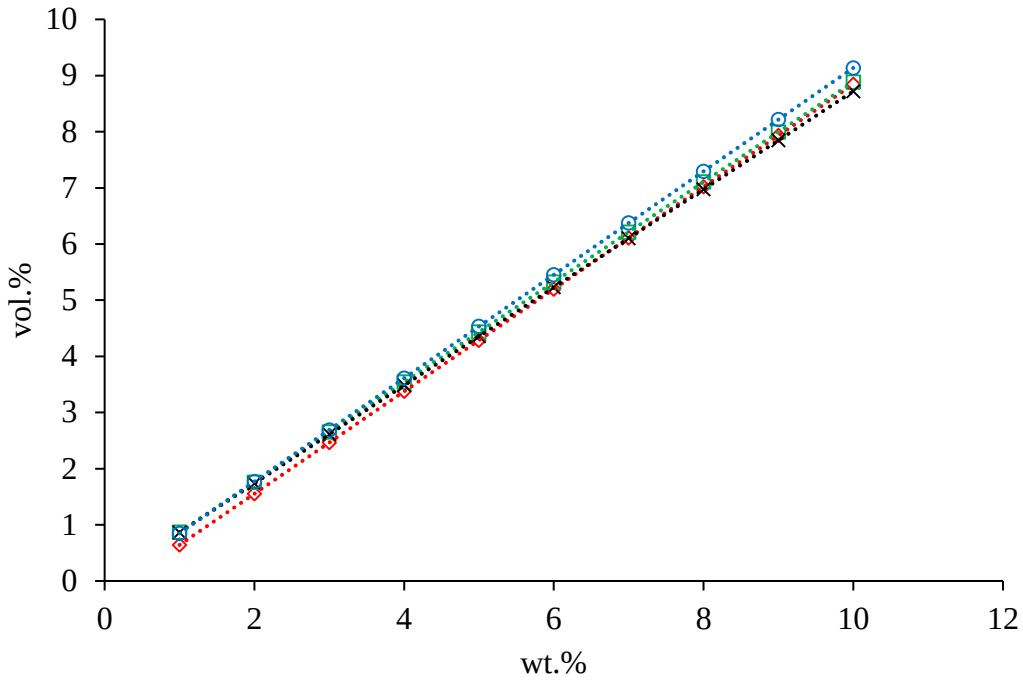

Figure 3.3 A plot of vol.% against wt.% of fibre suspensions. (○, blue) AF 400-30, (□, green) WF 101, (◊, red) WF 600 and (×, black) citrus fibre together with the linear trendline.

3.4.2 Surface tension of apple juice and fibre suspensions

Surface tension can be measured in several ways including Wilhelmy plate, Du Noüy ring, bubble pressure, sessile drop and falling methods. Each method has its own advantages and drawbacks. In this study, it was intended to either use the Wilhelmy plate or Du Noüy ring method. The approach was taken due to the nature of the concentrated apple juice and fibre suspensions. Both solutions exhibited high viscosity compared to water. Bubble pressure method works by generating gas bubbles and blows them through a capillary which is submerged in the sample liquid. The measurement of the surface tension is based on the known pressure inside of the gas bubbles as they emerge from the capillary into the liquid sample. The formation of the bubbles, however, may become abnormal due to the high viscosity of apple juice and fibre suspensions especially. This, in turn, will affect the final surface tension values. Hence, it is suggested that the measurement of surface tension using the bubble pressure method should be avoided. Meanwhile, the pendant drop method is unsuitable because it works by using a needle to suspend a drop. The shape of the drop then is used to calculate the surface tension. This method is especially inappropriate for fibre

suspensions as the fibre particles are large enough to not fit into the needle. The drop suspended then may not be the representative of the fibre suspensions.

In these experimental measurements, the Wilhelmy plate method was employed using a commercial apparatus Krüss K12 Tensiometer (Krüss GmbH, Hamburg, Germany). This method used a vertical platinum plate with known geometry that had been roughened to improve its wettability. The lower edge of the plate was brought into contact with the liquid surface and the 'Wilhelmy' force was measured by moving the plate up to the level of the liquid surface, as shown in Figure 3.4. The surface tension of the liquid was then calculated from the measured force using Equation 3.3.

$$\sigma = \frac{P_w}{l_w \cos\theta} \qquad \text{Equation 3.3}$$

where σ (mN/m) is the surface tension, P_w (mN) is the measured Wilhelmy force, l_w (m) is the wetted length and θ (°) is the contact angle between the tangent at the wetting line and the plate surface. θ was assumed to be zero since the plate surface has been treated to improve the wettability.

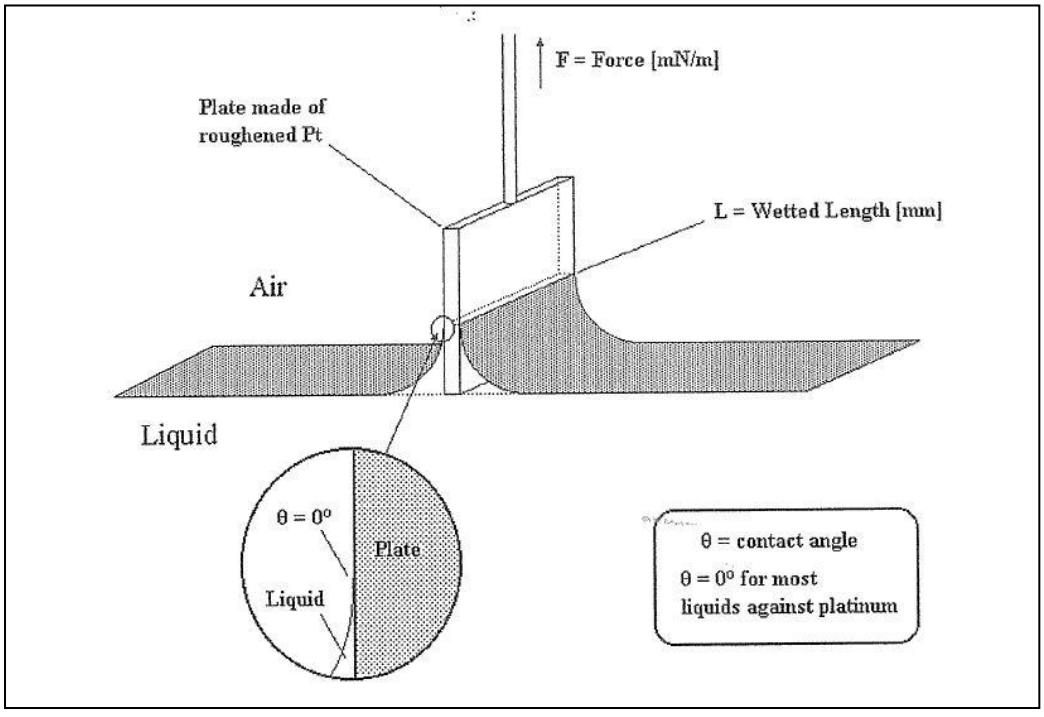

Figure 3.4 Factors affecting the surface tension calculation of the Wilhelmy plate method. (Image taken from the Krüss K12 Tensiometer Manual).

The overall movement of the plate during the measurement is depicted in Figure 3.5. For each measurement, a 30 mL solution was poured into a container and placed in a jacketed measurement vessel. A clean Wilhelmy plate was then inserted into the balance. The vessel was raised until the lower edge of the plate was levelled with the liquid as shown in Step 2. The remaining movements of the plate shown in Step 3 and 4 were being controlled automatically by the Krüss K12 Tensiometer.

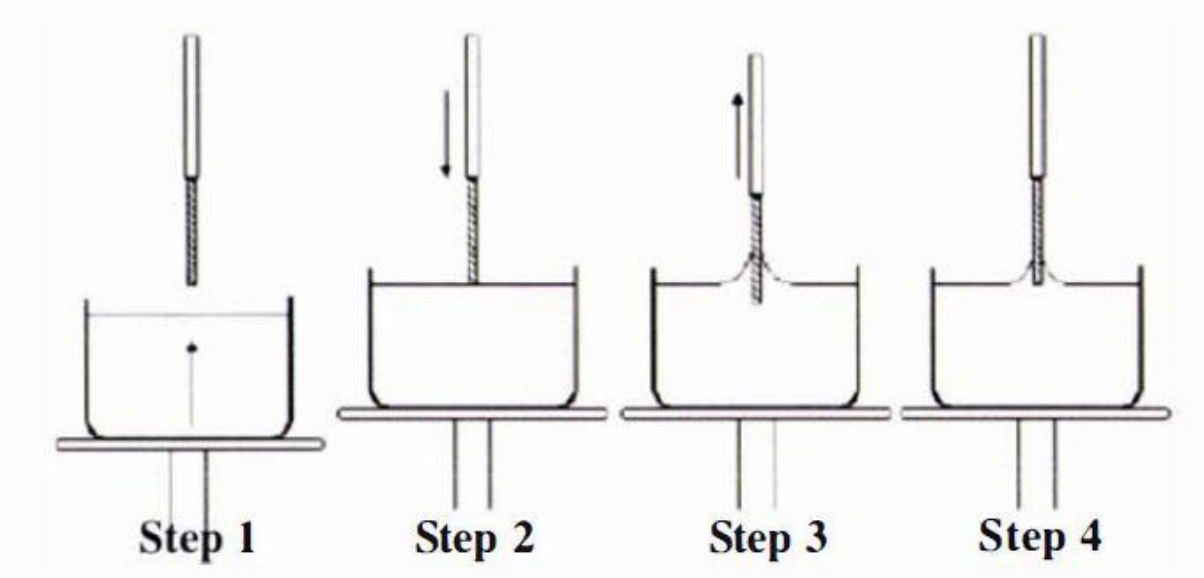

Figure 3.5 Overall movement of the plate during the measurement of surface tension based on Wilhelmy plate method. (Image taken from the Krüss K12 Tensiometer Manual).

3.4.2.1 Surface tension results and discussion

A series of measurements were taken for water at 20 °C as shown in Table 3.6. The average measured surface tension value of water was 72.4 $\pm$ 0.01 mN/m, which is very similar to the literature value of 72.7 mN/m at 20 °C (Vargaftik et al., 1983) (Appendix A).

Table 3.6: Surface tension value of water measured at 20 °C.

Measurement interval (s)	Surface tension (mN/m)
0	72.5
10	72.4
20	72.4
30	72.4
40	72.5
50	72.4
60	72.4
70	72.4
80	72.4
90	72.5

A series of measurements were performed on concentrated apple juice, 3.0 wt.%, 5.0 wt.% and 7.0 wt.% of different types of fibre suspensions at 20 °C. The measured surface tension values for water were approximately constant over time as shown in Table 3.6. In contrast, the measured surface tension values for concentrated apple juice and all types of fibre suspensions decreased over time as shown in Figure 3.6. This is strongly suspected to be due to the high viscosity of the solutions compared to water. With the high viscosity of the concentrated apple juice and fibre suspensions, it is suggested that a liquid film was formed that stuck to the plate. This caused an increase of load detected by the force measuring system which then translated into an increase in the measured surface tension value. The film eventually flowed back into the sample vessel over time and the measured surface tension value decreased. As shown in Figure 3.6, both concentrated apple juice and fibre suspensions showed a significant major decrease in the surface tension between t = 0 to t = 30 s. After t = 30 s and up to t = 270 s, the decrease in the surface tension was not as obvious as in the decrease between t = 0 to t = 30 s. It is suggested that between t = 0 and t = 30 s, the surface tension readings were affected by the high viscosity film that formed on the plate. It was preferred to use a single surface tension value throughout the study for both concentrated apple juice and fibre suspensions. A single surface tension value was obtained by averaging the surface tension values between t = 30 s and t = 270 s. The surface tension

between t = 0 to t = 30 s was excluded because the measurement was highly affected by the liquid film that stuck to the plate.

Three different measurements were performed for each liquid. The average surface tension value of concentrated apple juice was 64.7 ± 0.30 mN/m which is lower than water. Based on the high-performance liquid chromatography (HPLC) test performed by Sebastian Linnenkugel to identify and quantify components in the concentrated apple juice as explained in Section 3.2.1, the content of the apple juice was higher in fructose compared to glucose and sucrose with 68%, 15% and 14%, respectively. The surface tension of the apple juice depends on the composition of the sugar mixtures inside. Based on the study by Montañez-Soto et al. (2013), fructose caused a greater decrease in the surface tension of water, followed by sucrose and then glucose. This is because the intermolecular interactions between molecules of glucose are stronger than between molecules of sucrose and fructose, which is why fructose is the most soluble of these sugars. So, a higher concentration of fructose may result in a greater reduction in the surface tension of the concentrated apple juice. However, a separate study by Adhikari et al. (2007) showed the opposite. Fructose solutions showed a greater surface tension than water at all concentrations between 10 – 70%. This is because the cohesive strength of the water molecule is mainly due to hydrogen bonds and the number of these hydrogen bonds in water increases with the addition of fructose. A similar observation was obtained by Weast et al. (1988) with sucrose solutions. Since the concentrated apple juice which was made up of fructose and sucrose showed a lower surface tension value than water, it is highly possible that a surface-active agent or surfactant was presented inside the concentrated juice. However, at this stage, it is unknown which element inside the concentrated apple juice acted as the surfactant.

Three different measurements were performed for each fibre suspensions. As shown in Figure 3.6, at a similar fibre concentration of 5.0 wt.%, insignificant differences between the surface tension values of AF 400-30, WF 101, WF 600 and citrus fibre suspensions were observed. The surface tension of different types of fibres suspensions overlapped with each other at each time interval. In addition, Figure 3.7 which shows the average surface tension values for fibre suspensions at different concentrations, no clear trend between the surface tension and fibre concentrations was obtained. The surface tension values were scattered with minimum and maximum being 66.28 mN/m and 67.30 mN/m respectively. The scattering of the data may be due to the fact that the change in the surface tension of the concentrated apple juice with small changes in the concentration of fibres was so small

that the error involved in making the measurements obscured any regular trend. The average surface tension for each fibre suspensions is tabulated in Table 3.7. It was decided to average the scattered values of surface tension from Table 3.7 or Figure 3.7. This final average surface tension value will be used as a representation for all fibre suspensions at different concentrations used throughout this study. The final average surface tension value of fibre suspensions was 66.8 $\pm$ 0.09 mN/m.

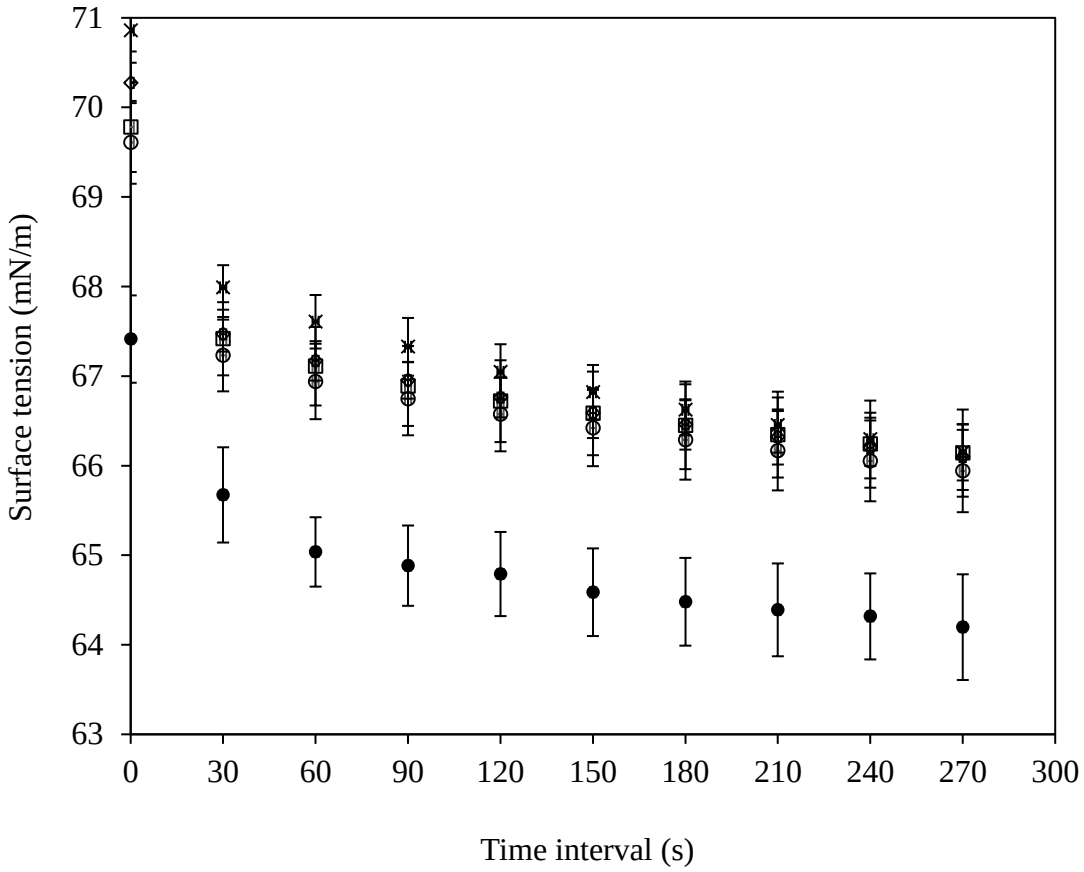

Figure 3.6 Surface tension profile of concentrated apple juice and fibre suspensions at 20 °C. (●) Concentrated apple juice, (○) 5.0 wt.% AF 400-30, (□) 5.0 wt.% WF 101, (◊) 5.0 wt.% WF 600 and (×) 5.0 wt.% citrus fibre suspensions.

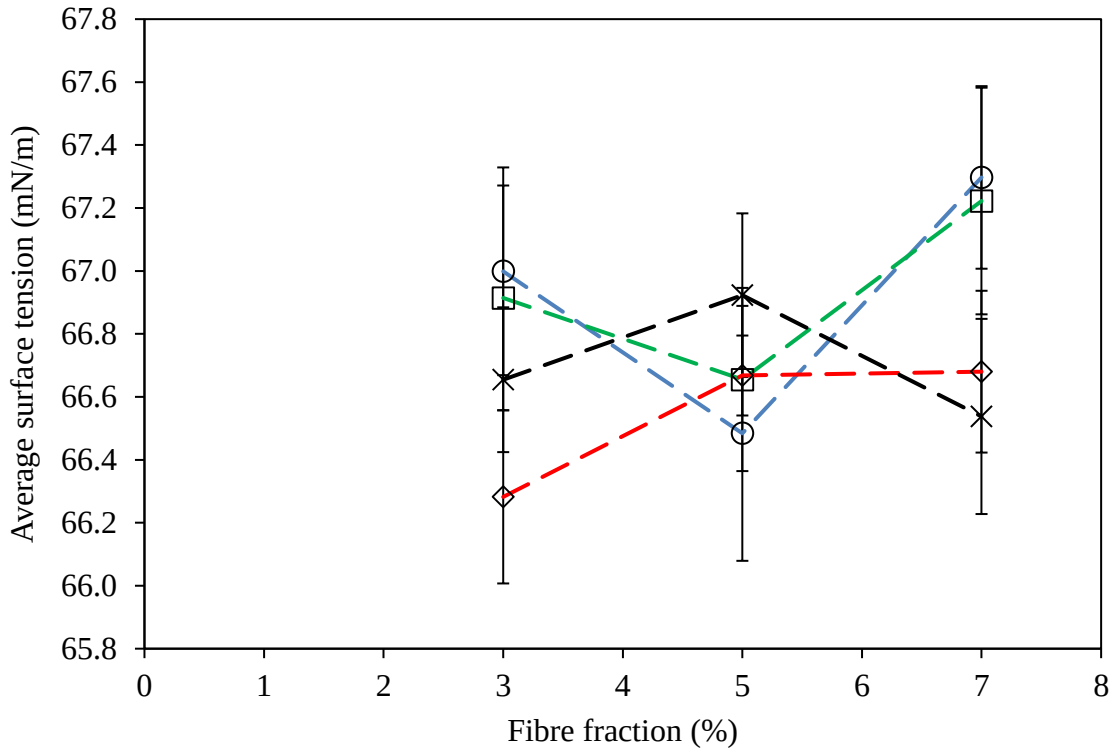

Figure 3.7 Average surface tension values of fibre suspensions at 3.0 wt.%, 5.0 wt.% and 7.0 wt.% fibre fractions calculated by averaging the surface tension at a time interval of 30 s – 270 s. (○, blue) AF 400-30, (□, green) WF 101, (◊, red) WF 600 and (×, black) citrus fibre suspensions.

Table 3.7: Tabulate data of the surface tension of each fibre suspensions at 3.0 wt.%, 5.0 wt.% and 7.0 wt.%, as depicted in Figure 3.7.

Fibres type	Fibre fraction (wt.%)	Surface tension (mN/m)
AF 400-30	3.0	67.0 ± 0.33
	5.0	66.5 ± 0.41
	7.0	67.3 ± 0.29
WF 101	3.0	66.9 ± 0.35
	5.0	66.7 ± 0.29
	7.0	67.2 ± 0.36
WF 600	3.0	66.3 ± 0.28
	5.0	66.7 ± 0.13
	7.0	66.7 ± 0.26
CF	3.0	66.7 ± 0.23
	5.0	66.9 ± 0.26
	7.0	66.5 ± 0.31
Minimum surface tension (mN/m)		66.3
Maximum surface tension (mN/m)		67.3
Average (mN/m)		66.8

3.4.2.2 Effect of temperature

Single measurement was taken for surface tension at different temperatures for water. Initial tests on water gave reproducible results when compared to the literature value (Appendix A), specifically being 71.3 mN/m at 30 °C, 69.5 mN/m at 40 °C, 67.9 mN/m at 50 °C and 66.2 mN/m at 60 °C. Similar to the surface tension of fibre suspensions at 20 °C, a series of measurements were taken for surface tension at other temperatures ranging between 20 °C and 70 °C and the average surface tension value at each temperature reading were then obtained by averaging the values between t = 30 s and t = 270 s. Figure 3.8 reports the surface tension of 5.0 wt.% WF 600 fibre suspension at different temperatures. Investigations on the effect of temperature were only performed on 5.0 wt.% WF 600 fibre suspension. The data was used in a further analysis on the effect of temperature during atomization.

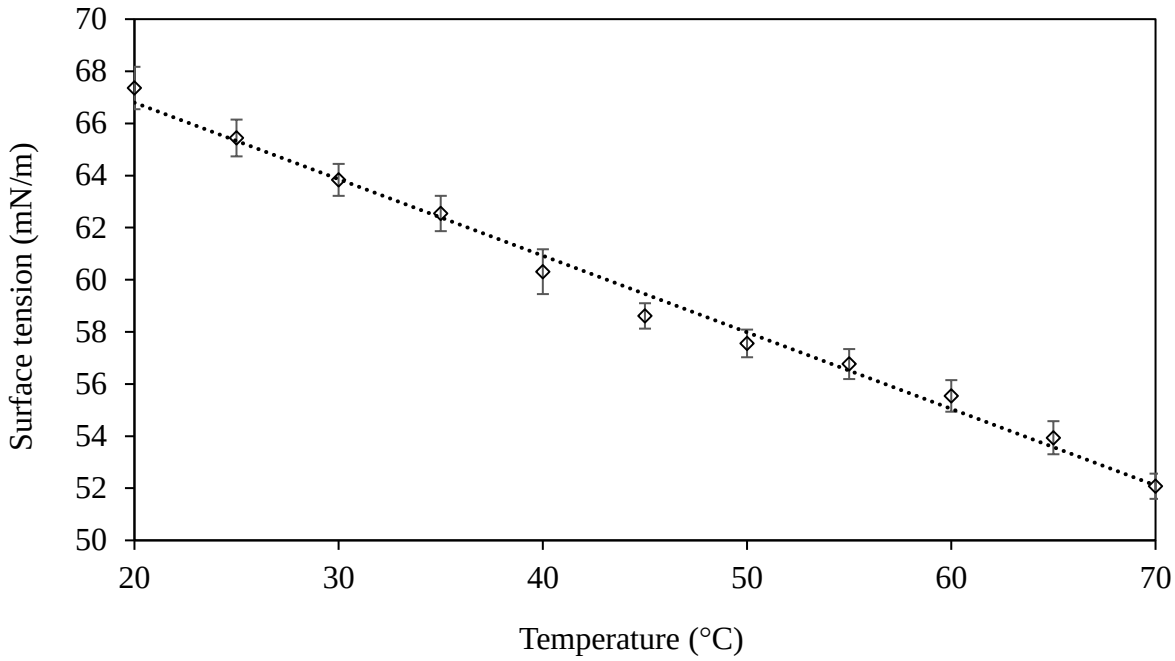

Figure 3.8 Surface tension of 5.0 wt.% WF 600 suspensions as a function of temperature.

3.5 Experimental methods

3.5.1 Rotary rheometer

Rheology tests were performed using a stress-controlled rheometer, model MCR 301 (Anton Paar GmbH, Graz, Austria), equipped with a coaxial cylinder. This MCR series rheometer was used in two different modes. Rotational mode was set during the steady shear rheology test while oscillatory mode was used to examine the small amplitude oscillatory shear properties. Cup and bob geometry were utilized throughout the study. To prevent wall slippage, the gap between the cup and bob, *H*, was varied in the range 0.30 – 2.0 mm depending on the fibre particle length. Specifically, the gap was set to be 10 times larger than the size of the fibre particle.

During the shear flow curve tests, the shear rate was increased step-by-step from 0 to 1000 s^{-1} and the change of viscosity was observed at the rate of 0.25 min/viscosity point. Three different measurements were performed for each sample. Shear viscosity measurements were carried out at temperatures of 20 °C, 25 °C, 30 °C, 35 °C and 40 °C. The results for these experiments are given in Section 4.1.

The main purpose of conducting the oscillatory test was to obtain the linear viscoelastic properties of the fibre suspensions. During the small amplitude oscillatory tests, the angular frequency was increased from 0.1 rad/s to 100 rad/s. Throughout the study, all tests were conducted in the linear viscoelastic region, which was found to be valid at 0.1% strain. Oscillatory tests were carried out at temperatures of 20 °C, 25 °C, 30 °C, 35 °C, 40 °C, 45 °C, 50 °C, 55 °C, 60 °C, 65 °C and 70 °C. The results for oscillatory measurements are presented in Section 5.1.

3.5.2 Capillary viscometer

As explained in Section 3.5.1, the shear viscosity measurements using a rotary rheometer was possible up until 1000 s^{-1} shear rate only. A in-house built capillary viscometer was used to obtain the measurements at shear rates greater than 1000 s^{-1} and up to 20 000 s^{-1}. Large, medium and small diameter capillary tubes were operated in the range of shear rates 500 s^{-1} < 8*V*/*D* < 20 000 s^{-1}, where *D* (m) is the tube diameter and *V* (m/s) is the average velocity inside the tube. However, 8*V*/*D* is the shear rate at the wall for Newtonian fluids only, and the true shear rate that accounts for non-Newtonian behavior of a liquid was used throughout the study when using the capillary viscometer. For non-Newtonian liquids with a power-law index, n, the true shear rate is given in Equation 3.4, where Q_L (mL/min) is the liquid flow rate (Fredrickson, 1964).

$$\dot{\gamma} = (8\mathrm{V}/\mathrm{D})[(3n+1)/4n] \qquad \text{Equation 3.4}$$

The large, medium and small tube diameters were 9.2 mm, 5.0 mm and 3.2 mm respectively. A differential pressure transmitter (Endress+Hauser, Reinach, Switzerland) was used to obtain the pressure drop across two points on each capillary tube while a volumetric flow meter transmitter (Endress+Hauser, Reinach, Switzerland) was used to obtain the volumetric flow rate. Measurements were undertaken at the same flow rate with capillaries with the same diameter, but one was twice the length of the other. The pressure reading of the shorter capillary was then subtracted from the longer. By doing this the entry and exit effects where subtracted thus leaving only the pressure drop in capillary. The capillary was calibrated with a Newtonian fluid of known viscosity in the range of the fibre

suspensions (corn syrup solutions typically). The results and discussion are presented in Section 4.2.

3.5.3 Capillary breakup extensional rheometer

There are few well-known methods that can be used to quantify the extensional effects of a fluid. These are the Filament Stretching Extensional Rheometer, FiSER^{TM} (Cambridge Polymer Group, Boston), the Capillary Breakup Extensional Rheometer, CaBER^{TM} (Cambridge Polymer Group, Boston and Haake) and the Cambridge Trimaster (Hallmark et al., 2016; Sachdev et al., 2016). These devices measure the necking of an extensionally-strained fluid filament as a function of time. The CaBER was first developed by McKinley and co-workers at MIT in conjunction with Cambridge Polymer Group. Conventional extensional rheometers are heavy, delicate and expensive. There was, therefore, a need for a portable device for measuring extensional behaviour. The first lightweight portable extensional rheometer was built by Collett et al. (2015). The portable rheometer works by monitoring the dynamics of a breakup of fluid filament following a short, rapid, extensional deformation. One can obtain information about the relaxation time, the extent of non-Newtonian behaviour and the time to break up for the fluid. The relaxation time parameter is of important value in atomization applications. Figure 3.9 shows the operation of the portable extensional rheometer (Hallmark et al., 2016). More theory and explanations on the extraction of relaxation time parameter from the portable extensional rheometer is presented in Section 5.2.

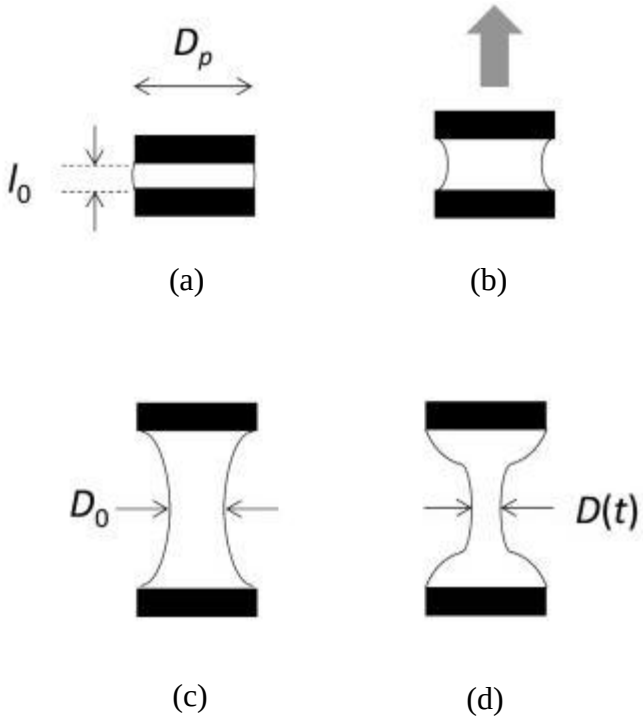

Figure 3.9 Diagram showing the CaBER operation. (a) A sample is loaded between pistons (b) The top piston moves upwards (c) A filament is formed with initial mid-point diameter D_0 (d) The filament thins until breakup. Image is reproduced from Hallmark et al. (2016).

3.5.3.1 Building of our own portable extensional rheometer

The portable extensional rheometer used throughout the study was designed and built in-house at Massey University based on the works by Hallmark et al. (2016). The portable extensional rheometer consisted of two parallel pistons of diameter, D_P, 4 mm separated by an initial gap of length, L_0, 1.5 mm. A liquid sample was loaded into the gap and the top plate was pulled apart rapidly to a final gap, L_f, 4.0 mm to impose an extensional deformation on the liquid sample. The portable extensional rheometer was built around a battery-powered solenoid that was capable of applying an abrupt stretch to a sample of fibre suspensions placed between the two 4 mm pistons thus creating an extensional field. The solenoid used was a Model 8.02.13.72 (HE & BS Benson Ltd). A small screw placed on the top of the solenoid was used to adjust the maximum travel of the top piston. The solenoid was housed on the upper body of the portable extensional rheometer and attached to the top piston while the bottom piston remained stationary and was mounted in the lower

body. The vertical adjustment of the upper body was possible via a knob. The knob can be securely locked using a small screw attached on its side.

The portable extensional rheometer was attached to an aluminium profile, onto which was also attached the lens support. A high-speed camera, XIMEA MQ003MG-CM (XIME GmbH, Münster, Germany) capable of up to 500 frames per second at a resolution of 640 × 480 pixels and a parfocal lens, Leica Monozoom 7 (Artisan Technology Group, IL, US) were used to carefully monitor the change in the filament diameter at the portable extensional rheometer. A set of coding was generated using MATLAB™ (2015b) software to digitally analyse the measurement of the filament diameter in each frame captured by the high-speed camera. The overall setup is shown in Figure 3.10. An example of the MATLAB coding was attached in Appendix B.

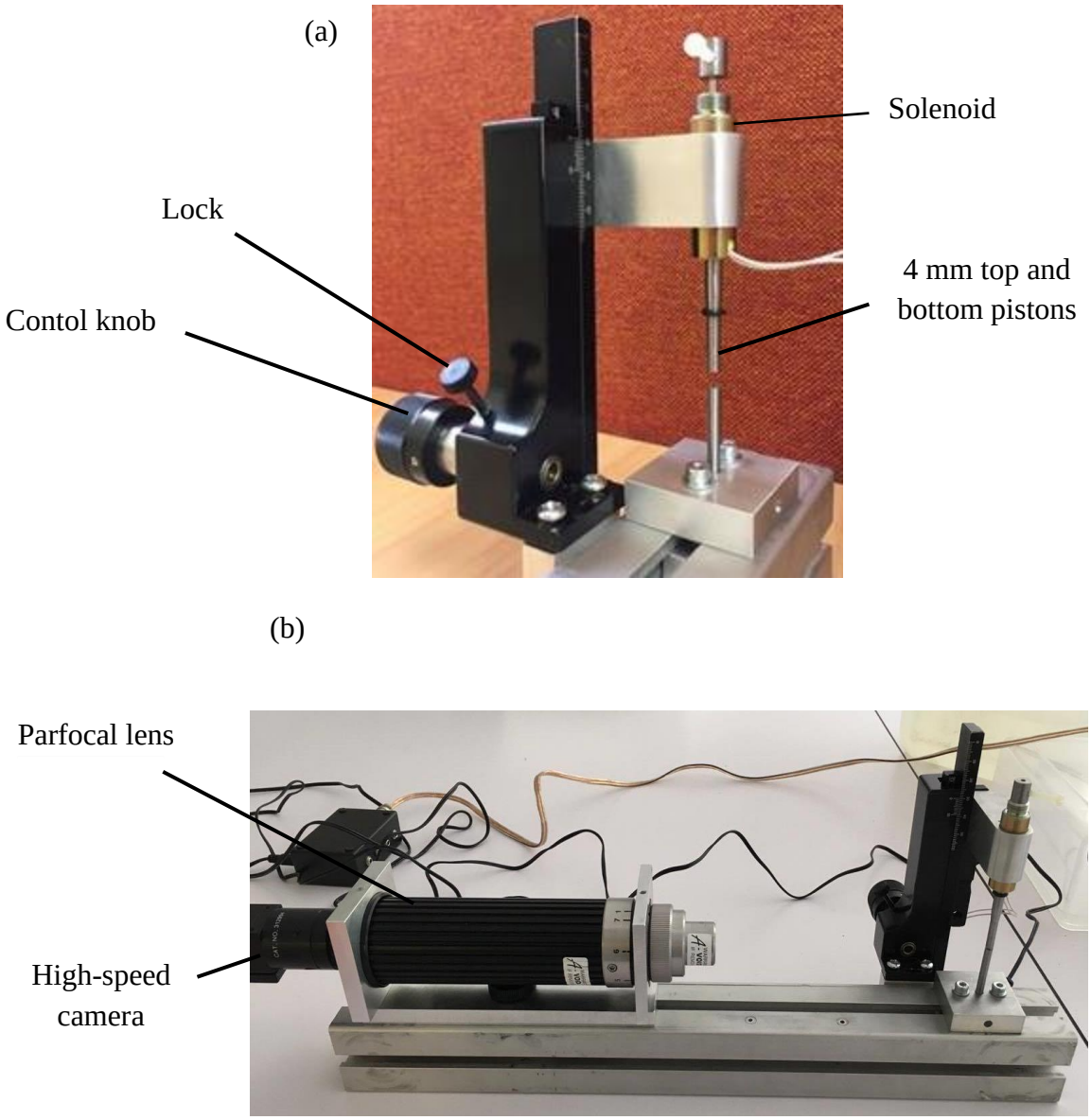

Figure 3.10 (a) Close-up view of the portable extensional rheometer (b) Photograph of the whole setup including camera, lens and the portable extensional rheometer.

3.5.3.2 Validation of the portable extensional rheometer

The validation of the portable extensional rheometer is necessary to justify the reliability in measuring the extensional properties. The validation was carried out based on two experimental approaches as explained below:

1) A series of measurements of piston positions as a function of time was performed to ensure the repeatability and accuracy of upper piston movement. This will ensure the uniform velocity profile of the upper piston for a specific displacement in different experiments. A plot of piston displacement over time is shown in Figure 3.11.
2) A series of identical filaments thinning experiments were carried out using a Newtonian oil viscosity standard (Cannon Instrument, PA, USA). The aim was to evaluate the reliability of the portable extensional rheometer to reproduce results from the literature.

Figure 3.11 shows the displacement of the upper piston at every 2 ms for five similar tests done separately on the portable extensional rheometer. A statistical analysis using SPSS Statistics was performed afterwards. Based on an intra-class correlation coefficient (ICC) test which was performed to evaluate the reproducibility of the piston movement, more than 0.9 correlation coefficients were obtained as shown in Table 3.8, which suggests that the portable extensional rheometer exhibited a high inter-run reliability between the five runs performed. This indicates that the reproducibility of the piston position, thus velocity, was excellent and the portable extensional rheometer was reliable enough to be used throughout the study.

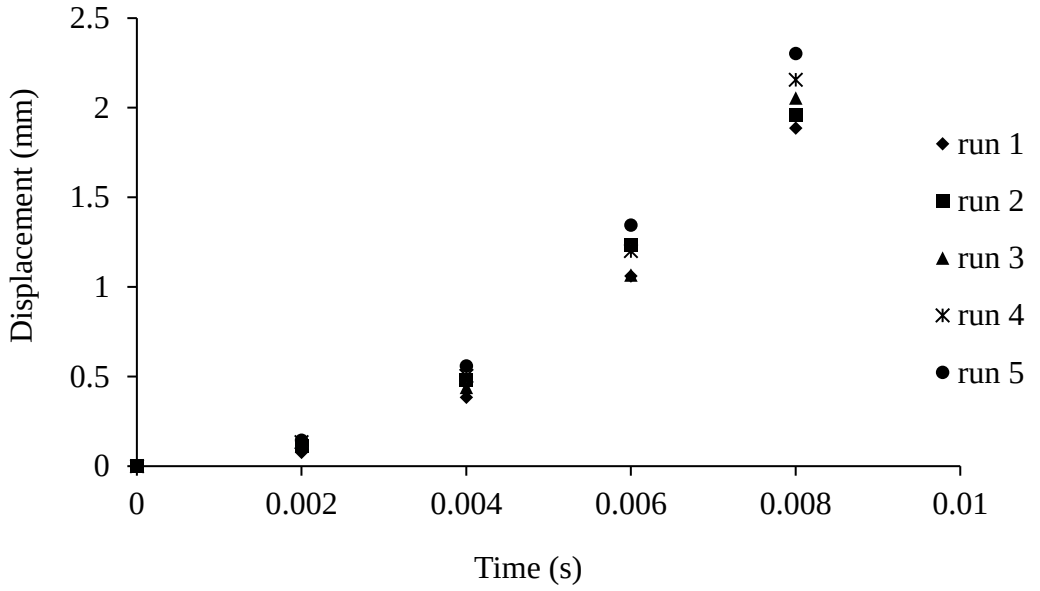

Figure 3.11 Evolution of piston displacement for five similar tests performed on the portable extensional rheometer. (♦) run 1 (■) run 2 (▲) run 3 (×) run 4 (●) run 5.

Table 3.8: Inter-run correlation matrix for the movement of the upper piston based on Figure 3.11.

ICC coefficient	Run 1	Run 2	Run 3	Run 4	Run 5
Run 1	1.000	0.998	0.999	0.999	0.999
Run 2	0.998	1.000	0.994	0.997	0.999
Run 3	0.999	0.994	1.000	0.999	0.998
Run 4	0.999	0.997	0.999	1.000	1.000
Run 5	0.999	0.999	0.998	1.000	1.000

Next, ten similar experiments on the portable extensional rheometer were carried out using a Newtonian oil viscosity standard of 35.1 Pa.s. The values of the oil filament diameter over time were recorded to calculate the viscosity. The methodology for calculating shear viscosity from the portable extensional rheometer setup using Equation 3.5 is discussed in detail by McKinley and Tripathi (2000).

$$\frac{\Delta D}{\Delta t} = \frac{(2X-1)\sigma}{3\mu_0} \qquad \text{Equation 3.5}$$

Here, σ (mN/m) is the surface tension, μ_0 (Pa.s) is the Newtonian viscosity, $\Delta D/\Delta t$ (mm/s) is the gradient of the filament thinning profile and *X* is a correction factor termed the 'shape factor' and is applied to Newtonian filament thinning with value of 0.713 (Papageorgiou, 1995). Based on Table 3.9, the average viscosity resulting from the ten experiments was 34.1 ± 0.7 Pa.s, which was statistically the same as the quoted standard value of 35.1 Pa.s. The variations of each experiment from the standard value also lied comfortably within the range of $\pm$ 10% which other authors have reported for extensional techniques (McKinley & Tripathi, 2000).

Based on the two validation steps, the portable extensional rheometer that was built in-house at Massey University, was suitable to be used to examine the extension rheological properties of fibre suspensions.

Table 3.9: Calculated viscosity values for 35.1 Pa.s standard Newtonian oil.

Experiment	Viscosity (Pa.s)	Variations from standard value
1	32.4	7.9%
2	32.2	8.4%
3	37.5	- 6.9%
4	37.3	-6.2%
5	36.0	-2.5%
6	32.6	7.1%
7	32.9	6.4%
8	32.8	6.5%
9	34.4	2.0%
10	33.0	6.1%
Average	34.1 ± 0.7	

3.5.4 Atomizer and Spray Setup

3.5.4.1 Two-fluid nozzle

A two-fluid (fluid cap 60100, air cap 120) based on external mixing was acquired from Spraying System New Zealand Limited (Auckland, New Zealand). The configuration of the nozzle is shown in Figure 3.12 along with the mixing region. In this work, a two-fluid nozzle was chosen for the atomization of fibre suspensions based on the following reasons:

1) The fibre suspensions exhibit extensional properties as discussed in Chapter 5. Previous work has shown that a common nozzle used in the industry such as a high-pressure nozzle, is not suitable to atomize extensional liquids, as discussed in Section 2.3 (Thompson and Rothstein, 2007; Stelter et al., 2002). Besides that, a visit to a well-known spray drying company; GEA Niro, at Copenhagen, Denmark has revealed that working with polymer solutions, a rotary atomizer usually fails in atomizing the extensional liquids (H. Schwartzbach, M. Reck, Sara, Jesper and others, personal communication, October 12, 2017).
2) The energy from the high-velocity air in the two-fluid nozzle is required to effectively atomize the fibre suspensions which exhibited extensional resistance. More discussion can be found in Chapter 6.

In general, the mechanism that occurs during a two-fluid atomization is one of a high-velocity air creating high frictional forces over liquid surfaces causing disintegration of the liquid into droplets (Masters, 1979). Marmottant and Villermaux (2004) have explained the mechanism of two-fluid atomization in more detail. Using a two-fluid nozzle and working with a Newtonian liquid, the overall breakup process was described by a sequence of instabilities. The liquid jet first experienced a high shear rate at its surface induced by the surrounding high-velocity flow of air. This led to the generation of waves on the jet surface. As the waves grew, the acceleration of the high-velocity air elongated ligaments of the liquid into the air stream. These stretched ligaments thinned down in the neck region and ultimately detached from the jet. After that, the detached ligaments fragmented and stabilized into smaller droplets. The mechanism of the atomization has been explained in more details in the literature review and discussion sections.

Figure 3.13 highlights the individual parts of the two-fluid nozzle which consisted of a fluid cap and an air cap. In the fluid cap, the diameter of the round liquid orifice (D_J) was 1.50 mm. The two-fluid nozzle used had an annular air orifice of diameter (D_i) and outer diameter (D_o) of 2.54 mm and 3.00 mm respectively. The liquid flow was supplied by a gear pump and measured using a graduated cylinder and stopwatch. The air flow rate was monitored using a pressure regulator and a rotameter. Spray tests were conducted at room temperature of 20 ± 1 °C and in atmospheric air. The schematic diagram of the nozzle setup is shown in Figure 3.14.

Some of the tests required the atomization to occur at temperatures greater than 20 °C and up until a maximum of 70 °C. The setup for the high-temperature atomization was exactly similar as in Figure 3.14, except that a 16 ft long heating tape was attached along the pipeline between the liquid tank and the inlet of the two-fluid nozzle. The heating tape (HTS/Amptek Co., Texas, USA) and a temperature sensor were both connected to a similar temperature controller. The temperature sensor probe was inserted into the pipeline near the two-fluid nozzle by making a hole so that the temperature sensor can accurately measure the temperature of the liquid inside the pipeline.

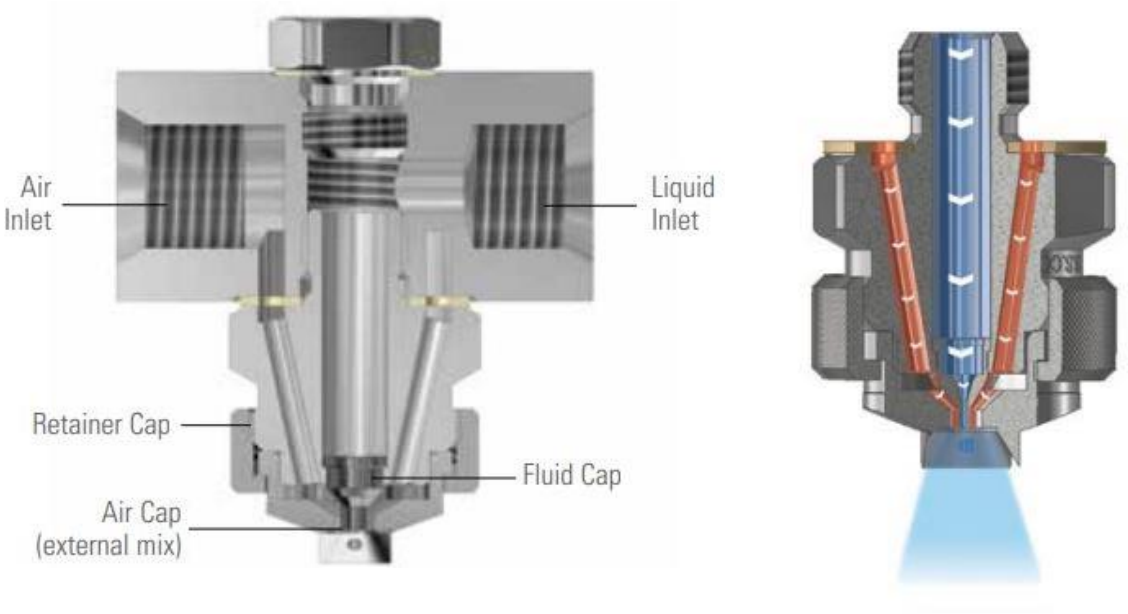

(a) Parts included in the two-fluid nozzle system

(b) Mixing of liquid and air outside of the orifice

Figure 3.12 Configuration of the two-fluid nozzle and the mixing region. (Image taken from Spraying System New Zealand Limited magazine).

(a) Fluid cap (code: 60100)

(b) Air cap from different angles (code: 120). (left image) top view of the air cap (right image) side view of the air cap

Figure 3.13 Two-fluid nozzle components. (Image taken from Spraying System New Zealand Limited magazine).

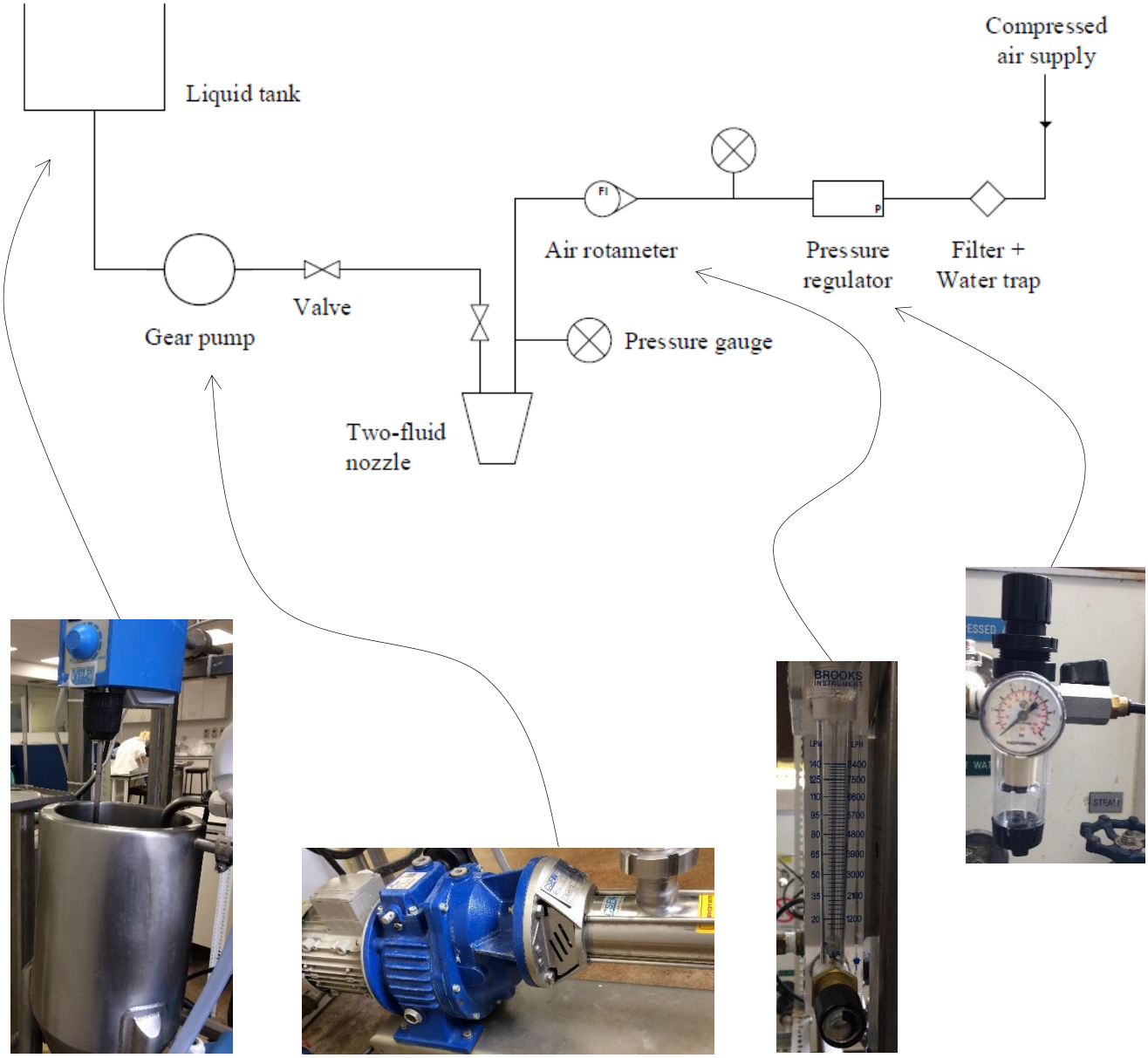

Figure 3.14 Schematic diagram of the whole spray setup which includes the liquid and air supply connections to the two-fluid nozzle. The dry air was supplied at 20 °C.

3.5.4.2 Ultrasonic-modulate two-fluid (UMTF) nozzle

Figure 3.15 shows the UMTF nozzle consisted of an annulus for airflow and an ultrasonic nozzle (SONAER Inc., USA). The cross-sectional area of the annulus was the same as in the two-fluid nozzle to allow for similar atomizing air velocity at any specific air flow rate. Air was supplied through 4 openings which were situated opposite to each other. The SONAER ultrasonic nozzle consisted of a central tube for liquid flow and a piezoelectric transducer. The piezoelectric transducer received an electrical input at frequency 40 kHz from a power generator Model FY2200S (FeelTech, Henan Province, China) and converted the input electrical energy into mechanical energy of vibration. The voltage used in the study was 100 volts peak to peak. The nozzle was geometrically configured such that the excitation of the piezoelectric transducer created a standing wave called capillary wave at the nozzle tip, where the tip diameter was 4.0 mm. Liquid was delivered to the nozzle tip through a concentric hole of 1.0 mm diameter using a pumping setup in Figure 3.14. In general, the mechanism that occurs during UMTF atomization is one of a capillary wave travels axially along the jet in the direction of the liquid flow with its amplitude growing due to the excitation of the transducer and is amplified by the air blowing around it.

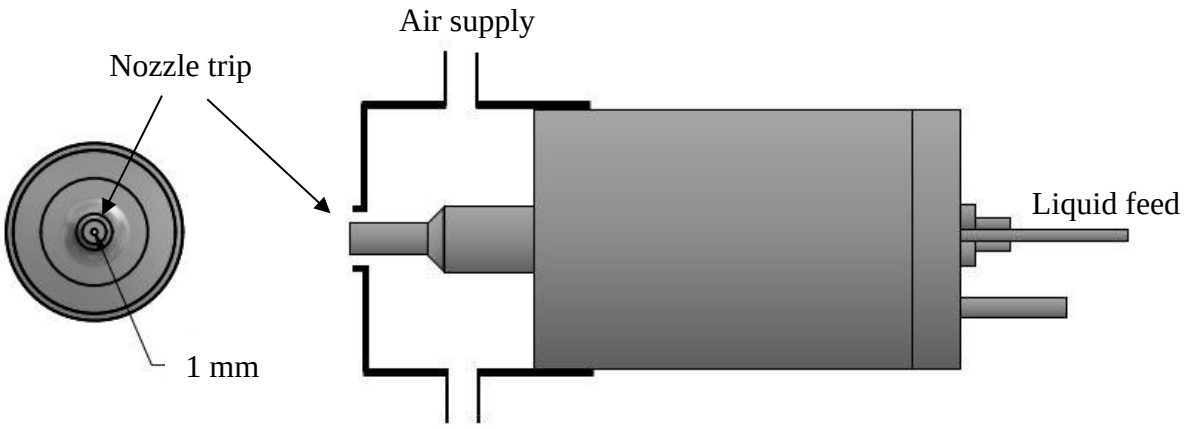

Figure 3.15 Ultrasonic-modulated two-fluid (UMTF) nozzle components which include the ultrasonic body and air compartment. The components inside the ultrasonic body such as the piezoelectric transducer is not shown in the image.

3.5.5 Photography

3.5.5.1 Flash photography technique

A high-intensity light source and a camera (MS85K, Mega Speed), equipped with a lens (Vivitar Series 1) were used for imaging atomization behaviour or spray breakup details. A backlit setup was used, in which the spray was situated between the light source and a camera so that the spray details such as liquid ligaments and droplets appeared dark on a bright background. The flash photography technique was performed at two different positions; at a position right after the nozzle exit and at a position 50 mm below the nozzle exit. It is desired to observe the early stage atomization pattern near the nozzle exit while a more complete atomization pattern or droplets was found at a position 50 mm below the nozzle. The 50 mm position after the nozzle exit has been used by several authors (Elversson et al., 2003; Nguyen & Rhodes, 1998).

1) Right after the nozzle exit or 10 mm below the nozzle.
   Atomization behaviour at this position includes the early stage of atomization, which includes the disturbed liquid jet, ligaments and filaments.
2) At a position 50 mm below the nozzle.
   Droplet sizing was attempted using an optical technique at this position far below the nozzle exit. It was desired to observe the droplets details including the size and shape. At least 100 images were captured for each experiment which corresponds to at least 1000 droplets observed and analysed.

A pulse generator (PM 5712, Philips) was connected to the high-intensity light source to yield a short pulse duration of 10 ns. The pulsing of the light source was to illuminate and ‘freeze’ the ligaments and droplets in mid-flight while a camera situated directly opposite to the light source captured the ligaments and droplets images through a far-field microscope lens (Vivitar Series 1). Images of droplets were then digitally processed using MATLAB image analysis to extract the data on droplet size. Appendix C shows in detail the newly developed and written MATLAB image analysis which describes the measurement procedures. The camera was mounted on a tripod to ease the changing and positioning of the camera between different positions below the nozzle exit. Figure 3.16

shows the schematic diagram of the flash photography setup that indicates clearly the position of each equipment.

3.5.5.2 DSLR technique

A 60 mm micro lens and SB-910 speedlight were attached to a Nikon D90 camera. The DSLR was used to capture the image of a whole spray for spray angle identification.

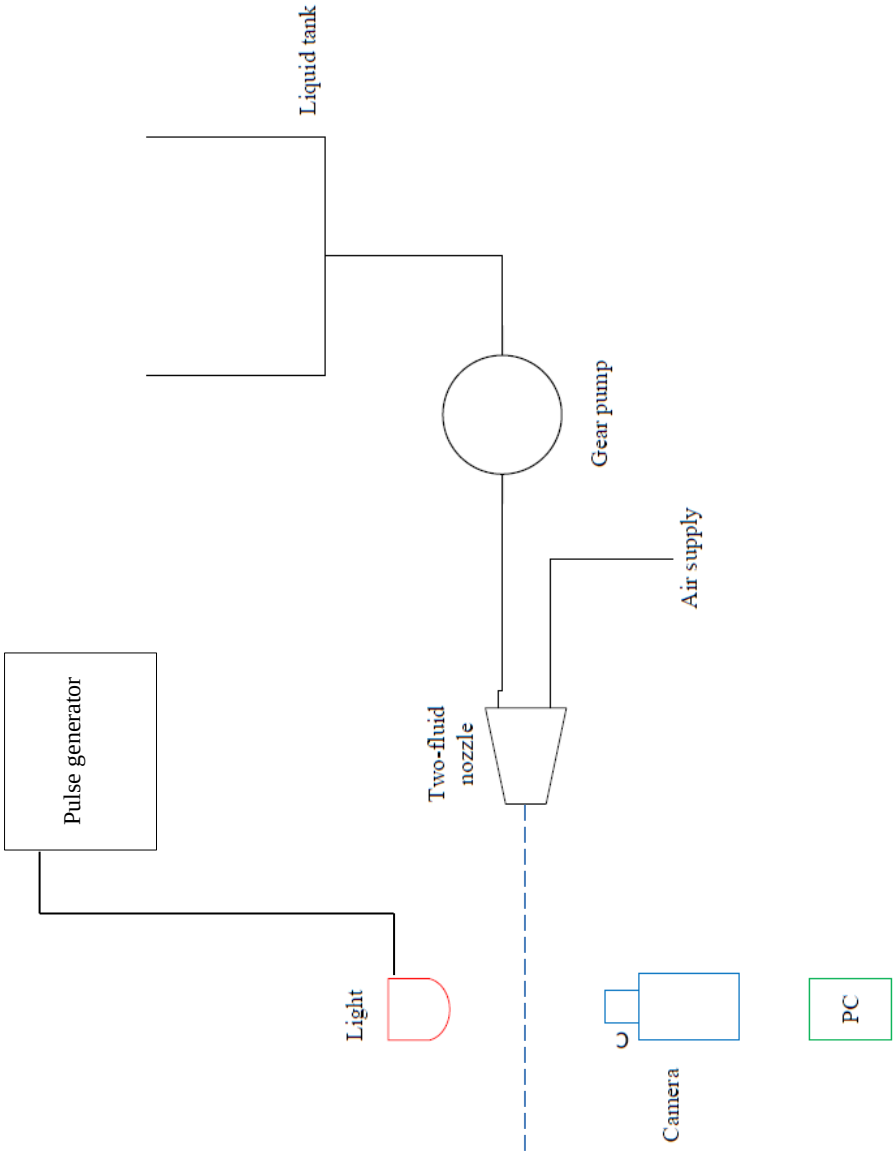

Figure 3.16 Schematic diagram of the flash photography technique.

3.5.6 Malvern Mastersizer S

A Malvern Mastersizer (Model S, Malvern Instruments Limited, Malvern, Worcestershire, UK) unit was modified to allow a spray to pass between the beam expander and the lens. Specifically, a multi-channel nozzle was put at the front side of both the beam expander and lens to act as a shield. Air was purged through the multi-channel nozzle to prevent droplet deposition, especially on the lens, as this will affect the results generated by the Malvern Mastersizer. A 1000 mm focal length lens was used with 10 000 sweeps. The lower and upper obscuration boundaries were set at 2 and 50%. Beam alignment and background signal measurement were checked between each measurement. The lens was also cleaned after each measurement to ensure more accurate results. The spray was positioned so that the laser beam was directed through the centre of the spray at a longitudinal axis of approximately 50 mm below the nozzle. Figure 3.17 shows the schematic diagram from the side view while Figure 3.18 shows a photograph of the modified Malvern Mastersizer.

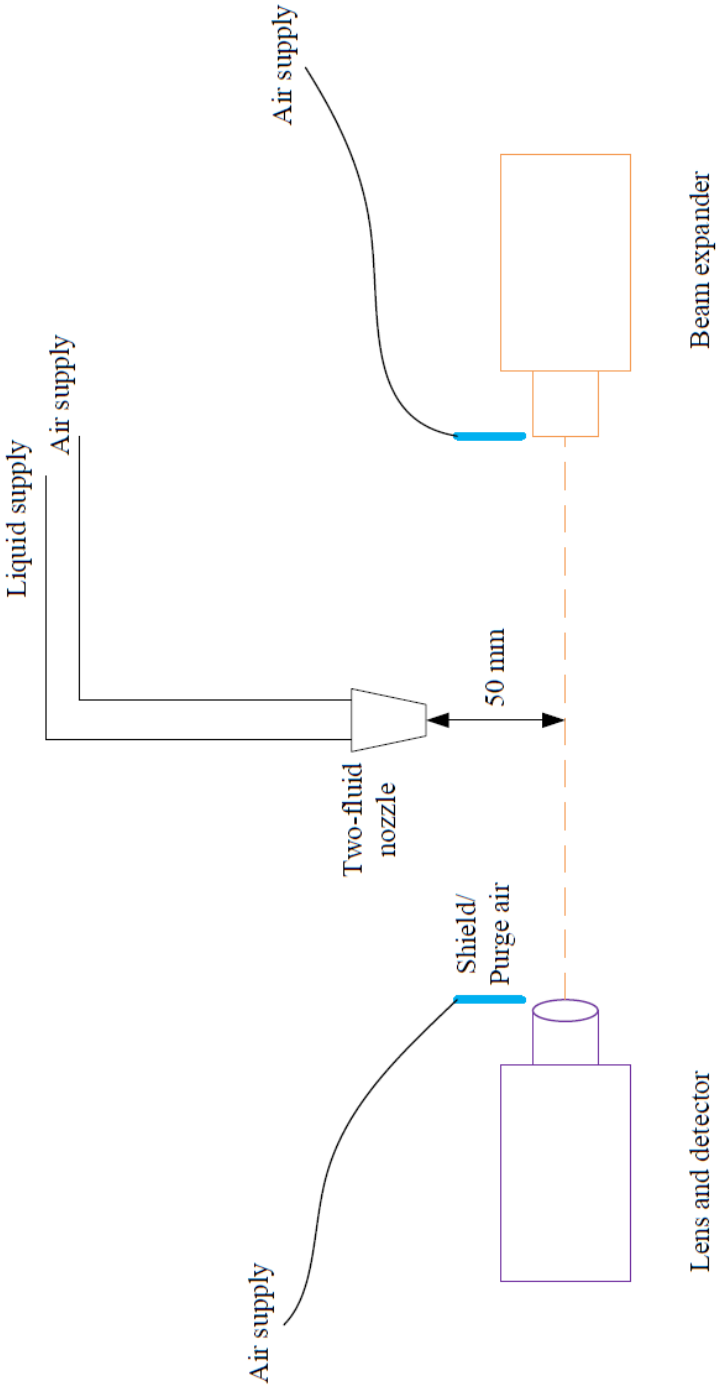

Figure 3.17 Schematic diagram of the Malvern Mastersizer S setup highlighting the position of a multi-channel nozzle (represented by a thick blue line) at the front of each lens and beam expander.

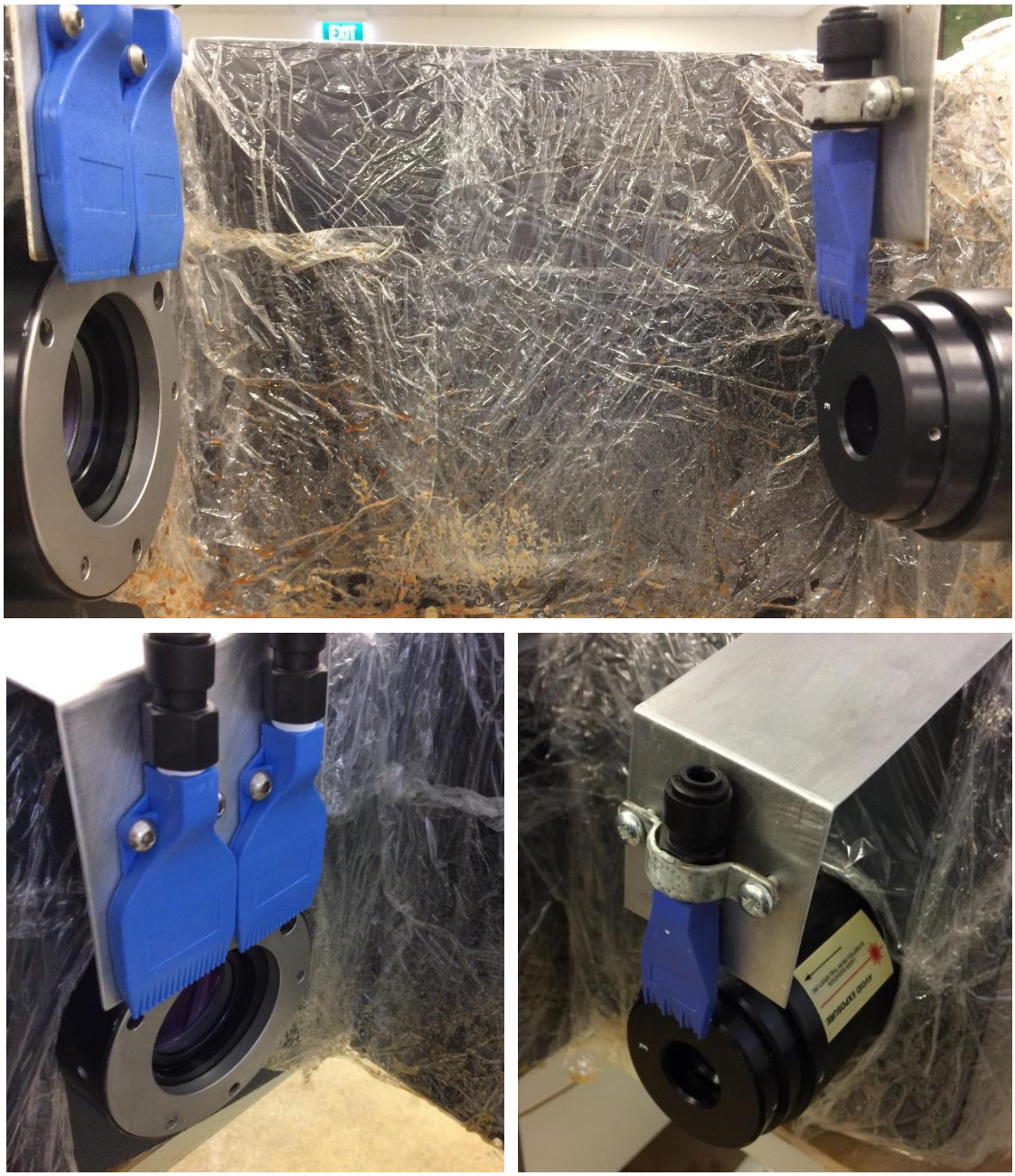

Figure 3.18 Photograph of the modified Malvern Mastersizer S showing the position of a multi-channel nozzle at the front of each lens and beam expander. (bottom left image) Lens and (bottom right image) beam expander.

3.5.7 Droplet size analysis

Throughout the study, droplet sizing results are presented using the D-values based on volumetric mean diameters. D(v,10), D(v,50) and D(v,90) were generated for each atomization run to acquire specific detail on the reduction in each individual D-value as atomization condition changes. Droplets size results were obtained and compared by two different methods:

1) Optical technique paired with Matlab image analysis as explained in Section 3.5.5.1.
2) Laser technique based on Malvern Mastersizer as explained in Section 3.5.6.

The D-values are the intercepts for 10%, 50% and 90% of the cumulative volume. Specifically, D(v,10) is the diameter at which 10% of the sample's volume is comprised of droplets with a diameter less than this value. D(v,50) is defined as the diameter where half of the sample's volume has droplets with a diameter less than this value. Similarly, D(v,90) is the diameter at which 90% of the sample's volume contains droplets with a diameter less than this value. Along with D-values, droplet size distributions were also acquired from the Malvern Mastersizer technique. Overall, the discussion on the atomization performance in Chapter 6 is based on D-values and droplets size distribution or span, supported also with the images of the atomization behaviour and patterns.

3.5.8 Spraying into liquid nitrogen

To see the actual droplets of the fibre suspensions after the atomization without drying the droplets, the fibre suspensions were sprayed into liquid nitrogen to freeze the droplets. Liquid nitrogen was filled into a chilly bin and the spraying were directed into the chilly bin. The frozen droplets were then picked up and put onto glass slides. The glass slides used for the microscope observation were first frost inside a container filled with dry ices. The frozen droplets were then examined under a microscope equipped with a temperature-controlled mechanism. Specifically, the microscope area, which was the area where the droplets were put to be observed, can be lowered to -20 °C by using liquid nitrogen. This microscope equipped with a temperature-controlled mechanism was built by Jolin Morel for a different project. Dry ices were also scattered on the microscope area. All these acts

were carried out to keep the temperature as low as possible to prevent the frozen droplets from melting once put under the microscope.

3.6 Conclusion

As a conclusion, Section 3.2 – 3.4 has outlined in detail the materials used in the study together with the physical properties of the materials. The materials used in the study includes a 60 °Brix concentrated apple juice and four types of fibres; AF 400-30, WF 101, WF 600 and citrus, with different length and aspect ratios. The aspect ratio of AF 400-30 and WF 101 fibres was 2 – 3 while the aspect ratio of WF 600 and citrus fibres was 8 – 10. The density of these fibre particles ranging between 1.47 g/cm^3 to 1.57 g/cm^3. Throughout the study, a single average bulk density and surface tension were used to represent the different types of fibre suspensions, at different concentrations. The average density and average surface tension of the bulk fibre suspensions at 20 °C was 1420 kg/m^3 and 66.78 mN/m, respectively.

Other than the density and surface tension, the shear and extensional properties of the fibre suspensions were also important. Section 3.5 outlined in detail the methods used to investigate the shear and extensional properties. Other than that, the atomization setup is also presented in detail in Section 3.5. The subsequent chapters; Chapters 4 and 5, explain the shear properties and extensional properties of the fibre suspensions respectively, while Chapter 6 explains the atomization of the fibre suspensions.

References

Adhikari, B., Howes, T., Shrestha, A., & Bhandari, B. R. (2007). Effect of surface tension and viscosity on the surface stickiness of carbohydrate and protein solutions. *Journal of Food Engineering, 79*(4), 1136-1143.

Collett, C., Ardron, A., Bauer, U., Chapman, G., Chaudan, E., Hallmark, B., . . . Wilson, D. I. (2015). A portable extensional rheometer for measuring the viscoelasticity of pitcher plant and other sticky liquids in the field. *Plant Methods, 11*(1), 16.

Elkins, E. R., Matthys, A., Lyon, R., & Huang, C. (1996). Characterization of commercially produced apple juice concentrate. *Journal of Food Composition and Analysis, 9*(1), 43-56.

Elversson, J., Millqvist-Fureby, A., Alderborn, G., & Elofsson, U. (2003). Droplet and particle size relationship and shell thickness of inhalable lactose particles during spray drying. *Journal of Pharmaceutical Sciences, 92*(4), 900-910.

Fredrickson, A. G. (1964). *Principles and applications of rheology*: Prentice-Hall.

Hallmark, B., Bryan, M., Bosson, E., Butler, S., Hoier, T., Magens, O., . . . Wibberley, S. (2016). A portable and affordable extensional rheometer for field testing. *Measurement Science and Technology, 27*(12), 125302.

Marmottant, P., & Villermaux, E. (2004). Fragmentation of stretched liquid ligaments. *Physics of Fluids, 16*(8), 2732-2741.

Masters, K. (1979). Spray drying handbook. *Spray drying handbook.*(Ed. 3).

McKinley, G. H., & Tripathi, A. (2000). How to extract the Newtonian viscosity from capillary breakup measurements in a filament rheometer. *Journal of Rheology, 44*(3), 653-670.

Meredith, R. (1956). Mechanical Properties of Textile Fibres.

Montañez-Soto, J. L., González-Hernández, L. H., Venegas-González, J., Nicanor, A. B., & González-Cruz, L. (2013). Effect of the fructose and glucose concentration on the rheological behavior of high fructose syrups. *African Journal of Biotechnology, 12*(12).

Mwaikambo, L., & Ansell, M. (2001). The determination of porosity and cellulose content of plant fibers by density methods. *Journal of Materials Science Letters, 20*(23), 2095-2096.

Nguyen, D., & Rhodes, M. (1998). Producing fine drops of water by twin-fluid atomisation. *Powder Technology, 99*(3), 285-292.

Papageorgiou, D. T. (1995). On the breakup of viscous liquid threads. *Physics of fluids, 7*(7), 1529-1544.

Sachdev, S., Muralidharan, A., & Boukany, P. E. (2016). Molecular processes leading to "necking" in extensional flow of polymer solutions: Using microfluidics and single DNA imaging. *Macromolecules*, 49(24), 9578-9585.

Stelter, M., Brenn, G., & Durst, F. (2002). The influence of viscoelastic fluid properties on spray formation from flat-fan and pressure-swirl atomizers. *Atomization and Sprays, 12*, 299-327.

Tamari, S. (2004). Optimum design of the constant-volume gas pycnometer for determining the volume of solid particles. *Measurement Science and Technology, 15*(3), 549.

Thompson, J. C., & Rothstein, J. P. (2007). The atomization of viscoelastic fluids in flat-fan and hollow-cone spray nozzles. *Journal of Non-Newtonian Fluid Mechanics, 147*, 11-22.

Vargaftik, N., Volkov, B., & Voljak, L. (1983). International tables of the surface tension of water. *Journal of Physical and Chemical Reference Data, 12*(3), 817-820.

Walker, J. C. (2006). *Primary wood processing: principles and practice:* Springer Science & Business Media.

Weast, R. C., Astle, M. J., & Beyer, W. H. (1988). *CRC handbook of chemistry and physics* (Vol. 69): CRC press Boca Raton, FL.

Chapter 4 Shear rheology of fibre suspensions

4.1 Shear rheology

This chapter presents the experimental characterization of different types of fibre suspensions that were made up of different aspect ratios; AF 400-30 and WF 101 with an aspect ratio of 2-3 and WF 600 and citrus fibres with an aspect ratio of 8-10. Comparisons were made with models of power-law, Krieger-Dougherty and Maron-Pierce.

Section 4.2.1 focuses on the rheology of the concentrated apple juice, Section 4.2.2 shows the shear viscosity of fibre suspensions as a function of fibre fraction and aspect ratio, Section 4.2.3 investigates the Krieger-Dougherty and Maron-Pierce relationships and Section 4.2.4 examines the effect of temperature on the shear viscosity of the fibre suspensions. Section 4.2.5 explains the combined effect of fibre fraction and temperature on the shear viscosity of fibre suspensions.

4.1.1 Concentrated apple juice

The viscosity of the concentrated apple juice was measured for a range of shear rate from 0.1 s^{-1} to 1000 s^{-1} in a rotary rheometer. Figure 4.1 shows the viscosity curve for the concentrated apple juice, as a function of shear rate. As shown in Figure 4.1, the viscosity of the concentrated apple juice was constant and followed a Newtonian behaviour. The average viscosity value of the concentrated apple juice was 0.29 Pa.s. Previously, Ibarz et al. (1987) have reported a value of 0.24 Pa.s for a similar concentration of apple juice but sourced and processed differently.

The aim of this study was not to spray and atomize concentrated apple juice. The concentrated apple juice cannot be atomized and spray dried due to its low glass transition temperature. Industrially, concentrated apple juice is usually spray dried by incorporating maltodextrin as a drying aid to raise the glass transition temperature (Verma & Singh, 2015). Both the concentrated apple juice and concentrated apple juice mixed with maltodextrin behave as simple Newtonian liquids (Manjunatha, & Raju, 2015). Although it was not desired to atomize the concentrated apple juice or apple juice with maltodextrin,

it is important to emphasize that the atomization of both liquids has been shown to be achievable. Atomization of Newtonian liquids, such as water and apple juice mixed with maltodextrin, are well-explored and well-understand and have been in practice for many years. The introduction of fibres into the concentrated apple juice, changed the flow characteristics from Newtonian to non-Newtonian.

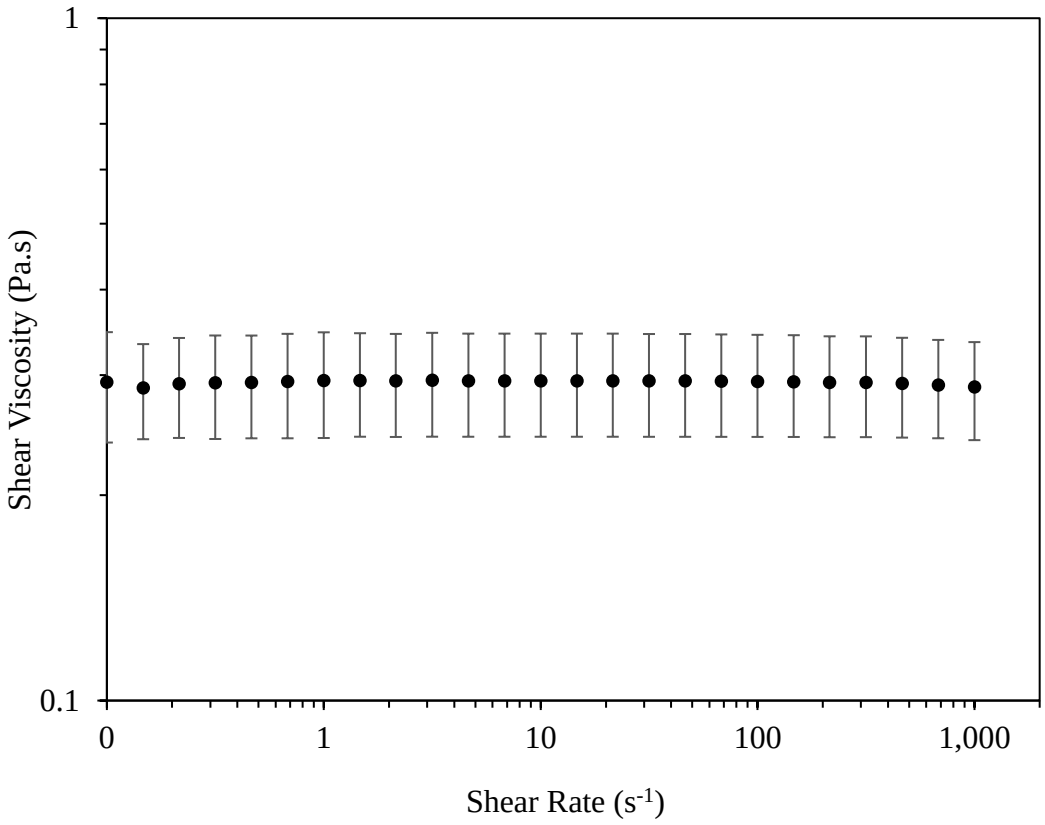

Figure 4.1 Viscosity curve for concentrated apple juice at shear rates up to 1000 s^{-1}.

4.1.2 Fibre suspensions

In the case of fibre suspensions, all measurements conducted in a rotary rheometer were the gap distance of the cup, H, was at least 10 times the fibre length, L. In this region, the wall effect was assumed to be negligible. All type of fibre suspensions in concentrated apple juice, when submitted to increasing shear, showed a non-Newtonian shear thinning behaviour compared to the Newtonian behaviour of the concentrated apple juice by itself.

Figure 4.2(a-d) shows the flow curves (shear stress against shear rate) for all 5.0 wt.% and 10.0 wt% AF400-30, WF 101, WF 600 and citrus fibre suspensions. Figures 4.3 and 4.4 shows the viscosity against shear rate curves for these fibre suspensions. As shown in Figure 4.2(a-d), the slope of the shear stress versus shear rate curve was not constant as the shear rate varied, especially for 10.0 wt.% AF 400-30, WF 101, WF 600 and citrus fibre suspensions. This indicates that all the fibre suspensions tested in this study were shear thinning liquids. Figures 4.3 and 4.4 show a clearer indication of the shear thinning behaviour, where the viscosity decreased with increasing shear rate. Shear thinning liquids are also called pseudoplastic liquids.

The shear thinning is observed because the fibres induce macromolecular structures into the fluid. This is due to hydrodynamic interactions and mechanical contacts between fibres. Upon shearing, the weak macro-structures breakdown reducing the apparent viscosity as the shear rate increases. It is suggested that the apparent viscosity will continue to reduce as fibres orientate themselves parallel to the flow direction (Bounoua et al., 2016; Djalili-Moghaddam & Toll, 2006).

Non-Newtonian behaviour can be modelled with a power function, given by Equation 4.1 in which the shear stress experienced by the fluid is related to the shear rate by a power constant, this is termed a power-law fluid

$$\tau_{shear} = k\dot{\gamma}^{n} \qquad \text{Equation 4.1}$$

where τ_{shear} (Pa) is the shear stress, $\dot{\gamma}$ (s^{-1}) is the shear rate, k ($Pa.s^{n}$) is the consistency index and n (-) is the flow index. Experimental data in Figure 4.2(a-d) was fitted with the power-law model and results showed that the power-law model provided a reasonable description of the experimental data of both 5.0 wt.% and 10.0 wt.% fibre suspensions. Table 4.1 lists the values of the fit parameters, k and n, based on the power-law model. The flow index, n, measures the degree of shear thinning behaviour, its value decreases as the rate of shear thinning or pseudoplasticity increases. Higher values of n were observed at the lower fibre fraction of 5.0 wt.% fibre suspensions while lower values of n were observed at a greater fibre fraction of 10.0 wt.% fibre suspensions, which indicates that non-Newtonian behaviour increases with the increased volume of fibres in the suspensions. The same relation was found by Grigelmo-Miguel et al. (1999) in peach dietary fibre

suspensions, by Bhattacharya et al. (1991) in tamarind kernel suspensions and by Mahmoud and Fugitt (1996) in a nutritional supplement containing oat fibre.

Concentrated apple juice was a simple Newtonian liquid which can be atomized. Addition of fibres introduces non-Newtonian behaviour. The 5.0 wt.% and 10.0 wt.% fibre suspensions were shear thinning liquids. It is well-known that the atomization performance is affected by the shear viscosity (Lefebvre, 1988), lower shear viscosity is preferable because the energy requirements for atomization are proportional to the fluid viscosity. Shear thinning of fibre suspensions means that during the atomization process, greater shear rates can be applied to the liquid fibre suspensions to attain a lower viscosity reducing the energic requirements for complete atomization. Concentrated milk solutions can be atomized at high solids concentrations due to their shear thinning behaviour (Teknotext, 1995).

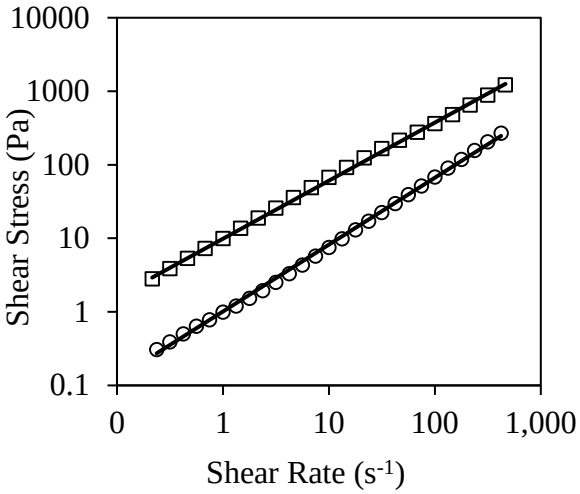

(a) AF 400-30

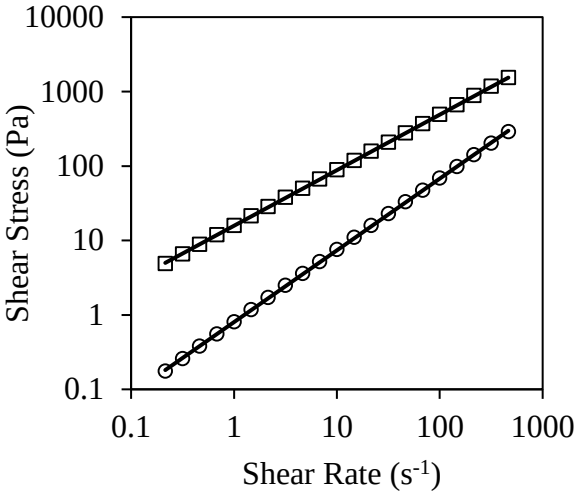

(b) WF 101

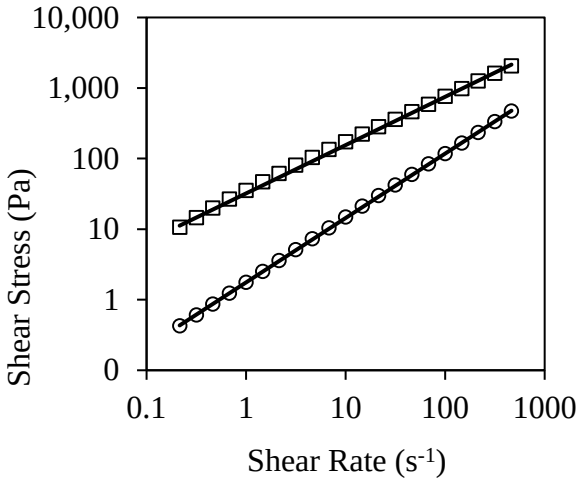

(c) WF 600

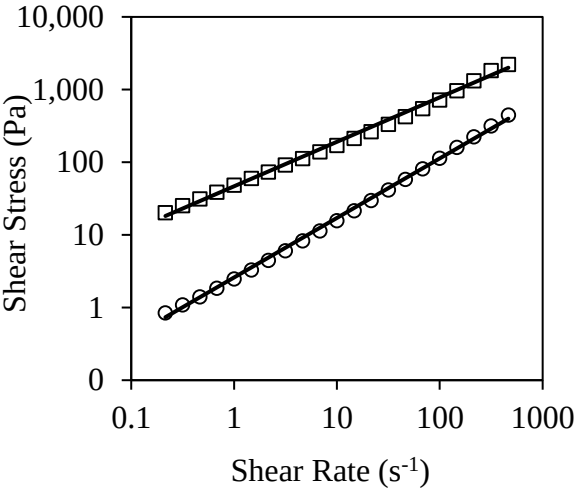

(d) citrus fibre

Figure 4.2 Flow curves of fibre suspensions, shear stress versus shear rate experimental data of (○) 5.0 wt.% and (□) 10.0 wt.% fibre suspensions with (−) power-law model fitting. (a) AF 400-30, (b) WF 101, (c) WF 600 and (d) citrus fibre.

Table 4.1: Power-law model fit parameters, k and n, for 5.0 wt.% and 10.0 wt.% fibre suspensions.

Fibre suspensions	Consistency index, k	Flow index, n	Consistency index, k	Flow index, n
	5.0 wt.%		10.0 wt.%	
AF 400-30	1.0 ± 0.04	0.91 ± 0.02	10 ± 1.30	0.79 ± 0.02
WF 101	1.0 ± 0.01	0.96 ± 0.00	16 ± 0.51	0.75 ± 0.01
WF 600	2.0 ± 0.02	0.91 ± 0.00	32 ± 3.56	0.68 ± 0.02
citrus fibre	3.0 ± 0.15	0.82 ± 0.01	47 ± 6.56	0.61 ± 0.02

For all aspect ratios, an increase in fibre fraction resulted in increased resistance to flow. This resulted in a greater apparent shear viscosity for the 10.0 wt.% fibre suspensions compared to 5.0 wt.% fibre suspensions at the same shear rates, see Figures 4.3 and 4.4. For a similar concentration of fibres, fibres with a greater aspect ratio exhibited a greater apparent shear viscosity at all shear rates. It means that both the fibre fraction and fibre aspect ratio are critical parameters associated with the suspension viscosity.

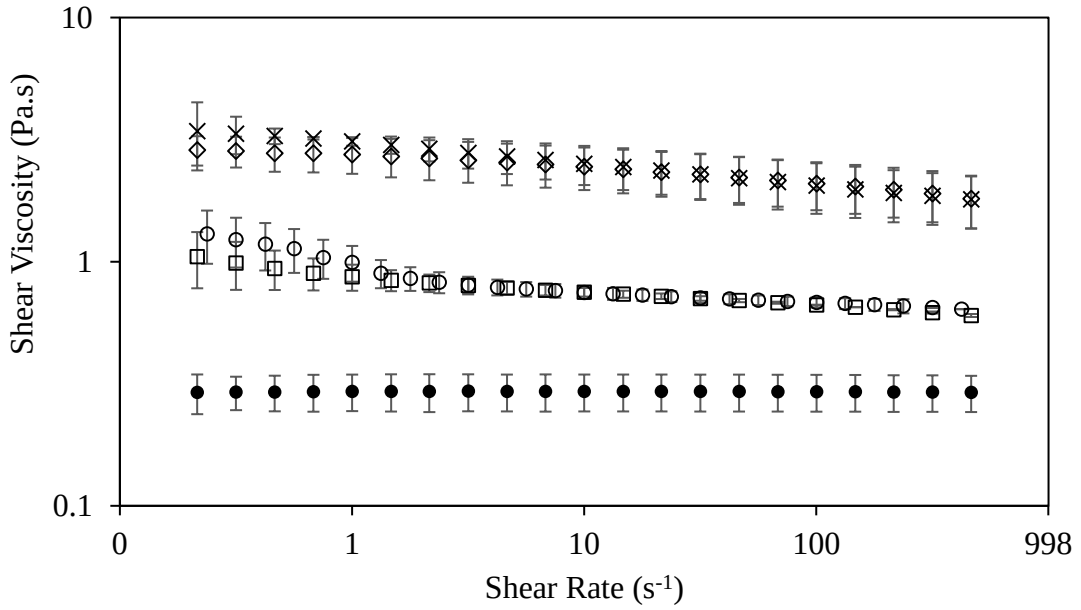

Figure 4.3 Apparent shear viscosity of 5.0 wt.% fibre suspensions as a function of aspect ratio. (●) concentrated apple juice, (○) AF 400-30 with aspect ratio 2 – 3, (□) WF 101 with aspect ratio 2 – 3, (◊) WF 600 with aspect ratio 8 – 10 and (×) citrus fibre with aspect ratio 8 – 10.

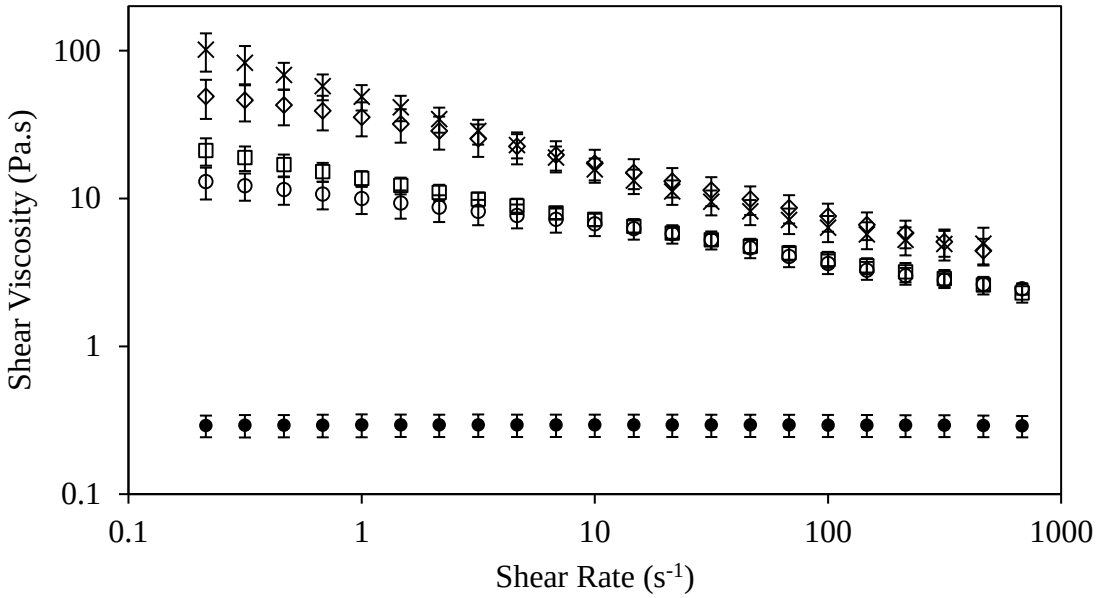

Figure 4.4 Apparent shear viscosity of 10.0 wt.% fibre suspensions as a function of aspect ratio. (○) AF 400-30 with aspect ratio 2 – 3, (□) WF 101 with aspect ratio 2 – 3, (◊) WF 600 with aspect ratio 8 – 10 and (×) citrus fibre with aspect ratio 8 – 10. Viscosity of concentrated apple juice is shown by the dashed line.

The viscosity of fibre suspensions is determined by the nature of molecular interaction between the fibres. The interaction depends mainly on the fibre concentration and aspect ratio. The interaction can be measured based on $n_f L^3$ and $n_f L^2 D_f$ values, where n_f (1/μm^3) is the number density of fibres, L (μm) is the fibre length and D_f (μm) is the fibre diameter (Djalili-Moghaddam & Toll, 2006). Tables 4.2 and 4.3 list the $n_f L^3$ and $n_f L^2 D_f$ values and the types of interaction presented for 5.0 wt.% and 10.0 wt.% fibre suspensions, respectively. When the interaction between fibres is weak, the suspension is said to be dilute, which occurs when $n_f L^3 << 1$. The 5.0 wt.% AF 400-30 and 5.0 wt.% WF 101 fibre suspensions fell in this regime, where the values of the $n_f L^3$ were 0.50 and 0.35 respectively. This explains the low viscosity exhibited by both fibre suspensions as shown in Figure 4.3. If the fibres interact mostly through hydrodynamic interactions, the suspension is said to be semi-dilute, which happens when $n_f L^3 > 1$ but $n_f L^2 D_f << 1$. The viscosity of 5.0 wt.% WF 600 and 5.0 wt.% citrus fibre suspensions, along with the 10.0 wt.% AF 400-30 and 10.0 wt.% WF 101 fibre suspensions, were greatly affected by the hydrodynamic interactions where the $n_f L^2 D_f$ values were 0.55, 0.45, 0.35 and 0.28 respectively. Lastly, 10.0 wt.% WF 600 and 10.0 wt.% citrus fibre suspensions were

considered concentrated, which means that additional non-hydrodynamic interactions such as non-hydrodynamic adhesive interactions, mechanical contacts between fibres as well as floc or network formation, were presented and influenced the suspension viscosity. This condition occurs when $n_f L^2 D_f > 1$. The $n_f L^2 D_f$ values for 10.0 wt.% WF 600 and 10.0 wt.% citrus fibre suspensions were similar at 1.10. Thus, the viscosity of each fibre suspension depended on the type of interaction that existed in the suspension regime. The type of interactions was a function of fibre fraction and aspect ratio. The strongest interactions existed in the concentrated suspensions that exhibited the greater apparent shear viscosity, while the weakest interactions were presented in the dilute suspensions and were confirmed by the lower apparent shear viscosities.

The viscosity of the fibre suspensions was a function of aspect ratio and fibre fraction. Based on Figure 4.3 and Figure 4.4, the 5.0 wt.% and 10.0 wt.% of AF 400-30 and WF 101 fibre suspensions can be said to exhibit similar apparent shear viscosity throughout the runs since both fibres had identical aspect ratios. Similar behaviour was also shown by WF 600 and citrus fibre suspensions. Theoretically, the atomization of the 5.0 wt.% AF 400-30 and 5.0 wt.% WF 101 fibre suspensions would require less energy compared to the 5.0 wt.% WF 600 and 5.0 wt.% citrus fibre suspensions, at a specific shear rate. Or, the atomization of the AF 400-30 and WF 101 fibre suspensions will probably produce smaller droplet sizes compared to WF 600 and citrus fibre suspensions, at a specific shear rate. This is because the shear viscosity that resists and controls the atomization performance was greater for WF 600 and citrus fibre suspensions. For a specific fibre suspension, a 5.0 wt.% fibre concentration will yield better atomization performance compared to a 10 wt.% fibre concentration due to its lower resistance or viscosity at all shear rates.

Table 4.2: The $n_f L^3$ and $n_f L^2 D_f$ values of each 5.0 wt.% fibre suspension along with the type of regime and interactions presented based on the $n_f L^3$ and $n_f L^2 D_f$ values.

5.0 wt.% fibre suspensions	$n_f L^3$	$n_f L^2 D_f$	Type of regime	Main interactions present
AF 400-30	0.50	-	Dilute	Weak/Negligible
WF 101	0.35	-	Dilute	Weak/Negligible
WF 600	5.55	0.55	Semi-dilute	Hydrodynamic interactions
citrus fibre	3.50	0.45	Semi-dilute	Hydrodynamic interactions

Table 4.3: The $n_f L^3$ and $n_f L^2 D_f$ values of each 10.0 wt.% fibre suspension along with the type of regime and interactions presented based on the $n_f L^3$ and $n_f L^2 D_f$ values.

10.0 wt.% fibre suspensions	$n_f L^3$	$n_f L^2 D_f$	Type of regime	Main interactions present
AF 400-30	1.10	0.35	Semi-dilute	Hydrodynamic interactions
WF 101	1.01	0.28	Semi-dilute	Hydrodynamic interactions
WF 600	-	1.10	Concentrated	Additional non-hydrodynamic interactions
citrus fibre	-	1.10	Concentrated	Additional non-hydrodynamic interactions

Other than fibre fraction and aspect ratio, fibre flexibility can also greatly influence the shear viscosity of the fibre suspensions. Flexible fibres usually exhibit greater viscosity compared to rigid fibres (Keshtkar et al., 2009). Fibre flexibility depends on the fibre stiffness, aspect ratio and the stress imposed on the fibres. Knowledge on Young's modulus, E_Y, of specific fibres is required to understand the effect contributed by the fibre stiffness towards fibre flexibility (Keshtkar et al., 2009). In this work, it was decided not to investigate the effect of fibre flexibility towards the rheology of fibre suspensions. Hence, fibre aspect ratio and concentration were the only parameters varied when looking at the rheology of fibre suspensions. It was expected that all fibres used in this study have

relatively low Young's modulus compared to synthetic fibres. It is also suggested that the Young's modulus between the different fibres used in this study are fairly similar, since the fibres' source is similar; all come from plant cells which are full of cellulosic elements. This can be supported by looking at the study by Facca et al. (2006), which shows that the Young's modulus of the natural fibre composites were all relatively similar and much lower than the Young's modulus of glass fibre composite.

Other than the shear thinning behaviour of the fibre suspensions, the viscosity of the different types of fibre suspensions was also independent of time based on timescale shown in Figure 4.5. Some non-Newtonian shear thinning fluids show a time-dependent change in viscosity and they are termed either thixotropic or rheopectic fluids. At a constant shear rate, the viscosity of thixotropic liquids decreases over time while the viscosity of rheopectic liquids increases. As shown in Figure 4.5, the concentrated apple juice and fibre suspensions were all non-thixotropic and non-rheopectic fluids.

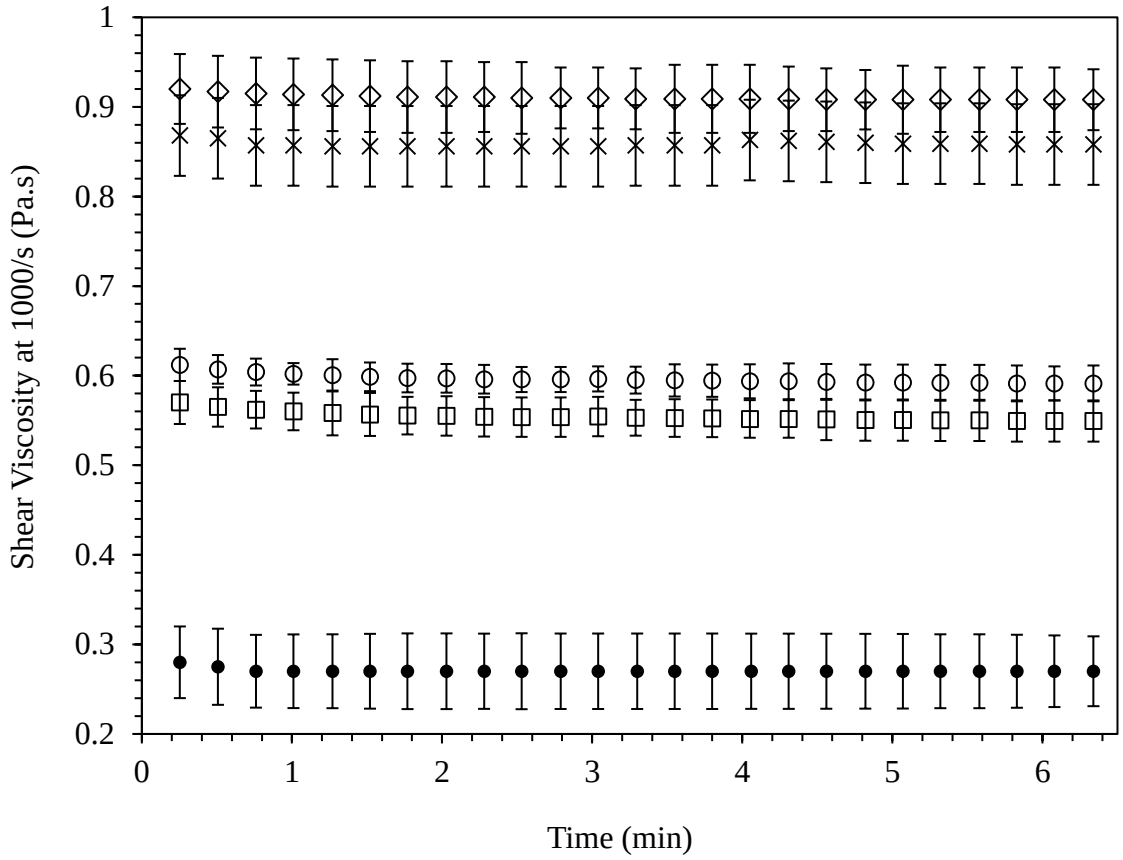

Figure 4.5 Apparent shear viscosity of 5.0 wt.% fibre suspensions as a function of time. (●) Concentrated apple juice, (○) AF 400-30 with aspect ratio 2 – 3, (□) WF 101 with aspect ratio 2 – 3, (◊) WF 600 with aspect ratio 8 – 10 and (×) citrus fibre with aspect ratio 8 – 10.

4.1.3 Fitting the Krieger-Dougherty and Maron-Pierce equations for fibre suspensions

The increase in the viscosity with volume fraction for suspensions containing particles with different average aspect ratio is usually characterized based on the Krieger-Dougherty (Krieger, 1972) and Maron-Pierce (Maron & Pierce, 1956) relationships shown in Equations 4.2 and 4.3 respectively.

$$\eta_r = (1 - \emptyset/\emptyset_C)^{-[\eta]\emptyset_C} \qquad \text{Equation 4.2}$$

$$\eta_r = (1 - \emptyset/\emptyset_C)^{-2} \qquad \text{Equation 4.3}$$

in which $[\eta]$ is the intrinsic viscosity, $\emptyset$ is the volume fraction of suspensions and $\emptyset_C$ is the critical volume fraction. Figure 4.6(a-d) shows the measured relative viscosities, η_r, together with best fit curves obtained by non-linear regression via Krieger-Dougherty and Maron-Pierce relationships as stated in Equations 4.2 and 4.3 respectively. The weight fraction of all fibre suspensions was converted into volume fraction, $\emptyset$, for the fitting purpose. More details on the conversion are explained in Section 3.4.1.1. The viscosity of fibre suspensions in the concentrated apple juice were only measurable up to $\emptyset$ = 0.09, as shown in Figure 4.6(a-d). Beyond these limits, the viscosity of the fibre suspensions was too great to be measured by the MCR 301 equipment. The vertical asymptotic in each figure indicates the corresponding critical volume fraction, $\emptyset_C$, obtained by fitting. Table 4.4 and Table 4.5 list the values of the fit parameters, $[\eta]$ and $\emptyset_C$, together with the correlation coefficients, C, as a measure of the quality of the fit, determined by Krieger-Dougherty and Maron-Pierce relations respectively.

In particular, as shown in Table 4.4, the intrinsic viscosity based on the Krieger-Dougherty relation of WF 600 fibre suspension was very similar to that of citrus fibre suspension. The intrinsic viscosity of low aspect ratio fibre suspensions of AF 400-30 and WF 101 was lower than WF 600 and citrus fibre suspensions. A similar conclusion can be drawn with respect to the critical volume fractions determined from Krieger-Dougherty and Maron-Pierce relations. As shown in Tables 4.4 and 4.5, the $\emptyset_C$ of WF 600 and citrus fibre suspensions were the same, as predicted by each relationship. The $\emptyset_C$ of WF 600 and citrus fibre suspensions which had a greater aspect ratio, were also lower than the $\emptyset_C$ of AF 400-30 and WF 101 which had a lower aspect ratio.

The critical volume fraction is defined as the concentration at which blocking of the flowability occurs. Although Table 4.4 and 4.5 shows $\emptyset_C$ values of more than 10.0 % and for some more than 20.0%, the actual setup during atomization which included the gear pump as presented in Section 3.5.4, could not efficiently pump a suspension with $\emptyset$ of more than 10.0%. Hence, it is suggested that the $\emptyset_C$ obtained from Krieger-Dougherty or Maron-Pierce relations based on MCR 301 rheometer, can only be treated as the maximum possible theoretical value before the suspensions stop flowing. Meanwhile, the actual maximum volume fraction of fibre suspensions, $\emptyset_{C,actual}$, that can be incorporated during atomization of the liquids, was highly dependent on the ability of the pump used. The $\emptyset_C$ extracted from Krieger-Dougherty and Maron-Pierce relations is not a reasonable value to be used during the atomization experiment. This is because the viscosity measurements were carried out at fibre volume fractions lower than half of the extrapolated value of $\emptyset_C$. For example, $\emptyset_C$ based on the Krieger-Dougherty equation for AF 400-30 fibre suspension was 0.25 whereas the viscosity measurements were only carried out up to 0.09. So, the $\emptyset_C$ based on Krieger-Dougherty and Maron-Pierce relations should only be treated as a fitting parameter. The predicted $\emptyset_C$ values had a physical meaning, but the prediction was very different from the actual because of the long-range prediction.

Mere visual inspection on Figure 4.6(a-d) indicated that both Krieger-Dougherty and Maron-Pierce fits were excellent for all types of fibre suspensions, and this is supported by the correlation coefficient value, C. To further determine which correlation is slightly better than the other, the resulting standard error of estimate from both correlations were calculated. Based on Zar (2013), after fitting multiple regression equations, the most reliable equation is chosen based on the one resulting in the smallest standard error of estimate. The standard error of estimate is tabulated in Tables 4.4 and 4.5 and the values were very similar between the two different correlations. When the standard error of estimates is very similar, Zar (2013) further suggests that a decision should be made by choosing the correlation with the least fitting parameter. More specifically, both Krieger-Dougherty and Maron-Pierce correlations consist of critical volume fraction parameter, $\emptyset_C$. In addition to that parameter, Krieger-Dougherty has an extra fitting parameter which is the intrinsic viscosity, $[\eta]$. Here, the $[\eta]$ is termed a dummy variable (Zar, 2013). By introducing a dummy variable into a Krieger-Dougherty correlation, the predicted relative viscosity did not yield any better or more accurate correlation to the measured relative viscosity when compared to the Maron-Pierce prediction. This is based on the correlation

coefficient, C, and the standard error of estimate tabulated in Tables 4.4 and 4.5. It means that the Maron-Pierce relationship is statistically better than the Krieger-Dougherty in representing and explaining the shear rheology of the fibre suspensions. This hypothesis is supported by Occam's razor (or Ockham's razor) principle which states that given two explanations of the data and all other things being equal, the simpler explanation is preferable or the one requires the least speculation (in this case is the number of fitting parameters) is more correct.

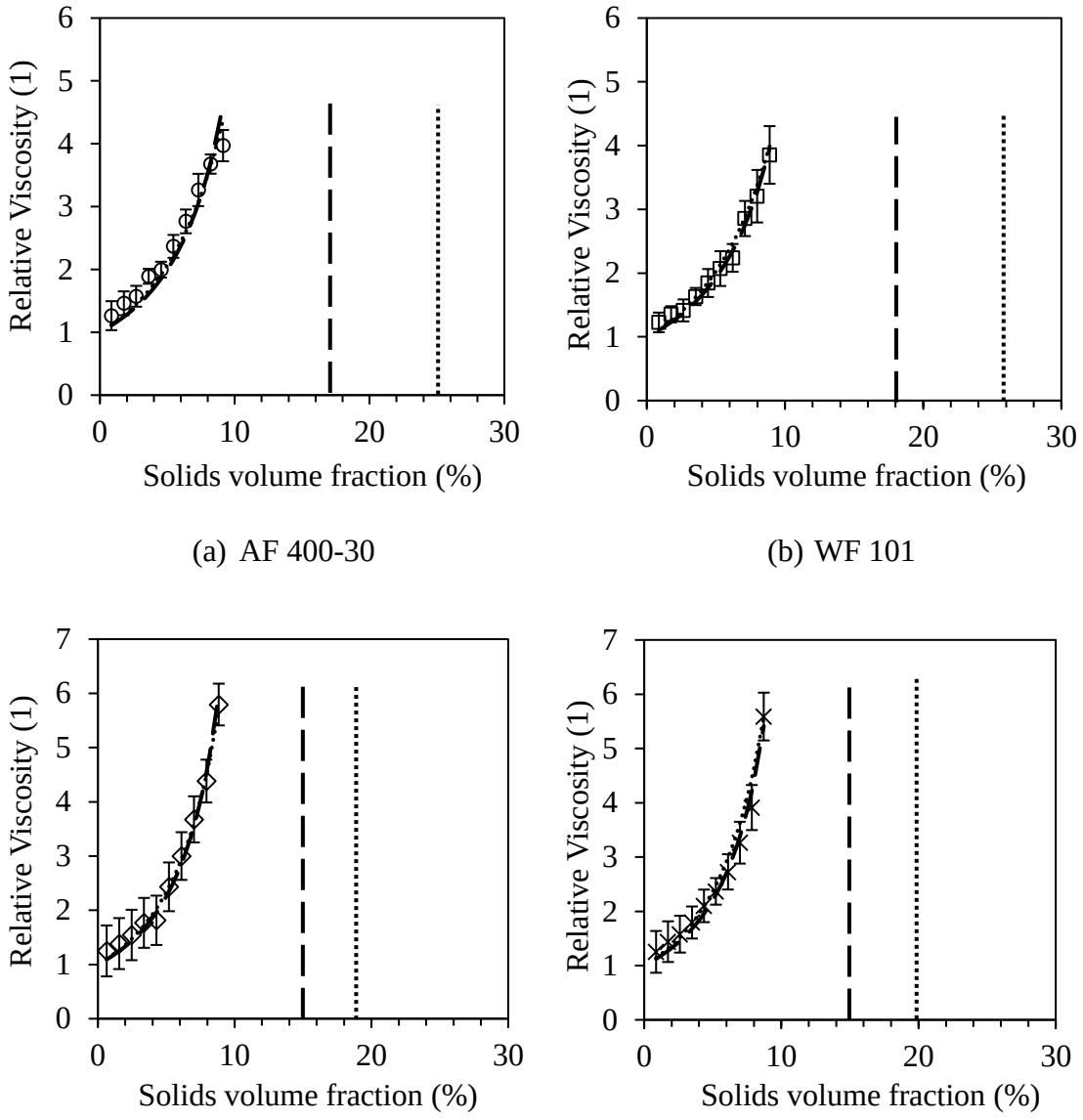

Figure 4.6 Concentration dependence of the relative viscosity of (a) AF 400-30, (b) WF 101, (c) WF 600 and (d) citrus fibre suspensions. The experimental data was fitted with Krieger-Dougherty (⋯⋯) and Maron-Pierce (− − − −) relationships. The corresponding critical volume fraction, $\emptyset_C$, obtained by fitting are indicated as vertical asymptotes. The measured shear viscosity corresponds to shear rate at 1000 s^{-1}.

Table 4.4: Fit parameters, $\emptyset_C$ and $[\eta]$, for the concentration dependence of the relative viscosity of suspensions with different fibres obtained with the Krieger-Dougherty relation.

Fibre suspensions	Critical volume fraction, $\emptyset_C$ (%)	Intrinsic viscosity, [η]	Correlation coefficient, *C*	Standard error of estimate
AF 400-30	25	13.0	0.97	0.2
WF 101	26	12.7	0.97	0.1
WF 600	19	14.6	0.95	0.1
Citrus fibre	20	15.0	0.96	0.2

Table: 4.5 Fit parameters, $\emptyset_C$ and $[\eta]$, for the concentration dependence of the relative viscosity of suspensions with different fibres obtained with the Maron-Pierce relation.

Fibre suspensions	Critical volume fraction, $\emptyset_C$ (%)	Correlation coefficient, *C*	Standard error of estimate
AF 400-30	17	0.96	0.3
WF 101	18	0.97	0.1
WF 600	15	0.94	0.1
Citrus fibre	15	0.95	0.2

4.1.4 Effect of temperature

The viscosity of liquids usually decreases with increasing temperature and the effect of temperature on the viscosity of fluid can be described by the Arrhenius relationship.

$$\mu = Ae^{-E_a/RT} \qquad \text{Equation 4.4}$$

where A (Pa.s) is a constant, E_a (kJ/mol) is the activation energy for viscous flow, R (kJ/mol.K) is a gas constant and T (K) is the temperature. The effect of temperature on viscosity was examined for 5.0 wt.% and 10.0 wt.% WF 600 fibre suspensions only. Figures 4.7 and 4.8 show the flow curves (shear stress versus shear rate) for the fibre suspensions at temperatures ranging between 20 to 40 °C. As shown in Figures 4.7 and 4.8, the 5.0 wt.% and 10.0 wt.% WF 600 fibre suspensions exhibited a shear thinning behaviour at all

temperatures. The experimental results showed that the behaviour of 5.0 wt.% and 10.0 wt.% WF 600 fibre suspensions were best fitted with the power-law model. The power-law model fit parameters, k and n, are tabulated in Table 4.6.

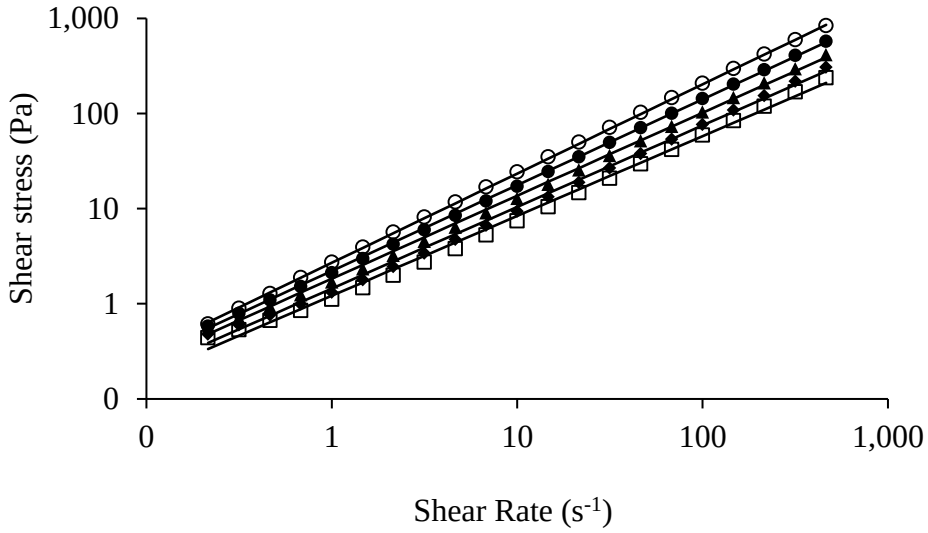

Figure 4.7 Flow curves for fibre suspensions at different temperatures of 5.0 wt.% WF 600 fibre suspensions at different temperatures. (○) 20 °C, (●) 25 °C, (▲) 30 °C, (♦) 35 °C, and (□) 40 °C all with (−) power-law model fitting.

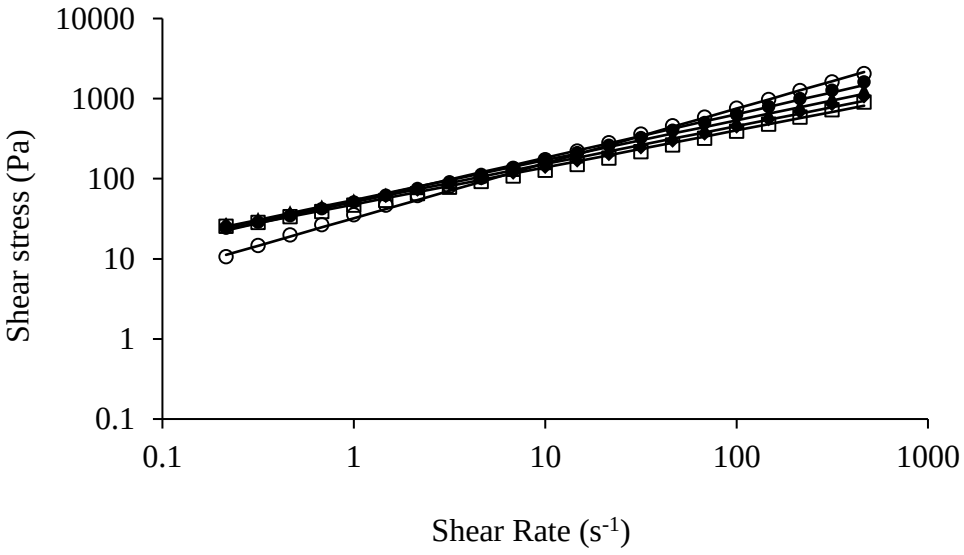

Figure 4.8 Flow curves for fibre suspensions at different temperatures of 10.0 wt.% WF 600 fibre suspensions at different temperatures. (○) 20 °C, (●) 25 °C, (▲) 30 °C, (♦) 35 °C, and (□) 40 °C all with (−) power-law model fitting.

Table 4.6: Power-law model fit parameters, k and n, of 5.0 wt.% and 10.0 wt.% WF 600 fibre suspensions at different temperature ranging between 20 °C and 40 °C.

Temperature (°C)	5.0 wt.% WF 600 fibre suspensions		10.0 wt.% WF 600 fibre suspensions	
	Consistency index, *k*	Flow index, *n*	Consistency index, *k*	Flow index, *n*
20 °C	2.7	0.91	32.1	0.68
25 °C	2.2	0.90	52.1	0.54
30 °C	1.8	0.87	54.3	0.50
35 °C	1.5	0.86	51.4	0.47
40 °C	1.2	0.84	47.7	0.46

In order to study the effect of temperature on the shear behaviour of fibre suspensions, the apparent viscosity was obtained at a shear rate of 100 s^{-1}. Previous study on the effect of temperature on flow behaviour of fibre suspensions specifically, utilized the apparent viscosity at 100 – 200 s^{-1} shear rates (Grigelmo-Miguel et al., 1999; Saravacos, 1970). To obtain the estimates of the parameters of the Arrhenius relationship, the logarithm of the viscosity was plotted against 1/T.

$$\ln(\mu_{app}) = \ln A - \frac{E_a}{RT} \qquad \text{Equation 4.5}$$

Figure 4.9 shows the effect of temperature on concentrated apple juice and pseudoplastic viscosity of 5.0 wt.% WF 600 and 10.0 wt.% WF 600 fibre suspensions according to the Arrhenius equation and the best fit lines were drawn. Table 4.7 shows the value of the constant A and activation energy E_a, and the determination coefficient obtained from the fitting of viscosity data. Activation energy at each fibre concentration were obtained from the slope of the corresponding straight line in Figure 4.9.

The activation energy of the 60 °Brix concentrated apple juice was approximately 60 kJ/mol. A previous study has reported an activation energy value of approximately 50-60 kJ/mol for a greater concentration of apple juice, 70 °Brix - 75 °Brix (Ibarz et al., 1987). As shown in Table 4.7, the activation energy decreased as the fibre fraction increased. Concentrated apple juice had the highest activation energy while the 10.0 wt.% fibre suspension had the lowest value. A similar trend was observed previously by Grigelmo-

Miguel et al. (1999) with peach dietary fibre suspensions, where the activation energy decreased as the suspension's concentration was increased. Saravacos (1970) also reported that the activation energy decreased significantly when suspended particles such as fibres were presented in the liquid. Briscoe et al. (1998) also concluded that the activation energy of PEO in aqueous solutions decreased as the PEO concentration was increased. For the concentrated apple juice which exhibited the highest activation energy, as the temperature was increased the solvent molecules absorbed the thermal energy and resulted in bond ruptures between molecules. With fibre suspensions, the fibre particles must be less sensitive to the thermal energy activation compared to the bonds between molecules. Thus, the addition of the fibre to the apple juice has a twofold effect; increasing the base viscosity (consistency) and decreases its sensitivity to thermal activation.

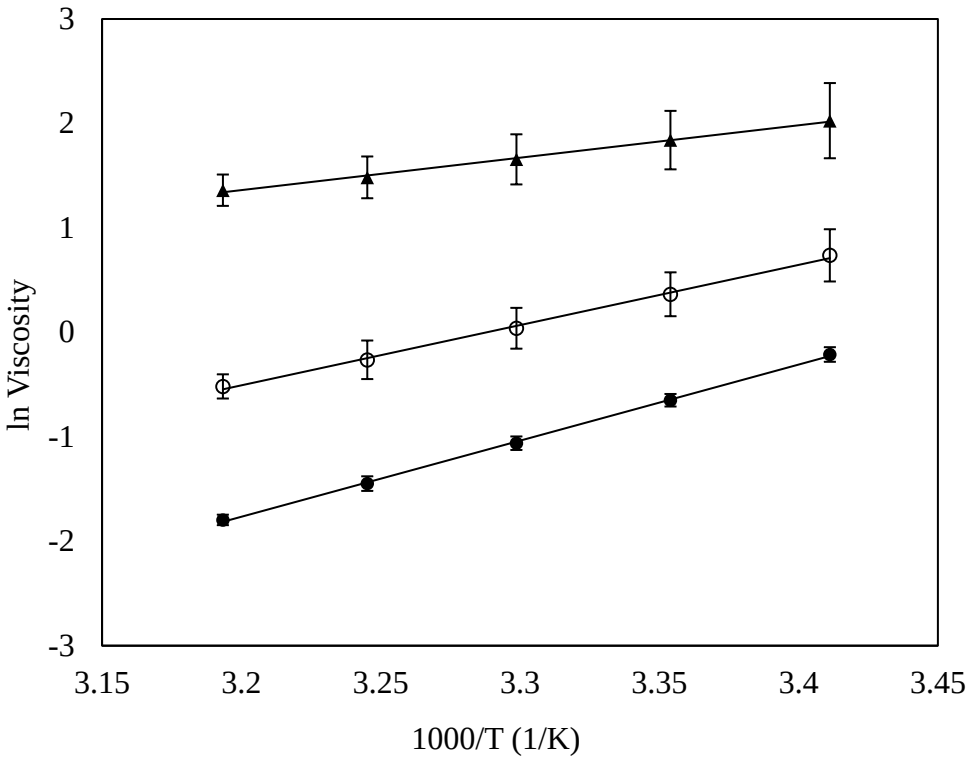

Figure 4.9 Arrhenius plot of the viscosity versus 1/T based on the Arrhenius equation to obtain the activation energy, E_a. (●) Concentrated apple juice, (○) 5.0 wt.% WF 600 and (▲) 10.0 wt.% WF 600 fibre suspensions.

Table 4.7: Value of constant, A and activation energy, E_a, obtained from the Arrhenius relationship for concentrated apple juice, 5.0 wt.% WF 600 and 10.0 wt.% WF 600 fibre suspensions.

Solutions	Activation energy (kJ/mol)	A (Pa.s)	Determination coefficient (R^2)
Concentrated apple juice	60	5.6×10^{-9}	0.99
5.0 wt.% WF 600	48	5.9×10^{-9}	0.99
10.0 wt.% WF 600	26	1.9×10^{-4}	0.99

4.1.5 Combined effect of temperature and concentration

To investigate the combined effect of temperature and concentration on the viscosity of fibre suspensions, a 3-D surface graph was created based on the experimental data obtained using MCR 301. The data used in the analysis are tabulated in Table 4.8. Figure 4.10 shows the 3-D surface plot with viscosity as the response variable (y-axis) and temperature and concentration as the predictor variables (x-axis and z-axis respectively). The darkest blue region in Figure 4.10 corresponds to the highest measured shear viscosity while the lightest blue region represents the lowest measured shear viscosity. As shown in Figure 4.10, the effect of concentration on viscosity of WF 600 fibre suspension was more pronounced than the effect of temperature. For example, as shown in Figure 4.10, the decrease in the concentration of the fibre suspensions along the z-axis resulted in a greater reduction in the shear viscosity compared to the viscosity reduction showed by the increase in temperature along the x-axis. To support the observation, an ANOVA test was performed on the data tabulated in Table 4.8. The result shows that the p-value was lower than 0.05, which means that the combined effect of temperature and concentration significantly affected the apparent viscosity of the fibre suspensions. Based on the ANOVA test, the coefficient of the temperature that affected the final viscosity value was only 0.11 while the coefficient for concentration was 89. It means that the contribution of concentration to the final viscosity value was much greater than the contribution by temperature.

In the atomization study, where shear viscosity is an important factor, more energy efficient atomization might be achieved by reducing the concentration of fibre suspensions, rather than increasing the temperature. Hence, during the atomization study, only the lowest

concentration of fibre suspensions; 5.0 wt.%, was tested for all fibre suspensions. Although results showed that temperature had a weak effect on shear viscosity compared to concentration, it is important to emphasize that in the case of fibre suspensions, the combined effect of high temperature and low concentration yielded the lowest viscosity fibre suspension. During the atomization study of the 5.0 wt.% fibre suspensions, the temperature was also increased to observe the effect on the atomization performance. More details are discussed in Chapter 6.

Table 4.8: The viscosity of WF 600 fibre suspensions at specific concentration and temperature. The data was obtained using MCR 301.

Apparent viscosity at 100 s^{-1} (Pa.s) ↘	Fibre suspensions concentration (wt.%) →		
Temperature (°C) ↓	5.0 wt.%	7.5 wt.%	10.0 wt.%
20	2.09	2.51	7.59
25	1.44	2.05	6.30
30	1.04	1.57	5.24
35	0.77	1.29	4.41
40	0.60	1.05	3.90

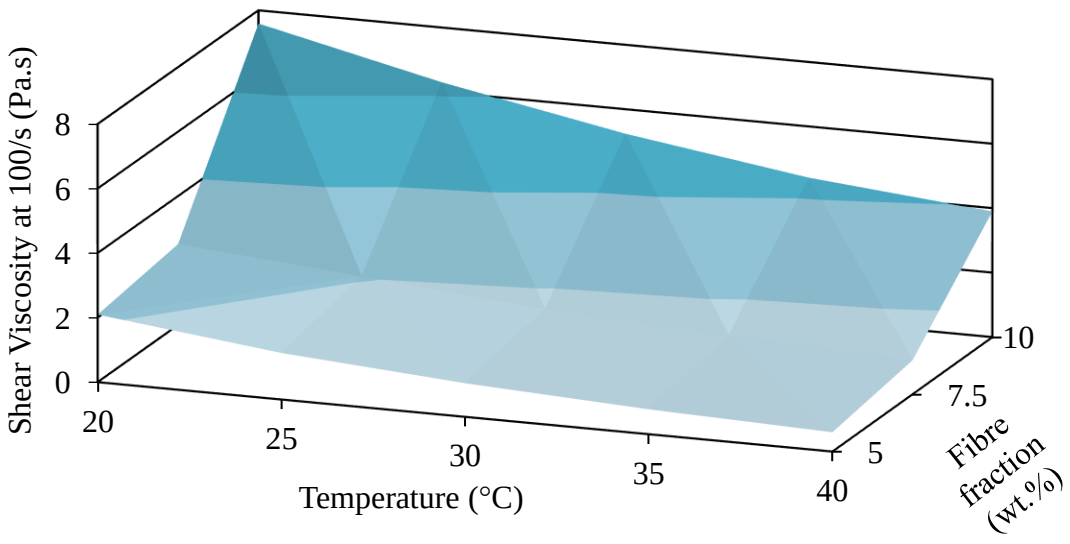

Figure 4.10 Combined effect of temperature and fibre fraction or concentration on the shear viscosity of WF 600 fibre suspension.

4.2 Shear rheology of fibre suspensions from a capillary viscometer

The previous Section 4.1 has explained in depth the shear rheology of fibre suspensions at different fibre aspect ratios, fibre concentration and temperature at shear rates up to 1000 s^{-1}, measured using a rotary rheometer. Similarly, previous studies and literature also discuss the shear rheology of any specific fluids up to shear rates of 500 or 1000 s^{-1}. The shear viscosity data extracted from the shear rate ranges between 0 to 1000 s^{-1} may be sufficient for certain applications. In atomization, the fluid is expected to experience much higher shear rates. This is due to the high flow rates passing through small orifices (> 1mm) in pressure nozzles or due to the fast-moving air velocity in two-fluid nozzles (Schröder et al., 2011).

In this section, the shear viscosity of the 5.0 wt.% AF 400-30, 5.0 wt.% WF 101, 5.0 wt.% WF 600 and 5.0 wt.% citrus fibre suspensions at shear rates higher than 1000 s^{-1} are discussed. Since atomization was the final objective of the study, it is important to measure the shear viscosity at a maximum possible shear rate to acquire an indication on the actual shear viscosity present during the atomization.

4.2.1 Fibre suspensions

The shear viscosity for 5.0 wt.% AF 400-30, 5.0 wt.% WF 101, 5.0 wt.% WF 600 and 5.0 wt.% citrus fibre suspensions measured using a capillary viscometer is shown in Figure 4.11. Three distinct regions can be observed on the plot of the flow curves (shear viscosity versus shear rate), as separated by the vertical dotted lines. At the lowest shear rates; $\dot{\gamma} \leq$ 2000 s^{-1}, the shear viscosity was obtained using the largest capillary diameter of 9.2 mm. At shear rates 3000 $s^{-1} \leq \dot{\gamma} \leq$ 11 500 s^{-1}, the shear viscosity was measured using the medium capillary diameter of 5.0 mm. The shear viscosity for 11 500 $s^{-1} \leq \dot{\gamma} \leq$ 20 000 s^{-1} shear rates was generated using the smallest capillary diameter of 3.2 mm.

As shown in Figure 4.11, the shear viscosity of 5.0 wt.% AF 400-30 and 5.0 wt.% WF 101 fibre suspensions were very similar, at every shear rates. Similar behaviour was also observed between the shear viscosity of 5.0 wt.% WF 600 and 5.0 wt.% citrus fibre suspensions. This was due to the similar aspect ratios between AF 400-30 and WF 101, and

also between WF 600 and citrus fibres. A similar observation was reported previously from the rotary rheometer data in Section 4.1.2. A closer observation of Figure 4.11 shows that the shear viscosity differences between the low aspect ratio fibre suspensions (5.0 wt.% AF 400-30 and 5.0 wt.% WF 101 fibre suspensions) and high aspect ratio fibre suspensions (5.0 wt.% WF 600 and 5.0 wt.% citrus fibre suspensions) reduced as the shear rates were increased. Particularly, the shear viscosity of 5.0 wt.% WF 600 and 5.0 wt.% citrus fibre suspensions can be said to approach the viscosity of 5.0 wt.% AF 400-30 and 5.0 wt.% WF 101 fibre suspensions more noticeably after the shear rate of 11 500 s^{-1}. This phenomenon was not visible from the rotary rheometer data in Section 4.1.2 due to the narrow range of possible shear rates.

The shear viscosity data obtained from the rotary rheometer was combined with the data generated by the capillary viscometer. The overall viscosity curves are shown in Figure 4.12. As shown in Figure 4.12, the shear viscosity at lower shear rates generated by the capillary viscometer coincided with the shear viscosity obtained from the rotary rheometer at high shear rates. Although some of the data did not coincide with each other, as in Figure 4.12 (a-b), it was obvious that the trend generated by the shear viscosity from the rotary rheometer was being continued by the shear viscosity generated using the capillary viscometer.

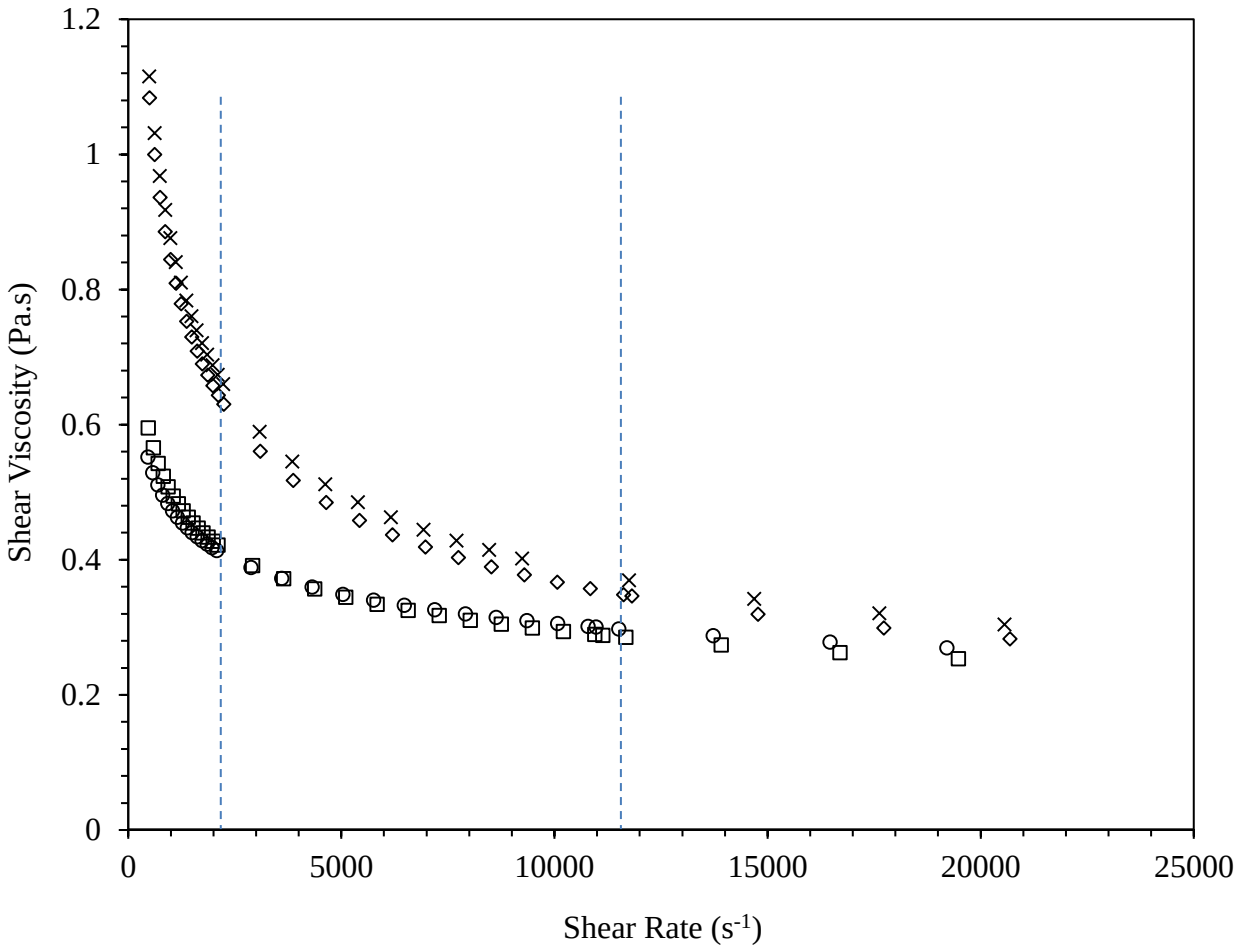

Figure 4.11: Viscosity curves for 5.0 wt.% fibre suspensions as a function of aspect ratio at shear rates up to 20 000/s. (○) AF 400-30 with an aspect ratio of 2 – 3, (□) WF 101 with an aspect ratio of 2 – 3, (◊) WF 600 with an aspect ratio 8 – 10 and (×) citrus fibre with an aspect ratio of 8 – 10. At shear rates $\dot{\gamma} \leq 2000$/s, the shear viscosity was obtained using the largest capillary diameter of 9.2 mm. At shear rates 3000/s $\leq \dot{\gamma} \leq$ 11 500/s, the shear viscosity was measured using the medium capillary diameter of 5.0 mm. At shear rates $\dot{\gamma} \geq$ 11 500/s, the shear viscosity was obtained using the smallest capillary diameter of 3.2 mm.

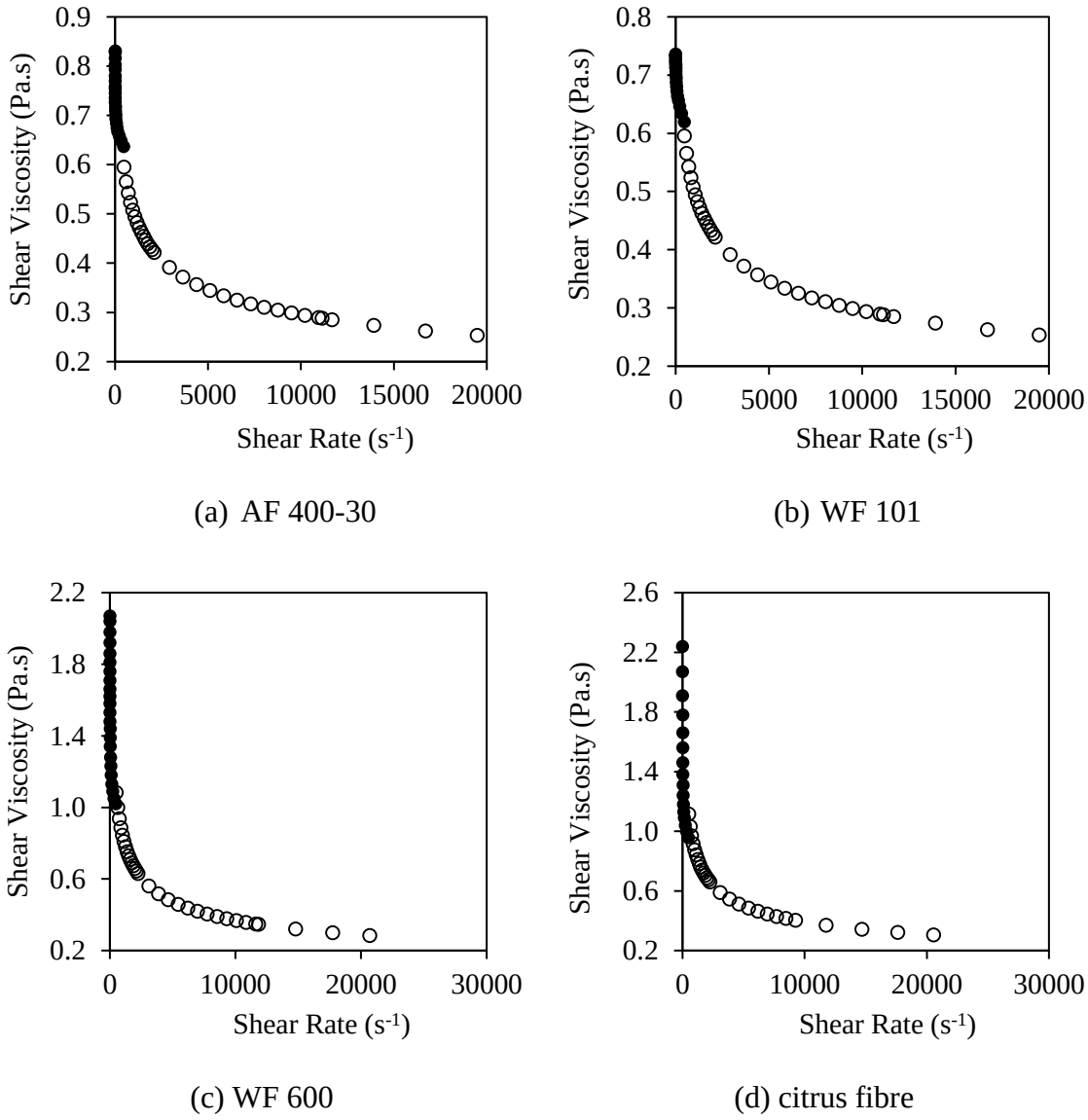

Figure 4.12 Viscosity curves of different fibre suspensions measured at shear rates $0 \leq \dot{\gamma} \leq 20\ 000\ s^{-1}$. (●) Shear viscosity measurements performed using the rotary rheometer and (○) shear viscosity measurements performed using the capillary viscometer.

Based on the data in Figure 4.11, it is suspected that the shear viscosity of all types of fibre suspensions; 5.0 wt.% AF 400-30, 5.0 wt.% WF 101, 5.0 wt.% WF 600 and 5.0 wt.% citrus fibre suspensions, will all reach a similar plateau at shear rates above 20 000 s^{-1}. This was not shown experimentally due to the working range limit of the capillary viscometer. Power-law model assumes that the shear viscosity will continuously decrease even though at infinite shear rates. Whereas, practically, a plateau will occur where at that point, the power-law model is not applicable anymore. Thus, it means that the shear viscosity above 20 000 s^{-1} shear rate should not be predicted based on the power-law model.

To predict the viscosity above 20 000 s^{-1} shear rate, the data in Figure 4.11 was fitted and modelled using the Cross equation. This is shown in Figure 4.13. The Cross model is an extension of the power-law model that includes the viscosity at inifnite shear rate. Based on the Cross model fitted data in Figure 4.13, the viscosity of the high aspect ratio fibre suspensions (5.0 wt.% WF 600 and 5.0 wt.% citrus fibre suspensions) started to coincide with the viscosity of the low aspect ratio fibre suspensions (5.0 wt.% AF 400-30 and 5.0 wt.% WF 101 fibre suspensions) at a shear rate of 25 000 s^{-1}. Beyond this shear rate, the shear viscosity of the different fibre suspensions were all relatively similar, ranging between 0.28 Pa.s and 0.32 Pa.s. It is suggested that at shear rate above 25 000 s^{-1}, plateauing occured. It means that beyond 25 000 s^{-1} shear rate, the shear viscosity of the 5.0 wt.% AF 400-30, 5.0 wt.% WF 101, 5.0 wt.% WF 600 and 5.0 wt.% citrus fibre suspensions were expected to be approximately similar with each other and would not reduce anymore. At 25 000 s^{-1} shear rate, the average viscosity of fibre suspensions was 0.28 $\pm$ 0.01 Pa.s. The average viscosity of concentrated apple juice, measured by the capillary viscometer, was 0.23 $\pm$ 0.02 Pa.s.

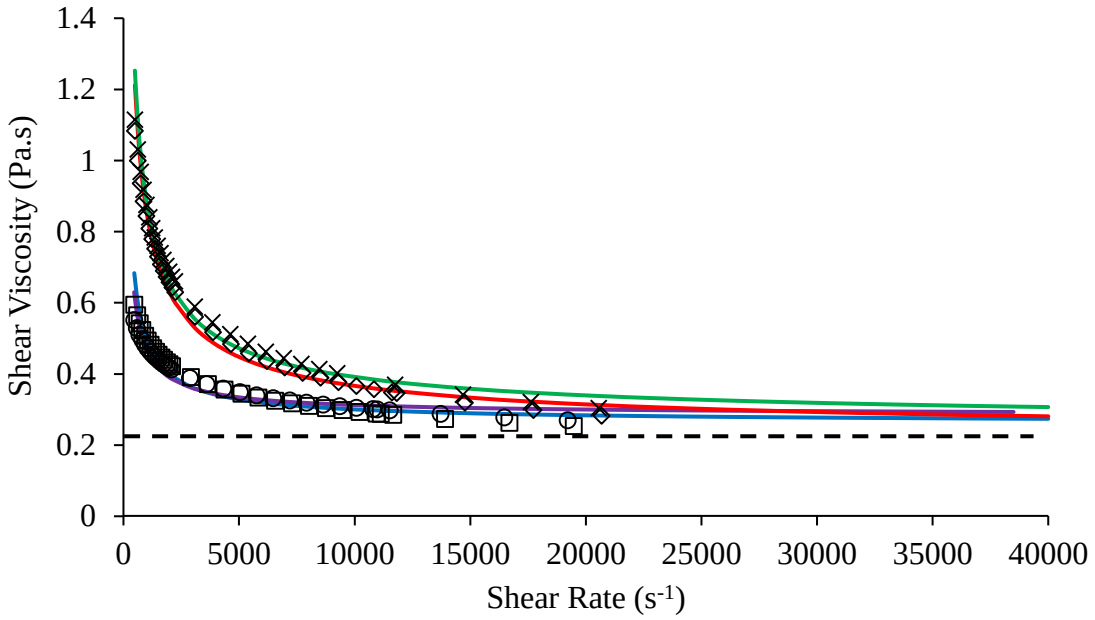

Figure 4.13 Shear viscosity of 5.0 wt.% fibre suspensions as a function of aspect ratio at shear rates up to 40 000 s^{-1}. Bullet points are the experimental data from Figure 4.11 (○) AF 400-30 with an aspect ratio of 2 – 3, (□) WF 101 with an aspect ratio of 2 – 3, (◊) WF 600 with an aspect ratio 8 – 10 and (×) citrus fibre with an aspect ratio 8 – 10. Full line represents the fitted Cross model (purple) AF 400-30, (blue) WF 101, (red) WF 600 and (green) citrus fibre. Viscosity of concentrated apple juice is shown by the dashed line.

Many studies often neglected the shear behaviour at much higher shear rates; at a shear rate greater than can be attained with a rotary rheometer. In atomization studies, it is inaccurate to explain the atomization mechanism or behaviour solely based on the shear resistance obtained from the rotary rheometer. Rotary rheometer only provided data up to 1000 s^{-1} shear rate. Meanwhile, a capillary viscometer produced data at shear rates up to 20 000 s^{-1}. In the case of fibre suspensions, the shear viscosity of different fibre suspensions approached a similar plateau value at shear rates above 20 000 s^{-1}. This observation was absent from the rotary rheometer results. The implication of this finding is very important. For example, from the capillary viscometer results shown in Figure 4.13, it is suggested that the influence of shear viscosity on the atomization performance will be fairly similar between 5.0 wt.% AF 400-30, 5.0 wt.% WF 101, 5.0 wt.% WF 600 and 5.0 wt.% citrus fibre suspensions, although they had different fibre aspect ratio. This is because the shear viscosity of these different fibre suspensions at very high shear rates were similar. From Figure 4.13, the capillary viscometer results also suggest that a plateau was likely to occur after a certain shear rate. This finding indicates that during the atomization, there is a limit to the effectivness of applying shear to decrease the viscosity for the purpose of making the fluid more sprayable, especially in the case of fibre suspensions.

Figure 4.14 shows the relative pressure drop data at the capillary entrance against flow rates obtained by using the smallest capillary diameter of 3.2 mm. The shear rates inside the 3.2 mm capillary corresponded to the high shear rates of more than 11 500 s^{-1}. As shown in Figure 4.14, all 5.0 wt.% fibre suspensions showed an exponential increase in pressure drop at the capillary entrance as the flow rates were increased, with R^2 values of more than 0.96. By looking at both Figures 4.12 and 4.13, it can be said that by using the smallest capillary diameter of 3.2 mm, as the flow rate was increased, the shear rate inside the capillary was also increased and that resulted in a decrease in the shear viscosity of the 5.0 wt.% fibre suspensions. However, the pressure drop at the capillary entrance also increased exponentially. Contraction flow at the capillary entrance region caused an extra pressure drop due to the stretching of fibre suspensions, in addition to the pressure drop contributed by the form drag, eddies and other effects due to the sudden change in diameter or flow area (Aho & Syrjala, 2006; Huang & Leong, 2002). The diameter of the pipe before the capillary entrance region was 9.0 mm. To see the sole effect of the fibre suspensions on the entrance pressure drop, the data in Figure 4.14 was plotted after dividing with the amount of pressure drop in the concentrated apple juice. The entrance pressure drop in the

concentrated apple juice was linear with R^2 value of more than 0.98 as shown in Figure 4.15. In the case of concentrated apple juice, the pressure drop at the capillary entrance must be due to all other effects but stretching of the fibre suspensions. After removing the effect by concentrated apple juice, the plotted pressure drop in Figure 4.14 can be attributed to the stretching of fibre suspensions with minimum effects of form drag.

The significant pressure drops due to the stretching of the fluid elements, in this case, fibre suspensions, as shown in Figure 4.14, means that along with the shear resistance, there was another resistance presented during the flow of fibre suspensions called extensional resistance (Binding et al., 1998; Huang & Leong, 2002). Similar to shear viscosity, this extensional resistance must be a function of the fibre aspect ratio. This is because, as shown in Figure 4.14, the pressure drops of the high aspect ratio fibre suspensions were very similar to each other and greater than the pressure drops of the low aspect ratio fibre suspensions. The overall capillary viscometer results indicate that at very high shear rates, the shear viscosity of different fibre suspensions were relatively low and similar between each other. Thus, from the shear viscosity point of view, it is possible that a good atomization performance should be easily achieved, as the shear viscosity that resists the atomization was relatively low. However, by taking into account the huge pressure drop at the capillary entrance, it means that there was another force called extensional resistance, along with the shear resistance, that will resist and control the atomization performance. The finding in Figure 4.14 also serves as the basis idea of excluding the common pressure nozzle for the atomization of fibre suspensions. This is because, with the common pressure nozzle, high pumping pressure needs to be supplied to reach the high shear rates inside the nozzle orifice. However, the increase in the pumping pressure will consequently contribute to an exponential increase in the pressure drop at the nozzle entrance, which makes the use of the common pressure nozzle inefficient.

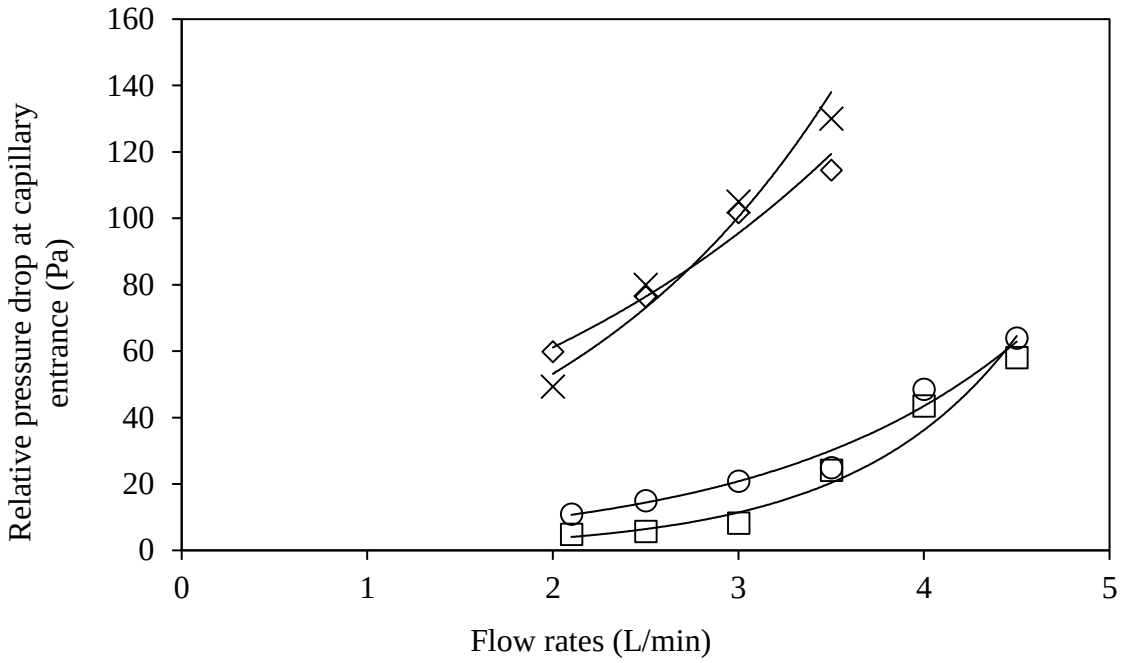

Figure 4.14 Pressure drop at the capillary entrance when using a 3.2 mm capillary (○) 5.0 wt.% AF 400-30, (□) 5.0 wt.% WF 101, (◊) 5.0 wt.% WF 600 and (×) 5.0 wt.% citrus fibre suspensions.

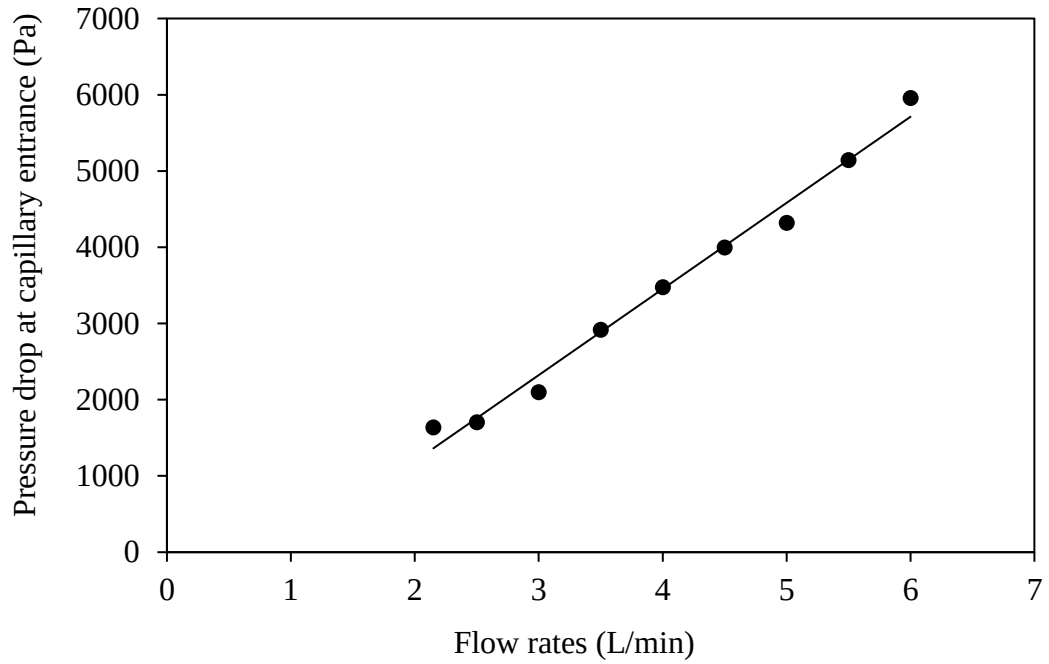

Figure 4.15 Pressure drop at the capillary entrance in concentrated apple juice when using a 3.2 mm capillary.

4.3 Conclusions

Shear rheology of fibre suspensions was investigated using a rotary rheometer and a capillary viscometer method.

- Tests performed on the rotary rheometer showed that the fibre suspensions behaved as non-Newtonian shear thinning liquids up to 1000 s^{-1} shear rates.
- Tests performed on the capillary viscometer further demonstrated that the shear thinning behaviour of fibre suspensions continued until the shear rate of 25 000 s^{-1}. A plateau occurred beyond the 25 000 s^{-1} shear rate. At this point, the shear viscosities of different fibre suspensions were very similar to each other.
- The shear viscosity of fibre suspensions was dependent on the fibre aspect ratio, fibre fraction and temperature, with a greater shear viscosity value for the greater fibre aspect ratio, higher fibre fraction and lower temperature respectively.
- The fibre suspensions showed significant entrance and exit effects. Suggesting the extensional resistance or viscosity are not as comprehensive as studies on the shear viscosity. The next chapter will examine in depth the extensional rheology of fibre suspensions. Meanwhile, Chapter 6 will unveil the more dominant force between the two resistances; shear and extensional, that resists and controls the atomization performance.

References

Aho, J., & Syrjala, S. (2006). Determination of the entrance pressure drop in capillary rheometry using Bagley correction and zero-length capillary. *Annual Transaction-Nordic Rheology Society, 14*, 143.

Bhattacharya, S., Bal, S., Mukherjee, R., & Bhattacharya, S. (1991). Rheological behaviour of tamarind (Tamarindus indica) kernel powder (TKP) suspension. *Journal of Food Engineering, 13*(2), 151-158.

Binding, D., Couch, M., & Walters, K. (1998). The pressure dependence of the shear and elongational properties of polymer melts. *Journal of Non-Newtonian Fluid Mechanics, 79*(2-3), 137-155.

Bounoua, S., Lemaire, E., Férec, J., Ausias, G., & Kuzhir, P. (2016). Shear-thinning in concentrated rigid fiber suspensions: Aggregation induced by adhesive interactions. *Journal of Rheology, 60*(6), 1279-1300.

Briscoe, B., Luckham, P., & Zhu, S. (1998). Rheological properties of poly(ethylene oxide) aqueous solutions. *Journal of Applied Polymer Science, 70*(3), 419-429.

Cheuyglintase, K. (2009). Spray drying of fruit juice with vegetable fibre as a carrier. *A thesis presented in fulfilment of the requirements of the degree of Doctor Philosophy in Chemical and Process Engineering at the University of Canterbury*.

Djalili-Moghaddam, M., & Toll, S. (2006). Fibre suspension rheology: Effect of concentration, aspect ratio and fibre size. *Rheologica Acta, 45*(3), 315-320.

Facca, A. G., Kortschot, M. T., & Yan, N. (2006). Predicting the elastic modulus of natural fibre reinforced thermoplastics. *Composites Part A: Applied Science and Manufacturing, 37*(10), 1660-1671.

Grigelmo-Miguel, N., Ibarz-Ribas, A., & Martín-Belloso, O. (1999). Rheology of peach dietary fibre suspensions. *Journal of Food Engineering, 39*(1), 91-99.

Huang, J. C., & Leong, K. S. (2002). Shear viscosity, extensional viscosity, and die swell of polypropylene in capillary flow with pressure dependency. *Journal of Applied Polymer Science, 84*(6), 1269-1276.

Ibarz, A., Vicente, M., & Graell, J. (1987). Rheological behaviour of apple juice and pear juice and their concentrates. *Journal of Food Engineering, 6*(4), 257-267.

Keshtkar, M., Heuzey, M., & Carreau, P. (2009). Rheological behavior of fiber-filled model suspensions: Effect of fiber flexibility. *Journal of Rheology, 53*(3), 631-650.

Krieger, I. M. (1972). Rheology of monodisperse latices. *Advances in Colloid and Interface Science, 3*(2), 111-136.

Lefebvre, A. (1988). *Atomization and sprays* (Vol. 1040). CRC press.

Mahmoud, M., & Fugitt, M. (1996). Rheological properties of a calorically dense nutritional supplement as a function of nitrogen source and dietary fiber. *Paper presented at the 1996 IFT Annual Meeting, Book of Abstracts, 80A-26*.

Manjunatha, S. S., & Raju, P. S. (2015). Rheological characteristics of reconstituted spray dried beetroot (Beta vulgaris L.) juice powder at different solid content, temperatures and carrier materials. *International Food Research Journal, 22*(6).

Maron, S. H., & Pierce, P. E. (1956). Application of Ree-Eyring generalized flow theory to suspensions of spherical particles. *Journal of Colloid Science, 11*(1), 80-95.

Saravacos, G. (1970). Effect of temperature on viscosity of fruit juices and purees. *Journal of Food Science, 35*(2), 122-125.

Schröder, J., Lederer, M., Gaukel, V., & Schuchmann, H. (2011). Effect of atomizer geometry and rheological properties on effervescent atomization of aqueous polyvinylpyrrolidone solutions. *Paper presented at the ILASS–Europe 24rd Annual Conference on Liquid Atomization and Spray Systems, Estoril, Portugal*.

Teknotext, A. B. (1995). Dairy Processing Handbook. *Published by Tetra Pak Processing Systems AB. S-221*, *86*, 387.

Verma, A., & Singh, S. V. (2015). Spray drying of fruit and vegetable juices – A review. *Critical Reviews in Food Science and Nutrition*, *55*(5), 701-719.

Zar, J. H. (2013). *Biostatistical analysis: Pearson New International Edition*. Pearson Higher Ed.

Chapter 5 Extensional rheology of fibre suspensions

Chapter 4 explained, in depth, the shear rheology of fibre suspensions. In this chapter the extensional rheology of the fibre suspensions will be explored. Studies on extensional rheology are relatively scarce. When explaining atomization performance, previous authors usually relate the performance to the shear rheology of the liquid only. This approach stays true for Newtonian liquids because Newtonian liquids do not display extensional resistance to fluid breakup. The linear viscoelastic and extensional properties of fibre suspensions were investiagted using a rotary viscometer and capillary breakup extensional rheometer, respectively.

5.1 Linear viscoelastic properties

Section 5.1.1 focuses on the linear viscoelasticity of different types of fibre suspensions while Section 5.1.2 discusses the effect of temperature on the viscoelasticity.

5.1.1 Small amplitude oscillatory shear properties

The linear viscoelasticity of each fibre type at 5.0 wt.% and 10.0 wt.% suspensions were studied to investigate the contribution of each fluid-like and solid-like behaviour of the suspensions towards the overall rheological properties. The linear viscoelasticity was investigated using an oscillatory test method performed on a rotary rheometer. Please refer to Section 3.5.1 for details on the oscillatory test method. At first, strain sweep measurements were performed on the fibre suspensions to determine the extent of the linear viscoelastic regime. For all fibre suspensions, it was found that the maximum strain limit for the linear regime is less than 1.0%. So, during the oscillatory tests, all tests were performed at a constant strain amplitude of 0.1% in order to ensure the tests proceeded within the linear regime. Figures 5.1 and 5.2 show the elastic modulus, *G'* and viscous modulus, *G"* versus the dynamic frequency for 5.0 wt.% and 10.0 wt.% fibre suspensions,

respectively. The *G'* and *G"* represent the solid-like and fluid-like behaviours of the suspensions, respectively.

As shown in Figures 5.1 and 5.2, both moduli increased with fibre concentration. As shown in Figure 5.1, the *G"* of 5.0 wt.% fibre suspensions were always higher than the *G'* for the whole range of frequencies studied, regardless of the fibre type or aspect ratio. It means that the fluid-like behaviour of 5.0 wt.% AF 400-30, 5.0 wt.% WF 101, 5.0 wt.% WF 600 and 5.0 wt.% citrus fibre suspensions prevailed over the solid-like behaviour which suggests the presence of weak entanglements networks (Piermaría et al., 2016; Xu et al., 2005). The networks were weak and the solvent flow properties dominated the rheology, thus the fibre suspensions show fluid-like behaviour. This observation can be supported by the analysis done in Chapter 4, Section 4.1.2, Table 4.2. Based on Table 4.2, there were no fibres entanglement or networks presents inside all the 5.0 wt.% fibre suspensions. *G'* and *G"* of 5.0 wt.% AF 400-30 and 5.0 wt.% WF 101 fibre suspensions were always lower than the *G'* and *G"* of 5.0 wt.% WF 600 and 5.0 wt.% citrus fibre suspensions which suggests that the *G'* and *G"* were a function of fibre aspect ratio.

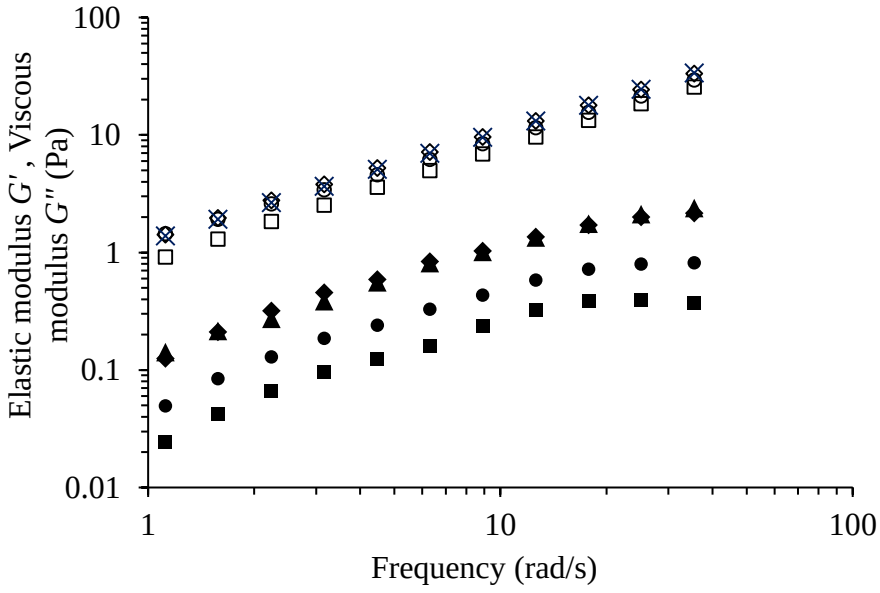

Figure 5.1 Elastic modulus (*G'*, filled symbols) and viscous modulus (*G"*, open symbols) for 5.0 wt.% fibre suspensions as a function of frequency based on small amplitude oscillatory measurements. (●, ○) AF 400-30, (■, □) WF 101, (♦, ◊) WF 600 and (▲, ×) citrus fibre.

As shown in Figure 5.2, the *G"* of 10.0 wt.% AF 400-30 and 10.0 wt.% WF 101 fibre suspensions were greater than the *G'*, similar to the behaviour observed in Figure 5.1. In contrast, the *G"* of 10.0 wt.% WF 600 and 10.0 wt.% citrus fibre suspensions were dominant at lower frequencies until reaching a crossover where the *G'* started to be dominant. It means that, within the linear viscoelasticity regime, the 10.0 wt.% WF 600 and 10.0 wt.% citrus fibre suspensions showed a significant solid-like behaviour. This behaviour is true for the fibre suspensions with a greater aspect ratio. A possible explanation for this solid-like behaviour is that the high aspect ratio fibres formed networks which can be easily broken down by deformation. This hypothesis can be supported by the analysis done in Chapter 4, Section 4.1.2, Table 4.3. Based on Table 4.3, there were non-hydrodynamic interactions present inside the 10.0 wt.% WF 600 and 10.0 wt.% citrus fibre suspensions, such as mechanical contacts between fibres as well as floc or network formation. Meanwhile, there were no such networks present inside the 10.0 wt.% AF 400-30 and 10.0 wt.% WF 101 fibre suspensions. *G'* and *G"* of 10.0 wt.% AF 400-30 and 10.0 wt.% WF 101 fibre suspensions were always lower than the *G'* and *G"* of 10.0 wt.% WF 600 and 10.0 wt.% citrus fibre suspensions which further shows that the *G'* and *G"* were a function of fibre aspect ratio.

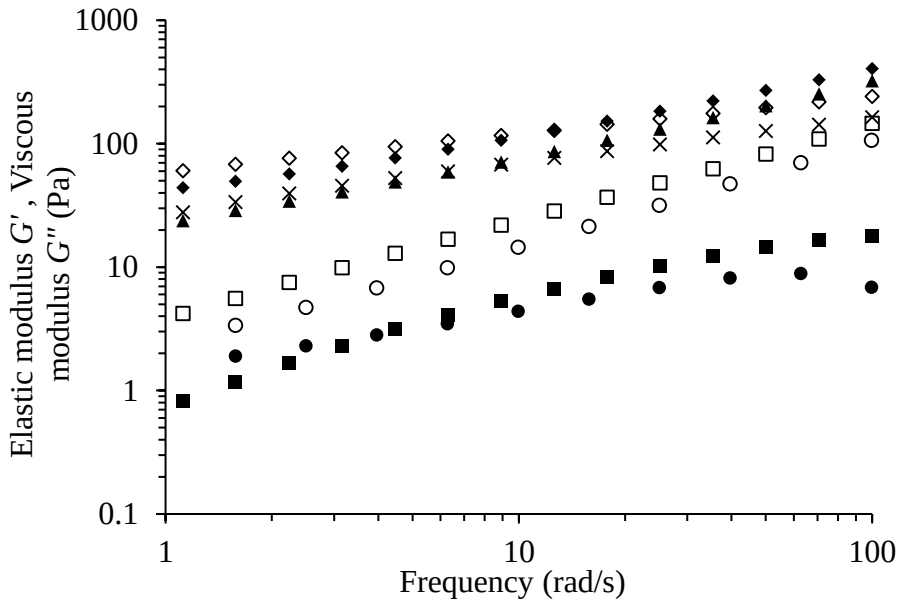

Figure 5.2 Elastic modulus (*G'*, filled symbols) and viscous modulus (*G"*, open symbols) for 10.0 wt.% fibre suspensions as a function of frequency based on small amplitude oscillatory measurements. (●, ○) AF 400-30, (■, □) WF 101, (♦, ◊) WF 600 and (▲, ×) citrus fibre.

Figures 5.1 and 5.2 indicate that at low concentrations, the fibre networks were weak, and the solvent dominated the rheology, so the suspensions showed liquid-like behaviour. But, beyond a critical concentration, such as 10.0 wt.% for the system studied here, the networks became stronger and hence elastic solid-like behaviour was observed. This behaviour agrees with previous studies done by Xu et al. (2005) and Damani et al. (1993). Figures 5.1 and 5.2 also show the dependence of solid-like, *G'* and fluid-like, *G''* behaviours on aspect ratio, in agreement with the findings by Kotsilkova (1992) and Guo et al. (2005), who found that both the elastic and viscous modulus of fibre suspensions increased with the fibre aspect ratio. They concluded that a more pronounced structure or network was formed by entangled fibres as the fibre aspect ratio increased.

The results from the linear viscoelasticity regime suggest that the fibre suspensions used in this study may not be purely viscous and show elastic behaviour. It means that the atomization behaviour of the fibre suspensions will not be purely influenced by the viscous forces but also by elastic forces. The method of using small amplitude oscillatory measurements to show the viscoelastic properties of fibre suspensions was reliable, but most studies were limited to linear measurements, i.e. measurements were done within the small linear deformations of 0.1% strain, whereas in atomization, the fibre suspensions can experience high strain deformations. Hence, there was a need for a different method to study the viscoelasticity of fibre suspensions as near as possible to the conditions occurring during atomization.

5.1.2 Effect of temperature

Section 4.1.4 has shown the effect of temperature on shear rheology. Particularly, Figure 4.9 shows that the shear viscosity of 5.0 wt.% WF 600 fibre suspension decreased as the temperature was increased. To examine the effect of temperature on the elasticity of fibre suspensions, the variation of *G'* against temperature was observed. Figure 5.3 shows the variation of *G'* for 5.0 wt.% WF 600 fibre suspension at temperatures between 20 °C and 70 °C and at a constant frequency of 10 rad/s or ~ 1 Hz. Previous studies usually observed the variations of *G'* with the temperature at 1 Hz frequency (Moberg et al., 2016; Pothan et al., 2003).

Figure 5.3 shows no significant trend in the increase or decrease in *G'* as the temperature was increased. It is possible to say that the *G'* was generally decreased as the temperature was increased from 20 °C to 70 °C, but the reduction was insignificant or very weak. The *G'* can be said to be fairly constant between 20 °C and 70 °C. *G'* represents the solid-like behaviour contributed by the fibres. Weak temperature-dependence of *G'* indicates that the fibres were not significantly thermally activated within the range tested; 20 °C and 70 °C. Thus, when the temperature was increased to 70 °C, while the fibre-solvent interactions became weaker, as proven in Section 4.1.4 on the shear rheology study, the fibre-fibre interactions stayed the same. A similar observation was obtained when using 10.0 wt.% WF 600 fibre suspension, as shown in Figure 5.4. ANOVA tests were performed on both 5.0 wt.% and 10.0 wt.% fibre suspensions to check whether there are any significant differences between the *G'* as the temperature was increased. The results show that the p-values were more than 0.05, which means that the *G'* at different temperatures were all equal, thus the effect of temperature on *G'* was insignificant. The previous study by Chindam et al. (2014) showed the indistinct trend of the *G'* of microfibres film as the temperature was increased at least to 70 °C. Other studies by Pothan et al. (2003) and Moberg et al. (2016) reported that the *G'* of banana fibre and cellulose nanofibrils composites insignificantly decreased when the temperature was increased to 60-70 °C.

Overall, while the shear rheology of fibre suspensions was strongly affected by temperature, the dependence of elasticity of fibre suspensions on temperature was relatively weak, at least within the temperature range of 20 °C to 70 °C. Atomization performance is influenced by the shear and extensional resistance. The results indicate that as the temperature increases the energic requirements of atomization may become dominated by the extensional resistance, as the shear resistance at increasing temperatures decreases.

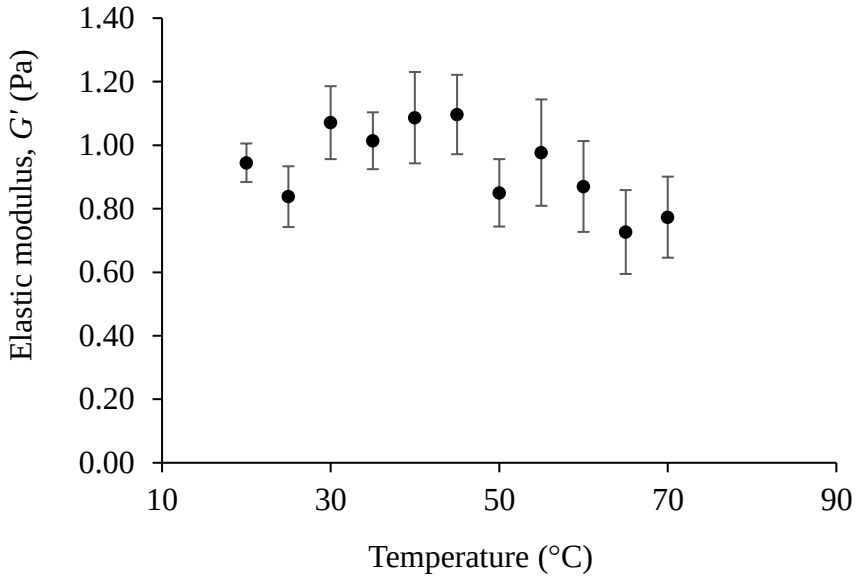

Figure 5.3 The effect of temperature on the elastic modulus, *G'* of 5.0 wt.% WF 600 fibre suspension.

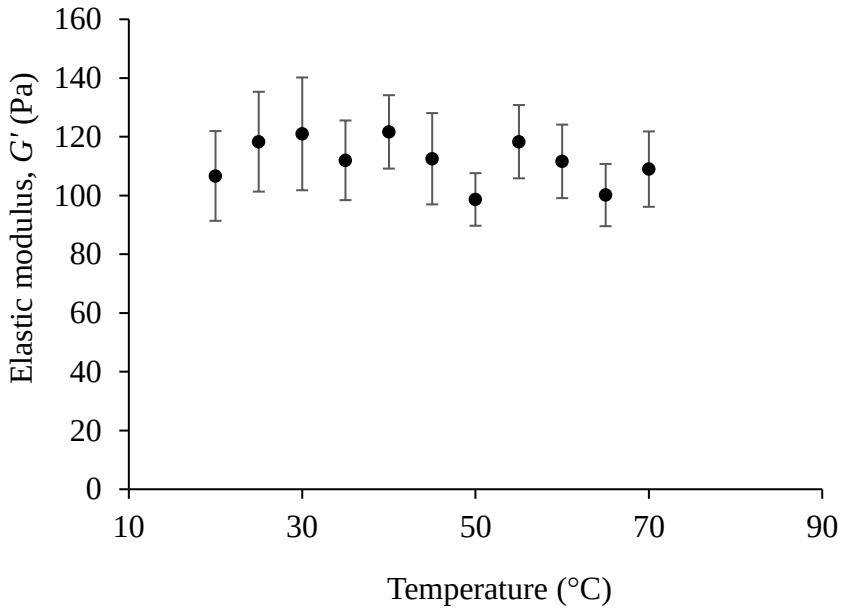

Figure 5.4 The effect of temperature on the elastic modulus, *G'* of 10.0 wt.% WF 600 fibre suspension.

5.2 Capillary breakup extensional rheometer

Recently, different types of extensional rheometers have been utilized in investigating extensional properties of materials, especially polymer solutions. In this section, the extensional properties of the fibre suspensions are discussed based on the capillary breakup method performed on a portable extensional rheometer. Section 5.2.1 shows the difference in the capillary breakup of concentrated apple juice and fibre suspensions, highlighting the measurement of relaxation time. The relaxation time is one of the extensional properties essential for predicting the atomization performance (fluid breakup). Sections 5.2.2 and 5.2.3 each explains the effect of fibre aspect ratio on the relaxation time and apparent extensional viscosity of fibre suspensions, respectively.

5.2.1 Concentrated apple juice VS. fibre suspensions

Extensional rheology of the concentrated apple juice and fibre suspensions were investigated based on the observation of the mid-plane diameter profile of a stretched liquid. The stretching of the concentrated apple juice and fibre suspensions were followed by the thinning process of the filaments. Please refer to Section 3.5.3 for more details on the capillary breakup method. To keep the initial filament configuration (before stretching) close to cylindrical with insignificant bulging effects, the capillary breakup test employed axial separation so that $h_0/R_0 \leq 1/\sqrt{Bo}$ (Rodd et al., 2004). h_0 (mm) is the initial separation between the upper and lower piston, R_0 (mm) is the initial sample radius and Bo is the Bond number. Both h_0 and R_0 correspond to the value before the stretching occurred and were 1.5 mm and 2.0 mm respectively. The Bond number, Bo is shown in Equation 5.1.

$$Bo = \rho g {R_0}^2/4\sigma \qquad \text{Equation 5.1}$$

where ρ (kg/m^3) is the density of the liquid and g (m/s^2) is the gravitational constant and σ (N/m) is the surface tension. In the current study, Bo was calculated to be 0.2.

The filament mid-plane diameter profiles of concentrated apple juice and 7.0 wt.% WF 600 fibre suspension are shown in Figure 5.5. The profiles of the mid-plane diameter, D_{mid} versus time were measured on the portable extensional rheometer constructed for this

project. Theoretically, the breakup of a Newtonian liquid follows a linear diameter profile where the liquid breaks directly after the stretching. The stages involved are stretch and breaking stages (stretch-breaking). It means that the dependence of filament thinning diameter on time is linear. Based on Figure 5.5, the filament thinning profile of the concentrated apple juice is linear. In contrast, the filament thinning profile of 7.0 wt.% WF 600 fibre suspension is non-linear. Particularly, the filament mid-plane diameter thins down exponentially with time. Liquids with extensional properties usually display an exponential profile where the filament passes through stretch, relaxation and breaking stages (stretch-relaxation-breaking). This is clearly portrayed by the fibre suspension in Figure 5.5. While concentrated apple juice behaves like a Newtonian liquid with no extensional properties, the suspension with added fibres follows non-Newtonian shear thinning behaviour with added extensional properties. Such exponential decay with time, shown in Figure 5.5, is a characteristic of a pure extensional flow which has been previously reported in the literature (Hallmark et al., 2016; Jaishankar et al., 2015; Piermaría et al., 2016).

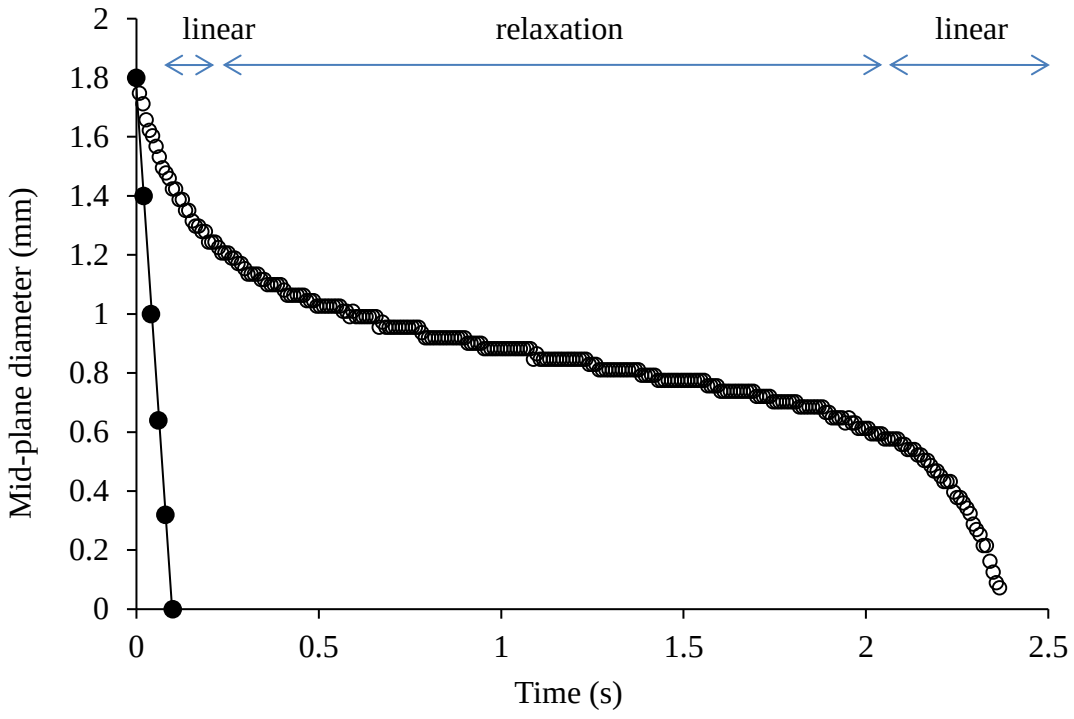

Figure 5.5 Filament diameter profile of (●) concentrated apple juice and (○) 7.0 wt.% WF 600 fibre suspension measured on a portable extensional rheometer.

A closer observation of Figure 5.5 indicates that the fibre suspension initially starts to thin or decay by a similar mechanism as the Newtonian concentrated apple juice, as can be seen from the linear decrease in the mid-plane diameter. The similar thinning dynamic or mechanism implies that the role of fibres was absent during this stage. The fibre particles remained in their equilibrium conformation and thus, were not influencing the thinning dynamic. It is also possible that the filament thinning dynamic was still influenced by the inertia of the stretching applied to the liquid and thus resulted in the linear decrease profile. However, based on Figure 5.5, after the linear decrease, the thinning dynamic starts to diverge. The start of the divergence point is what is referred to as the onset of necking. At the onset of necking, the fibres orientate, stretch, and elongate due to the pure extensional flow created inside the filament. The orientation, stretching and elongation of the fibres during the extensional flow created a dominant extensional resistance that opposed the deformation of the filament or the thinning process and consequently contributed to the formation of a stable filament. This phenomenon is manifested in the relaxation stage shown in Figure 5.5. This behaviour of fibre suspension is similar to the behaviour of most polymer solutions (Piermaría et al., 2016). During the last stage, the thinning dynamic diverges back into a linear decrease, as shown in Figure 5.5. In this regime, the fibres have reached the maximum stretching and elongation such that the extensional resistance could not resist the thinning anymore. This led to a sudden quick decay in the filament mid-plane diameter until finally broken up.

The exponential thinning profile of the 7.0 wt.% WF 600 fibre suspension can be divided into different regimes according to the thinning mechanisms explained above. Generally, based on Figure 5.5, there is a linear regime and an exponential regime. Technically, the regimes can be labelled as inertia-capillary, viscous-capillary and elasto-capillary regimes. The identification of each regime helps in determining the relaxation time, τ of a specific fibre suspension as a quantitative study of the extensional rheology of fibre suspensions.

The exponential filament diameter profile of fibre suspension in Figure 5.5 theoretically follows Equation 5.2 (Bazilevsky et al., 1990; Entov & Hinch, 1997).

$$\frac{D(t)}{D_0} = \left(\frac{GD_0}{4\sigma}\right)^{1/3} \exp[-t/(3\tau_r)] \qquad \text{Equation 5.2}$$

in which G (Pa) is the elastic modulus, D_0 (mm) is the initial filament mid-plane diameter before the stretching, σ (N/mm) is the surface tension and τ_r (s) is the relaxation time in

the Oldroyd-B model or also known as Upper Convected Maxwell model. Therefore, the capillary breakup test of fibre suspensions performed on a portable extensional rheometer yields the characteristic relaxation time of the fibre suspension, τ_r in elongation or extensional flow. Relaxation time is the characteristic time scale for viscoelastic stress growth in a uniaxial elongational flow (Rodd et al., 2004). Regression of Equation 5.2 to the experimental data of the 7.0 wt.% WF 600 fibre suspension is shown in Figure 5.6.

Figure 5.6 was plotted in a log graph to accurately visualize the fit of the regression line to the experimental data. Based on Figure 5.6, it is obvious and visible that there are initial and final stages in which the exponential decay of Equation 5.2 does not fit the data anymore. These stages are drawn inside the dashed rectangular regions. At very early times, the filament bridge had just been formed and the fibre suspension had not felt the strong extensional flow field yet or the fibres had not started stretching yet. During this initial stage, the mid-plane diameter of the fibre suspension thinned down due to the balance between capillarity and a mixture of inertia and viscous forces. Meanwhile, at the final stage, the fibres had reached their maximum stretching or extensibility limits such that they cannot extend anymore, so the filament breaks. This means that the fibres contribution to the extensional resistance is saturated. Based on the experimental data points in Figure 5.6, after the finite extensibility of the fibres, the mid-plane diameter quickly falls to zero in a somewhat like a linear manner. Meanwhile, the predicted regression line continues to decay very slowly. This phenomenon can be explained by the fact that the exponential decay in Equation 5.2 from Oldroyd-B model was originally predicted on the infinite extensibility of a polymer chain and as consequence, the thinning filament was presumed to never break which is physically impossible (Bazilevsky et al., 1990).

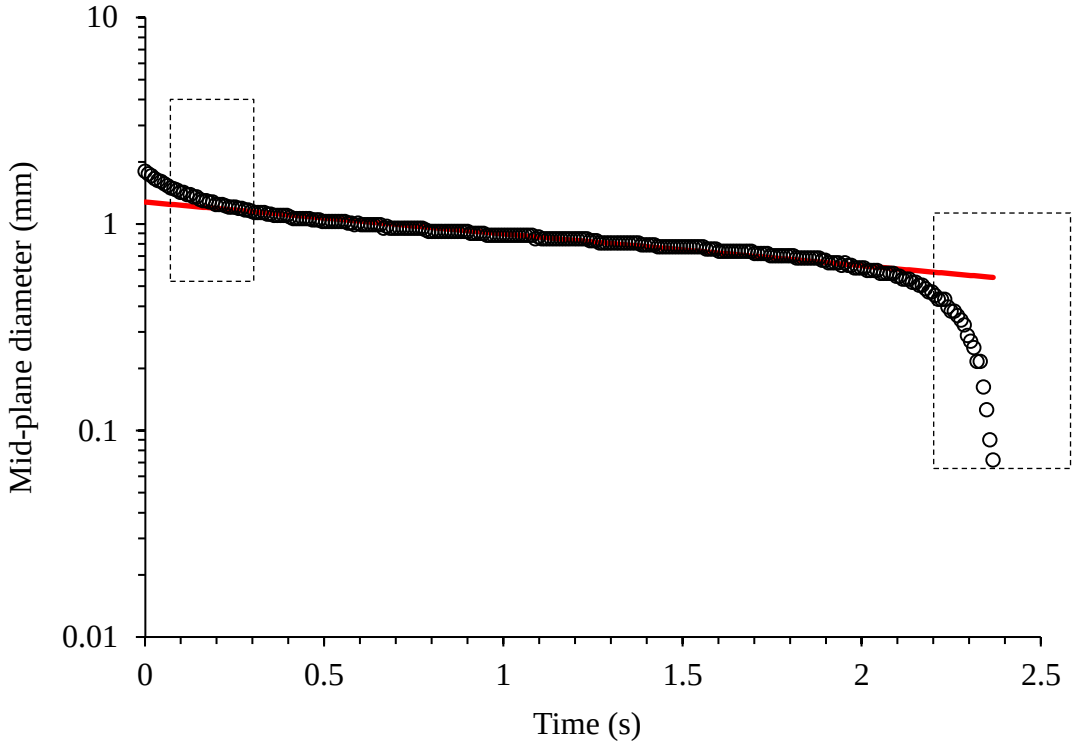

Figure 5.6 Exponential filament diameter profile of the 7.0 wt.% WF 600 fibre suspension. (○) Experimental data and (red solid line) Regression line based on Equation 5.2. The dashed rectangles contain intolerable deviated data points from the model predictions.

Figure 5.7 shows a more detailed graph, characterizing the stages based on different regression equations. As mentioned previously, during the early stage, the filament thinning profile was dominated by the balance between capillarity, inertia and viscous forces. At first, the mid-plane diameter thinned down with a timescale set by an inertia-capillary balance (also known as the Rayleigh timescale), as shown in Equation 5.3.

$$\tau_R \equiv 1.95\sqrt{\rho {R_0}^3/\sigma} \qquad \text{Equation 5.3}$$

where τ_R (s) is the Rayleigh timescale. The τ_R of 7.0 wt.% fibre suspension plotted in Figure 5.7 is 0.023 s, as represented by the orange colour bullets. Immediately following the inertia-capillary regime is a visco-capillary regime characterized by the linear decrease in the mid-plane diameter profile, which was plotted in blue colour bullets. In this regime, the capillary forces were balanced by the shear viscosity of the fibre suspensions. The mid-plane diameter of the filament decreased linearly with time following Equation 5.4.

$$D(t) = D_0 - \left(\frac{2x-1}{6}\right)\left(\frac{\sigma}{\mu_0}\right)t \qquad \text{Equation 5.4}$$

where D_0 (mm) is the initial filament mid-plane diameter during the start of the visco-capillary regime. Regression of Equation 5.4 was performed on the experimental data between the time, t = 0.024 s and t = 0.200 s. t = 0.024 s was the start of the visco-capillary regime right after the inertia-capillary regime while t = 0.200 s was selected based on the time when the regression line in Equation 5.2 starts to coincide with the experimental data in Figure 5.6. Regression line of Equation 5.4 is shown in Figure 5.7. Refer to Appendix D for a more detailed calculation regarding Equations 5.2-5.4.

The linear viscous thinning regime is followed by an elasto-capillary regime in which the filament mid-plane diameter decays exponentially and is given by Equation 5.2. At this regime, the capillary pressure arising from the surface tension is balanced purely by the stress arising from the fluid elasticity. Regression of Equation 5.2 was performed on the filament diameter data but excluding the initial and final stages inside the dashed rectangular regions. This is shown in Figure 5.7. Regression of Equation 5.2 enables the measurement of the relaxation time, τ_r for the 7.0 wt.% WF 600 fibre suspension in Figure 5.7. The τ of 7.0 wt.% WF 600 fibre suspension is 0.7 $\pm$ 0.03 s. The τ, obtained based on the regression analysis, was used to predict the atomization performance. By doing so, the predicted atomization performance of different fibre suspensions matches very well with the experimental atomization performance. Please refer to Chapter 6 on atomization performance. Hence, the exponential filament thinning curves produced in this study, together with the regression fit based on Equation 5.2, are reliable in generating the characteristic relaxation time, τ_r of fibre suspensions. Future works may modify or generate better constitutive equations to describe the flow phenomenon of fibre suspensions in an extensional flow field. The current analysis, which used the simplest method; Equation 5.2, can be used as a starting point. For each fibre suspension, three filament thinning profiles were produced using the portable extensional rheometer. The plot in Figure 5.7 represents only one curve from the three filament thinning profiles.

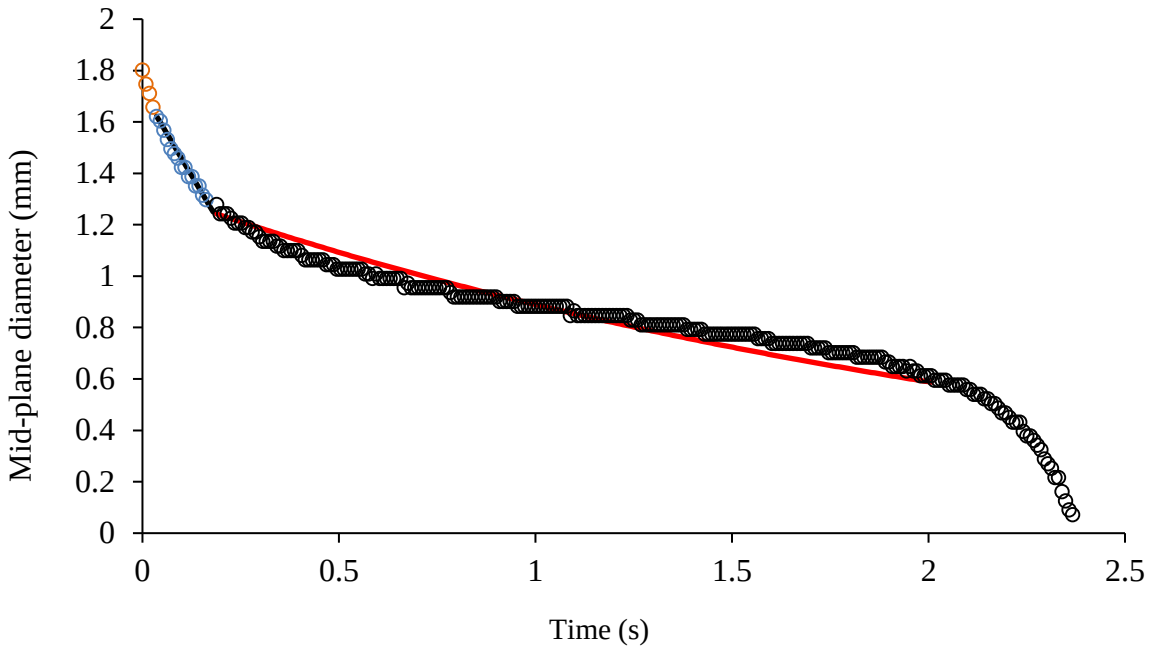

Figure 5.7 Filament diameter profile of the 7.0 wt.% WF 600 fibre suspension highlighting the identified different regimes. (○, orange colour) inertia-capillary regime, (○, blue colour) visco-capillary regime and (○, black colour) elasto-capillary regime. (black line) Regression line based on the visco-capillary regime and (red line) regression line based on the elasto-capillary regime.

5.2.2 Effect of fibre aspect ratios on relaxation time, τ_r

The extensional rheology of different fibre suspensions were examined based on the capillary breakup test performed on a portable extensional rheometer. Figures 5.8 and 5.9 show the filament diameter profiles as a function of time for 5.0 wt.% and 7.0 wt.% fibre suspensions, respectively. Based on Figures 5.8 and 5.9, it is apparent that the relaxation phases of 5.0 wt.% and 7.0 wt.% AF 400-30 and WF 101 fibre suspensions are less obvious when compared to the 5.0 wt.% and 7.0 wt.% WF 600 and citrus fibre suspensions. This is due to the WF 600 and citrus fibres having greater fibre aspect ratios than the AF 400-30 and WF 101 fibres. The capillary breakup test conditions were all similar. Hence, it means during the capillary breakup tests, by applying the same strength of extensional deformation, individual fibre particles unravelled and evolved at different rates and thus contributed to different steady-state extensions. Figures 5.8 and 5.9 show the greater fibre aspect ratios of WF 600 and citrus fibres required more time to unravel, stretch and elongate before reaching the critical condition where the filaments finally break. In other words, it

means the longer and greater aspect ratio fibres created stronger extensional resistance inside the filament during the thinning process. This explains the longer relaxation phase of WF 600 and citrus fibre suspensions compared to the AF 400-30 and WF 101 fibre suspensions which are relatively short. As mentioned previously, the relaxation phase corresponds to the stress arising from the liquid elasticity.

In addition to the contribution by the individual fibres, fibre aggregates were also present during the flow. The greater aspect ratio fibres such as WF 600 and citrus fibres induced greater probability of fibre interaction which then form stronger fibre aggregates. When stretching and extensional deformation were applied to the fibre suspensions, stronger fibre aggregates required longer time to deform and break compared to the looser aggregates formed by the lower aspect ratio of AF 400-30 and WF 101 fibres. This reasoning can also be supported by the apparent longer relaxation phase of each 7.0 wt.% fibre suspension when compared to its corresponding 5.0 wt.% fibre suspension because the 7.0 wt.% fibre suspension developed stronger fibre aggregates.

For each fibre suspension, three different capillary breakup tests were performed. Figures 5.8 and 5.9 show a representation of one curve for each fibre suspension. Appendix E contains all the filament thinning curves used in acquiring the average relaxation time of a specific fibre suspension. A similar analysis as explained in Section 5.2.1 was performed on all filament thinning curves plotted in Appendix E to determine the relaxation time, τ_r. The τ_r values for the fibre suspensions are tabulated in Table 5.1. Figure 5.10 clearly highlights the similarity and difference in the relaxation time of fibre suspensions based on the fibre aspect ratios.

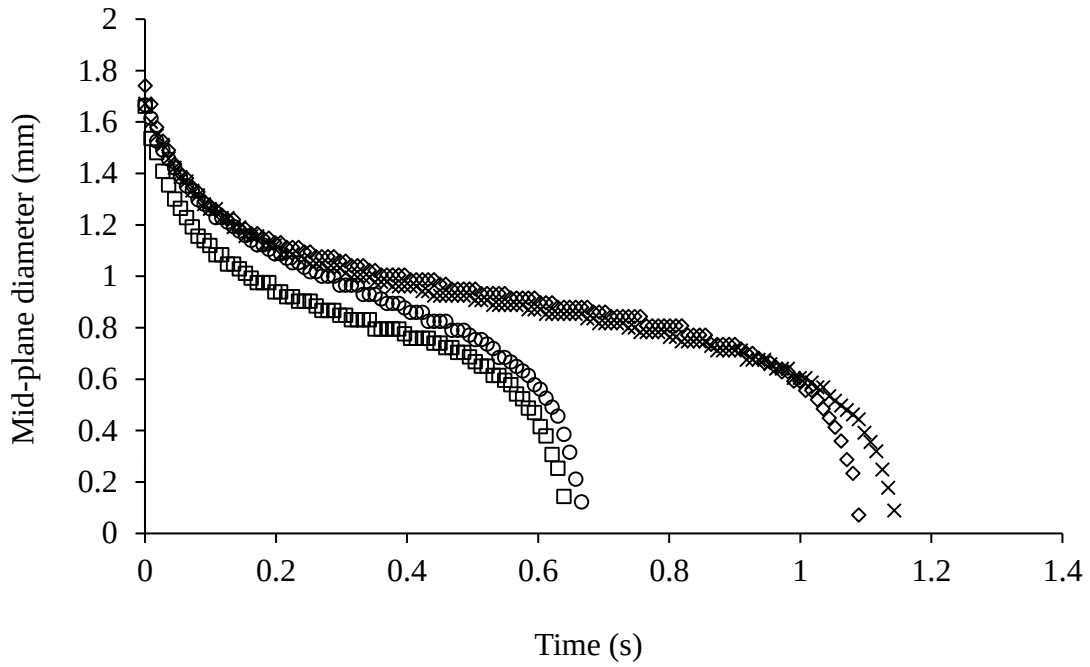

Figure 5.8 Filament diameter profile of 5.0 wt.% fibre suspensions measured on a portable extensional rheometer. (○) AF 400-30, (□) WF 101, (◊) WF 600 and (×) citrus fibre.

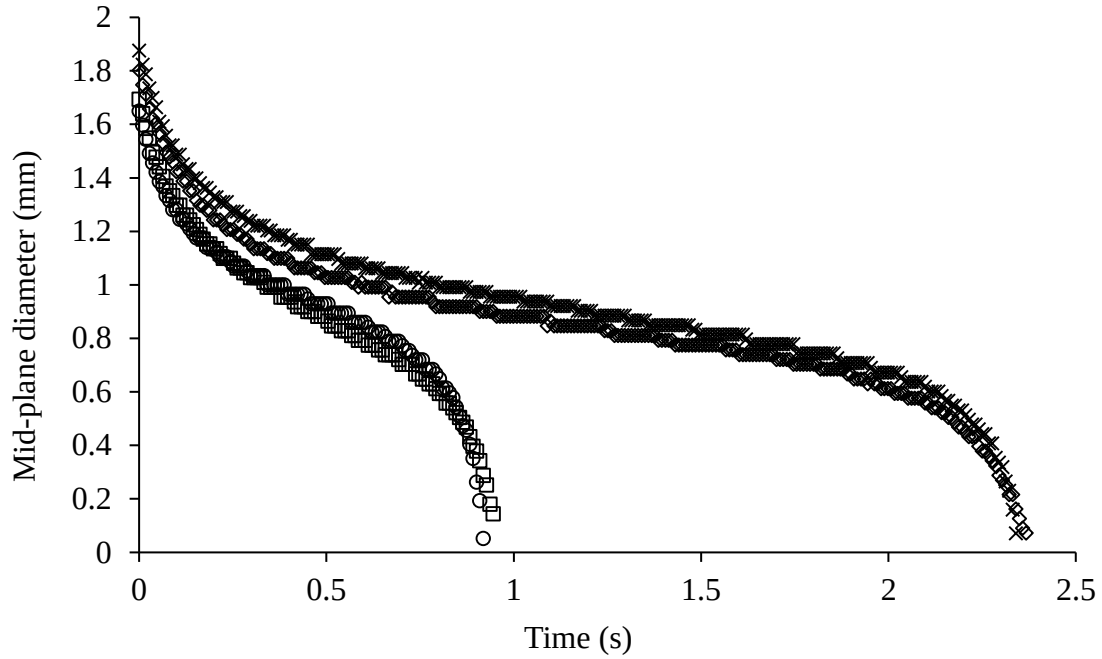

Figure 5.9 Filament diameter profile of 7.0 wt.% fibre suspensions measured on a portable extensional rheometer. (○) AF 400-30, (□) WF 101, (◊) WF 600 and (×) citrus fibre.

Table 5.1 Relaxation time, τ_r for 5.0 wt.% and 7.0 wt.% of different fibre suspensions measured using the portable extensional rheometer.

Fibre suspensions	Aspect ratio	Fibre fraction (wt.%)	Relaxation time, τ_r (s)
AF 400-30	2-3	5.0	0.12 ± 0.01
		7.0	0.25 ± 0.01
WF 101	2-3	5.0	0.15 ± 0.01
		7.0	0.24 ± 0.02
WF 600	8-10	5.0	0.34 ± 0.03
		7.0	0.70 ± 0.03
Citrus fibre	8-10	5.0	0.33 ± 0.03
		7.0	0.72 ± 0.06

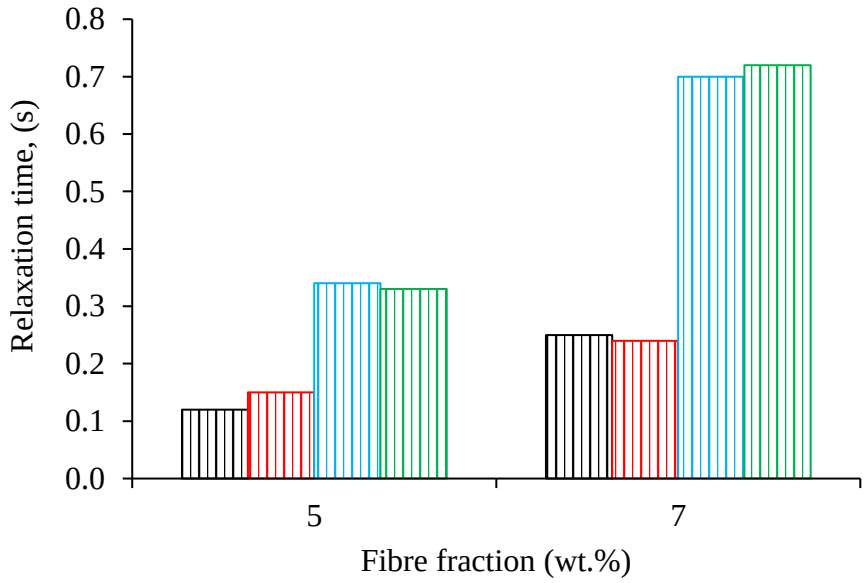

Figure 5.10 Relaxation time of 5.0 wt.% and 7.0 wt.% fibre suspensions. (black shading) AF 400-30 with aspect ratio 2-3, (red shading) WF 101 with aspect ratio 2-3, (blue shading) WF 600 with aspect ratio 8-10 and (green shading) citrus fibre with aspect ratio 8-10.

5.2.3 Effect of fibre aspect ratios on extensional viscosity

Other than the relaxation time, τ_r of fibre suspensions, apparent extensional viscosity of fibre suspensions can be calculated as an another way to quantify the extensional rheology. Anna and McKinley (2001) have shown that during the capillary breakup test, the filament diameter profile could be differentiated to find the transient extensional viscosities, η_E^+ based on Equation 5.5 (Anna & McKinley, 2001).

$$\eta_E^+ = -\sigma/(dD(t)/dt) \qquad \text{Equation 5.5}$$

Equation 5.5 uses the derivative of the filament diameter profile, $dD(t)/dt$ in calculating the η_E^+. To find the derivative of the mid-plane diameter, $dD(t)/dt$ of fibre suspensions, the measured data of the mid-plane diameter, $D(t)$ plotted in Figures 5.8 and 5.9 were directly differentiated by applying a polynomial order of 3 to 5. The $D(t)$ used in the differentiation includes the visco-capillary and elasto-capillary regimes. Hencky strain, $\varepsilon(t)$ as in Equation 5.6 is the strain experienced by the filament at the axial mid-plane at time t and thus can be defined using the mid-plane filament diameter during the capillary breakup test.

$$\varepsilon(t) = 2 \ln (D_0/D(t)) \qquad \text{Equation 5.6}$$

Figures 5.11 and 5.12 show the variation of η_E^+ of the 5.0 wt.% and 7.0 wt.% fibre suspensions as a function of Hencky strain, respectively, obtained by using Equation 5.5. Appendix F shows a detailed example in calculating the η_E^+ for the 7.0 wt.% WF 600 fibre suspension. The physical meaning of the plot of the η_E^+ against Hencky strain is very similar to the interpretation of the plot of shear viscosity against shear rates. The two peaks displayed by some of the curves in Figures 5.11 and 5.12 are suspected to be due to the difference in the order of the polynomial function applied during the differentiation and is regarded as insignificant. This is because, changing the polynomial order, for example from 3 to 5, will change the curves from one peak to two peaks. The polynomial order for each fibre suspension was appointed based on the quality of the fit to the experimental data. The exponential filament thinning profiles as opposed to the linear profile shown in Figures 5.8 and 5.9 are adequate to indicate that the fibre suspensions exhibit extensional behaviour, along with shear rheology. However, the plot of the η_E^+ against Hencky strain is important to determine the dominant resistance between the shear and extensional viscosities.

Based on Figures 5.11 and 5.12, the 5.0 wt.% and 7.0 wt.% fibre suspensions show a trend where the extensional viscosity first increases against the Hencky strain and after that, the extensional viscosity keeps on decreasing for the rest of the Hencky strain. The increase in the transient extensional viscosity happened when the fibres orientate, stretch and elongate due to the pure extensional flow created inside the filament. Whereas the peak in the extensional viscosity curve occurred when the fibres reached the critical stretching point. After that, the extensional resistance could not resist the thinning, and this led to the decay in the transient extensional viscosity. The trend for the fibre suspensions is different from the behaviour observed previously on polymer solutions, where the latter usually incorporates only an increase in the extensional viscosity or called extension thickening (Eastman et al., 2000; Jaishankar et al., 2015; Sachdev et al., 2016). The studies on extensional viscosity are very scarce, especially with regard to fibre suspensions. The only study done on fibre suspensions used carbon nanofibre by Xu et al. (2005), their results showed carbon fibre suspensions behaved as an extension thinning liquids.

For both 5.0 wt.% and 7.0 wt.% fibre concentrations, the extensional viscosity is greater for the higher aspect ratio fibres. Figures 5.11 and 5.12 indicate that the extensional viscosity of fibre suspensions is dependent on the fibre aspect ratio, similar to the shear viscosity. It is well-established that the transient extensional viscosity, η_E^+ of some liquids with extensional behaviour, can be orders of magnitude larger than the corresponding shear viscosity (Jaishankar et al., 2015). By comparing the apparent extensional viscosity of 5.0 wt.% fibre suspensions in Figure 5.11 to the shear viscosity in Figure 4.3, the fibre suspensions can be said to have relatively greater extensional viscosity compared to the shear viscosity. Trouton ratio, Tr, as shown in Equation 5.7, is a ratio of the transient extensional viscosity to the zero-shear viscosity, μ_0 and Tr is constant at 3 for Newtonian fluids.

$$Tr = \eta_E^+ / \mu_0 \qquad \text{Equation 5.7}$$

In the case of fibre suspensions, the Tr is not constant and at every Hencky strain, the Tr is always more than 8. It shows the dominance of extensional resistance over shear resistance in a flow consists of both shear and extensional flow fields.

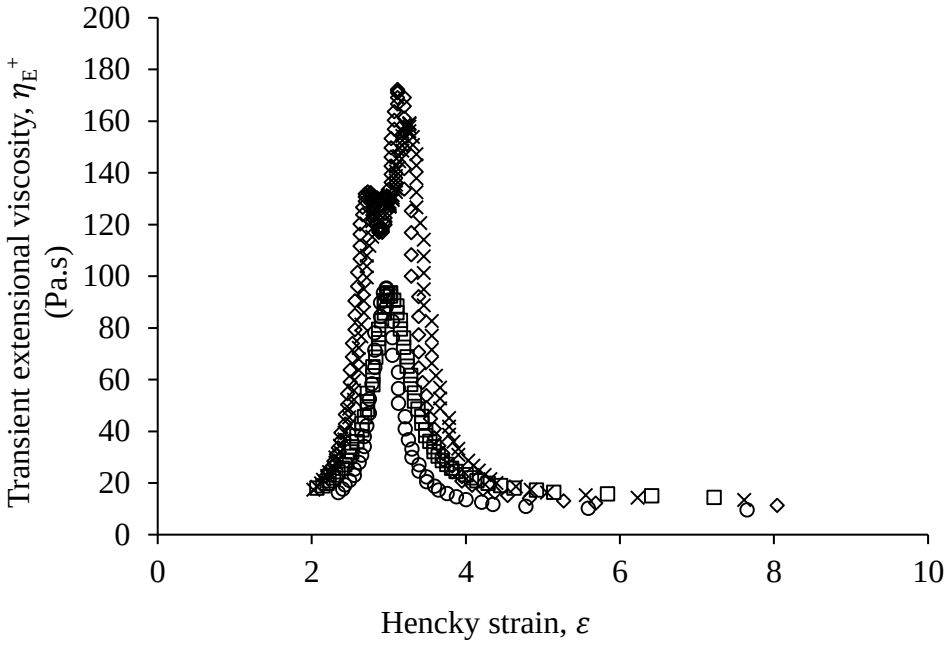

Figure 5.11 Transient extensional viscosity of different 5.0 wt.% fibre suspensions obtained by using Equation 5.7. (○) AF 400-30 with aspect ratio 2 – 3, (□) WF 101 with aspect ratio 2 – 3, (◊) WF 600 with aspect ratio 8 – 10 and (×) citrus fibre with aspect ratio 8 – 10.

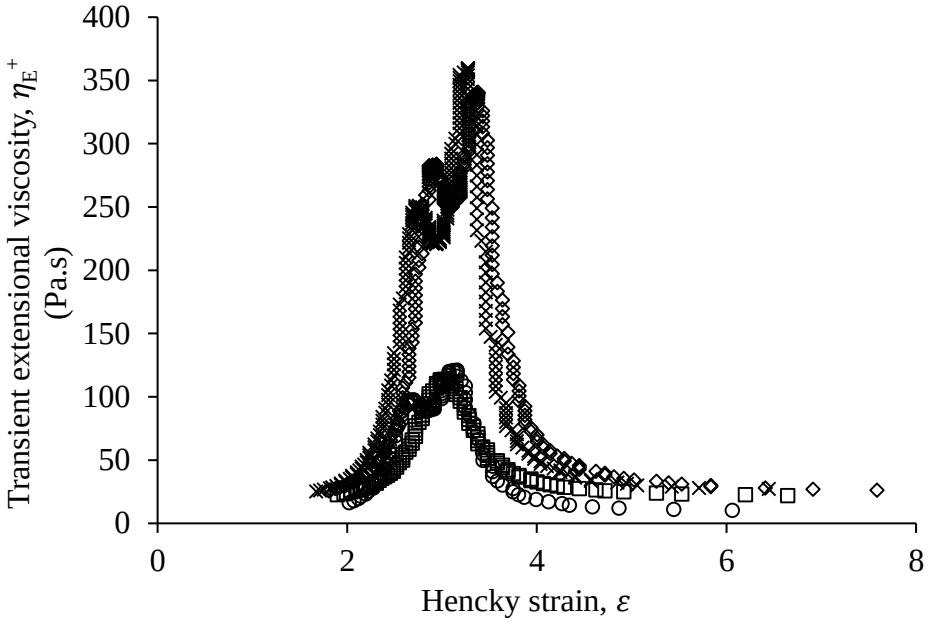

Figure 5.12 Transient extensional viscosity of different 7.0 wt.% fibre suspensions obtained by using Equation 5.7. (○) AF 400-30 with aspect ratio 2 – 3, (□) WF 101 with aspect ratio 2 – 3, (◊) WF 600 with aspect ratio 8 – 10 and (×) citrus fibre with aspect ratio 8 – 10.

5.3 Conclusions

- The small-amplitude oscillatory test showed that fibre suspensions behave as viscoelastic liquids. The elastic modulus, *G'* of the fibre suspensions represents the solid-like behaviour. It remained fairly constant as the temperature was varied.
- The capillary breakup tests performed on a portable extensional rheometer confirmed that fibre suspensions exhibit extensional behaviour, based on the exponential filament diameter profiles.
- Relaxation time, τ_r and transient extensional viscosity, η_E^+ were calculated to quantitatively study the extensional rheology of fibre suspensions. Both properties were dependent on the fibre aspect ratio and fibre fraction, with greater τ and η_E^+ for the higher aspect ratio fibres and greater fibre fraction.
- The transient extensional viscosity, η_E^+ of fibre suspensions, was relatively greater than its corresponding shear viscosity.

References

Anna, S. L., & McKinley, G. H. (2001). Elasto-capillary thinning and breakup of model elastic liquids. *Journal of Rheology, 45*(1), 115-138.

Bazilevsky, A., Entov, V., & Rozhkov, A. (1990). Liquid filament microrheometer and some of its applications. *Paper presented at the Third European Rheology Conference and Golden Jubilee Meeting of the British Society of Rheology*.

Chindam, C., Lakhtakia, A., Brown, N. R., Orfali, W., & Awadelkarim, O. O. (2014). Frequency-and temperature-dependent storage and loss moduli of microfibrous thin films of Parylene C. *Materials Letters, 116*, 296-298.

Damani, R., Powell, R. L., & Hagen, N. (1993). Viscoelastic characterization of medium consistency pulp suspensions. *The Canadian Journal of Chemical Engineering, 71*(5), 676-684.

Eastman, J., Goodwin, J., & Howe, A. (2000). Extensional viscosity of aqueous solutions of SDS and PVP measured on the rheometrics RFX. *Colloids and Surfaces A: Physicochemical and Engineering Aspects, 161*(2), 329-338.

Entov, V., & Hinch, E. (1997). Effect of a spectrum of relaxation times on the capillary thinning of a filament of elastic liquid. *Journal of Non-Newtonian Fluid Mechanics, 72*(1), 31-53.

Guo, R., Azaiez, J., & Bellehumeur, C. (2005). Rheology of fiber filled polymer melts: Role of fiber-fiber interactions and polymer-fiber coupling. *Polymer Engineering & Science, 45*(3), 385-399.

Hallmark, B., Bryan, M., Bosson, E., Butler, S., Hoier, T., Magens, O., . . . Wibberley, S. (2016). A portable and affordable extensional rheometer for field testing. *Measurement Science and Technology, 27*(12), 125302.

Jaishankar, A., Wee, M., Matia-Merino, L., Goh, K. K., & McKinley, G. H. (2015). Probing hydrogen bond interactions in a shear thickening polysaccharide using nonlinear shear and extensional rheology. *Carbohydrate Polymers, 123*, 136-145.

Kotsilkova, R. (1992). Dynamic rheological properties of glass fiber suspensions. *Theoretical and Applied Rheology*, 856-858.

Moberg, T., Tang, H., Zhou, Q., & Rigdahl, M. (2016). Preparation and viscoelastic properties of composite fibres containing cellulose nanofibrils. *Journal of Nanomaterials, 2016*, 30.

Piermaría, J., Bengoechea, C., Abraham, A. G., & Guerrero, A. (2016). Shear and extensional properties of kefiran. *Carbohydrate Polymers, 152*, 97-104.

Pothan, L. A., Oommen, Z., & Thomas, S. (2003). Dynamic mechanical analysis of banana fiber reinforced polyester composites. *Composites Science and Technology, 63*(2), 283-293.

Rodd, L. E., Scott, T. P., Cooper-White, J. J., & McKinley, G. H. (2004). Capillary break-up rheometry of low-viscosity elastic fluids. *Applied Rheology* HML Report 04-P-04.

Sachdev, S., Muralidharan, A., & Boukany, P. E. (2016). Molecular processes leading to "necking" in extensional flow of polymer solutions: Using microfluidics and single DNA imaging. *Macromolecules, 49*(24), 9578-9585.

Xu, J., Chatterjee, S., Koelling, K. W., Wang, Y., & Bechtel, S. E. (2005). Shear and extensional rheology of carbon nanofiber suspensions. *Rheologica Acta, 44*(6), 537-562.

Chapter 6 Two-fluid atomization of fibre suspensions

Chapter 6 describes the atomization behaviour and performance when using a two-fluid nozzle. Previous Chapters 4 and 5 have discussed the shear and extensional rheology of fibre suspensions, respectively. The rheology of the fibre suspensions plays an important role in the atomization of the fibre suspensions, as will be explained in this chapter.

Section 6.1 presents the atomization parameters used throughout the atomization experiments. Section 6.2 briefly justifies the selection of a two-fluid nozzle as the main nozzle used to atomize the fibre suspensions and Section 6.3 shows the atomization pattern of the non-Newtonian viscoelastic fibre suspensions when atomized using the two-fluid nozzle. Section 6.4 discusses in detail the droplet size analysis of the fibre suspensions based on experimental observations while Section 6.5 validates the droplet sizes using theoretical predictions. Section 6.6 shows the morphology of the droplets with fibres inside the droplets. Lastly, Sections 6.7 and 6.8 both examine the effect on the atomization performance when some of the atomization parameters were changed. These include the increase in feed temperature, the addition of an ultrasonic mechanism to the two-fluid nozzle and the change in the inlet feed rates.

6.1 Atomization parameters

The experiments were mainly conducted at a constant liquid flow rate, Q_L of 90 mL/min, which produced a velocity inside the liquid orifice, U_L of 0.85 m/s. The atomizing air velocities, U_A through the annular orifice were varied between 40 m/s and 240 m/s. The corresponding liquid Reynolds number, Re_L as in Equation 6.1, was maintained constant, while the Weber number, We as in Equation 6.2 was varied between 4.5×10^4 and 1.2×10^6.

$$Re_L = \rho_L U_L D_J/\mu = \frac{\rho_L {U_L}^{2-n} {D_J}^n}{K\left(\frac{3n+1}{4n}\right)^n 8^{n-1}} \quad \text{Equation 6.1}$$

$$We = \rho_L (U_L - U_G)^2 D_J/\sigma \quad \text{Equation 6.2}$$

where ρ_L (kg/m^3), μ (Pa.s), σ (N/m) are the density, shear viscosity and surface tension of the fibre suspensions, respectively. D_J (mm) is the jet diameter and U_L (m/s) and U_G (m/s) are the velocity of the fibre suspensions and atomizing air, respectively. The final form of Re_L in Equation 6.1 shows the modified Reynolds number for non-Newtonian fluids.

The characteristic shear viscosity used in calculating the Re_L was chosen based on the wall shear rate, $\dot{\gamma}$ (s^{-1}) experienced inside the orifice. For non-Newtonian liquids with a power-law index, n, such as fibre suspensions, the shear rate is given in Equation 6.3, where Q_L (mL/min) is the liquid flow rate (Fredrickson, 1964).

$$\dot{\gamma} = (3n + 1/n)\left(Q_L/\pi\left(D_J/2\right)^3\right) \qquad \text{Equation 6.3}$$

The calculated shear viscosity based on the instantaneous wall shear rate should only be taken as an approximation. Based on Equation 6.3, the shear rate inside the liquid orifice was calculated to be approximately 5000 s^{-1} for all fibre suspensions. This shear rate inside the liquid orifice corresponds to the Re_L of between 4 and 5 depending on the type of fibre suspensions. Strain or extension rates inside the liquid orifice can be estimated based on Equation 6.4 (Lindstedt et al., 2005), where H (m) is the orifice length. Based on Equation 6.4, the bulk strain rate inside the orifice was calculated to be approximately 900 s^{-1}.

$$S_b = 2\,(U_L/H) \qquad \text{Equation 6.4}$$

The calculated value of strain rate can only be referred to as bulk strain rate, as it uses the bulk nozzle exit velocity of the liquid while in reality, the strain or extension of liquid mainly occurs outside of the orifice when the high atomizing air velocity stretches the liquids or ligaments. Similarly, the predicted shear rate, based on Equation 6.3, is true only inside the nozzle orifice. During the atomization process, when a high atomizing air velocity impacts the surface of the liquid jet, it is certain that the actual shear rate during the atomization is far greater than can be predicted by Equation 6.3. Hede et al. (2008) proposed a relationship, as shown in Equation 6.5, to calculate the shear rate during the atomization after the liquid exits the nozzle orifice, with an assumption that momentum is transferred between the liquid feed and atomizing air in the mixing zone, and both leave the atomization zone at a constant average velocity, U_{av}. It means that the relationship by Hede et al. (2008) predicts the maximum allowable shear rate during the atomization at a specific air velocity, and this prediction is true right at the nozzle exit only, when the liquid

is first being impacted by the high air velocity. The shear rate is expected to reduce further downstream from the nozzle exit.

$$\dot{\gamma} = 2\left((U_{av} - U_L)/D_J\right) \qquad \text{Equation 6.5}$$

Based on Equation 6.5, at an atomizing air velocity of 40 m/s, the estimated shear rate during the atomization is approximately 25 000 s^{-1}, while at an atomizing air velocity of 150 m/s, the shear rate exceeds 50 000 s^{-1}.

The shear and strain rates based on Equations 6.3-6.5 were calculated as approximations. The actual shear and strain rates can be predicted accurately by using a high-speed imaging technique, by observing the micro shearing and stretching of the liquids and ligaments. As explained in Chapter 3, Section 3.5, a strobe-light technique was used throughout the atomization experiments with the purpose to freeze the ligaments and droplets, to clearly observe the atomization patterns, shape and size of the droplets. The reason for not utilizing the high-speed camera technique is because of the limitation of that technique at very high air velocities. By applying an air velocity of more than 150 m/s, a high-speed camera with at least 15 000 fps is needed to capture the atomization patterns, and this was not available. The use of the strobe-light technique produced adequate images of the atomization patterns and droplets, but, the velocity data was missing. The velocity data is useful to accurately predict the shear and strain rates during the atomization. The main purpose of Chapter 6 is to show the atomization patterns of fibre suspensions and how they proceed as the air velocity was increased. It is also important to differentiate the atomization mechanisms between the liquids with extensional resistance and the liquids with only shear resistance. Based on the broad purposes of Chapter 6, the actual shear and strain rates during the atomization may not be necessary to know at this stage, instead, the Weber number, We which represents the disruptive forces contributed by the high atomizing air velocity, is the main parameter to be stated in characterizing and explaining the atomization patterns.

6.2 Choice of the two-fluid nozzle

At the very high shear rates encountered at the nozzle of more than 10 000 s^{-1}, the shear viscosities of 5.0 wt.% fibre suspensions are reduced. This is shown in Section 4.2.1, Figure 4.11, where the viscosity of the fibre suspensions was measured using a capillary

viscometer. Due to pumping limitation, only data up to 20 000 s^{-1} is shown in Figure 4.11. As shown in Figure 4.11, the viscosity of each fibre suspension can be said to approximately reach a plateau limitation at a shear rate above 30 000 s^{-1}. Therefore, the shear thinning of the fibre suspensions was finished such that increasing the shear rate above a certain value would not reduce the shear viscosity further. Figure 4.11 subtly shows that the use of a conventional pressure nozzle to atomize the fibre suspensions may not be efficient. The principal of the pressure nozzle is the conversion of pressure energy within the liquid into kinetic energy by applying high pumping pressure. As shown in Figure 4.11, increasing the pumping energy, and hence increase the bulk flow rate through the nozzle and the shear rates after a certain point, will not result in any significant decrease in shear viscosity. The rheology study shows that fibre suspensions exhibit extensional resistance along with the shear resistance. The two-fluid nozzle was chosen due to its ability to supply high atomizing air velocity to stretch the ligaments of the fibre suspensions and thus overcome the extensional resistance, a mechanism that is not available in the single fluid pressure nozzle and rotary atomizer.

6.3 Breakup visualization

The atomization behaviour patterns and features captured during the atomization experiments give an insight into the fluid breakup mechanisms involved during the atomization of fibre suspensions by high atomizing air velocity. The main purpose is to compare the breakup features between Newtonian liquid and shear thinning fibre suspensions with extensional properties and to observe the changes induced by the extensional properties of the fibre suspensions.

6.3.1 Effect of shear rheology

Figure 6.1 contains images showing the breakup of concentrated apple juice, where Figure 6.2 shows the breakup of fibre suspensions. The atomization patterns shown in Figure 6.2 indicate the atomization appearances of all fibre suspensions looked very similar. The atomizing air velocity applied were all the same, approximately 40 m/s. Upon applying 40 m/s air velocity to the fibre suspensions, all fibre suspensions broke up and displayed a rope-like ligament pattern. The liquid streams or ligaments remained intact and underwent

erratic excursions away from the centreline. This breakup pattern is very similar to a Newtonian liquid breakup shown in Figure 6.1, specifically the concentrated apple juice without fibres. The concentrated apple juice exhibits shear resistance with no extensional resistance to breakup. This suggests the dominant resistance during atomization at 40 m/s atomizing air velocity was the shear viscosity of the fibre suspensions. At 40 m/s atomizing air velocity, the shear rate is more than 20 000 s^{-1}, as suggested by Hede et al. (2008). At this shear rate, the difference in the shear viscosity of the fibre suspensions with different aspect ratios is insignificant. This situation resulted in the very similar breakup pattern.

Other than the similar breakup patterns between 5.0 wt.% AF 400-30, 5.0 wt.% WF 101, 5.0 wt.% WF 600 and 5.0 wt.% citrus fibre suspensions, the appearances of all sprays were marked by an extremely short jet breakup length. The images in Figure 6.2 were taken at a position 10 mm below the nozzle, which means all fibre suspensions achieved a breakup length of, at most, 10 mm. Figure 6.3 shows the full spray images of 5.0 wt.% AF 400-30, 5.0 wt.% WF 101, 5.0 wt.% WF 600 and 5.0 wt.% citrus fibre suspensions. The sprays were captured with a DSLR camera. The spray angle of all 5.0 wt.% fibre suspensions was at least 40°, the specified cone angle of the nozzle. This indicates that a fully developed spray was produced for all types of fibre suspensions.

As shown in Figure 6.1, the breakup of Newtonian apple juice seems more vigorous and well-dispersed, with some observable droplets. Figure 6.2 shows that the breakup of 5.0 wt.% fibre suspensions was less vigorous with significantly thick unstable ligaments. This is due to the significantly greater shear viscosity of 5.0 wt.% fibre suspensions compared to the lower shear viscosity of apple juice. If the 5.0 wt.% fibre suspensions have negligible extensional resistance like Newtonian liquids such as water and the concentrated apple juice, increasing the atomizing air velocity will disintegrate the ligaments by collapsing the ligaments into a multiplicity of small droplets immediately downstream of the atomizer (Chigier & Farago, 1992). This is because a greater air velocity provides a greater shear rate to the fibre suspensions. At that high-velocity high shear rate, the shear viscosity of the fibre suspensions is lower and allows the formation of droplets immediately downstream from the atomizer. However, as shown in the rheology study, the fibre suspensions exhibited extensional resistance. Hence, although the fibre suspensions have a low shear viscosity, the extensional resistance can prevent the formation of complete atomization immediately downstream from the atomizer.

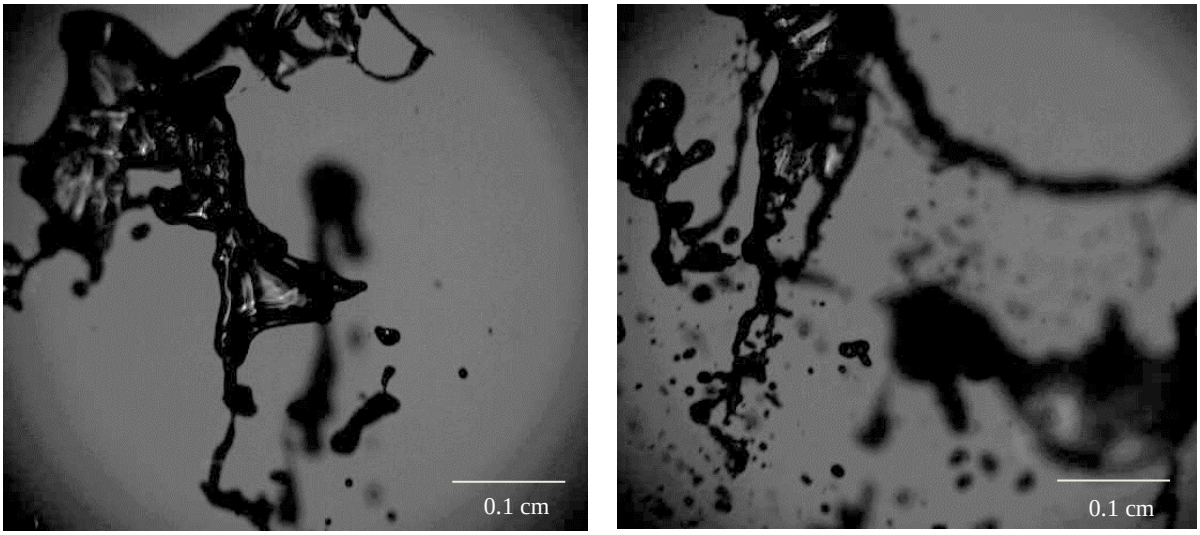

Figure 6.1 Photographs of the breakup of Newtonian concentrated apple juice, at an atomizing air velocity of 40 m/s. Images were captured at a position 10 mm below the nozzle exit.

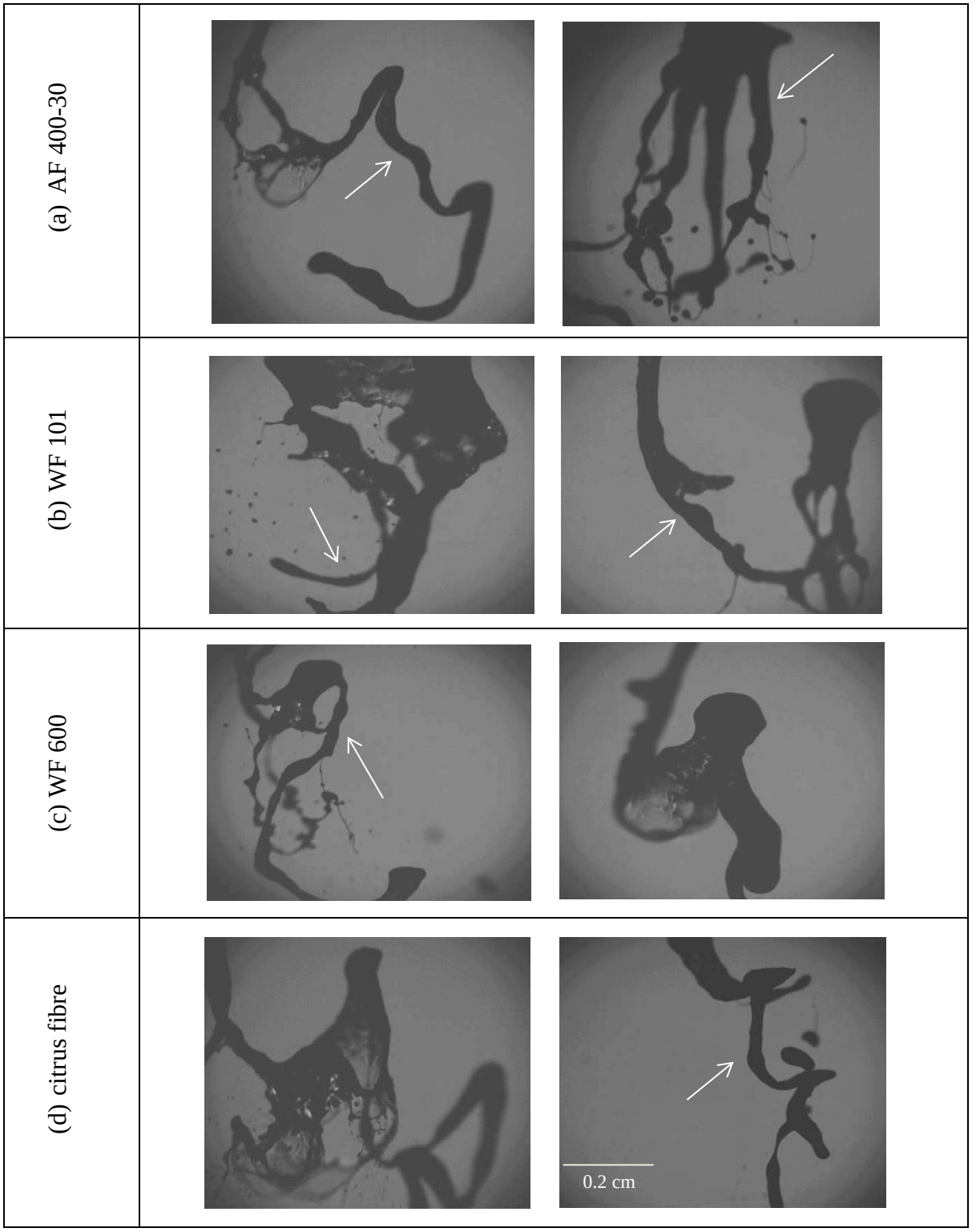

Figure 6.2 Photographs of the breakup of 5.0 wt.% fibre suspensions at an atomizing air velocity of 40 m/s. (a) AF 400-30 (b) WF 101 (c) WF 600 and (d) citrus fibre. Images were captured at a position 10 mm below the nozzle exit. Ligaments are pointed out by white arrows.

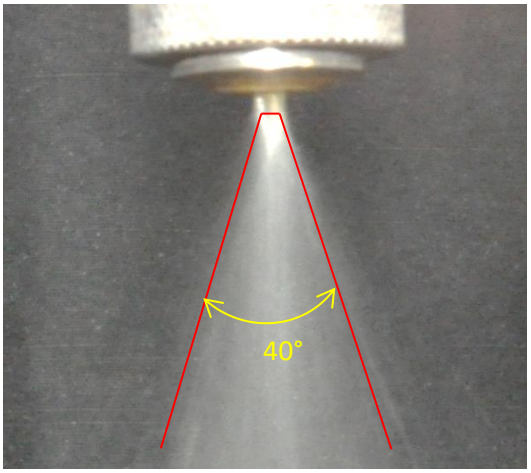

(a) AF 400-30

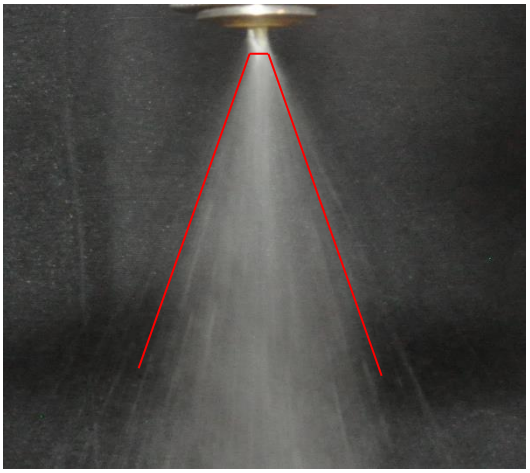

(b) WF 101

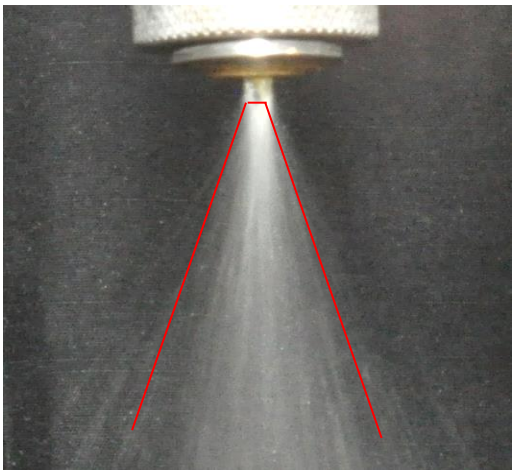

(c) WF 600

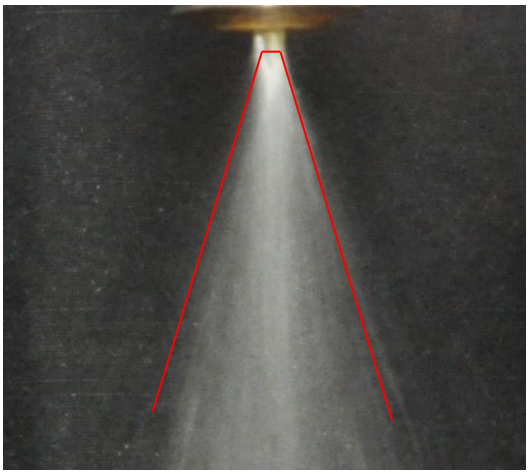

(d) citrus fibre

Figure 6.3 Full spray images showing the spray angle for each 5.0 wt.% fibre suspensions (a) AF 400-30 (b) WF 101 (c) WF 600 and (d) citrus fibre. The spray angles for all fibre suspensions appeared to be at least 40°.

Concentrated apple juice is a simple Newtonian liquid with insignificant extensional properties (the extensional viscosity is approximately three times the shear viscosity). Increasing the atomizing air velocity to approximately 60 m/s directly disintegrated the ligaments of Newtonian apple juice by collapsing the ligaments into a multiplicity of small droplets immediately downstream of the atomizer. This is shown in Figure 6.4. The greater air velocity provided a greater shear rate to the liquid that produced the formation of droplets immediately downstream from the atomizer. This behaviour was not observed during the atomization of fibre suspensions at a greater air velocity above 40 m/s.

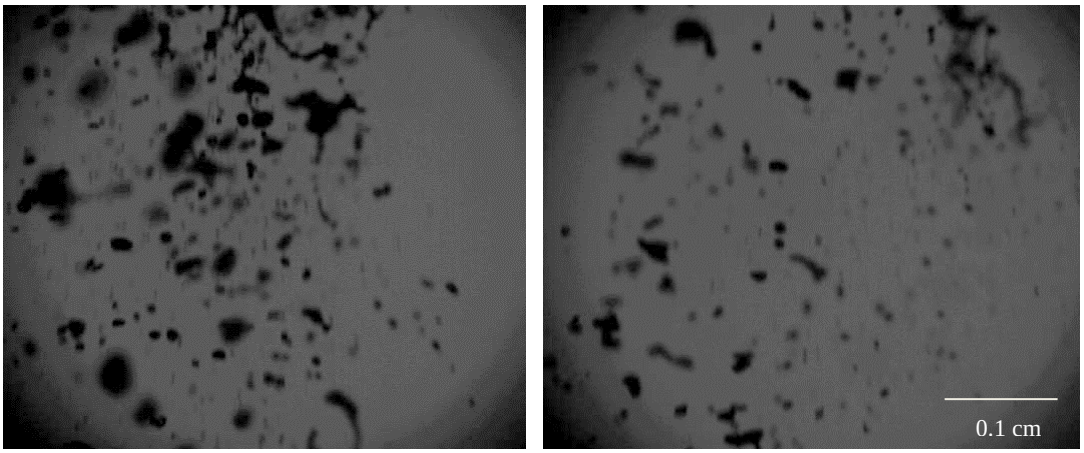

Figure 6.4 Photographs of the breakup of Newtonian concentrated apple juice, at an atomizing air velocity of 60 m/s. Images were captured at a position 10 mm below the nozzle exit.

6.3.2 Effect of extensional rheology

Unlike the breakup pattern dominated by shear viscosity, as shown in Figure 6.2, the pattern with extensional resistance dominance is very different. The latter usually incorporates a pattern where the liquid stream is well-dispersed and does not remain intact. As shown in Figure 6.5, increasing the atomizing air velocity to 150 m/s did not result in the dispersion of ligaments into droplets right after the nozzle as in the case of Newtonian liquid atomization shown in Figure 6.4. Instead, the 5.0 wt.% AF 400-30, 5.0 wt.% WF 101, 5.0 wt.% WF 600 and 5.0 wt.% citrus fibre suspensions, which exhibited extensional properties, displayed a pattern of filamentary structures, connecting successive droplets

together. The presence of the filaments prevented the pinch-off of droplets between each other. A clear illustration of the situation is shown in Figure 6.5. Red circles in Figure 6.5 highlight the droplets, while the yellow arrows point to the pinch-off or necking region of a filament. Due to the extensional properties of fibre suspensions, as evidenced from the rheology study in Chapter 5, Section 5.2.1, the elastic filament induced additional tensile stresses in their cross-sections at the pinch-off points, this increases its stability against capillary forces and, thus, inhibited the breakup. This means the breakup of the filaments was delayed and thus affected the final droplet formation. This breakup pattern is very similar to polymer solutions which also exhibit extensional properties (Chao et al., 1984; Hoyt et al., 1974).

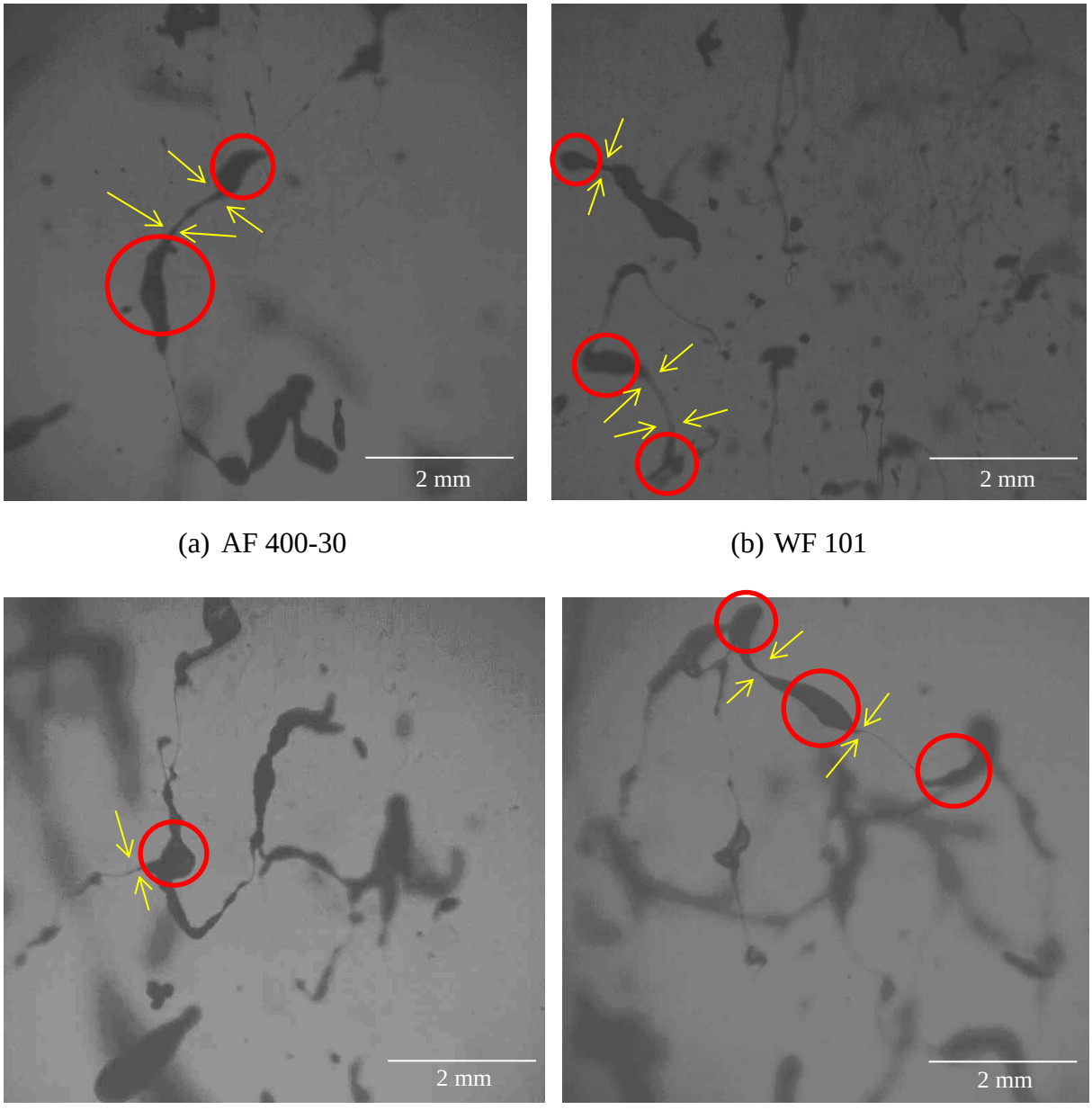

(a) AF 400-30 (b) WF 101

(c) WF 600 (d) citrus fibre

Figure 6.5 Photographs of the breakup of 5.0 wt.% fibre suspensions at an atomizing air velocity of 150 m/s. (a) AF 400-30 (b) WF 101 (c) WF 600 and (d) citrus fibre. Images were captured at a position 10 mm below the nozzle exit.

Unlike extensional liquids, a Newtonian liquid breakup does not show the presence of stretched filaments (Aliseda et al., 2008; Bailardi et al., 2010; Ochowiak et al., 2017). This is evident during the atomization of concentrated apple juice, see Figure 6.4. The Newtonian breakup also had a high stretching rate at high atomizing air velocity. However, the stretched ligaments thinned down very quickly as a result of the capillary force and were not resisted by the extensional resistance. This is clearly portrayed by the difference in the filament thinning profile between Newtonian liquid and fibre suspensions as shown in Chapter 5, Section 5.2.1, Figure 5.5. While the Newtonian liquid thinned linearly, the filament thinning of 5.0 wt.% AF 400-30, 5.0 wt.% WF 101, 5.0 wt.% WF 600 and 5.0 wt.% citrus fibre suspensions occurred exponentially. Consequently, the filament of the 5.0 wt.% fibre suspensions broke up later compared to the Newtonian liquid. Based on Section 5.2.1, Newtonian liquids such as water or concentrated apple juice will undergo filament thinning that breaks during the visco-capillary regime, while the 5.0 wt.% fibre suspensions break up during the elasto-capillary regime.

Marmottant and Villermaux (2004) successfully explained the key fluid mechanical features of a spray. By using a two-fluid nozzle and working with a Newtonian liquid, the overall breakup process can be described by a sequence of instabilities. The liquid jet first experiences a high shear rate at its surface, induced by the surrounding high-velocity flow of air. This leads to the generation of waves on the jet surface. As the waves grow, the acceleration of the high-velocity air elongates ligaments of the liquid into the air stream. These stretched ligaments thin down in the neck region and ultimately detach from the jet. After this, the detached ligaments fragment and stabilize into smaller droplets. Based on Figure 6.5, the modification to the breakup pattern of fibre suspensions as compared to a Newtonian breakup can be said to occur mainly when the fluid element reached a large strain and rapid deformation rate that was generated in the final breakup and pinch off stages. Based on the mechanisms worked out by Marmottant and Villermaux (2004), it is believed that in the case of the fibre suspensions, shear resistance first controls the early breakup stage while extensional resistance controls the final breakup stage. At first, the calm liquid jet of fibre suspensions was disturbed to create waves or instabilities on the liquid surface. These waves and instabilities are not generated through pulling or stretching of the thick liquid jet by the surrounding atomizing air. Rather, the air sheared the outer jet surface which then generated multiple thin liquid elements. This is referred to as ligaments, as shown in Figure 6.2. At this stage, the shear viscosity opposed the destabilization of the

jet or formation of waves and instabilities on the jet surface. Only after the formation of ligaments did the air act to pull or stretch the multiple thin liquid elements or ligaments to further break the ligaments and disperse them into a multiplicity of smaller droplets. At this stage, the extensional viscosity resists the fragmentation of the ligaments into smaller droplets by inducing additional tensile stresses or resistance at the cross-sections during the pinch-off of ligaments or droplets. This is what is seen as filaments in Figure 6.5.

Based on Figure 6.5, all the 5.0 wt.% fibre suspensions showed a similar atomization pattern where the droplets were connected to each other by filaments. The filaments were seen to undergo a large stretching motion before they broke up, resulting in long threads of liquid attached to droplets. Increasing the atomizing air velocity, and thus the extensional rate, was expected to break the filaments faster compared to at 150 m/s atomizing air velocity. Atomization or liquid breakup is a function of both disruptive and stabilizing forces and occurs when the former force overcomes the latter. Increasing the atomizing air velocity increases the disruptive forces while the stabilizing forces remained the same. Figure 6.6 shows the atomization behaviour at the greater atomizing air velocity of 195 m/s. The quality of the images was reduced due to the higher atomizing air velocity. A mere observation of the atomization images at a greater atomizing air velocity of 195 m/s indicated that more filaments had already broken up at a position 10 mm below the nozzle. As shown in Figure 6.6, more droplets appeared to have pinched off and broken from the filaments. At the same time, some unbroken filaments still existed along with the pinched off droplets. This might be due to the non-homogenous breakup nature that occurred during the atomization. For example, not all the volume of the liquid jet that exited the nozzle underwent similar atomization mechanisms at a particular time. This also explains the differences in the thickness between the ligaments of a similar fibre suspension and the droplet size distribution that will be explained in a later section.

It is difficult to evaluate the efficiency of the atomization based on the images of the ligaments and filaments only taken at a position immediately after the nozzle exit. The quality of the images was also reduced by the higher atomizing air velocity. The observation and conclusions made, based on Figures 6.2, 6.5 and 6.6, are also inconclusive. But, these images are still important in highlighting the difference in the atomization pattern between the Newtonian solution and liquids with extensional properties, such as fibre suspensions. The unique atomization pattern, which consisted of filamentary structures, were due to the extensional properties that resisted the stretching of the ligaments. To better

understand the effect of extensional resistance on atomization, atomization images were captured at a position 50 mm below the nozzle. This was carried out to see the effect of extensional resistance on the final droplet formation. Figure 6.7 shows the droplet formation of 5.0 wt.% AF 400-30, 5.0 wt.% WF 101, 5.0 wt.% WF 600 and 5.0 wt.% citrus fibre suspensions at an atomizing air velocity of 150 m/s. The images were converted into binary images to ease the observation and analysis for droplet size measurements.

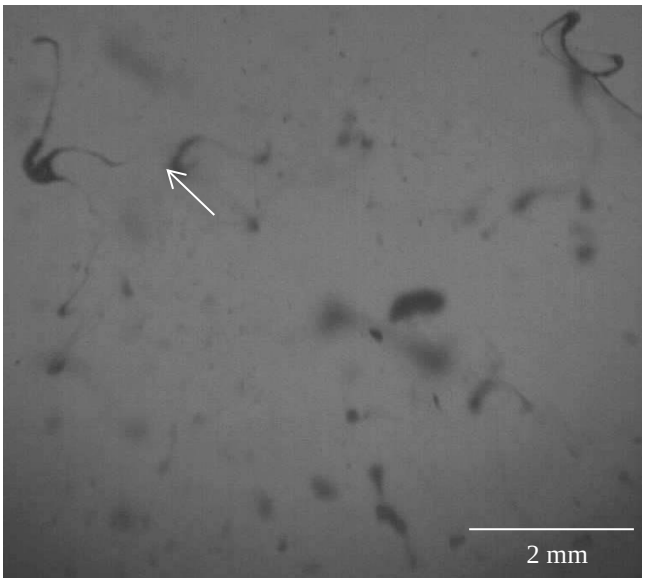

(a) AF 400-30

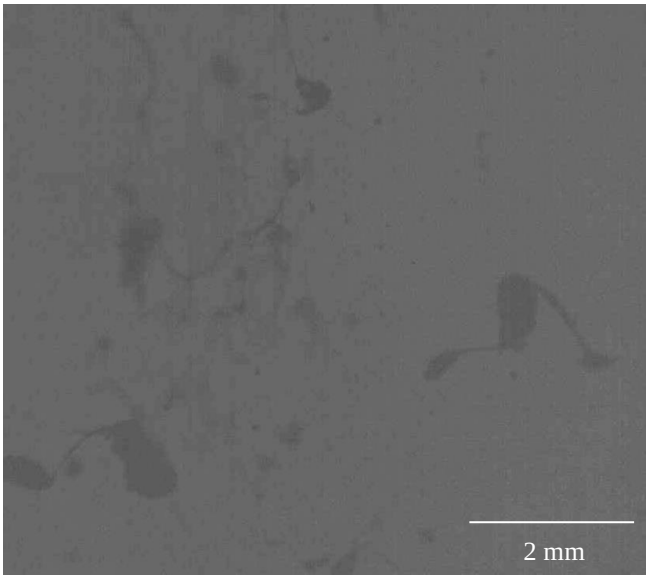

(b) WF 101

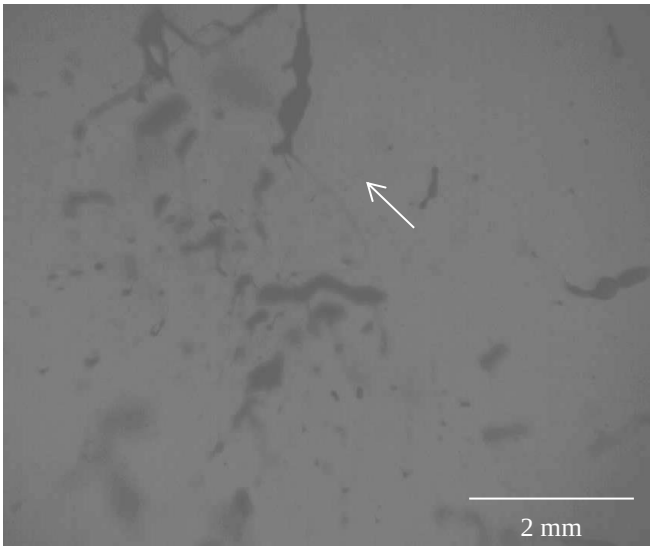

(c) WF 600

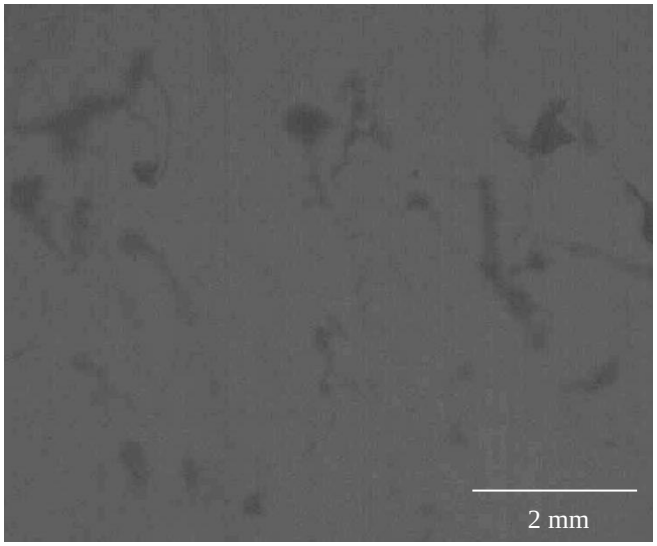

(d) citrus fibre

Figure 6.6 Photographs of the breakup of 5.0 wt.% fibre suspensions at an atomizing air velocity of 195 m/s. (a) AF 400-30 (b) WF 101 (c) WF 600 and (d) citrus fibre. Images were captured at a position 10 mm below the nozzle exit. White arrows are pointed out at droplets which one end was suggested to have visibly pinched off from the filaments.

Figure 6.7 shows that the droplet formation of liquid with extensional resistance was very different from Newtonian droplets. Many previous works have shown the spherical and symmetrical droplets of Newtonian liquids (Verma & Singh, 2015). In contrast, the atomization of fibre suspensions, which exhibit extensional properties, results in the formation of non-spherical and non-symmetrical droplets at a position 50 mm below the nozzle. Specifically, the droplets were characterised by the presence of a bridge between them. The existence of bridges, unsymmetrical droplets and non-spherical droplets were all the consequences of a delay in the filament breakup at position 10 mm below the nozzle. Based on the Newtonian breakup, the detachment of ligaments from the liquid jet is ultimately followed by the fragmentation of the ligaments into a cascade of droplets. Beyond that point, usually, the droplets will be dispersed into smaller droplets due to the equilibrium effect of surface tension (Lefebvre, 1988). However, in the case of 5.0 wt.% fibre suspensions, the breakup of filamentary structures was delayed, see Figure 6.5. It can be observed that successive droplets are connected, or chunk of ligaments stay together. This prevents the fragmentation of the ligaments into individual droplets. This later inhibits the stabilization of the droplets into equilibrium size and shape at a position far below the nozzle, such as at a position 50 mm below the nozzle. Droplets in Figure 6.7 were characterised by the non-spherical shape and the presence of bridges. This must be due to the insufficient time for the droplets to reach the equilibrium condition because of the delay in the filament breakup. It is also possible that the strain rates or disruptive forces applied were not enough to break the filaments at a position 10 mm below the nozzle. As a result, some droplets at a position 50 mm below the nozzle were still connected by a bridge or filaments.

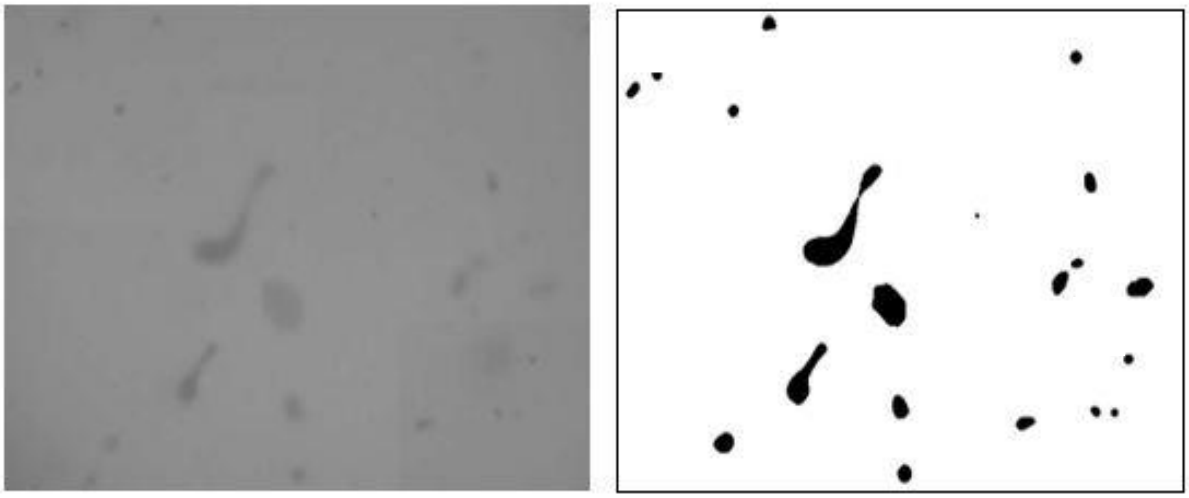

(a) AF 400-30

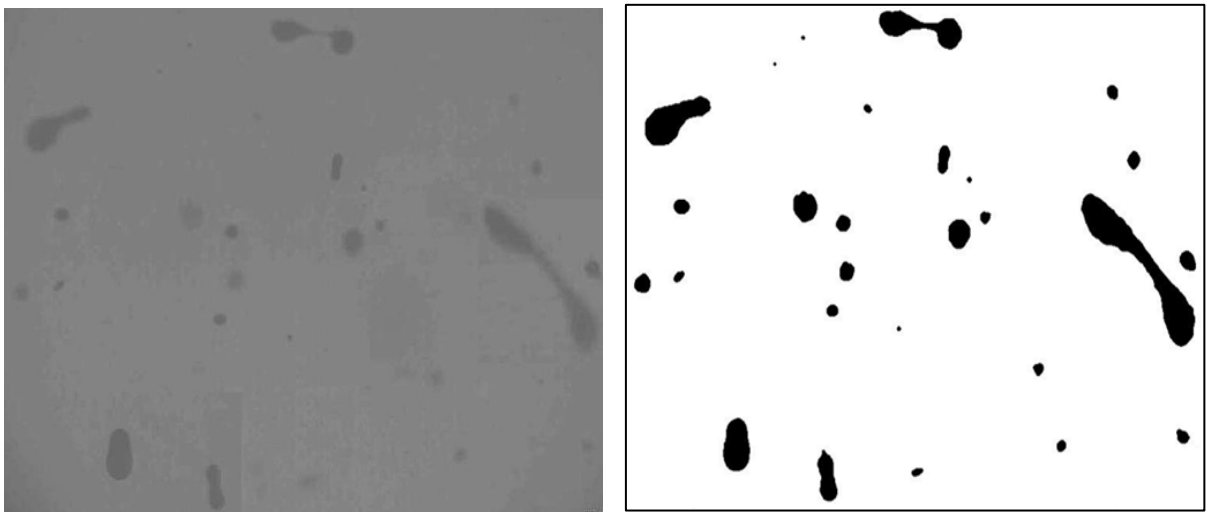

(b) WF 101

Continue →

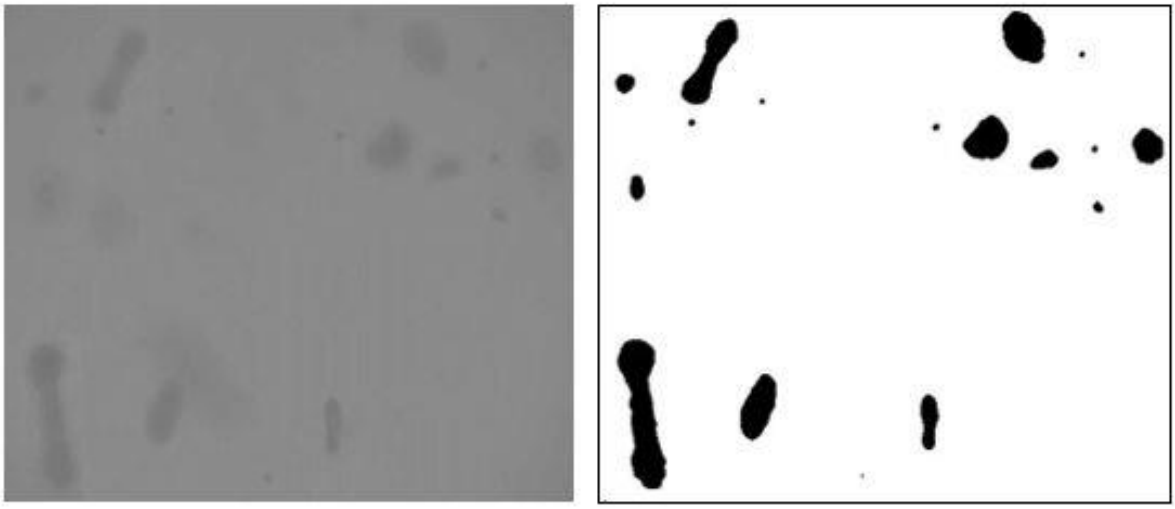

(c) WF 600

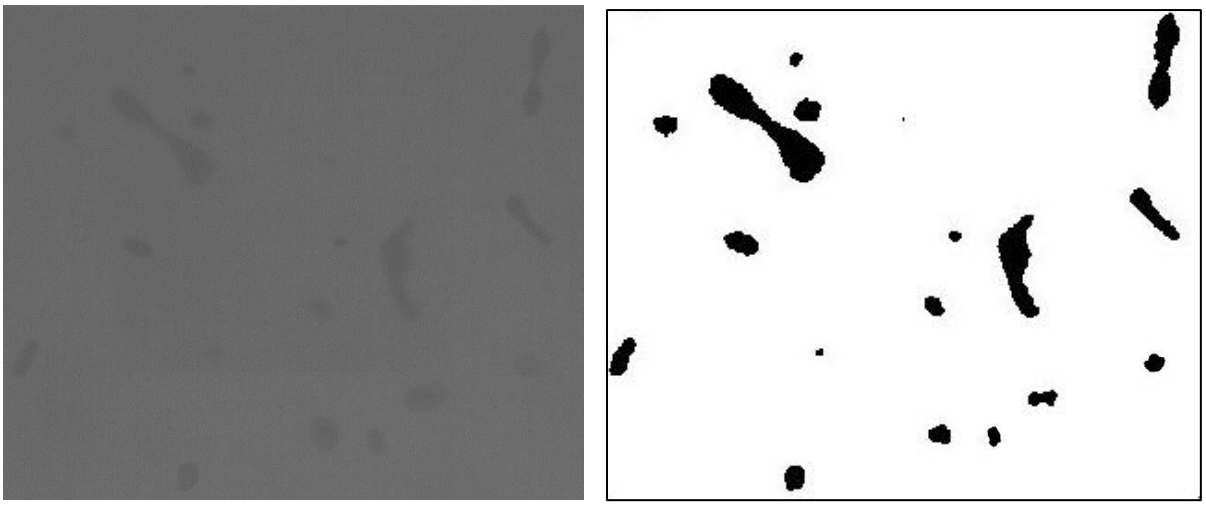

(d) citrus fibre

Figure 6.7 Photographs of the droplets of 5.0 wt.% fibre suspensions at an atomizing ai velocity of 150 m/s. (a) AF 400-30 (b) WF 101 (c) WF 600 and (d) citrus fibre. Images were captured at a position 50 mm below the nozzle exit. Each image was converted into a binary image for clearer observation and easier analysis.

As mentioned earlier, increasing the atomizing air velocity provided enough force to stretch and break the filaments shown in Figure 6.5. The breakup of the filaments then resulted in a better droplet formation at a position 50 mm below the nozzle. This is evident in Figure 6.8. The atomizing air velocity was increased to 195 m/s. Figure 6.8 shows a more spherical and symmetrical final droplets formation. The presence of bridges between droplets due to the insufficient forces to stretch and break the filaments beforehand, was also reduced. The breakup of filaments or pinch-off of droplets at a position 10 mm below the nozzle at a much higher atomizing air velocity provided enough time for all droplets to stabilize into symmetrical spherical droplets. Large unsymmetrical droplets were also able to disintegrate and stabilize into smaller droplets due to the surface tension effect.

For all fibre suspensions, the presence of bridges between droplets was absent when the atomizing air velocity was increased to 195 m/s. A closer observation on Figure 6.8 indicates the droplets of 5.0 wt.% AF 400-30 and 5.0 wt.% WF 101 fibre suspensions were smaller, more spherical and more symmetrical compared to the droplets of 5.0 wt.% WF 600 and 5.0 wt.% citrus fibre suspensions when the atomization occurred at the much greater atomizing air velocity of 195 m/s. This might be due to the fibres' aspect ratio. Based on the extensional rheology study in Chapter 5, the 5.0 wt.% WF 600 and 5.0 wt.% citrus fibre suspensions exhibited greater extensional viscosity during stretching due to the greater fibres' aspect ratio. As a consequence, the atomization of these fibre suspensions is predicted to produce larger droplets. The deduction, made solely based on the observation from Figure 6.8, is not compelling and robust. Furthermore, other images in Figures 6.5 – 6.7 do not show any clear, apparent and distinct differences between the atomization pattern and droplets of the lower aspect ratio fibre suspensions and higher aspect ratio fibre suspensions. Thus, droplet size analysis was used to look at the effect of the extensional rheology due to fibre aspect ratio on the atomization performance.

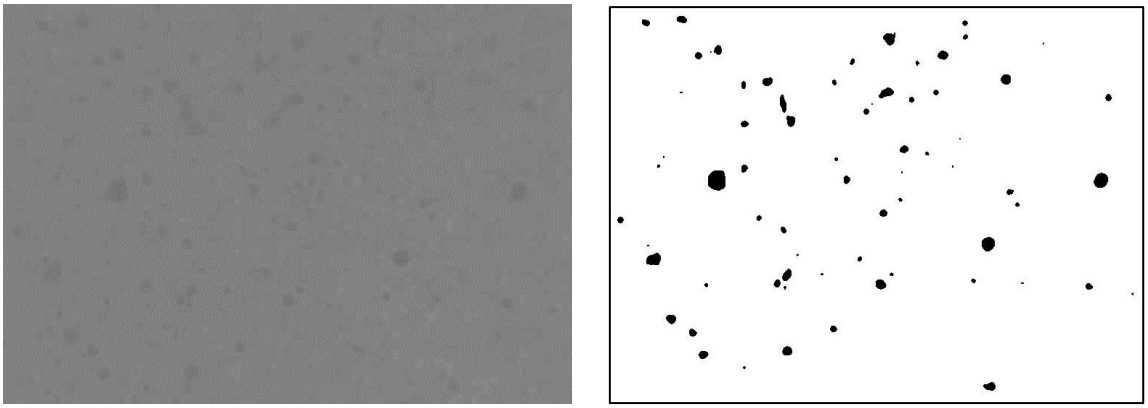

(a) AF 400-30

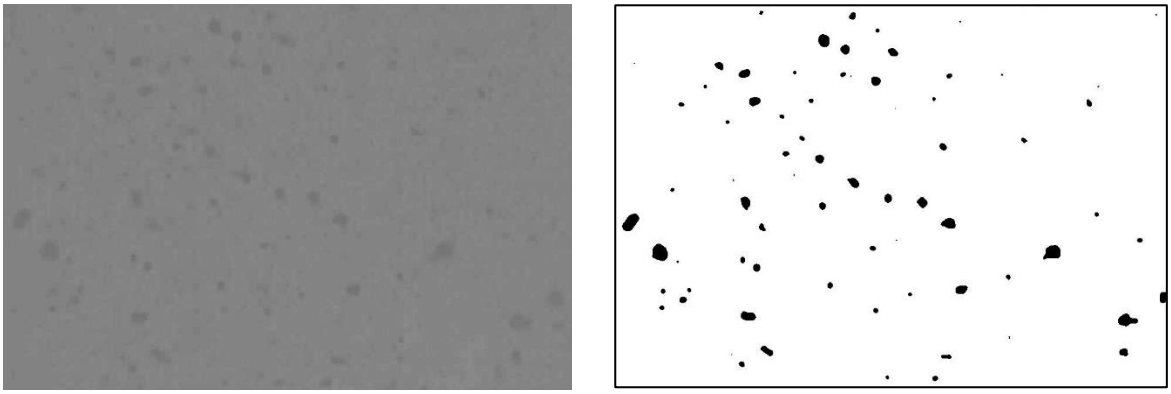

(b) WF 101

Continue →

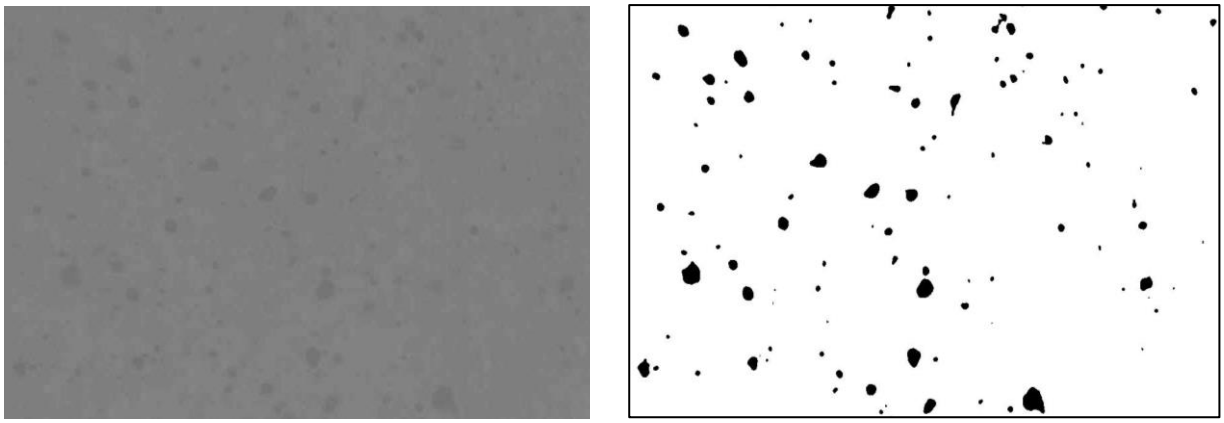

(c) WF 600

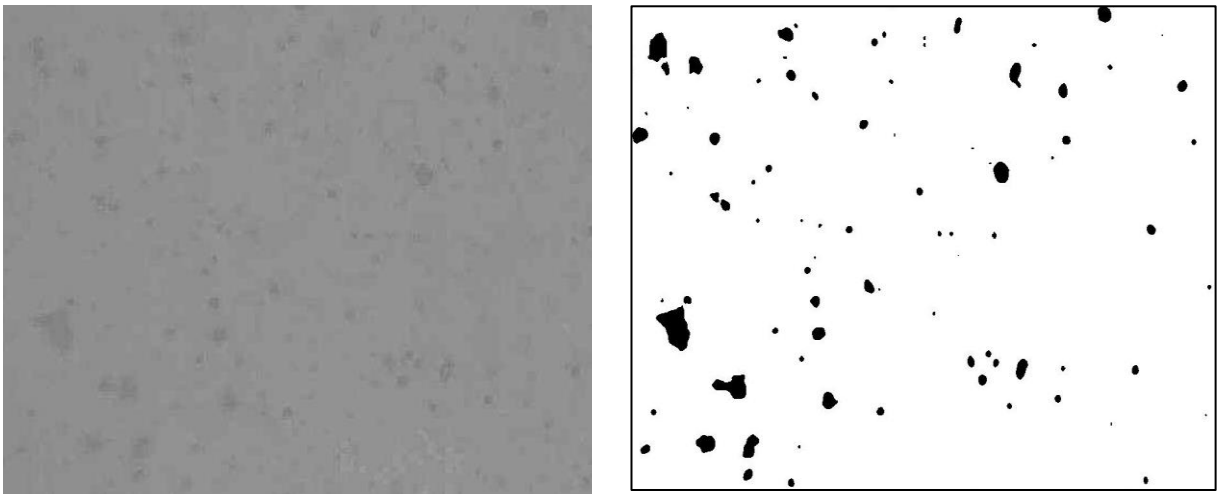

(d) citrus fibre

Figure 6.8 Photographs of the droplets of 5.0 wt.% fibre suspensions at an atomizing air velocity of 195 m/s. (a) AF 400-30 (b) WF 101 (c) WF 600 and (d) citrus fibre. Images were captured at a position 50 mm below the nozzle exit. Each image was converted into a binary image for clearer observation and easier analysis.

6.4 Droplet size measurement

6.4.1 Effect of atomizing air velocity

Evaluating the ability of atomization performance through a qualitative comparison of several captured images alone may be misleading. Hence, it is necessary to perform droplet size analysis on all fibre suspensions of 5.0 wt.% AF 400-30, 5.0 wt.% WF 101, 5.0 wt.% WF 600 and 5.0 wt.% citrus fibre suspensions. The flash photography technique produced images of droplets such as in Figures 6.7 and 6.8. MATLAB image analysis was then performed on the images taken at a position 50 mm below the nozzle. Appendix C shows the MATLAB code generated to analyse the droplets produced by the flash photography technique.

D(v,10) is the diameter at which 10% of the sample's volume is comprised of droplets with a diameter less than this value. D(v,50) is defined as the diameter where half of the sample's volume has droplets with a diameter less than this value. Similarly, D (v,90) is the diameter at which 90% of the sample's volume contains droplets with a diameter less than this value. Figure 6.9 plots the D(v,10), D(v,50) and D(v,90) values for the droplet sizes of the 5.0 wt.% AF 400-30, 5.0 wt.% WF 101, 5.0 wt.% WF 600 and 5.0 wt.% citrus fibre suspensions obtained from the MATLAB image analysis as a function of air velocity. When the atomizing air velocity was increased from 150 m/s to 240 m/s, the droplet sizes of all 5.0 wt.% fibre suspensions were reduced. As shown earlier, the atomization of the fibre suspensions at an atomizing air velocity of 150 m/s produced filamentary structures at 10 mm below the nozzle, where the filamentary structures connected chunks of ligaments or droplets to each other. It means that most of the droplets were not directly pinched-off from the filaments right below the nozzle. As a consequence, some of the droplets were still connected by a bridge at a position 50 mm below the nozzle due to insufficient force to stretch and break the filaments and there was less time for droplets to reach equilibrium shape and size. The later breakup of filaments and the presence of the unbroken filaments or bridges, non-spherical and non-symmetrical droplets at a position far below the nozzle consequently resulted in large droplet size measured by the MATLAB image analysis. Increasing the air velocity to 240 m/s provided greater strain rates and thus sufficient disruptive forces to stretch and break the filaments at a position 10 mm below the nozzle. The breakup of the filaments and pinched-off of droplets right after the nozzle led to the

formation of more symmetrical spherical droplets at a position 50 mm below the nozzle. The presence of bridges connecting droplets together was also reduced. All these consequences resulted in the smaller droplet sizes measured by the MATLAB image analysis.

As shown in Figure 6.9, increasing the atomizing air velocity during the atomization reduced the droplet sizes regardless of the fibre types. Atomization occurs when disruptive forces overcome the stabilizing forces of the fluid. In the case of the two-fluid atomization of fibre suspensions, the atomizing air velocity was the disruptive force that stretches the liquids or ligaments while the surface tension, shear and extensional resistance resist the breakup of the ligaments which then reduced the atomization performance as a whole. Increasing the atomizing air velocity and thus the extensional strain rate was efficient in stretching and breaking the ligaments which improved the atomization performance by reducing the population of large droplets in the size distribution. The atomization performance here means the formation of smaller droplets at a position 50 mm below the nozzle that will affect the efficiency of drying in the spray dryer. While increasing the atomizing air velocity in two-fluid atomization was efficient, increasing the pumping pressure in pressure nozzle atomization is predicted to be inefficient. This was discussed in detailed in Section 4.2.1 where increasing the pumping pressure inside a capillary viscometer increased the shear rates, but, at the same time induced significance pressure drop at the nozzle entrance due to the elasticity of the fibre suspensions. It shows that the atomization of fibre suspensions with extensional properties should utilize a two-fluid nozzle due to its ability to supply high atomizing air velocity as a means to provide a large enough extensional strain rate to break the ligaments of the fibre suspensions.

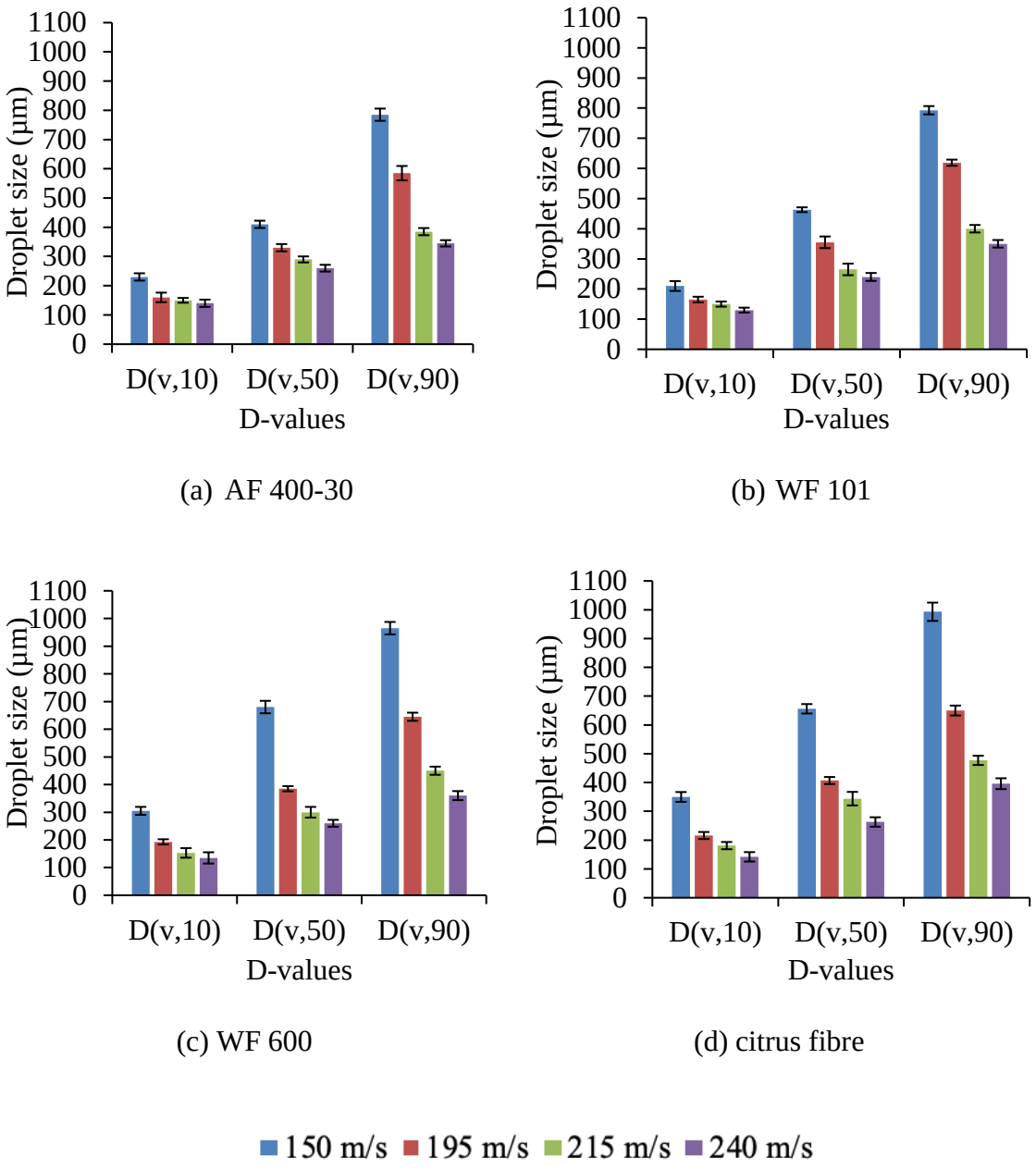

Figure 6.9 Droplet size distribution analysis based on the droplet formation at position 50 mm below the nozzle. The results were generated based on the MATLAB image analysis. Atomizing air velocity was increased from 150 m/s to 240 m/s. (a) 5.0 wt.% AF 400-30 (b) 5.0 wt.% WF 101 (c) 5.0 wt.% WF 600 and (c) 5.0 wt.% citrus fibre suspensions.

The droplet sizes of the fibre suspensions during the two-fluid atomization was also measured using a Malvern Mastersizer S. The results generated using a Malvern Mastersizer are shown in Figure 6.10. The results generated by MATLAB image analysis and Malvern Mastersizer were compared based on two analyses which were the Passing-Bablok and the paired t-test analyses.

The Passing-Bablok analysis is a method validation analysis, it tests the null hypothesis that there is a relationship between two variables, which were the D-values generated by MATLAB and Malvern Mastersizer methods, are linear. A p-value of more than 0.05 was obtained for each type of fibre suspensions, which gives strong evidence that the two methods showed a linear relationship. The linear relationship between the D-values generated by MATLAB and Malvern Mastersizer means that a good correlation exists between the D-values. The results of the p-value for each fibre suspension from the Passing-Bablok analysis are tabulated in Table 6.1. Figure 6.11 shows an example of the linear relationship between the droplet sizes generated using MATLAB image analysis and Malvern Mastersizer method, obtained through a regression analysis. The droplet sizes include all the D-values of 5.0 wt.% WF 600 fibre suspension between 150 m/s and 240 m/s atomizing air velocity. The plot further indicates that a good correlation was obtained between the droplet sizes generated by the two different methods. To support the statement, Table 6.2 shows the slope produced by MATLAB image analysis method, for example as shown in Figure 6.11, were statistically the same as 1 for all types of fibre suspensions. This indicates that the slope produced by MATLAB image analysis method were statistically the same as the slope produced by Malvern Mastersizer method. Appendix G explains in more detailed about the Passing-Bablok method, especially the regression analysis that produced Figure 6.11.

A second analysis was performed to support the findings from the Passing-Bablok analysis. The paired t-test is usually used to determine if there is significant difference between the means of two groups which the two groups may be related in certain features. In the atomization of fibre suspensions, the two groups were the D-values generated by MATLAB image analysis and the D-values obtained by Malvern Mastersizer. During the t-test, each D-value generated using MATLAB image analysis was paired with the corresponding D-value obtained using the Malvern Mastersizer. For example, the D(v,10) of 5.0 wt.% WF 600 at an atomizing air velocity of 150 m/s generated using the MATLAB image analysis was paired with the corresponding D(v,10) of 5.0 wt.% WF 600 obtained using the Malvern

Mastersizer. Similar pairings were set for D(v,50) and D(v,90) for all fibre suspensions, at different atomizing air velocities. The paired D-values were then analysed using the t-test. The null hypothesis assumed that the true mean difference was equal to zero. P-values of more than 0.05 was obtained for all pairings which indicate strong evidence that the two methods gave the same results. In other words, it means that there was no significant difference between the means of the two different methods. It indicates that the means of the D-values generated by MATLAB image analysis were similar to the means of the D-values obtained using the Malvern Mastersizer. Table G1 in Appendix G listed the p-values for each pairing.

Table 6.1 p-value obtained through the Passing-Bablok analysis based on the comparison between the D-values generated by MATLAB image analysis and Malvern Mastersizer.

Fibre suspension	p-value
5.0 wt.% AF 400-30	0.893
5.0 wt.% WF 101	0.441
5.0 wt.% WF 600	0.893
5.0 wt.% citrus fibre	0.893

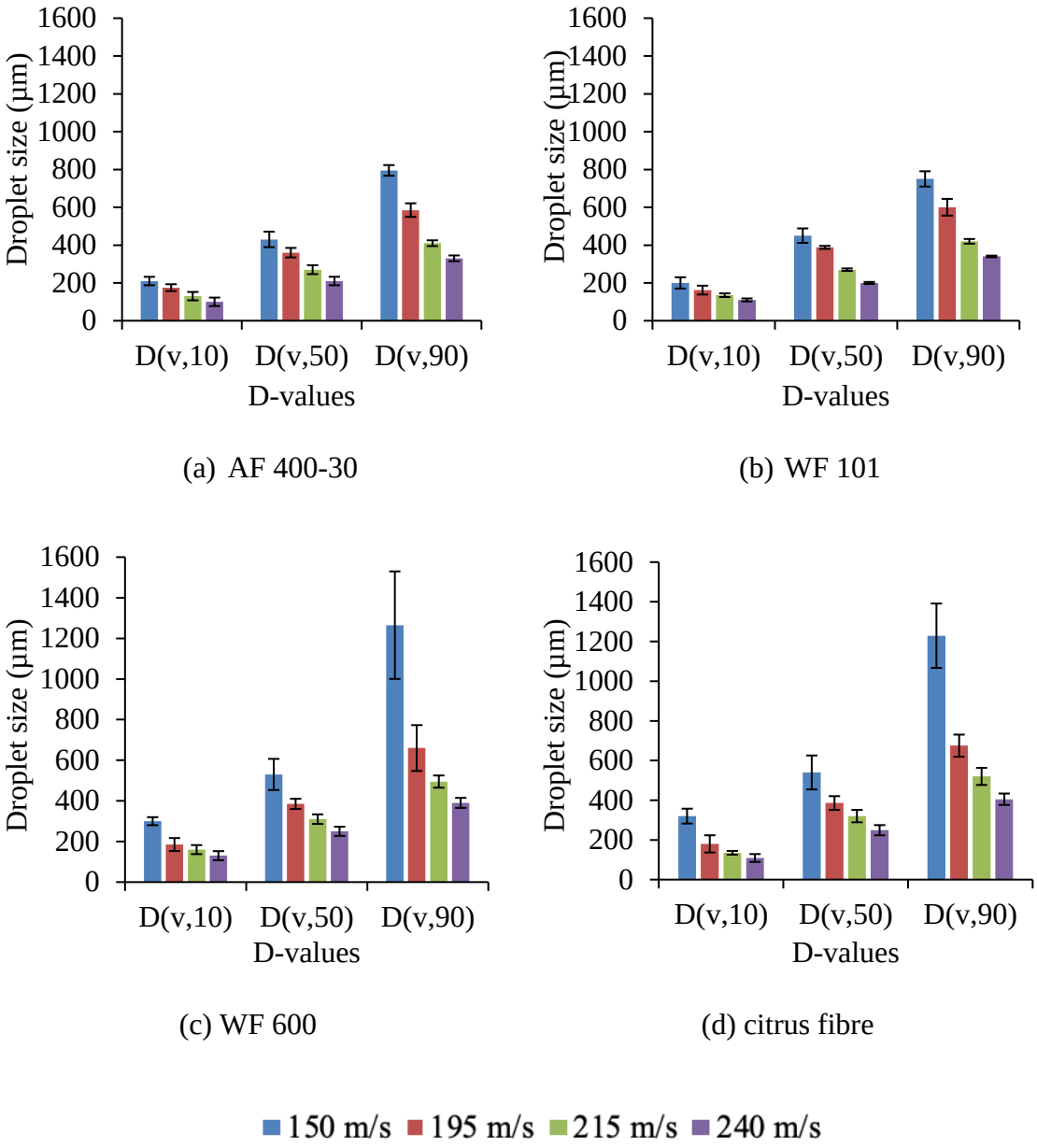

Figure 6.10 Droplet size analysis based on droplet formation at position 50 mm below the nozzle. The results were obtained using a Malvern Mastersizer. Atomizing air velocity was increased from 150 m/s to 240 m/s. (a) 5.0 wt.% AF 400-30 (b) 5.0 wt.% WF 101 (c) 5.0 wt.% WF 600 and (c) 5.0 wt.% citrus fibre suspensions.

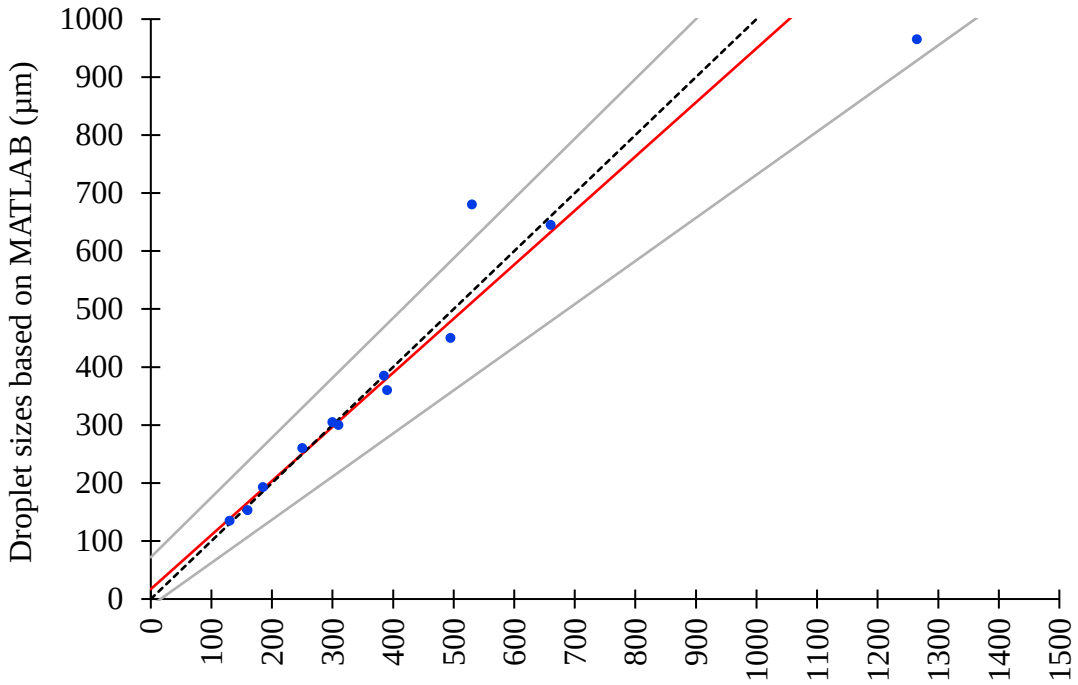

Figure 6.11 A plot showing the relationships between MATLAB image analysis and Malvern Mastersizer. (o) Experimental results based on MATLAB image analysis for 5.0 wt.% WF 600 fibre suspension, (----) the ideal situation if Y (MATLAB results) perfectly equals to X (Malvern Mastersizer results), (—) fitted regression line based on MATLAB image analysis data and (—) regression line confidence bands (95% confidence interval). Refer to Appendix G for clarification.

Table 6.2 Slopes coefficients based on the Passing-Bablok analysis.

Fibre suspensions	Slope coefficient	Lower bound 95%	Upper bound 95%
5.0 wt.% AF 400-30	0.94	0.78	1.00
5.0 wt.% WF 101	1.00	0.86	1.07
5.0 wt.% WF 600	0.93	0.74	1.03
5.0 wt.% CF	0.86	0.74	1.00

Based on Figures 6.9 and 6.10, increasing the atomizing air velocity reduced the D(v,90), followed by the D(v,50) and had the least effect on D(v, 10). The less significant reduction in D(v, 10) could be due to the atomization performance reaching its limit of size reduction where the surface tension forces that hold the droplets and the aerodynamic pressure outside the droplets are in equilibrium with the droplets internal pressure (Lefebvre, 1988). The D(v,90) reduced significantly compared to the D (v,10) due to the absence of large and connecting droplets at much greater atomizing air velocities. Hence, the smaller droplets represented by the D(v,10) were controlled by the surface tension pressure limit where increasing the atomizing air velocity did not significantly reduce the D(v,10). Meanwhile, the bigger droplets or D(v,90) was controlled by the atomizing air velocity where increasing the air velocity significantly overcame the extensional resistance and produced smaller droplets.

6.4.2 Effect of fibre aspect ratio

Figures 6.9 and 6.10 show that the D-values of low aspect ratio fibre suspensions of 5.0 wt.% AF 400-30 and 5.0 wt.% WF 101 were lower than the high aspect ratio fibre suspensions of 5.0 wt.% WF 600 and 5.0 wt.% citrus fibre suspensions, especially at the lowest atomizing air velocity of 150 m/s. This is due to the greater extensional resistance exhibited by the 5.0 wt.% WF 600 and 5.0 wt.% citrus fibre suspensions, due to the longer fibres and higher aspect ratio. A clearer interpretation is shown in Figure 6.12(a) which shows the difference in the D-values as a function of fibre aspect ratios at an atomizing air velocity of 150 m/s.

As shown in Figure 6.12(a), the D-values of the fibre suspensions with high aspect ratios of 8 – 10 were higher than the fibre suspensions with low aspect ratios of 2 – 3. However, increasing the atomizing air velocity to 240 m/s reduced the difference between the D-values. This is visible in Figure 6.12(b) which shows the difference in the D-values as a function of fibre aspect ratios at atomizing air velocity of 240 m/s. As shown in Figure 6.12(a), the difference in the D(v,90) of the low and high aspect ratio fibre suspensions at 150 m/s are large, while Figure 6.12(b) shows that the difference in the D(v,90) becomes significantly smaller when the atomizing air velocity was increased to 240 m/s. It is suggested increasing the atomizing air velocity to 240 m/s or beyond may not yield much difference in the droplet sizes between the low and high aspect ratio fibre suspensions. This

must be due to the limits in the extensional resistance resisting breakup. Possibly at an atomizing air velocity of 150 m/s, the resistance in the high aspect ratio fibre suspensions was greater so the fibres resist the breakup stronger compared to the low aspect ratio fibre suspensions. At 240 m/s atomizing air velocity, the disruptive forces are great enough that the extensional resistance is overcome so there is no observed difference between the breakup of the short and long fibre suspensions. This can be supported by looking at the span. Figure 6.13 shows the reduction in the span when the atomizing air velocity was increased from 150 m/s to 240 m/s. Increasing the atomizing air velocity from 150 m/s to 240 m/s reduced the span of all 5.0 wt.% fibre suspensions. The spans of the low aspect ratio fibre suspensions of 5.0 wt.% AF 400-30 and 5.0 wt.% WF 101 were visibly lower than the spans of the high aspect ratio fibre suspensions of 5.0 wt.% WF 600 and 5.0 wt.% citrus fibre suspensions at atomizing air velocity of 150 m/s. However, the spans of all low and high aspect ratio fibre suspensions were similar when the atomizing air velocity was increased to 240 m/s.

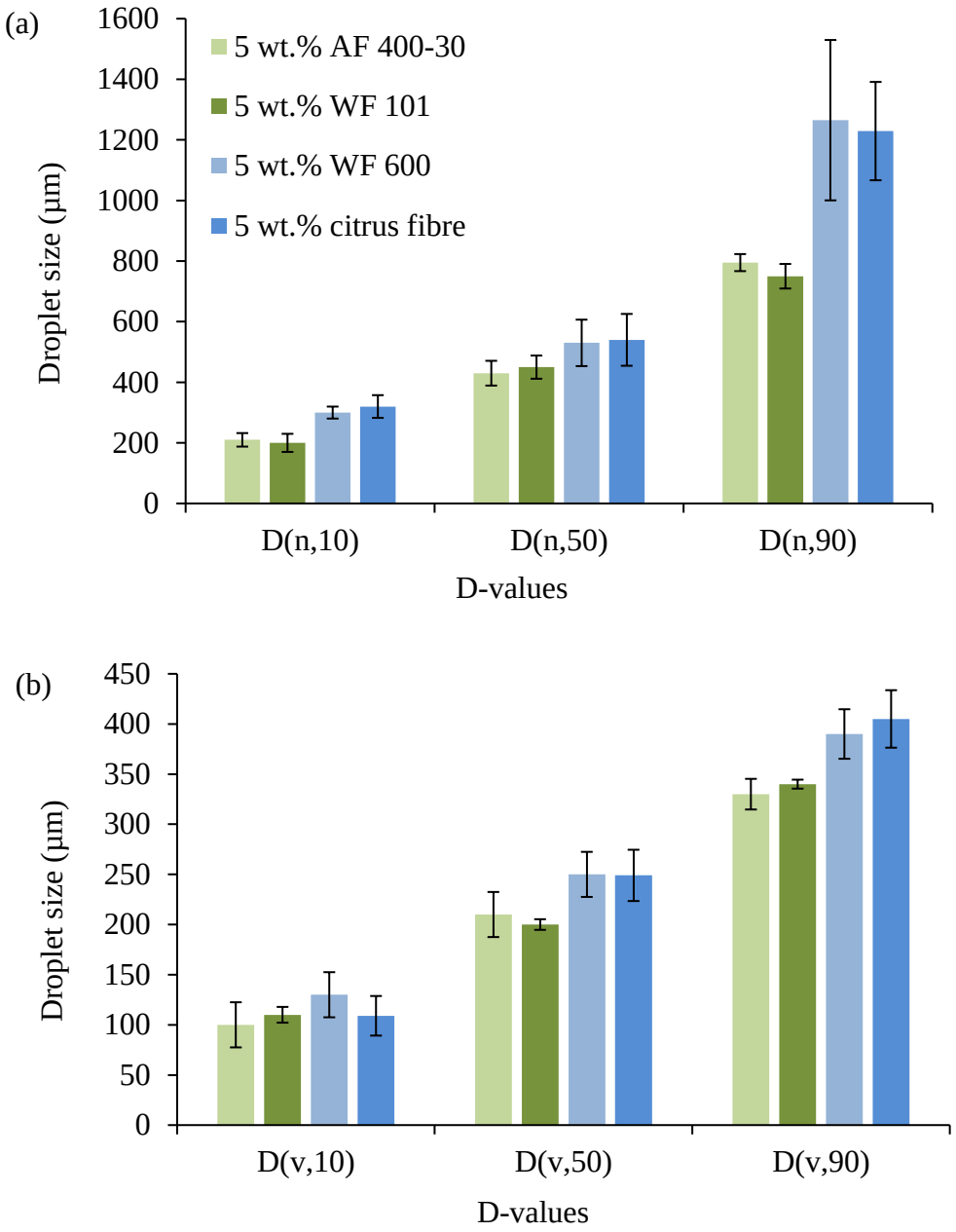

Figure 6.12 D-values of the 5.0 wt. % AF 400-30 and 5.0 wt.% WF 101 fibre suspensions with aspect ratios of 2 – 3, and the 5.0 wt.% WF 600 and 5.0 wt.% citrus fibre suspensions with aspect ratio of 8 – 10. (a) At an atomizing air velocity of 150 m/s and (b) at an atomizing air velocity of 240 m/s. The D-values shown are taken from the Malvern Mastersizer results.

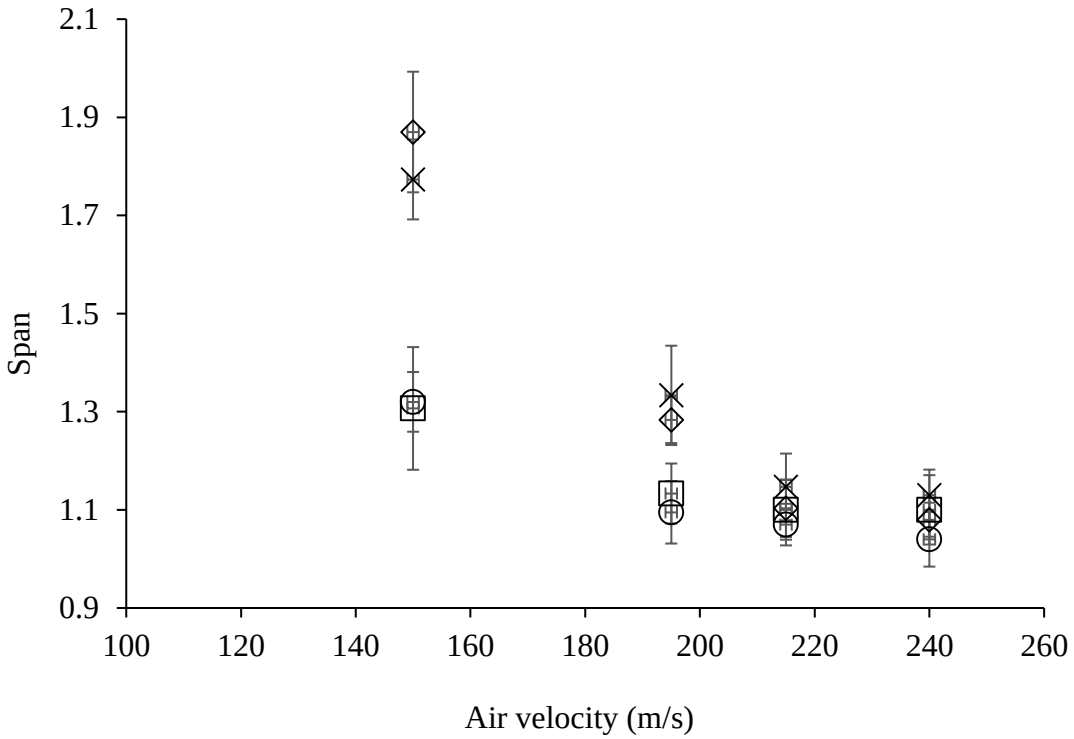

Figure 6.13 Span of droplet size distribution, [D(v,90) – D(v,10)] / D(v,50), as a function of increasing atomizing air velocity. (○) 5.0 wt.% AF 400-30 (□) 5.0 wt.% WF 101 (◊) 5.0 wt.% WF 600 and (×) 5.0 wt.% citrus fibre suspensions. The error bars refer to the standard deviation of the sample.

Overall, it is evident that the droplet sizes of fibre suspensions were bigger than Newtonian liquids where the atomization of Newtonian liquids in a two-fluid nozzle usually produced droplets with average droplet sizes of less than 150 μm (Aliseda et al., 2008; Buckner & Sojka, 1991). This agrees with previous studies by Christanti and Walker (2006), Mansour and Chigier (1995) and Mun et al. (1999). All these studies show that the addition of elasticity can lead to significant changes in atomization performance, especially in the production of larger average droplet sizes of the sprays.

In atomizing extensional liquids, greater disruptive forces are required. This is evident from the Weber number, *We* used in this study. Previous authors suggested a critical *We* between 4 and 100, above which the atomization occurs (Derby, 2010; Hanson et al., 1963; Wierzba, 1990). Throughout this study, the minimum *We* of 4.5×10^4 did not yield complete atomization, as shown in Figure 6.2. This is highly related to the parameter that is being considered as the stabilizing force in generating the *We* equation, as shown in Equation 6.2. In Equation 6.2, surface tension is regarded as the dominate stabilizing force opposing

atomization. However, this is only true for Newtonian liquids as they exhibit insignificant extensional behaviour. In fibre suspensions atomization, the extensional behaviour of the liquid dominates the atomization resistance. A much greater disruptive force is required to overcome the extensional resistance as suggested by the *We* needed in this study to induce atomization. The relatively lower critical *We* reported by previous authors is true only for Newtonian liquids or water. Thus, there is a need in revising the critical *We* requires to achieve atomization for liquids such as fibre suspensions.

6.5 Theoretical prediction of droplet sizes in a two-fluid nozzle

Atomization is the process of disrupting liquid sheets into droplets due to the disruptive and stabilizing forces. By identifying the forces involved, previous works have developed different correlation equations in attempts to predict the atomization performance, specifically the droplet sizes (Aliseda et al., 2008; Masters, 1979; Rajan & Pandit, 2001; Varga et al., 2003). However, as the importance of extensional rheology in influencing the atomization of non-Newtonian liquids was not studied, all the models do not include the effect of extensional properties such as the extensional viscosity or relaxation time of the liquids. This section shows the difference in the droplet sizes of fibre suspensions predicted using two different theoretical equations. Aliseda et al. (2008) developed a theoretical equation to predict the droplet sizes inside a two-fluid nozzle and Keshavarz et al. (2015) extended the equation to include the properties of extensional rheology in their prediction.

6.5.1 Prediction of droplet size of fibre suspensions using Keshavarz et al. (2015) relationship

During the atomization, the enhanced resistance of the fibre suspensions to stretching coming from the extensional properties of the fibre suspensions plays a key role in controlling the dynamics of the filament breakup. As shown in Figure 6.5, this additional resistance led to the appearance of elongated filaments connecting successive droplets to each other. Keshavarz et al. (2015) developed a theoretical equation to explore the effects of viscoelasticity on the average droplet size during the atomization. Specifically, the equation relates the effect of liquid relaxation time, τ_r to the number average droplet

diameter, $\langle d \rangle_{VE}$. Relaxation time, τ_r is one of the extensional properties that has been discussed in depth in Chapter 5, Section 5.2.

Equation 6.6 shows the equation developed by Keshavarz et al. (2015). $\langle d \rangle_{VE}$ (µm) is the average droplet size, specifically D(n,50) for viscoelastic liquids, D_J (mm) is the jet diameter which is similar to the orifice diameter, U_A (m/s) is the atomizing air velocity, σ (mN/m) is the surface tension and c is a constant. We and Oh are the Weber number and Ohnesorge number respectively based on the jet shearing, while De_{R_l} and Oh_{R_l} are the Deborah number and Ohnesorge number based on the ligament stretching.

$$\frac{\langle d \rangle_{VE}}{D_J} \cong 1.2\left(\frac{\sigma}{\rho {U_A}^2 D_J}\right)^{\frac{1}{2}}\left[1 + We^{\frac{1}{6}}Oh^{\frac{2}{3}}\right] \times \left[\frac{\left(\frac{\sqrt{8}c}{6}\right){Oh_{R_l}}^{-1}}{\left(\frac{\sqrt{8}c}{6}\right){Oh_{R_l}}^{-1} + {Oh_{R_l}}^2 - ln\left(1 + \frac{cDe_{R_l}}{3Oh_{R_l}}\right)}\right]$$

– Equation 6.6

Equation 6.6 was extended from the Newtonian correlation by Aliseda et al. (2008). By referring to the Equation 6.6, the first term on the right-hand side of the equation represents the competing effect of shear viscosity and surface tension on the average droplet size, first predicted by Aliseda et al. (2008). That explains the calculation of *Oh* and *We* number based on the jet diameter. The final overall form of Equation 6.6 includes all of the competing effects of shear viscosity, surface tension and elasticity on overall mean droplet sizes as proposed by Keshavarz et al. (2015). The second term on the right-hand side of Equation 6.6 represents the effect of extensional resistance in influencing the average droplet size. The calculation of Oh_{R_l} and De_{R_l} is based on the extracted data from capillary breakup extensional rheometer discussed in Chapter 5, Section 5.2.

Figure 6.14 shows the predicted average droplet sizes, D(n,50), of 5.0 wt.% AF 400-30, 5.0 wt.% WF 101, 5.0 wt.% WF 600 and 5.0 wt.% citrus fibre suspensions obtained via non-linear regression of Equation 6.6. *c* in Equation 6.6 is a single fitting constant and the value is tabulated in Appendix H for each 5.0 wt.% fibre suspensions. As shown in Figure 6.14, for all types of fibre suspensions, good correlations were obtained between the

experimental and theoretical values of droplet sizes. A maximum of 12.0 % deviation of experimental value from the theoretical value was obtained and correspond to the D(n,50) of 5.0 wt.% WF 600 at 150 m/s. Other than that, most of the deviations vary between 2 – 7 %. Refer to Appendix H for more details regarding the regression of Equation 6.6.

As shown in Figure 6.14, increasing the atomizing air velocity reduced the droplet size of the fibre suspensions. This has been shown experimentally in Figures 6.9 and 6.10. Besides that, based on Figure 6.14, the high aspect ratio fibre suspensions of 5.0 wt.% WF 600 and 5.0 wt.5 citrus fibre exhibited greater average droplet size compared to the low aspect ratio fibre suspensions of 5.0 wt.% AF 400-30 and 5.0 wt.% WF 101. The good correlations between the experimental values and the predicted values of droplet size in Figure 6.14 prove the atomization of fibre suspensions was dominated by the extensional properties of the fibre suspensions, with the shear properties and surface tension only having minor roles. This demonstrates the importance of incorporating the extensional properties or elasticity during the atomization of fibre suspensions or other non-Newtonian liquids, especially if the atomization performances or droplet sizes are forecasted theoretically without experimental observation. The consequence of excluding the elasticity and thus relying on the shear viscosity and surface tension as the sole sources of disruptive forces is discussed after this.

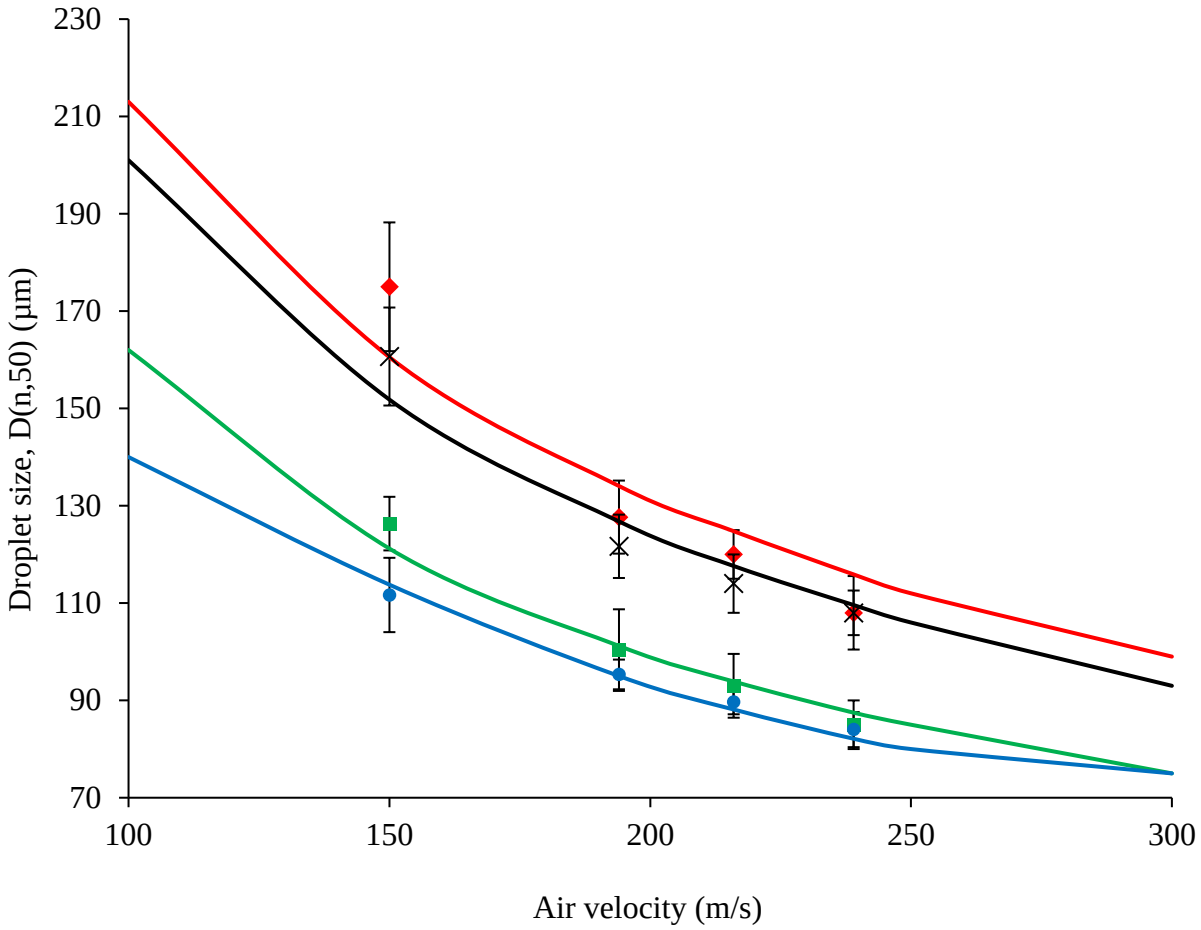

Figure 6.14 Relationships between the droplet sizes obtained experimentally and predicted theoretically based on Keshavarz et al. (2015), Equation 6.6. (○) 5.0 wt.% AF 400-30, (□) 5.0 wt.% WF 101, (◊) 5.0 wt.% WF 600 and (×) 5.0 wt.% citrus fibre suspensions are the average droplet size of fibre suspensions obtained experimentally, while the theoretical prediction for each fibre suspension is represented by the full line.

6.5.2 Prediction of droplet size of fibre suspensions using Aliseda et al. (2008) relationship

Figure 6.15 shows the theoretical mean droplet size of 5.0 wt.% WF 600 fibre suspensions when predicted using a correlation published by Aliseda et al. (2008), it does not include the effect of extensional properties. As shown in Figure 6.15, the mean droplet sizes of the 5.0 wt.% WF 600 predicted using Aliseda et al. (2008) correlation were very different from the experimental observations. Droplet sizes of 5.0 wt.% AF 400-30, 5.0 wt.% WF 101 and 5.0 wt.% citrus fibre suspensions predicted using Aliseda et al. (2008) equation are not shown in Figure 6.15 because the values were very similar to the predicted values shown

by the 5.0 wt.% WF 600 fibre suspension. Using Aliseda et al. (2008) correlation, it implies that only shear viscosity and surface tension affect the atomization performance or the droplet sizes. The shear viscosity of the different 5.0 wt.% fibre suspensions were all very similar at all atomizing air velocities. This is due to the very high shear rates of greater than 25 000 s^{-1} were achieved at all the atomizing air velocities, and the shear viscosities of the different aspect ratio fibre suspensions were all relatively similar at that high shear rates. For the 5.0 wt.% WF 600 fibre suspension shown in Figure 6.15, the predicted droplet sizes based on Aliseda et al. (2008) relationship were very small, ranging between 10 µm to 30 µm, whereas, the mean droplet sizes from the experimental observation were very large exceeding 100 µm at all atomizing air velocities. This indicates the use of simple Newtonian correlations, such as Aliseda et al. (2008) equation, is not accurate and reliable in predicting the atomization performance of non-Newtonian fibre suspensions. It also implies that the relatively bigger droplet sizes of the fibre suspensions were probably due to the extensional resistance or elasticity of the suspensions, with little effect by shear viscosity. The predicted droplet size of the Newtonian concentrated apple juice based on the Aliseda et al. (2008) relationship yielded a good correlation and a better correspondence to the experimental observation compared to the non-Newtonian fibre suspension. This is shown in Figure 6.15.

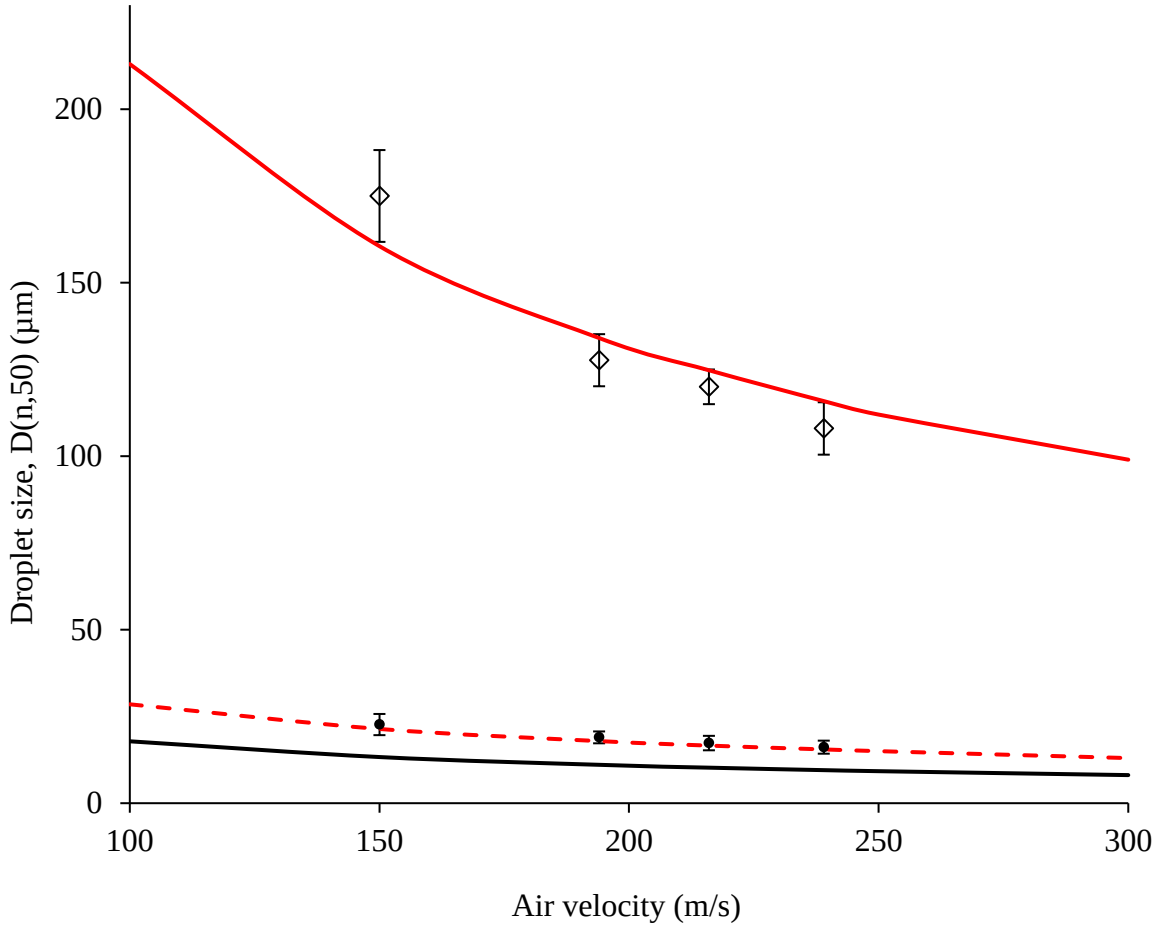

Figure 6.15 Relationships between the mean droplet sizes obtained experimentally and predicted theoretically based on Keshavarz et al. (2015) and Aliseda et al. (2008) relationships. (•) Concentrated apple juice, (−) theoretical droplet size of concentrated apple juice based on Aliseda et al. (2008), (◊) 5.0 wt.% WF 600 fibre suspension, (----) theoretical droplet size of 5.0 wt.% WF 600 fibre suspension based on Aliseda et al. (2008) and (−) theoretical droplet size of 5.0 wt.% WF 600 fibre suspension based on Keshavarz et al. (2015) equation.

6.6 Morphology of frozen droplets inside liquid nitrogen

The atomization of fibre suspensions from a liquid into droplets will be followed by the drying into a powder. Although the drying of the droplets was not of interest in this study, however, it is important to prove that the fibres can act as a drying aid during the drying inside a spray dryer. The drying of concentrated apple juice without drying aid produces a sticky powder. At first, it was unknown how the fibres placed themselves after the atomization, either they accumulate inside the droplets or they are sticking out from the

droplets. It is also essential to demonstrate the fibres are not separated from the droplets during the atomization. Complete separation of the fibres from the droplets means that the fibres will not be effective in assisting the drying of the sticky apple juice droplets. Most importantly, in the case of atomization, the separation could result in a bimodal or multimodal drop size or particle size distribution. This is because the size distribution of the fibres and size distribution of the droplets could possibly establish bimodal distribution with two different peaks. In the next section, the characteristic of the droplet size distribution of the fibre suspensions is shown to be a normal distribution, which indicates that no separation occurred. In this analysis, the visualization of the actual droplets further supports the no separation hypothesis.

Section 3.5.8 explains in detail on the method of spraying into liquid nitrogen to freeze the droplets and using a temperature-controlled microscope to observe the droplets. Figure 6.16 shows the frozen droplets of 5.0 wt.% WF 600 fibre suspension when atomization occurred at 195 m/s atomizing air velocity. Most of the droplets had a spherical shape. First observation on Figure 6.16 reveals that the droplets all stick together. This is expected since during the spraying into the liquid nitrogen, the droplets freeze rapidly to ice, and when two or more ice spheres meet each other, they stick due to the adhesion effect of the ice (Ryzhkin & Petrenko, 1997).

Figure 6.17 shows the frozen droplets images at higher magnification. The fibres appear to be enclosed in the droplets. The images suggest there was no separation during the atomization of fibre suspensions using a two-fluid nozzle at high atomizing air velocity. This indicates that the two-fluid nozzle is reliable in producing droplets with the fibres remaining enclosed in the drops, the fibres can assist the drying of the wet droplets and normal drop size distributions were attained during the atomization.

As shown in Figure 6.17, there were air bubbles trapped inside the droplets. These air bubbles most likely caused by dissolved air in the solution. Other than the air bubbles, some of the frozen droplets in Figures 6.16 and 6.17 appear bigger with the size exceeding 800 µm and as a maximum of 1000 µm. Based on MATLAB and Malvern Mastersizer methods, the D(v,90) of 5.0 wt.% WF 600 fibre suspension at atomizing air velocity of 195 m/s was approximately 700 µm. The relatively big frost droplets resulted from spraying into the liquid nitrogen may be due to the coalescence of droplets. When two or more drops float or levitate on the surface of liquid nitrogen, the drops first do not interact, but they move

closer to each other. When the curvatures of liquid nitrogen under the drops meet each other, drop coalescence occurs (Kim et al., 2011). Drop coalescences of the 5.0 wt.% WF 600 fibre suspension could possibly result in the bigger drop sizes compared to the results by MATLAB and Malvern Mastersizer methods. The spraying into the liquid nitrogen proceeded for 10 seconds. Thus, it is also possible that during the spraying into the liquid nitrogen, the later sprayed liquid drop met with the prior sprayed liquid drop that had already turned into a solid ice sphere. The liquid drop then surrounded the solid ice sphere and a spherically concentric liquid shell was formed around the solid ice sphere. This contributed to the bigger final drop size.

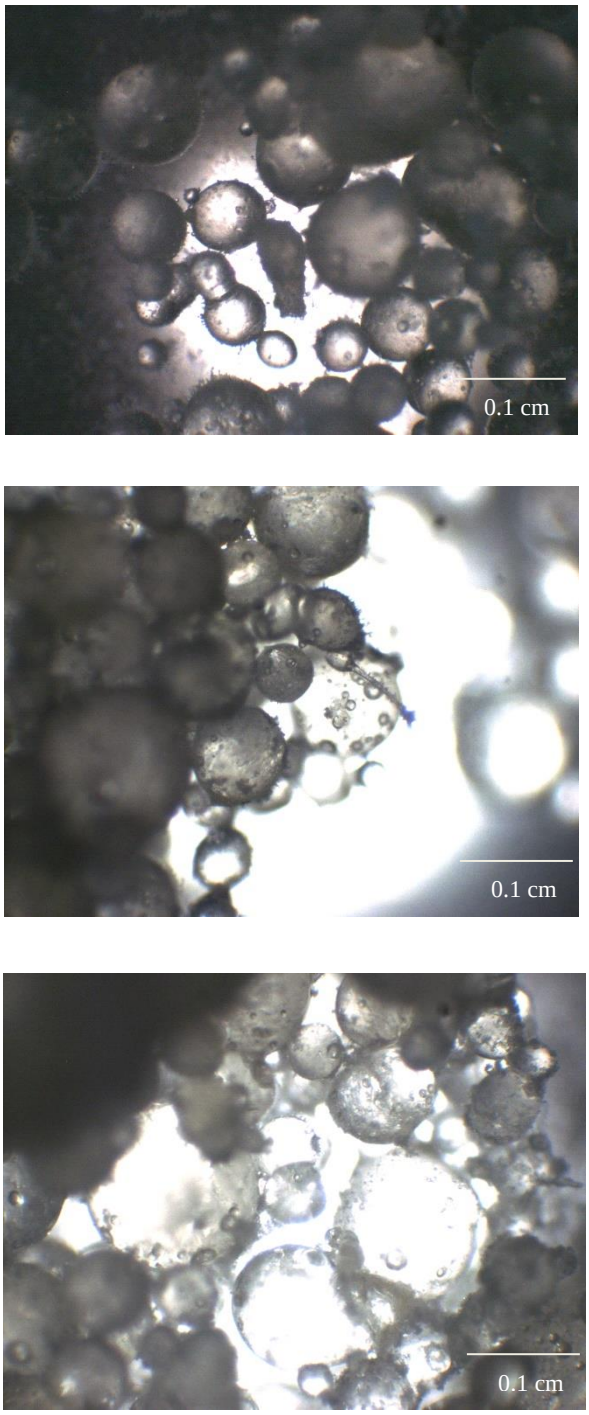

Figure 6.16 Frozen droplets of 5.0 wt.% WF 600 fibre suspension stick together after the spraying of the fibre suspension into a container filled with liquid nitrogen. The images correspond to 4x magnification.

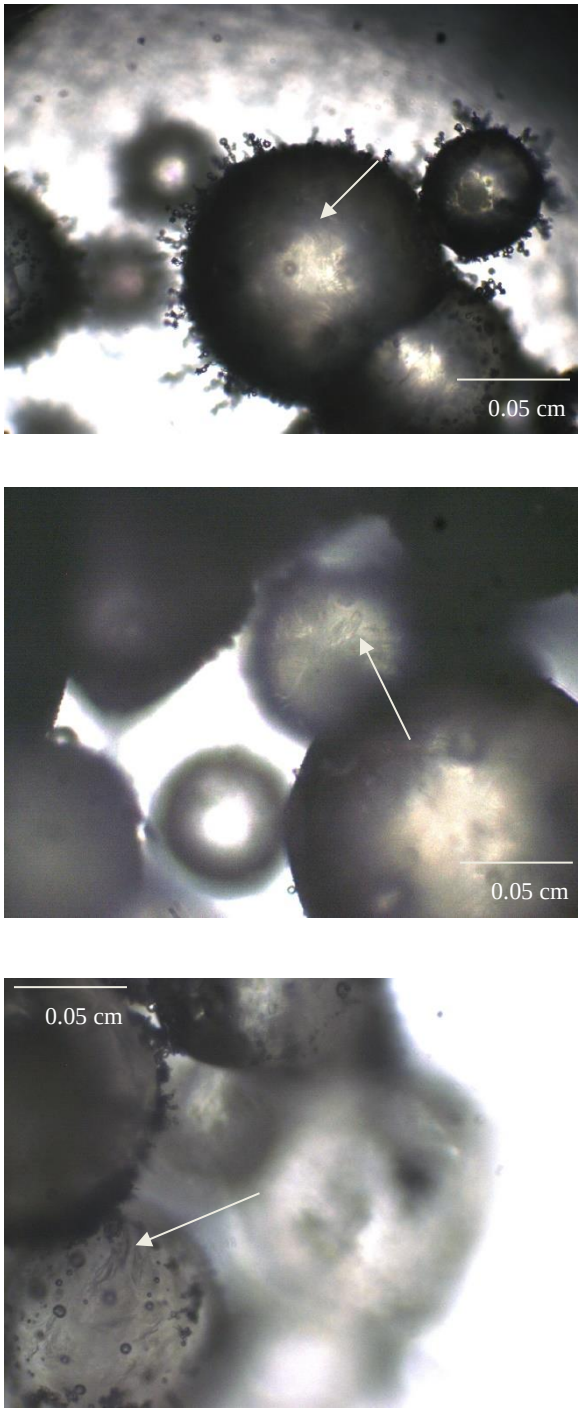

Figure 6.17 Zoomed-in images of the frozen droplets of 5.0 wt.% WF 600 fibre suspension showing the fibres inside the frozen droplets. Fibres are pointed out by the white arrows. The images correspond to 10x magnification.

6.7 Improving the atomization performance

Atomization of fibre suspensions was shown to yield bigger droplets compared to the atomization of simple Newtonian liquids. The Newtonian fluid (apple juice) atomization usually produced droplets with an average size of less than 150 µm (Aliseda et al., 2008; Buckner & Sojka, 1991) while the atomization of fibre suspensions produced droplets ranging between 200 – 250 µm at a high atomizing air velocity of 240 m/s. This section attempts to change or modify some of the parameters involved to improve the atomization performance of the fibre suspensions. Improving the atomization performance means producing smaller droplets to prepare for the drying stage inside a spray dryer.

6.7.1 Effect of increasing feed temperature during atomization

Industrially, spray drying of fruit juices usually proceeds at a temperature greater than the room temperature (Brennan et al., 1971; Goula et al., 2008; Mani et al., 2002). Specifically, the feed inlet is usually preheated to temperatures as high as 80 °C (Mani et al., 2002; Verma & Singh, 2015). Pre-heating the feed inlet to a temperature greater than the room temperature before the spray drying process improves the overall economic value of the spray drying process, as less energy needs to be supplied in terms of the hot gas to dry the liquid into dry powder and reduced shear viscosity to reduce pumping requirements. A study by Shu et al. (2006) shows that increasing the feed inlet temperature from 35 to 55 °C resulted in a better atomization effect when spray drying because it led to a lower shear viscosity of the feed. By increasing the temperature of the fibre suspensions prior to the atomization, this study seeks to see if the atomization performance can be improved, or if smaller droplet sizes can be produced.

The atomization of 5.0 wt.% WF 600 fibre suspension was performed by varying the temperature of the fibre suspension between 20 to 70 °C. The atomization of the fibre suspension at greater inlet temperatures was evaluated using the Malvern Mastersizer. Section 3.5.4.1 explains in detailed the pre-heated method. As shown in Figure 6.18 (a), increasing the inlet temperature from 20 to 70 °C produced smaller droplet sizes especially regarding D(v,50) and D(v,90). At an atomizing air velocity of 150 m/s, increasing the inlet temperature reduced the D(v,90) from more than 1000 µm to around 650 µm while the

D(v,50) reduced from approximately 550 µm to around 390 µm. In contrast, D(v,10) underwent insignificant changes. The effect of the inlet temperature on atomization performance was investigated at greater atomizing air velocities. As shown in Figure 6.18 (b), increasing the inlet temperature from 20 to 70 °C at an atomizing air velocity of 195 m/s significantly reduced the D(v,90), although the reduction is less obvious compared to at 150 m/s atomizing air velocity. Meanwhile, the D(v,50) and D(v,10) seem to undergo very minor reductions compared to the D(v,90). When the atomizing air velocity was further increased to 215 m/s and 240 m/s, the D(v,90) underwent an insignificant reduction, this was similar to the D(v,50) and D(v,10). This can be seen in Figure 6.18 (c-d).

Overall, it means increasing the inlet temperature did not reduce the D(v,10) at all atomizing air velocities and slightly reduced the D(v,50). Whereas, in the case of the D(v,90), increasing the inlet temperature considerably reduced the droplet sizes at the lowest atomizing air velocity of 150 m/s. At atomizing air velocities beyond 195 m/s, no meaningful reduction was observed for all the D-values. Previous Sections 3.4.2.2 and 4.1.4 show that the surface tension and shear viscosity of the fibre suspensions reduced when the temperature was increased. Meanwhile, Section 5.1.2 shows that the elasticity of the fibre suspensions was insignificantly reduced when the temperature was increased.

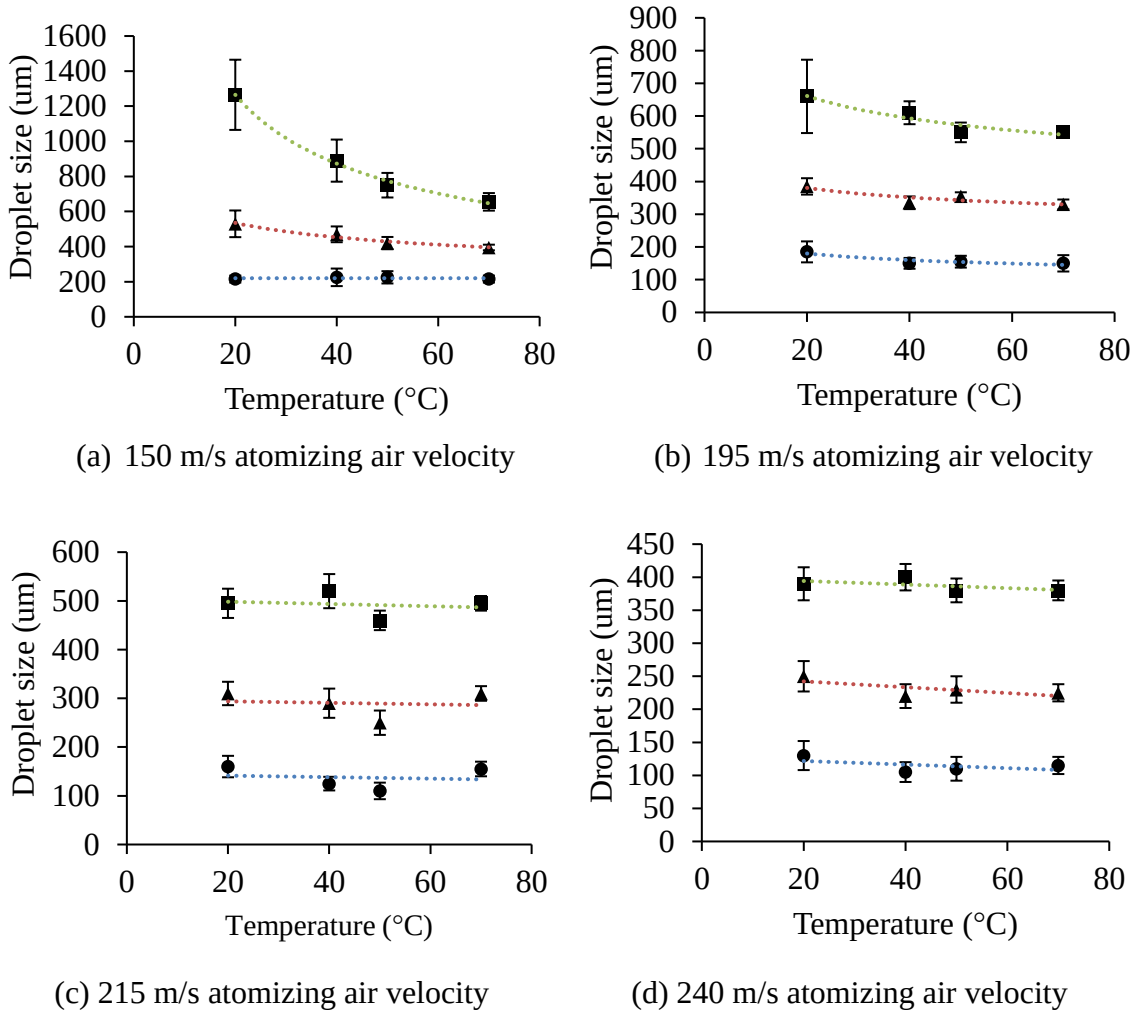

Figure 6.18 The D-values against the increasing feed temperature of the 5.0 wt. % WF 600 fibre suspension (a) at an atomizing air velocity of 150 m/s, (b) at an atomizing air velocity of 195 m/s, (c) at an atomizing air velocity of 215 m/s and (d) at an atomizing air velocity of 240 m/s. The D-values shown were obtained using the Malvern Mastersizer method. (●) D(v,10), (▲) D(v,50) and (■) D(v,90).

At the lowest atomizing air velocity of 150 m/s, the effect of surface tension and shear viscosity still existed, along with the extensional viscosity. Increasing the inlet temperature allowed the jet to be disrupted and sheared better or more intensely as the surface tension and especially the shear viscosity, were reduced. For example, the sheared jet of fibre suspensions shown in Figure 6.2 looks less disrupted compared to the sheared jet of Newtonian concentrated apple juice in Figure 6.1 at a similar atomizing air velocity, due to the greater shear viscosity of the fibre suspensions. Increasing the inlet temperature of the

fibre suspensions yielded a better breakup due to shearing of the liquid jet at a much lower shear viscosity. This then proceeded with the stretching of the ligaments into droplets. This means the effect of the surface tension and shear viscosity affect the overall performance of the fibre suspension atomization. However, at much greater atomizing air velocity of more than 150 m/s, the effect of the shear viscosity on atomization performance was minimal which means the atomization was dominated by the extensional resistance. Extensional resistance insignificantly reduced with increasing temperature. This explains the insignificant reduction in droplet sizes when the atomization proceeded at greater inlet feed temperatures.

Another explanation can be gained by comparing the competing effect of temperature and atomizing air velocity. Increasing of the inlet temperature and atomizing air velocity both change the conditions of atomization. Increasing the atomizing air velocity provides greater disruptive forces during the atomization and increasing the inlet temperature lessens the stabilizing forces during the atomization. At atomizing air velocity of 150 m/s, both the temperature and atomizing air velocity significantly influenced the atomization performance (droplet size distribution). However, at an atomizing air velocity of 195 m/s and beyond, the rate of the disruption due to the very high velocity of air exceeded the rate of the reduction in the stabilizing forces, and thus the atomizing air velocity dominated and controlled the whole atomization performance. Lowering the stabilizing forces gave no significant effect on the atomization performance. It means that, the extensional resistance of the fibre suspensions that negatively impact the drop size distribution and produced a wider distribution when compared to other Newtonian liquids or liquids with no elasticity, was overwhelmed and affected by the high atomizing air velocity but not the high temperature. As shown in Figure 6.19, at an atomizing air velocity of 150 m/s, increasing the inlet temperature from 40 to 70 °C shifted the drop size distribution to smaller droplet sizes and produced a narrower distribution. In contrast, at a greater atomizing air velocity of 240 m/s, increasing the inlet temperature did not significantly change the drop size distribution when compared to the change that occurred at 150 m/s atomizing air velocity.

Figures 6.18 and 6.19 suggest that the atomization of fibre suspensions at 150 m/s atomizing air velocity should undertake at a higher inlet temperature as this approach resulted in smaller droplet sizes, and thus better atomization. In contrast, the atomization of the fibre suspensions at 195 m/s atomizing air velocity and beyond, does not necessarily need to occur at high temperatures as there were insignificant changes in the droplet sizes.

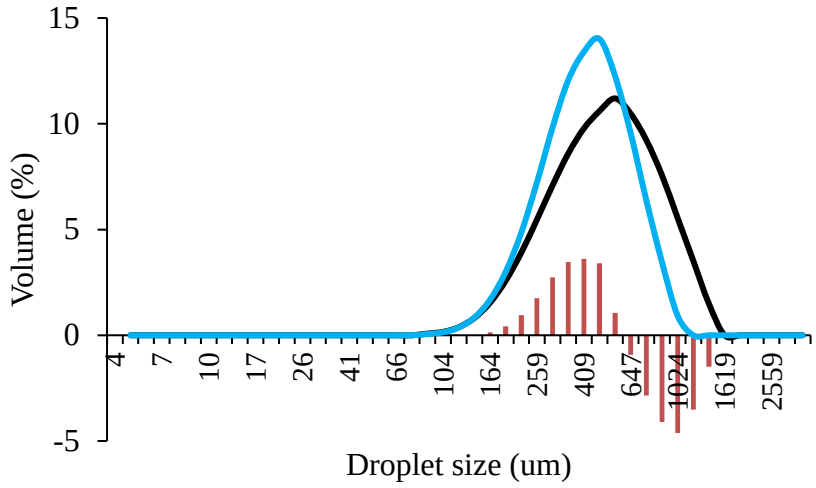

(a) Increasing the temperature from 40 °C to 70 °C at a constant atomizing air velocity of 150 m/s.

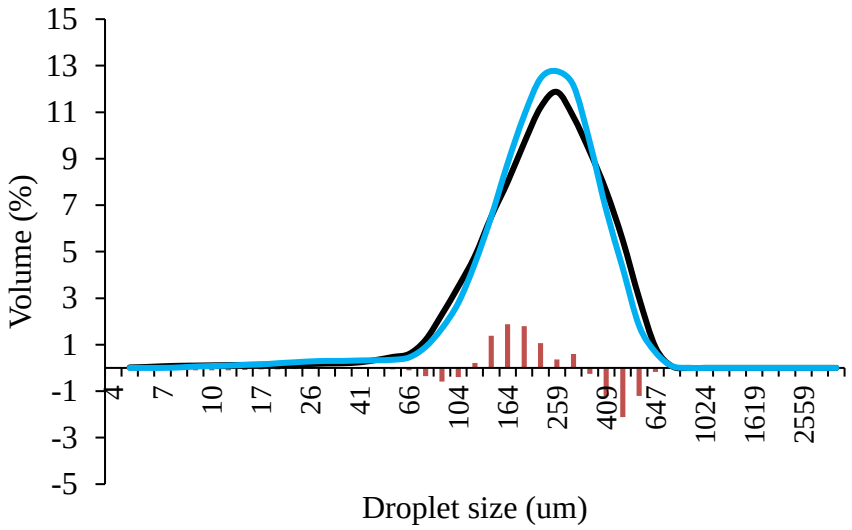

(b) Increasing the temperature from 40 °C to 70 °C at a constant atomizing air velocity of 240 m/s.

Figure 6.19 The change in the drop size distributions of the 5.0 wt.% WF 600 fibre suspension when the feed temperature was increased from 40 °C to 70 °C. (a) At an atomizing air velocity of 150 m/s and (b) at an atomizing air velocity of 240 m/s. (━) At an inlet temperature of 40 °C, (━) at an inlet temperature of 70 °C and (red bar) reduction that occurred when subtracting the distribution curve at 70 °C with the curve at 40 °C.

6.7.2 Effect of adding an ultrasonic mechanism to a two-fluid nozzle to produce ultrasound-modulated two-fluid (UMTF) atomization

Simple pressure nozzle and rotary atomizers are widely known in a spray drying industry. A two-fluid nozzle, although relatively well-known, is not well-explored and well-utilized. A new spray technique, called ultrasound-modulated two-fluid (UMTF) atomization, combines the ultrasound mechanism with the two-fluid mechanism. It is based on resonance between capillary waves generated by ultrasound and those generated by high atomizing air velocity. When functioning on its own, both techniques produced capillary waves which are regarded as ligaments in two-fluid atomization and standing waves in ultrasonic atomization. During the UMTF atomization, ultrasound creates capillary waves and the high atomizing air velocity magnifies the amplitude of the waves.

Previous sections have shown the atomization performance of the fibre suspensions when using a two-fluid nozzle. The atomization was controlled by extensional resistance or elasticity, along with minimal effects by shear viscosity and surface tension. Adding the ultrasound mechanism to the two-fluid nozzle was first seen as an opportunity to improve the atomization performance of the two-fluid nozzle. To make it clear, the purpose here was to compare the performance between the two-fluid atomization with the UMTF atomization. It was not intended to investigate the performance of ultrasonic atomization. The hypothesis was that the vibration of the fibre suspensions at the nozzle tip due to the ultrasound mechanism will push and pull the liquid, and thus create standing waves or ligaments. The continued pushing and pulling actions of the liquid can be translated as stretching of the standing waves or ligaments. The application of a fast-moving atomizing air velocity will further stretch the ligaments and disperse the ligaments into droplets. The combined effect of ultrasound and high atomizing air velocity was expected to stretch the ligaments better at a position immediately below the nozzle exit and thus contribute to a better atomization performance compared to the performance of a pure two-fluid nozzle.

In the study, the UMTF atomization utilized a 5.0 wt.% WF 600 fibre suspension, a 60 kHz frequency, 100 Volts peak-to-peak voltage and 150 m/s atomizing air velocity. Two conditions were investigated, which were the two-fluid atomization of the fibre suspension with ultrasound switched off and two-fluid atomization with ultrasound switched on. Surprisingly, the performances of the two atomization were very similar. There were

filamentary structures at the position right below the nozzle exit, and the filamentary structures remained the same when the ultrasound was on. Several runs with different atomization conditions were performed which included lowering the fibre content to 3.0 wt.% WF 600 fibre suspension, increasing the voltage to the maximum allowable of 140 Volts and increasing and reducing the atomizing air velocity. All of these conditions still resulted in a very similar atomization performance between the pure two-fluid and UMTF nozzles. This observation suggests that the ultrasound mechanism was absent during the UMTF atomization. To understand deeper, the behaviour of the waves induced solely by the vibrating ultrasound mechanism was observed at 60 kHz and 100 Volts conditions, and in the case of fibre suspensions, no waves were produced. That is why the UMTF atomization of 5.0 wt.% WF 600 fibre suspension was very similar to the pure two-fluid atomization, as only the fast-moving atomizing air velocity acted to stretch the ligaments. With water, waves produced by the vibrating ultrasound mechanism were obviously present that resulted in an immediate break into droplets even without the application of fast-moving air velocity.

Previous studies have successfully improved the atomization of extensional and viscoelastic liquids by adding an ultrasound mechanism to a two-fluid nozzle (Tsai & Luu, 2000). However, all of them were using extensional liquids with low shear viscosity such as 9.2×10^{-3} Pa.s and 0.134 Pa.s. The relatively greater shear viscosity of the concentrated apple juice and fibre suspensions prevented the formation of waves by the ultrasound mechanism. This is because, the vibrational or oscillatory energy into the liquid was adsorbed due to viscous dissipation, instead of exciting the liquids into standing waves. In the case of the concentrated apple juice, the liquid first remained on the nozzle tip surface. The viscous dissipation that occurred at the nozzle tip possibly increased the temperature and after some time, the temperature of the liquid on the surface was increased. This behaviour reduced the shear viscosity of the concentrated apple juice at the nozzle tip. That is why atomization of concentrated apple juice using an ultrasound mechanism was observed after some time. However, this pattern was not observed with the fibre suspensions. Ramisetty et al. (2013) showed that no atomization is possible when liquid shear viscosity increases above the threshold value, even though viscous dissipation can increase the temperature at the nozzle tip during ultrasonic atomization.

The trials using UMTF nozzle highlights the importance of shear viscosity in affecting the overall atomization performance. In the case of fibre suspension atomization, it is believed

that the study on UMTF nozzle can be extended further that may yield a better atomization performance when compared to the use of a pure two-fluid nozzle. This may be possible by applying more energy to create the standing waves or vibrating the nozzle at a greater frequency. In the current study, the investigation on UMTF atomization was stopped due to the limited capabilities of the UMTF available. At this stage, it was concluded that the addition of ultrasound mechanism to the two-fluid atomization is not an efficient approach during the atomization of fibre suspensions.

6.8 Case study

This section intends to prepare for the continuation of the atomization process for the next stage e.g. to industrialize or capitalize the two-fluid atomization method of fibre suspensions. The atomization process that occurs inside a spray dryer is followed by a drying process. Spray dryers have different capacities. The two available spray dryers at Massey University are a small-scale spray dryer with 45 mL/min feed rate and a pilot plant-scale spray dryer with 250 mL/min feed rate. Previous sections show that the fast-moving air velocity is the key mechanism in atomizing the fibre suspensions using a two-fluid nozzle due to the high stretching rate of the ligaments or filaments. The aim of this section was to investigate whether the two-fluid nozzle can be used inside the two scale spray dryers to successfully atomize the fibre suspensions. The findings found so far on the two-fluid atomization of 5.0 wt.% fibre suspensions were used to predict and substantiate the performance inside the two spray dryers. Weber number, *We*, as shown in Equation 6.2 is used to represent the ratio of disruptive forces to the stabilizing forces. Changing the feed rates will affect the *We* number.

Table 6.3 shows the conditions and parameters during the atomization of 5.0 wt.% WF 600 fibre suspension at different feed rates but at a similar atomizing air velocity of 150 m/s. To predict the atomization performance inside the two spray dryers, a three-dimensional plot was built, as shown in Figure 6.20, which can be regarded as an atomization map. The data used to build the plot was taken from the droplet sizes of 5.0 wt.% AF 400-30, 5.0 wt.% WF 101, 5.0 wt.% WF 600 and 5.0 wt.% citrus fibre suspensions explained previously in Section 6.4.1. Based on the plot, it is desired to predict the D(v,50) inside the two different feed rate spray dyers based on the competing effect between *We* (which represents

the disrupting force due to the fast-moving atomizing air velocity) and relaxation time, τ_r (which represents the stabilizing force due to the extensional resistance). The atomization map is not for general or universal use, instead, it was built purposely to predict the D(v,50) inside the two different spray dryers. The map is also limited to certain ranges of *We* and τ only.

Table 6.3 The conditions and parameters involved during three different atomization cases. The original study corresponds to the parameters used in the previous sections when explaining the atomization behaviour of fibre suspensions while case studies 1 and 2 correspond to the decrease and increase of the feed rates from the original study, respectively.

Parameters	Original study	Case study 1 (inside a small-scale spray dryer)	Case study 2 (inside a pilot plant-scale spray dryer)
Orifice size (mm)	1.5	1.5	1.5
Feed rate (mL/min)	90	45	250
Feed velocity (m/s)	0.85	0.50	2.5
Atomizing air velocity (m/s)	150	150	150
Weber number, *We*	5.89×10^5	5.92×10^5	5.76×10^5

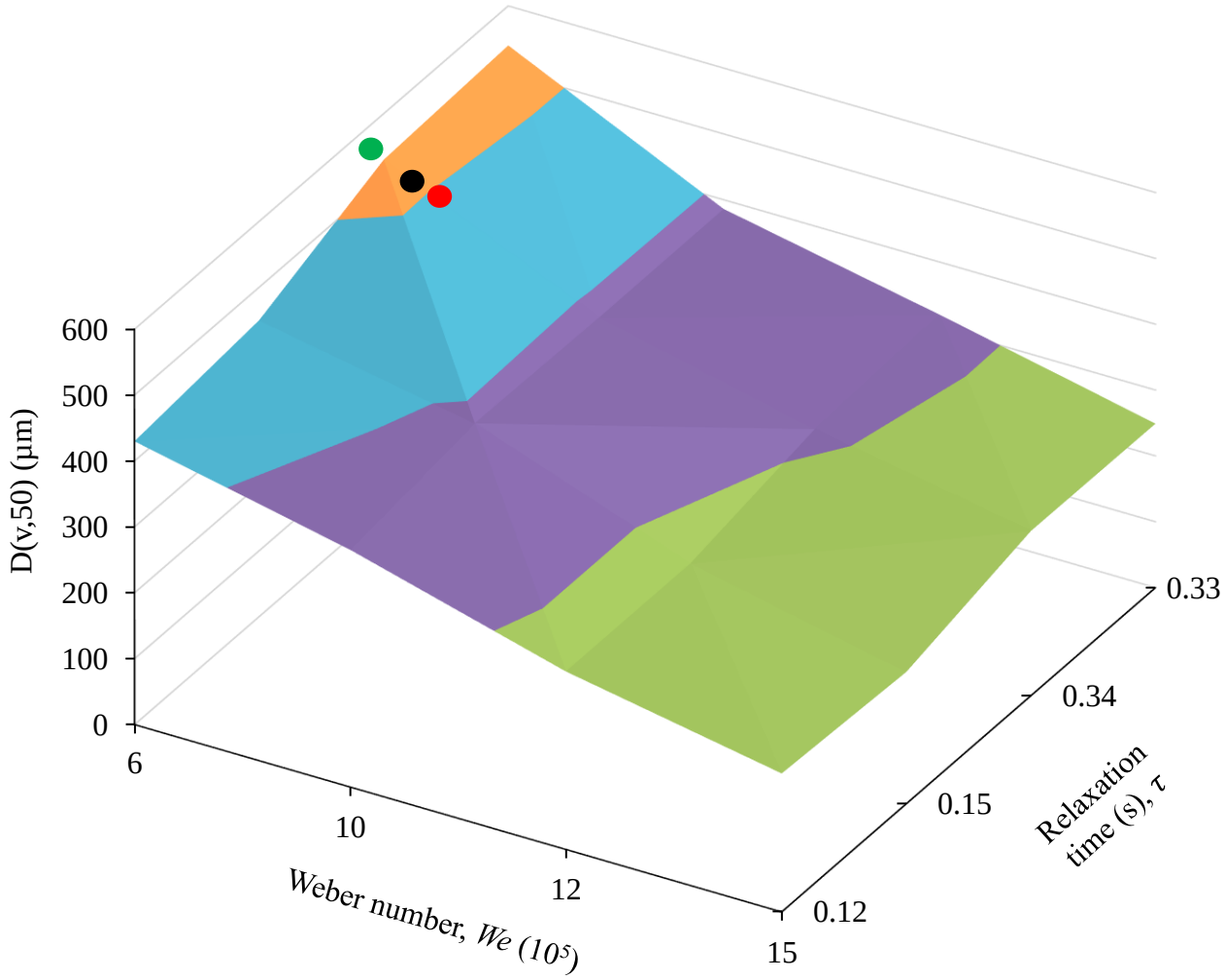

Characterization of the atomization performance based on the plot				
Ratings (from 5-worst to 1-best)			Descriptions	D(v,50)
	5	all atomized and produced droplets but differed in drop sizes and bridge connecting droplets	incomplete atomization (a lot of unbroken filaments)	500-600
	4		coarse atomization (still with some unbroken filaments)	400-500
	3		acceptable atomization performance	300-400
	2		good atomization	200-300
	1		desired atomization	100-200
	0	undesirable	fine atomization	0-100

Figure 6.20 Atomization map that shows the effect of two parameters which are the Weber number, We and the relaxation time, $\boldsymbol{\tau_r}$ on the final droplet size, D(v,50), during the atomization of fibre suspensions.

As shown in Table 6.3, the *We* of the different case studies were very close to each other. This also applied to the *We* at greater atomizing air velocities. All case studies dealt with 5.0 wt.% WF 600 fibre suspension, which corresponds to the relaxation, τ, of 0.34 in Figure 6.20. The value of the *We* at 150 m/s atomizing air velocity of each case was identified and pointed out in Figure 6.20. Theoretically, it was predicted that the change in the feed rate from the original rate of 90 mL/min to 45 mL/min and 250 mL/min will result in an insignificant change in the D(v,50), since the *We* were very close to each other. This is obvious from the plot in Figure 6.20. Experiments were conducted at different feed rates of 45 mL/min and 250 mL/min to confirm the hypothesis above. The parameters involved during the experiments were as tabulated in Table 6.3. From the experimental observation, the D(v,50) of the atomization at 45 mL/min feed rate was very similar to the D(v,50) of when atomization occurred at 90 mL/min, with a maximum difference of approximately 5.0% only. In contrast, incomplete atomization or large droplets were observed at a position 50 mm below the nozzle exit, when the feed rate was increased to 250 mL/min. This is evidenced in Figure 6.21, where no droplets but big chunks of unfinished sheared and strained liquid are obvious in the images. The images were taken at a position 50 mm below the nozzle exit, at an atomizing air velocity of 150 m/s and at a feed rate of 250 mL/min. Similar conditions but with a feed rate of 90 mL/min produced a better atomization performance and smaller droplets as in Figure 6.7, where droplets are visible in the images. Increasing the air velocity beyond 150 m/s at a feed rate of 250 mL/min still resulted in an incomplete atomization, or at least, large chunks of liquids were observed, as shown in Figure 6.21. These findings confirm that the two-fluid nozzle can be used inside the small-scale spray dryer to atomize the fibre suspensions, but in contrast, the two-fluid nozzle could not be used inside the pilot plant-scale spray dryer which indicates that different nozzles need to be used.

The atomization of 5.0 wt.% fibre suspensions is possible inside the small-scale spray dryer with a feed rate of 45 mL/min by using the current nozzle, but unfeasible inside the pilot plant-scale spray dryer with a feed rate of 250 mL/min. Previously, the fast-moving atomizing air velocity, represented by the high *We*, was accepted as the mechanism that controls the atomization of the fibre suspensions. However, this hypothesis is proven to have a limitation. The high *We*, as occurred inside the pilot plant-scale spray dryer was very similar to the other cases but resulted in inefficient atomization compared to the other cases that managed to achieve complete and good atomization. The limitation to the effect of *We*,

and thus the fast-moving air velocity in atomizing the fibre suspensions, is set by the ratio of atomizing air flow rate to liquid feed rate, $\dot{m}_A/\dot{m}_L$. Table 6.4 lists the corresponding $\dot{m}_A/\dot{m}_L$ for each case. The $\dot{m}_A/\dot{m}_L$ of 0.25 corresponds to the feed rate of the original study at 90 mL/min and is regarded as the lowest ratio possible to maintain a good atomization performance of fibre suspensions. Atomization of fibre suspensions that occurs below the ratio limit of 0.25 will result in incomplete or inefficient atomization, like in the case of the pilot plant-scale spray dryer. Previous studies also show that during a two-fluid atomization, the droplet sizes were significantly increased, or the atomization performance were poorer when the $\dot{m}_A/\dot{m}_L$ went below 0.2 or 0.3. Refer to the plots of droplet sizes against $\dot{m}_A/\dot{m}_L$ in Figure 6.22, reproduced from Nimmo et al. (2002), Azevedo et al. (2013) and Krawczyk et al. (2016). Chan et al. (2012) concluded that the critical value of $\dot{m}_A/\dot{m}_L$ is 0.25.

Overall, it means that a good atomization performance of fibre suspensions was achieved by using a two-fluid nozzle that utilized the mechanism of a fast-moving air velocity to shear the liquid jet, break and stretch the ligaments into droplets. Increasing the atomizing air velocity resulted in a greater *We*, and thus a better atomization performance and smaller droplet sizes. The atomization performance was controlled by the high atomizing air velocity and *We*, as long as the atomization occurred at an air-to-liquid ratio, $\dot{m}_A/\dot{m}_L$ of greater than 0.25.

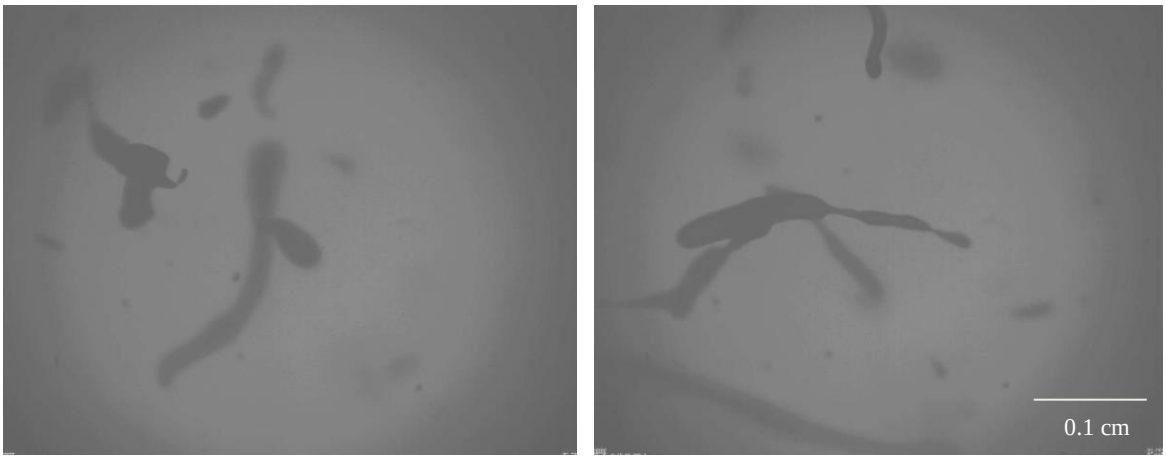

Figure 6.21 Photographs of the droplets of 5.0 wt.% WF 600 fibre suspension at an atomizing air velocity of 150 m/s and at a feed rate of 250 mL/min. Images were captured at a position 50 mm below the nozzle exit.

Table 6.4 The corresponding ratio of atomizing air flow rate to liquid feed rate, $\dot{m}_A/\dot{m}_L$, for each case with different feed rates.

Case	Feed rate (mL/min)	$\dot{m}_A/\dot{m}_L$
Original study	90 mL/min	0.25
Case study 1 (inside a small-scale spray dryer)	45 mL/min	0.46
Case study 2 (inside a pilot plant-scale spray dryer)	250 mL/min	0.08

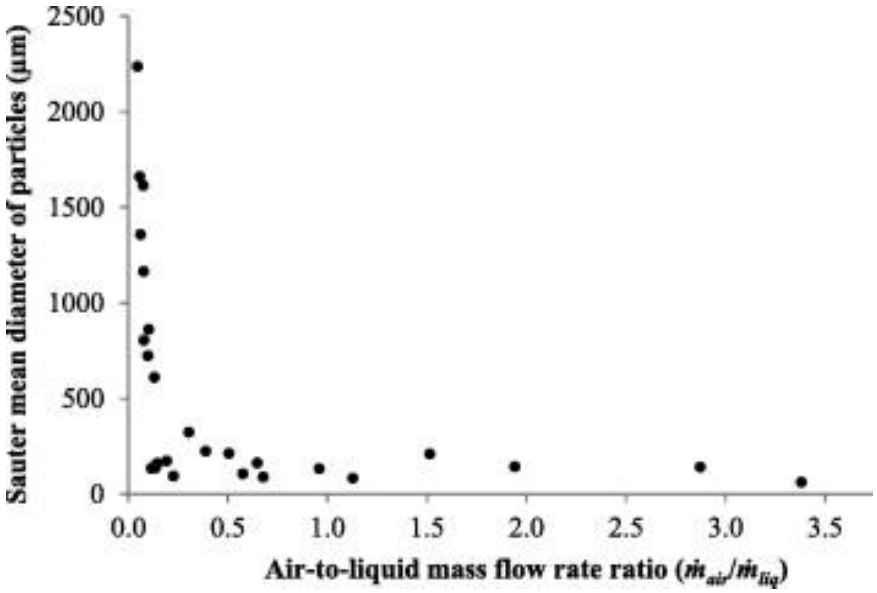
Sauter mean diameter of particles (μm)
2500
2000
1500
1000
500
0
0.0
0.5
1.0
1.5
2.0
2.5
3.0
3.5
Air-to-liquid mass flow rate ratio ($\dot{m}_{air}/\dot{m}_{liq}$)

(a)

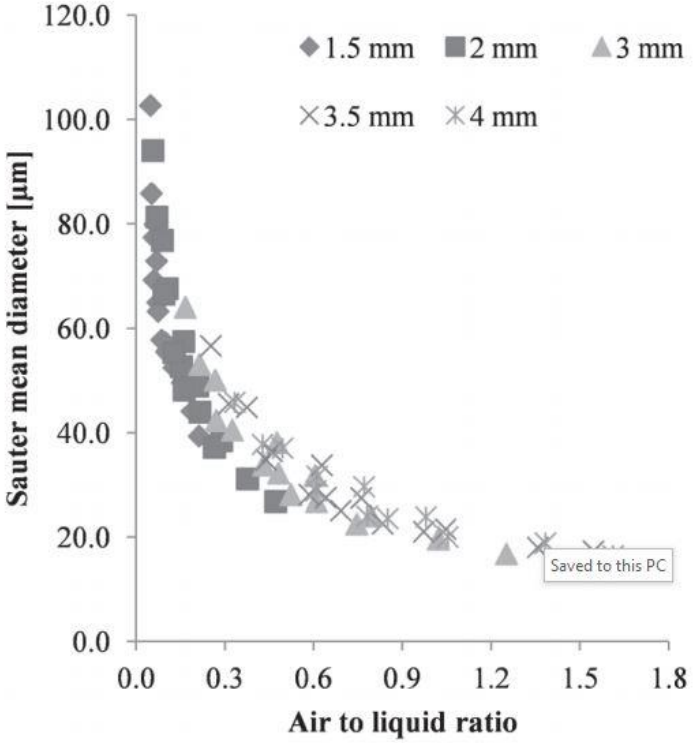
1.5 mm
2 mm
3 mm
3.5 mm
4 mm
Sauter mean diameter [μm]
120.0
100.0
80.0
60.0
40.0
20.0
0.0
0.0
0.3
0.6
0.9
1.2
1.5
1.8
Air to liquid ratio
Saved to this PC

(b)

Continue →

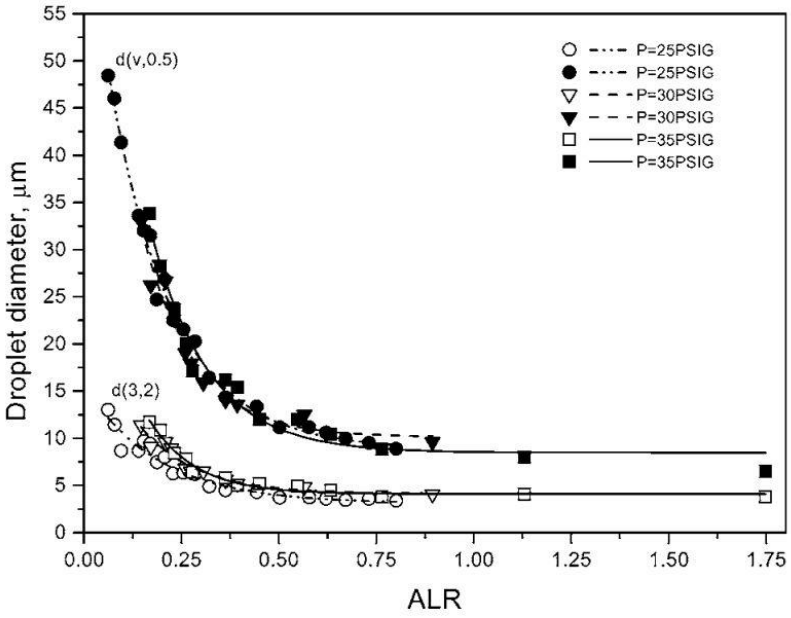

(c)

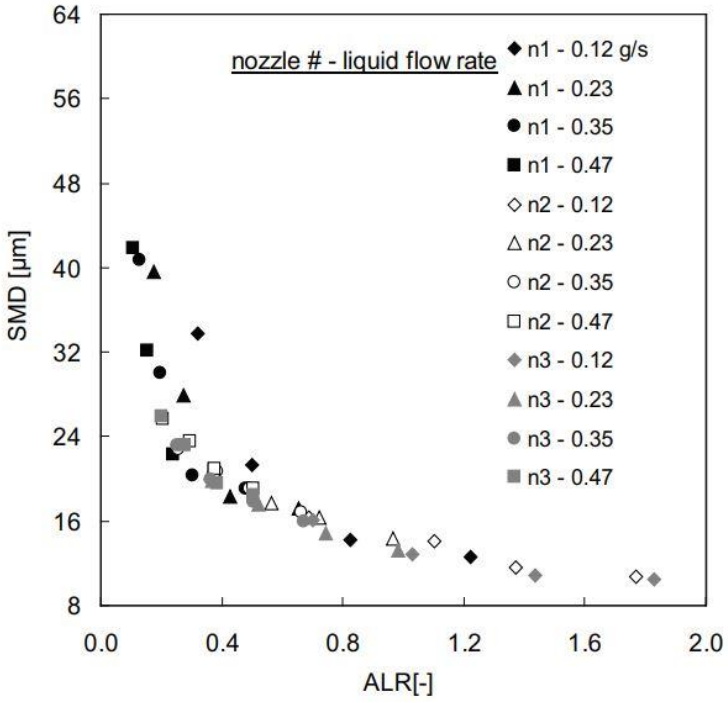

(d)

Figure 6.22 The relationships between droplet sizes and air-to-liquid ratio, $\dot{m}_A/\dot{m}_L$, reproduced from literature. (a) Chan et al. (2012), (b) Krawczyk et al. (2016), (c) Nimmo et al. (2002) and (d) Azevedo et al. (2013).

6.9 Conclusions

- Visualization studies of the atomization performance of fibre suspensions which exhibited both shear and extensional properties were carried out. The shear rheology of fibre suspensions did not suggest any significant difference in the atomization performance when compared to Newtonian atomization.
- However, when the atomizing air velocity was increased, the spray visualization showed that the extensional rheology of the fibre suspensions significantly affected the atomization behaviour, specifically at the final breakup stage. The final breakup pattern of the fibre suspensions showed filamentary structures connecting successive droplets together. This pattern is absent in Newtonian atomization.
- These filamentary structures contributed to the formation of large droplet sizes of fibre suspension droplets.
- Droplet size analysis showed that the size of fibre suspension droplets was highly dependent on the aspect ratio of fibres used but this effect was reduced when much greater atomizing air velocity was applied during the atomization.
- This study shows that the atomization of fibre suspensions, which exhibited extensional properties, can be achieved by using a two-fluid nozzle and at high atomizing air velocity. The atomization should always proceed at $\dot{m}_A/\dot{m}_L$ above 0.25. At these conditions, smaller spherical droplets of fibre suspensions were produced that will assist the performance of drying in the spray dryer.
- The droplet sizes of the fibre suspensions that were obtained experimentally, were validated and compared with the theoretical prediction by using Keshavarz et al. (2015) relationship. The experimental and theoretical droplet sizes matched very well.
- Using a two-fluid nozzle, the droplets sizes of the fibre suspensions insignificantly reduced when the temperature of the inlet fibre suspensions was increased. No change was observed to the atomization performance when an ultrasonic mechanism was added to the two-fluid nozzle.
- Morphology of the frozen droplets of fibre suspensions revealed that the fibres were trapped inside the droplets.

References

Aliseda, A., Hopfinger, E., Lasheras, J. C., Kremer, D., Berchielli, A., & Connolly, E. (2008). Atomization of viscous and non-Newtonian liquids by a coaxial, high-speed gas jet. Experiments and droplet size modeling. *International Journal of Multiphase Flow, 34*(2), 161-175.

Azevedo, C. G., de Andrade, J. C., & de Souza Costa, F. (2013). Effects of nozzle exit geometry on spray characteristics of a blurry injector. *Atomization and Sprays, 23*(3).

Bailardi, G., Negri, M., & Ciezki, H. (2010). Several aspects of the atomization behavior of various Newtonian fluids with a likeon-like impinging jet injector. *Paper presented at the Proceedings of the 23rd European Conference on Liquid Atomization and Spray Systems.*

Brennan, J., Herrera, J., & Jowitt, R. (1971). A study of some of the factors affecting the spray drying of concentrated orange juice, on a laboratory scale. *International Journal of Food Science & Technology, 6*(3), 295-307.

Buckner, H. N., & Sojka, P. E. (1991). Effervescent atomization of high-viscosity fluids: Part I. Newtonian liquids. *Atomization and Sprays, 1*(3).

Chan, E.-S., Lim, T.-K., Ravindra, P., Mansa, R. F., & Islam, A. (2012). The effect of low air-to-liquid mass flow rate ratios on the size, size distribution and shape of calcium alginate particles produced using the atomization method. *Journal of Food Engineering, 108*(2), 297-303.

Chao, K., Child, C., Grens, E., & Williams, M. (1984). Antimisting action of polymeric additives in jet fuels. *AIChE Journal, 30*(1), 111-120.

Chigier, N., & Farago, Z. (1992). Morphological classification of disintegration of round liquid jets in a coaxial air stream. *Atomization and Sprays, 2*(2).

Christanti, Y., & Walker, L. M. (2006). Quantifying air atomization of viscoelastic fluids through fluid relaxation times. *Atomization and Sprays, 16*(7).

Derby, B. (2010). Inkjet printing of functional and structural materials: Fluid property requirements, feature stability, and resolution. *Annual Review of Materials Research, 40*, 395-414.

Fredrickson, A. G. (1964). *Principles and applications of rheology*: Prentice-Hall.

Goula, A. M., Karapantsios, T. D., Achilias, D. S., & Adamopoulos, K. G. (2008). Water sorption isotherms and glass transition temperature of spray dried tomato pulp. *Journal of Food Engineering, 85*(1), 73-83.

Hanson, A., Domich, E., & Adams, H. (1963). Shock tube investigation of the breakup of drops by air blasts. *The Physics of Fluids, 6*(8), 1070-1080.

Hede, P. D., Bach, P., & Jensen, A. D. (2008). Two-fluid spray atomisation and pneumatic nozzles for fluid bed coating/agglomeration purposes: A review. *Chemical Engineering Science, 63*(14), 3821-3842.

Hoyt, J., Taylor, J., & Runge, C. D. (1974). The structure of jets of water and polymer solution in air. *Journal of Fluid Mechanics, 63*(4), 635-640.

Keshavarz, B., Sharma, V., Houze, E. C., Koerner, M. R., Moore, J. R., Cotts, P. M., . . . McKinley, G. H. (2015). Studying the effects of elongational properties on atomization of weakly viscoelastic solutions using Rayleigh Ohnesorge Jetting Extensional Rheometry (ROJER). *Journal of Non-Newtonian Fluid Mechanics, 222*, 171-189.

Kim, H., Lee, Y., & Cho, H. (2011). Levitation time measurement of water drops on the surface of liquid nitrogen. *Journal of the Korean Physical Society, 58*(6), 1628-1632.

Krawczyk, P., Badyda, K., & Młynarz, S. (2016). Effect of the air to water ratio on the performance of internal mixing two-fluid atomiser. *Chemical and Process Engineering, 37*(4), 461-471.

Lefebvre, A. (1988). *Atomization and sprays* (Vol. 1040): CRC press.

Lindstedt, R., Luff, D., & Whitelaw, J. (2005). Velocity and strain-rate characteristics of opposed isothermal flows. *Flow, turbulence and combustion, 74*(2), 169-194.

Mani, S., Jaya, S., & Das, H. (2002). Sticky issues on spray drying of fruit juices. *Paper presented at the ASAE/CSAE North-Central Intersectional Meeting.*

Mansour, A., & Chigier, N. (1995). Air-blast atomization of non-Newtonian liquids. *Journal of Non-Newtonian Fluid Mechanics, 58*(2–3), 161-194.

Marmottant, P., & Villermaux, E. (2004). Fragmentation of stretched liquid ligaments. *Physics of Fluids, 16*(8), 2732-2741.

Masters, K. (1979). Spray drying handbook. *Spray drying handbook.*(Ed. 3).

Mun, R. P., Young, B. W., & Boger, D. V. (1999). Atomisation of dilute polymer solutions in agricultural spray nozzles. *Journal of Non-Newtonian Fluid Mechanics, 83*(1–2), 163-178.

Nimmo, W., Hind, D., Ali, N., Hampartsoumian, E., & Milne, S. (2002). The production of ultrafine zirconium oxide powders by spray pyrolysis. *Journal of Materials Science, 37*(16), 3381-3387.

Ochowiak, M., Matuszak, M., & Włodarczak, S. (2017). The analysis of pneumatic atomization of Newtonian and non-Newtonian fluids for different medical nebulizers. *Drug Development and Industrial Pharmacy, 43*(12), 1999-2010.

Rajan, R., & Pandit, A. (2001). Correlations to predict droplet size in ultrasonic atomisation. *Ultrasonics, 39*(4), 235-255.

Ramisetty, K. A., Pandit, A. B., & Gogate, P. R. (2013). Investigations into ultrasound induced atomization. *Ultrasonics Sonochemistry, 20*(1), 254-264.

Ryzhkin, I. A., & Petrenko, V. F. (1997). Physical mechanisms responsible for ice adhesion. *The Journal of Physical Chemistry B, 101*(32), 6267-6270.

Shu, B., Yu, W., Zhao, Y., & Liu, X. (2006). Study on microencapsulation of lycopene by spray-drying. *Journal of Food Engineering, 76*(4), 664-669.

Tsai, S. C., & Luu, P. (2000). Ultrasound-modulated two-fluid atomization of dilute polymer solutions. *AIChE Journal, 46*(8), 1650-1661.

Varga, C. M., Lasheras, J. C., & Hopfinger, E. J. (2003). Initial breakup of a small-diameter liquid jet by a high-speed gas stream. *Journal of Fluid Mechanics, 497*, 405-434.

Verma, A., & Singh, S. V. (2015). Spray drying of fruit and vegetable juices – A review. *Critical Reviews in Food Science and Nutrition, 55*(5), 701-719.

Wierzba, A. (1990). Deformation and breakup of liquid drops in a gas stream at nearly critical Weber numbers. *Experiments in Fluids*, *9*(1-2), 59-64.

Chapter 7 Conclusions and Recommendations

Atomization of fibre suspensions occurs before the drying stage inside a spray dryer. Atomization performance of fibre suspensions depends on various factors, these can be divided into two categories; the physical properties of the fibre suspensions and nozzle parameters. The physical properties include the shear and extensional rheology, and the density and surface tension of the fibre suspensions. The main nozzle parameters consist of the type of nozzle, the feed flow rate and temperature, and the atomizing air velocity.

These conclusions were gained when answering the questions addressed in the introduction in Chapter 1.

A) *Is it possible to spray or atomize the fibre suspension from a liquid into droplets?*
Yes, atomization of fibre suspension from a liquid into droplets is possible and achievable.

B) *What factors influence the successful atomization from a liquid into droplets?*
Shear and extensional rheology of the fibre suspensions influenced the atomization performance. Surface tension also affected the atomization but was a minor factor.

The fibre suspensions were shown to be a shear thinning liquid with a Newtonian plateau. Tests performed on a rotary rheometer showed the shear viscosity of the fibre suspensions reduced as the shear rates was increased up to 1000 s^{-1}. Extended studies performed on a capillary viscometer showed that the shear viscosity further reduced up until approximately 30 000 s^{-1} shear rate, and beyond that point, a plateau viscosity was reached. The shear viscosity is dependent on the fibre aspect ratio where low aspect ratio fibre suspensions exhibited lower shear viscosity relative to the high aspect ratio fibre suspensions. The difference in the shear viscosity between the low and high aspect ratio fibre suspensions reduced at greater shear rates and eventually they reached a similar plateau value. A number of previous studies in the literature have shown the shear thinning behaviour of the fibre suspensions. All studies were restricted to lower range of shear of less than 1000 s^{-1} shear rates, no previous study demonstrated the occurrence of the viscosity

plateau. The capability to show the shear thinning behaviour of fibre suspensions at shear rates of more than 20 000 s^{-1} is important and useful as this high range of shear rates is applicable in the atomization process. It showed there is an operational limit to the effectiveness of the application shear to reducing the energy requirements for atomization.

Stretching of the fibre suspensions resulted in an extensional resistance or elasticity. This conclusion was deduced based on the capillary breakup extensional rheometer technique where the rheometer was built in-house for this study. The relaxation time, τ_r and the transient extensional viscosity, η_E^+ were calculated to quantitatively study the extensional rheology of the fibre suspensions. Both properties were dependent on the fibre aspect ratio, with greater τ and η_E^+ for the higher aspect ratio fibres. The transient extensional viscosity, η_E^+ of fibre suspensions, was relatively greater than its corresponding shear viscosity at a similar fibre fraction. The extensional rheology of the fibre suspensions influenced the selection of the nozzle design and its performance. The effect of extensional rheology of a liquid on atomization performance is one of the things that previous studies have neglected.

C) *What type of atomization technique, or what type of atomizer can be used to achieve the successful atomization from a liquid into droplets?*

Successful atomization of fibre suspensions from a liquid into droplets can be achieved by using a two-fluid nozzle and at high atomizing air velocity.

The two-fluid nozzle was chosen as the main nozzle to atomize the fibre suspensions. This study has shown that fibre suspensions can be successfully atomized from a liquid into droplets by using a two-fluid nozzle and at high atomizing air velocity. Although the atomization performance was low, and droplet sizes were relatively big at a low atomizing air velocity of 150 m/s due to the extensional resistance of the fibre suspensions, the performance was improved, and droplets sizes were reduced at the higher atomizing air velocity of 240 m/s. The two-fluid nozzle, together with the atomization conditions found in the study, can be applied during the spray drying inside a small-scale spray dryer.

D) Is the selected atomization technique or atomizer able to produce droplets as needed by the drying stage?

Yes. By using the two-fluid nozzle and at high atomizing air velocity, small, symmetrical and spherical droplets were produced that match the usual requirements inside the spray dryer. The final average droplet sizes produced were in the range of 200 – 250 µm.

E) What are the limitations of the findings?

The research, while answering many questions about the atomization of fibre suspensions, has also raised a lot of questions that were not addressed. Questions identified but were not answered are listed below. These questions should be answered in the future work.

i) What is the actual shear and extensional rates experienced by the fibre suspensions during the atomization using a two-fluid nozzle? The current study has theoretically predicted the shear and extensional rates but due to limited capabilities, this was not confirmed experimentally. Although the actual values are not experimentally known during the atomization, the ability to demonstrate the expected values is a useful addition to the literature.

ii) More extensional rheology studies using a wider range of fibres should be continued, especially by looking at the effect of aspect ratio and flexibility of the fibres. This includes the measurement of Young's modulus of the different fibres used.

iii) The addition of an ultrasonic mechanism to improve the atomization performance by a two-fluid nozzle should be explored in more depth. The equipment capabilities were limited in the current study, and a more powerful ultrasonic may demonstrate different results.

iv) Because of the rheology of fibre suspensions shown in the study, it was decided that a simple pressure nozzle and rotary atomizer would be unlikely to work. This is an area that should be confirmed experimentally.

Other recommended future work includes:

i) A dimensional analysis study to characterize the atomization performance of extensional liquids should follow. This should include the development of an atomization map specifically for extensional liquids. The existence of

the atomization map will aid in scaling up the process during atomization or spray drying.

ii) Studies on the drying of fibre suspensions inside a spray dryer by using a two-fluid nozzle should follow.

Appendices

Appendix A Surface tension of water at different temperatures.

The following table listed the surface tension of water at different temperatures ranging between 5 °C to 90 °C. The data is reproduced from Vargaftik et al. (1983).

Temperature (°C)	Surface tension (mN/m)
5	74.95
10	74.23
15	73.50
20	72.75
25	71.99
30	71.20
35	70.41
40	69.60
45	68.78
50	67.94
55	67.10
60	66.24
65	65.36
70	64.47
75	63.58
80	62.67
85	61.75
90	60.82

Appendix B MATLAB code generated to digitally measure the filament diameter during the filament thinning process on portable extensional rheometer.

The following coding was written to standardize the measurement of filament diameter. The coding could be used to analyse a single, or hundreds or thousands of images. Step by step procedures in executing the measurement are as follow:

1) Select the desired file that contains the images of filament by specifying the file URL.

```
URL ='G:\Trial with 52% 55degre\Run 12\Run 12_files\';
srcFiles = dir([URL '******.tif']);
total_image = length(srcFiles);
tt=5;
```

2) Read the first image after the stretching stop, based on the file specified in the URL and put the image name into the coding.

```
first_image = imread ([URL, '000098', '.tif']);
```

3) Filter the image and convert it to binary image.

```
fst =imsharpen(first_image);
fst = medfilt2(fst, [tt tt]);
fst = im2bw(fst,0.3);
fst = imfill(fst,'holes');
fst = bwareaopen(fst, 400);
fst = ~fst;
figure
imshow(fst)
[fst, rect] = imcrop(fst);
imshow(fst)
hold on
```

4) Specify and record the interested coordinates in the first image.

```
disp('Choose top left point to measure, then press enter')
[x1, y1] = getpts;
[x1] = round(x1);
[y1] = round(y1);
disp('Choose bottom left point to measure, then press enter')
[x2, y2] = getpts;
[x2] = round(x2);
[y2] = round(y2);
disp('Choose upper sizing point to measure, then press enter')
[x3, y3] = getpts;
[x3] = round(x3);
[y3] = round(y3);
disp('Choose lower sizing point to measure, then press enter')
[x4, y4] = getpts;
[x4] = round(x4);
[y4] = round(y4);
i=1;
```

5) Get the horizontal distance between point 3 and point 4 that has been selected previously for the sizing scale.

```
for y=y3:y4
    C=fst(y,:);
    [p1,q1]=find(1==mean(C,3),1,'first');
    [p2,q2]=find(1==mean(C,3),1,'last');
    q1 = q1(1);
    q2 = q2(1);
    allsize(i,:) = 4/(q2-q1);
    P = plot([q1 q2], [y y], 'r-')
    i = i+1
end
    size = mean(allsize);
```

6) Apply procedures 3-5 to a set of images.

```
    o = 1;
for no_image = 000098:total image
    b = imread([URL, num2str(no_img,'%06i'), '.tif']);
    b=imsharpen(b);
    b= medfilt2(b, [tt tt]);
    b = im2bw(b,0.30);
    b = imfill(b,'holes');
    b = bwareaopen(b, 400);
    b = ~b;
    b = imcrop(b,rect);
    figure
    imshow(b)
    hold on
```

7) Find all the horizontal widths between x1 and x2 along the specified height y1 and y2 for a single image. Then, find the minimum value from the horizontal widths after finishing the loop. The loop stops at the image where the filament breaks.

```
    j=1;
for y=y1:y2
    D=b(y,:);
    [p3,q3]=find(1==mean(D,3),1,'first');
    [p4,q4]=find(1==mean(D,3),1,'last');
    q3 = q3(1);
    q4 = q4(1);
    P = plot([q3 q4], [y y], 'c-')
    width_for_1_image(j,:) = (q4-q3)*size;
    j = j+1;
end
    width(o,:) = min(width_for_1_image)
    o = o+1;
end
```

Appendix C MATLAB image analysis for droplets.

The following coding was written to measure the size of the droplets in a single image. The image may contain a single, or hundreds or thousands of droplets. Step by step procedures in executing the measurement are as follow. These procedures were repeated for a number of images to get the size of at least 1000 droplets.

1) Read the image.

```
X = imread('140000307.JPG');
%% Increase brightness %%
X = X + 100;
figure
imshow (X)
%% Specifying image known width in mm %%
width = 11;
%% To get scaling to multiply with pixel dimension at the end to get mm %%
scalingPerimeter = width/size(X,2);
scalingArea = (width/size(X,2))^2;
```

2) Change the background to white, while the droplets are in black. Crop the image to get an area filled with the interested droplets.

```
BW = im2bw(X,0.61);
figure
imshow (BW)
[BW, rect] = imcrop(BW);
```

3) Smoothen the image and remove any particles due to noise.

```
BW = medfilt2(BW,[7 7]);
```

```
figure
imshow (BW)
BW =~BW;
B = bwareaopen(BW, 2);
B=~B;
figure
imshow (B)
```

4) Apply contour to the image and segmented the droplets in the contoured image.

```
hold on
mask = false(size(B));
mask(50:100,40:100) = true;
BW= activecontour(B, mask, 200, 'edge');
visboundaries(BW,'Color','b');
title('Segmented image in blue');
```

5) Use ‘regionprops’ to calculate the properties of the segmented droplets. The properties include the number of droplets in the image and the centroid, area and perimeter of each droplet.

```
BW = ~BW;
s = regionprops(BW,'centroid','Area','Perimeter', 'MajorAxisLength');
centroids = cat(1, s.Centroid);
plot(centroids(:,1),centroids(:,2), 'b*')
numberOfBlobs = size(s, 1);
textFontSize = 10;
labelShiftX = -7;
for k = 1:numberOfBlobs
blobArea(k,:) = s(k).Area * scalingArea;
blobPerimeter(k,:) = s(k).Perimeter * scalingPerimeter;
blobMajorAxisLength(k,:) = s(k).MajorAxisLength * scalingPerimeter;
blobRoundness(k,:) = 4 * s(k).Area ./ (pi * s(k).MajorAxisLength.^2);
blobCentroid = s(k).Centroid;
```

```
        text(blobCentroid(1) + labelShiftX, blobCentroid(2), num2str(k),'Color','red',
        'FontSize', textFontSize, 'FontWeight', 'Bold');
        numberOfBlobs_inRow(k,:) = k;
end
```

6) Return the properties of the droplets found in procedure (5) in a table.

```
        TableOfProperties = table(numberOfBlobs_inRow, blobArea,blobPerimeter,
        blobMajorAxisLength, blobRoundness);
```

Appendix D Calculation of Rayleigh time, τ_R and relaxation time, τ_r from the inertia-capillary and elasto-capillary regimes respectively.

The following example shows the calculation for 7.0 wt.% WF 600 suspension. Other types and concentration of fibre suspensions should follow the same steps. Please refer Figure D1 for clearer interpretation. Step by step calculations are as follow:

1) Determination of Rayleigh time, τ_R

$$\tau_R = 1.95\sqrt{\rho {R_0}^3/\sigma} \qquad \text{Equation 5.3}$$

in which R_0 is the initial radius of the thinning filament, σ and ρ are the surface tension and density of the liquid respectively. Average density and surface tension were used. As the initial radius of filament is similar for all tests, the Rayleigh times, τ_R for every suspension are the same.

$$\tau_R = 1.95\sqrt{\rho {R_0}^3/\sigma} = 1.95\sqrt{\frac{1180\ \frac{kg}{m^3} \times (2 \times 10^{-3})^3}{66.78 \times 10^{-3}\ \frac{N}{m}}} = 0.023\ s$$

From the filament diameter profile of 7.0 wt.% WF 600 fibre suspension in Figure D1, the first 0.023 s is the inertia-capillary regime.

2) Determination of visco-capillary regime

$$D(t) = D_0 - \left(\frac{2x-1}{6}\right)\left(\frac{\sigma}{\mu_0}\right)t \qquad \text{Equation 5.4}$$

where D_0 is the initial diameter of the filament during the start of the visco-capillary regime. Regression of Equation 5.4 to the experimental data between t = 0.024 s and t

= 0.200 s in Figure D1 yield a linear regression line. This is shown in Figure D1. The regression analysis yields a x-value of 0.69. Previously, McKinley and Tripathi (2000) reported a value of x = 0.71 for the visco-capillary similarity solution.

3) Determination of relaxation time, τ_r

The data points after the viscous-capillary regime are simply assigned to be within the elasto-capillary regime.

$$\frac{D(t)}{D_0} = \left(\frac{GD_0}{2\sigma}\right)^{1/3} \exp[-t/(3\tau)] \qquad \text{Equation 5.2}$$

Regression of Equation 5.2 to the experimental data in the elasto-capillary regime enables the extraction of relaxation time, τ_r. For each fibre suspension, for example, 7.0 wt.% WF 600 fibre suspension, 3 filament diameter profiles similar to in Figure D1 were produced. Steps 1 to 3 were then applied to the other filament diameter profiles. In the case of 7.0 wt.% WF 600 fibre suspension, the average τ is equal to 0.7 $\pm$ 0.03 s.

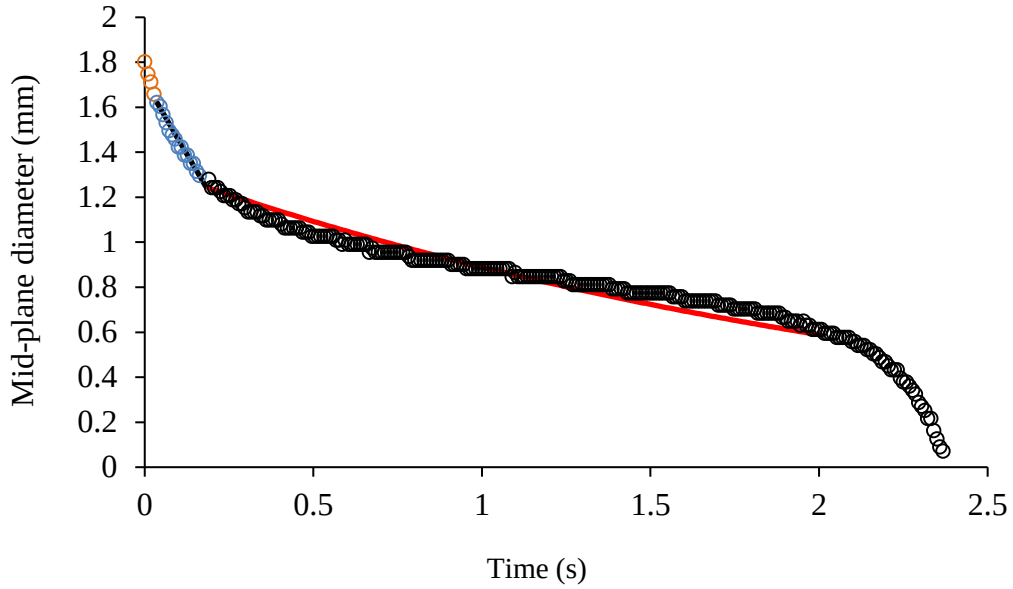

Figure D1: Filament diameter profile of the 7.0 wt.% WF 600 fibre suspension highlighting the identified different regimes. (○, orange colour) inertia-capillary regime, (○, blue colour) visco-capillary regime and (○, black colour) elasto-capillary regime. (black line) Regression line based on the visco-capillary regime and (red line) regression line based on the elasto-capillary regime.

Appendix E Filament diameter profiles for 5.0 wt.% and 7.0 wt.% fibre suspensions at 3 different measurements.

The following graphs show the filament thinning profile of 5.0 wt.% and 7.0 wt.% AF 400-30, WF 101, WF 600 and citrus fibre suspensions. Three capillary breakup tests were performed and thus three filament thinning profiles were produced for each fibre suspension.

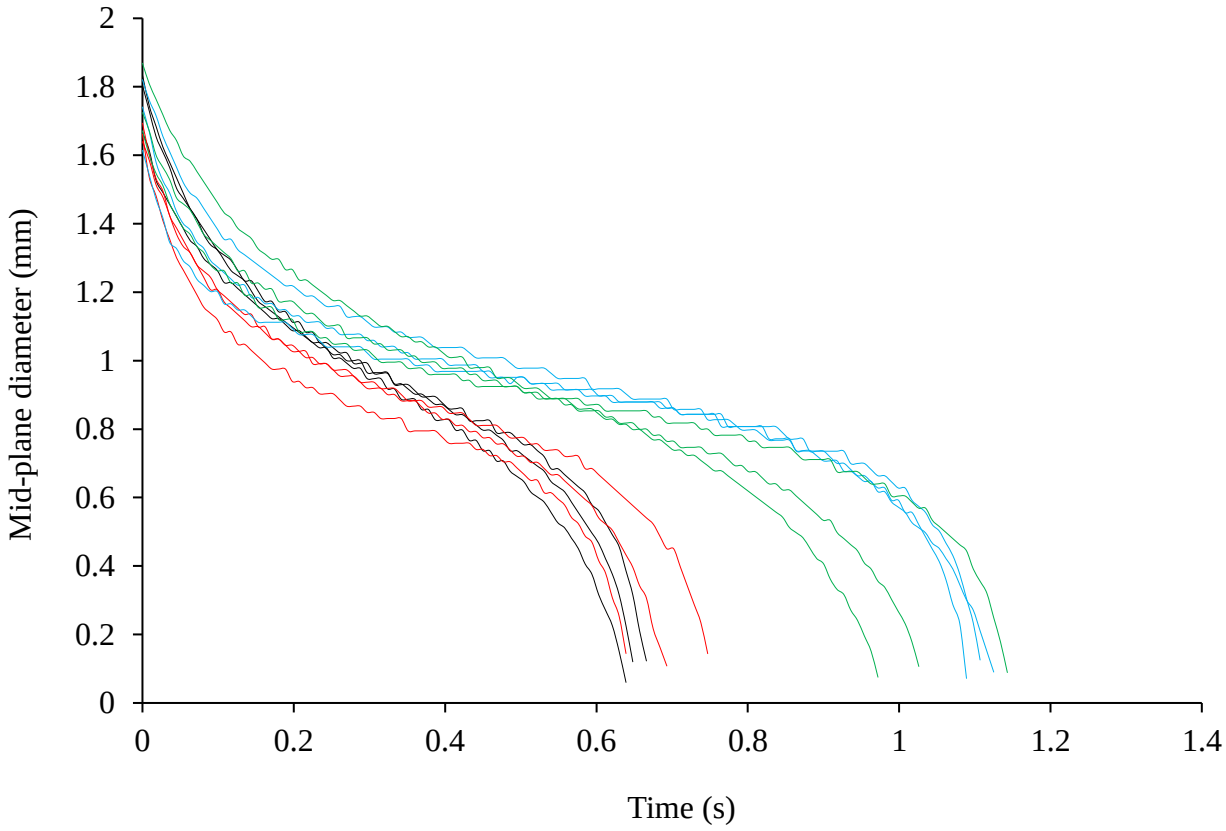

Figure E1 Filament diameter profile of 5.0 wt.% fibre suspensions measured on the portable extensional rheometer. (black line) AF 400-30 (red line) WF 101 (blue line) WF 600 and (green line) citrus fibre.

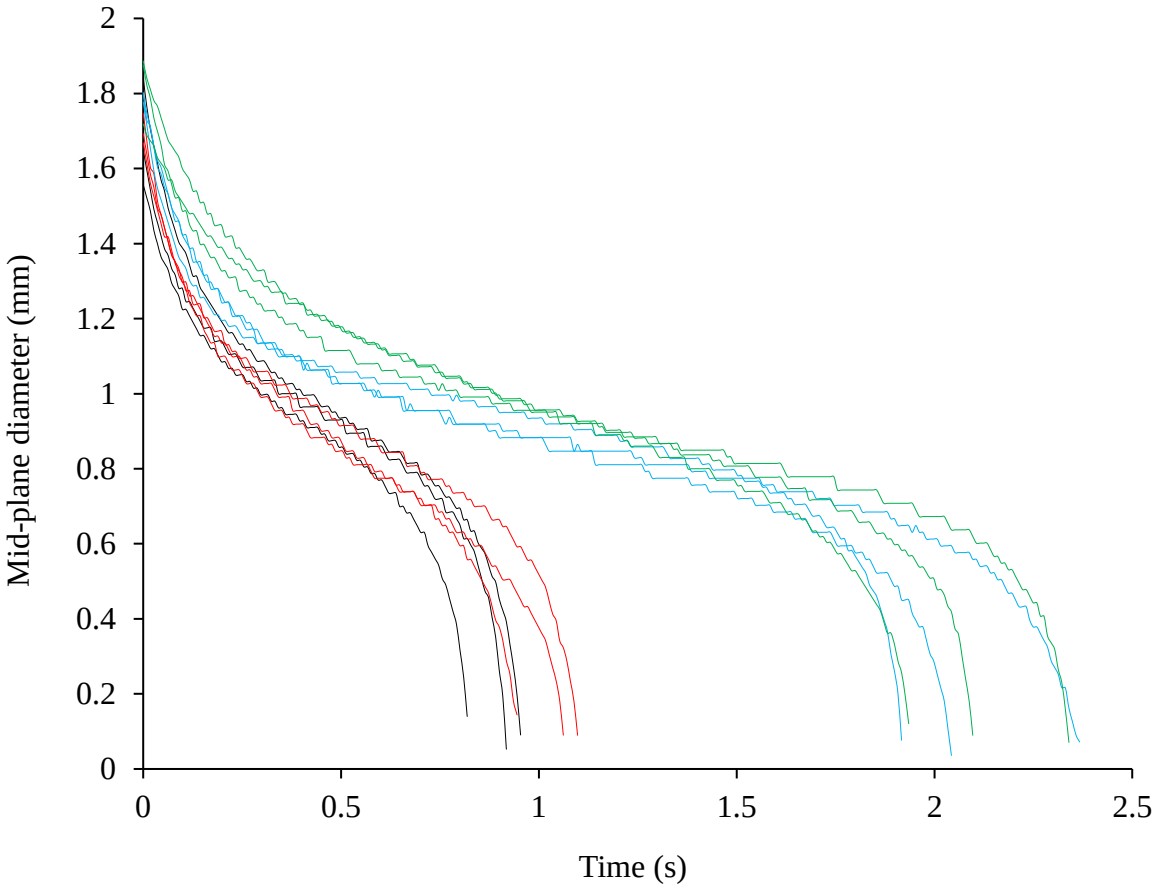

Figure E2 Filament diameter profile of 7.0 wt.% fibre suspensions measured on the portable extensional rheometer. (black line) AF 400-30 (red line) WF 101 (blue line) WF 600 and (green line) citrus fibre.

Appendix F Calculation of apparent extensional viscosity, η_E^+.

The following example shows the calculation for 7.0 wt.% WF 600 suspension. Other types and concentration of fibre suspensions should follow the same steps. Step by step calculations are as follow:

1) A similar filament diameter profile used in Figure D1 to determine the relaxation time, τ_r, was used again to obtain the transient extensional viscosity, η_E^+. The experimental data included in the calculation of the transient extensional viscosity, η_E^+ consists of the filament diameter from the visco-capillary and elasto-capillary regimes. A polynomial function was then fitted into the experimental filament diameter data, with certain polynomial order that best fits the data. For example, based on Figure F1, the function is as follow:

   $D(t) = -0.34t^5 + 2.04t^4 - 4.67t^3 + 5.13t^2 - 2.96t + 1.69$

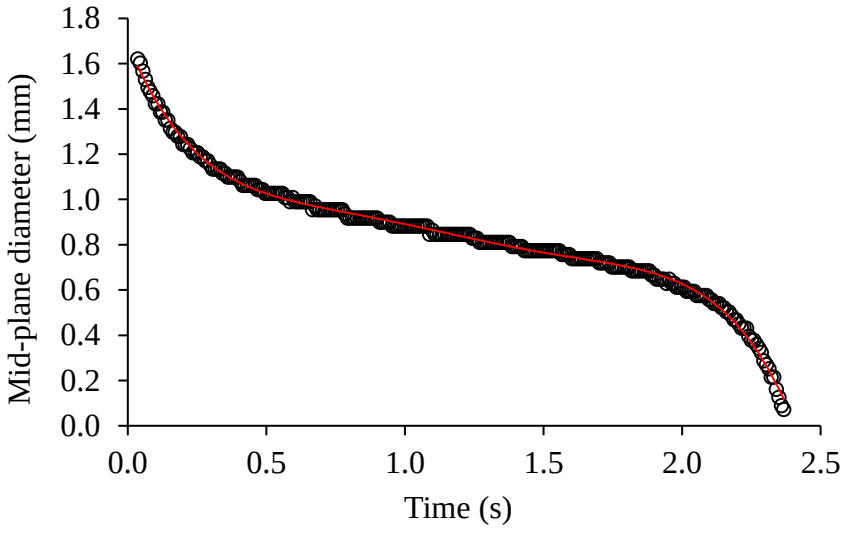

Figure F1 Filament diameter profile of the 7.0 wt.% WF 600 fibre suspension, with fitted polynomial function.

2) The function was then differentiated. The derivative is as follow:

   $dD(t)/dt = -1.7t^4 + 8.16t^3 - 14.01t^2 + 10.26t - 2.96$

The final derivative value, $dD(t)/dt$, for example, at time, $t = 0.5\ s$ for data in Figure F1 is equal to $-0.42\ mm/s$ or $-4.2\ \times 10^{-4}\ m/s$.

3) The final derivative value at every second was calculated as in step (2), and input into Equation 5.5 to find the transient extensional viscosity, η_E^+. Average surface tension was used for all fibre suspensions.

$$\eta_E^+ = -\sigma/(dD(t)/dt) \qquad \text{Equation 5.5}$$

$$\eta_E^+ = -\frac{66.78 \times 10^{-3}\ N/m}{-4.2\ \times 10^{-4}\ \frac{m}{s}} = 159\ Pa.s$$

Step (3) was repeated for the time range in Figure F1, to generate a curve of transient extensional viscosity, η_E^+.

Appendix G Passing-Bablok and Bland-Altman analyses to compare the D-values obtained by two different methods; MATLAB image analysis and Malvern Mastersizer.

1) Passing-Bablok regression analysis

   Let say:

   i) The droplet sizes generated by MATLAB image analysis = Y

   ii) The droplet sizes generated by Malvern Mastersizer = X

   Ideally, the results generated by MATLAB image analysis and Malvern Mastersizer are similar if Y = X.

   So, ideally $Y = (1)X + 0$

   Where 1 is the slope coefficient and 0 is the intercept. By implying that Malvern Mastersizer is the standard method, Passing-Bablok attempts to estimate the slope coefficient and intercept of the MATLAB image analysis results by regression to the experimental data. An ideal situation is to obtain a slope coefficient equal to 1 and an intercept equal to 0. However, in Passing-Bablok analysis, a 95% confidence interval (95% CI) was calculated with regard to the slope coefficient and intercept, to see whether a value of 1 and 0 lies within the 95% CI, respectively. An example of Passing-Bablok analysis performed on 5.0 wt.% WF 600 fibre suspension is shown in Figure G1.

   Based on Figure G1, the 95% CI for the slope coefficient is between 0.80 to 1.03 while the 95% CI for the intercept is between -12.00 to 72.00. It means that it is plausible to say that a slope coefficient of 1 and an intercept of 0 were obtained. This indicates that Y = X, or the droplet sizes generated by MATLAB image analysis is similar to the droplet sizes generated by Malvern Mastersizer at similar experimental conditions.

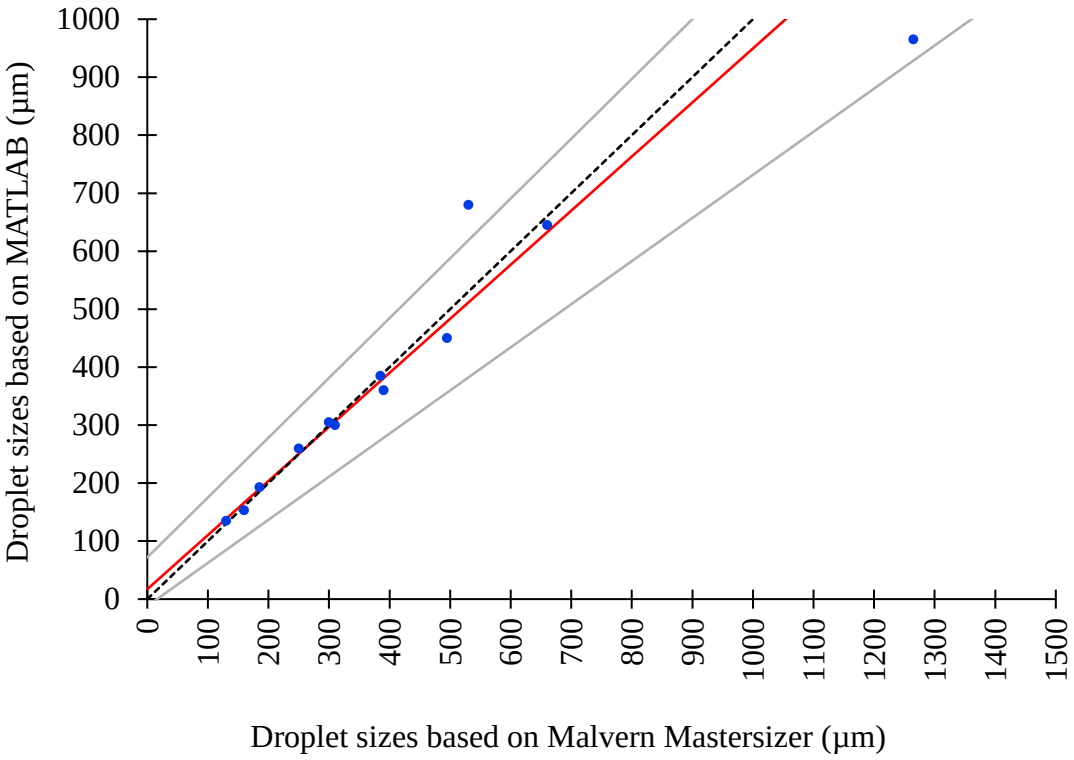

Figure G1 A plot showing the relationships between MATLAB image analysis and Malvern Mastersizer. (○) Experimental results based on MATLAB image analysis, (- - - -) the ideal situation if Y (MATLAB results) perfectly equals to X (Malvern Mastersizer results), (—) fitted regression line based on MATLAB image analysis data and (—) regression line confidence bands.

2) t-test analysis

A t-test is usually used to determine if there is significant difference between the means of two groups which the two groups may be related in certain features. In the atomization of fibre suspensions, the two groups were the D-values generated by MATLAB image analysis and the D-values obtained by Malvern Mastersizer. During the t-test, each D-value generated using MATLAB image analysis was paired with the corresponding D-value obtained using the Malvern Mastersizer. For example, the D(v,10) of 5.0 wt.% WF 600 at an atomizing air velocity of 150 m/s generated using the MATLAB image analysis was paired with the corresponding D(v,10) of 5.0 wt.% WF 600 obtained using the Malvern Mastersizer. Similar pairings were set for D(v,50) and D(v,90) for all fibre suspensions, at different

atomizing air velocities. The paired D-values were then analysed using the t-test. The advantage of the t-test is that it includes the standard deviation of each group, along with the means.

A p-value was computed to test the null hypothesis that the difference between the means of the two groups is equal to zero. A p-value of more than 0.05 was obtained for all pairings which means that there was no significant difference between the means of the D-values generated by MATLAB image analysis and the means of the D-values obtained using the Malvern Mastersizer. Table G1 shows the p-values for each pairing.

Table G1 p-value obtained through the Passing-Bablok analysis based on the comparison between the D-values generated by MATLAB image analysis and Malvern Mastersizer.

Fibre suspension	Atomizing air velocity (m/s)	D(v,10)	D(v,50)	D(v,90)
5.0 wt.% AF 400-30	150	0.42	0.78	0.37
	195	0.93	0.09	0.86
	215	0.17	0.44	0.91
	240	0.05	0.32	0.29
5.0 wt.% WF 101	150	0.96	0.24	0.75
	195	0.65	0.07	0.35
	215	0.71	0.09	0.22
	240	0.58	0.06	0.42
5.0 wt.% WF 600	150	0.06	0.12	0.21
	195	0.68	0.59	0.89
	215	0.07	0.07	0.08
	240	0.19	0.58	0.66
5.0 wt.% citrus fibre	150	0.26	0.13	0.27
	195	0.77	0.83	0.56
	215	0.08	0.86	0.12
	240	0.11	0.30	0.92

Appendix H Parameters involved during the theoretical prediction of droplet sizes, D(n,50), based on Keshavarz et al. (2015) relationship.

This appendix shows the details of the parameters involved during the theoretical prediction of droplet size of fibre suspensions. Equation 6.6 was taken from Keshavarz et al. (2015).

$$\frac{\langle d\rangle_{VE}}{D_J} \cong 1.2\left(\frac{\sigma}{\rho {U_A}^2 D_J}\right)^{\frac{1}{2}}\left[1+We^{\frac{1}{6}}Oh^{\frac{2}{3}}\right]\times\left[\frac{\left(\frac{\sqrt{8}c}{6}\right){Oh_{R_l}}^{-1}}{\left(\frac{\sqrt{8}c}{6}\right){Oh_{R_l}}^{-1}+{Oh_{R_l}}^{2}-ln\left(1+\frac{cDe_{R_l}}{3Oh_{R_l}}\right)}\right]$$

- Equation 6.6

$\langle d\rangle_{VE}$ (µm) is the average droplet size, specifically D(n,50) for viscoelastic liquids, D_J (m) is the jet diameter which is similar to the orifice diameter, U_A (m/s) is the atomizing air velocity and σ (N/m) is the surface tension. We, Oh, De_{R_l} and Oh_{R_l} are the Weber number, Ohnesorge number and Deborah number respectively, and are as follow:

$$We = \frac{\rho_L (U_L - U_A)^2 D_J}{\sigma}$$

$$Oh = \frac{\mu}{\sqrt{\rho R_0 \sigma}}$$

$$De_{R_l} = \frac{\tau}{\tau_R}$$

$$Oh_{R_l} = \frac{\mu}{\sqrt{\rho R_0 \sigma}}$$

ρ_L (kg/m^3) is the liquid density, U_L (m/s) is the liquid velocity, μ (Pa.s) is the shear viscosity of the fibre suspensions at shear rate more than 30 000 s^{-1} assuming that viscosity plateau was reached at high atomizing air velocity (Refer to Section 4.2.1 for clarification), τ_r (s) is the relaxation time and τ_R (s) is the Rayleigh time. R_0 (mm) in Oh is the initial radius of the jet while R_0 (mm) in Oh_{R_l} is the initial radius of the thinning filament. Value of De_{R_l}

for each fibre suspension was calculated based on the data from the runs on capillary breakup extensional rheometer. The example calculations of We, Oh, De_{R_l} and Oh_{R_l} for 5.0 wt.% WF 600 fibre suspension are as follow:

$$We = \frac{\rho_L (U_L - U_A)^2 D_J}{\sigma} = \frac{1420\ \frac{kg}{m^3} \times (0.85 \frac{m}{s} - 150 \frac{m}{s})^2 \times 0.0015\ m}{66.78 \times 10^{-3} \frac{N}{m}} = 7.0 \times 10^5$$

$$Oh = \frac{\mu}{\sqrt{\rho R_0 \sigma}} = \frac{0.20\ Pa.s}{\sqrt{1420\ \frac{kg}{m^3} \times \left(\frac{0.0015}{2}\right) m \times 66.78 \times 10^{-3} \frac{N}{m}}} = 0.75$$

$$De_{R_l} = \frac{\tau}{Rayleigh\ time} = \frac{0.34}{0.023} = 14.78$$

$$Oh_{R_l} = \frac{\mu}{\sqrt{\rho R_0 \sigma}} = \frac{0.20\ Pa.s}{\sqrt{1420\ \frac{kg}{m^3} \times (0.002) m \times 66.78 \times 10^{-3} \frac{N}{m}}} = 0.46$$

After computing all the values of We, Oh, De_{R_l} and Oh_{R_l}, regression of Equation 6.6 was performed and produced the curves plotted in Figure 6.14 in Section 6.5.1. *c* in Equation 6.6 is a single fitting constant and the value is tabulated in Table H1.

Table H1 *c* values obtained from the regression of Equation 6.6 to the experimental data of each 5.0 wt.% fibre suspension.

Fibre suspension	*c* value
5.0 wt.% AF 400-30	2.02
5.0 wt.% WF 101	2.73
5.0 wt.% WF 600	4.38
5.0 wt.% citrus fibre	4.10

Appendix I Publications.

1) Rozali, S. N., Paterson, A. H., Hindmarsh, J. P., & Huffman, L. M. (2019). Understanding the shear and extensional properties of pomace-fibre suspensions prior to the spray drying process. *LWT*, *99*, 138-147.

MASSEY UNIVERSITY
GRADUATE RESEARCH SCHOOL

STATEMENT OF CONTRIBUTION
DOCTORATE WITH PUBLICATIONS/MANUSCRIPTS

We, the candidate and the candidate's Primary Supervisor, certify that all co-authors have consented to their work being included in the thesis and they have accepted the candidate's contribution as indicated below in the *Statement of Originality*.

Name of candidate:	Siti Nadjiha Mohd Rozali
Name/title of Primary Supervisor:	Prof Tony Paterson
Name of Research Output and full reference:	
Rozali, S. N., Paterson, A. H., Hindmarsh, J. P., & Huffman, L. M. (2019). Understanding the shear and extensional properties of pomace-fibre suspensions prior to the spray drying process. LWT, 99, 138-147.	
In which Chapter is the Manuscript /Published work:	Chapters 4 & 5
Please indicate:	
• The percentage of the manuscript/Published Work that was contributed by the candidate:	100%
and	
• Describe the contribution that the candidate has made to the Manuscript/Published Work:	
The candidate carried out all laboratory work and data analysis. The candidate drafted the manuscript and did the amendments during manuscript revision.	
For manuscripts intended for publication please indicate target journal:	
Candidate's Signature:	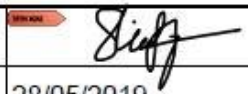
Date:	28/05/2019
Primary Supervisor's Signature:	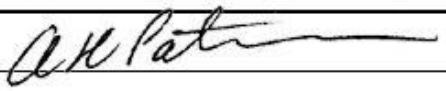
Date: May 2019	

Contents lists available at ScienceDirect

LWT - Food Science and Technology

journal homepage: www.elsevier.com/locate/lwt

Understanding the shear and extensional properties of pomace-fibre suspensions prior to the spray drying process

Siti N.M. Rozali[a,*], Anthony H.J. Paterson[a], Jason P. Hindmarsh[b], Lee M. Huffman[c]

[a] School of Engineering and Advanced Technology, Massey University, New Zealand
[b] Institute of Food Science and Technology, Massey University, New Zealand
[c] The New Zealand Institute for Plant & Food Research Ltd, New Zealand

ARTICLE INFO

Keywords:
Extensional rheology
Fibre suspensions
Pomace fibres
Shear rheology

ABSTRACT

Pomace fibre is the left-over plant from juice processing which has several health-promoting properties. Fibre has potentially been recognized as a drying aid in the spray drying of fruit juice. In the present work, shear and extensional properties of different fibre suspensions were assessed and compared. Unlike fruit juice, which displays Newtonian behaviour, fibre suspensions exhibit shear thinning behaviour with dependence on the fibre fraction and aspect ratio and significant extensional properties as measured with a capillary break-up rheometer. The extensional properties of the fibre suspensions make it more difficult to atomize them. This study shows the importance of assessing both shear and extensional properties of fibre suspensions before incorporating them in spray drying.

1. Introduction

Pomace is the by-product or waste material that remains after pressing fruit to extract the juice. Juice is widely used in food products. A lot of studies have been done on fruit juices ranging from its composition, physical properties, rheology and production of juice powder by spray drying (Camerlingo et al., 2007; Hobani, 1998; Juszczak & Fortuna, 2003; Verma & Singh, 2015; Vitali & Rao, 1984). In contrast, pomace is usually treated as a waste. Many studies, in fact, show that pomace is a rich source of minerals, protein and fibres (Boyer & Liu, 2004; Farahnaky, Abbasi, Jamalian, & Mesbahi, 2008; Sudha, Baskaran, & Leelavathi, 2007).

Pomace fibres have long been recognized as having a positive effect on human health and nutrition (Anderson & Chen, 1979; Coudray et al., 1997; Montagne, Pluske, & Hampson, 2003). Recently, there has been an interest in the potential use of pomace fibres as a drying aid in the spray drying of fruit juices. In spray drying applications, the sprayability of a fluid is influenced by its rheology (Keshavarz et al., 2015). The atomization process, which occurs in a spray dryer, converts bulk liquid into a spray due to the action of turbulence and aerodynamic interaction but it is opposed by the viscosity. High viscosity can forestall the breakup which leads to a lower atomization efficiency such as a longer breakup time or bigger droplet sizes.

Previous studies on the rheology of fibre suspensions mainly focused on synthetic fibres which are widely used in processes such as injection moulding (Crowson, Folkes, & Bright, 1980; Laun, 1984; Thomason, 2002). Most of the existing studies have been devoted to the relation between suspension shear viscosity and the fibre concentration, fibre geometry and fibre orientation (Bibbó, 1987; Ganani & Powell, 1985; Kitano & Kataoka, 1981). The effect of fibres on the shear viscosity of suspensions is complex. Factors that affect the shear viscosity include fibre particle size and shape, particle size distribution, fibre volume fraction, fibre flexibility, aspect ratio and shear rate (Djalili-Moghaddam & Toll, 2006; Pabst, Gregorová, & Berthold, 2006). The fibre aspect ratio is $\alpha = L/D$, where L and D are the length and diameter of the fibres respectively.

Fibres can be divided into rigid and flexible fibres. Effective stiffness, which characterized the relative importance of fibre stiffness, has been proposed by Switzer III & Klingenberg (2003), as shown in Eq. (1). It is used as a criterion for fibre flexibility.

$$S^{eff} = E_Y \pi D^4 / 64 \eta_m \dot{\gamma} L^4 \quad (1)$$

where E_Y is the Young modulus of the fibres (Pa), η_m is the viscosity of suspending fluid ($Pa \times s$) and $\dot{\gamma}$ is the shear rate ($1/s$). As $S^{eff} \to 0$, the fibres behave like completely flexible threads, whereas for $S^{eff} \to \infty$, the fibres become rigid. Previous works have shown that fibre flexibility enhances both viscosity and the storage and loss moduli (Keshtkar, Heuzey, & Carreau, 2009; Kitano, Kataoka, & Nagatsuka, 1984; Kotsilkova, 1992; Soszynski & Kerekes, 1988).

Fibres can be regarded as elongated particles and elongated

* Corresponding author.
E-mail addresses: S.Mohd-Rozali@massey.ac.nz, nadjiharozali@gmail.com (S.N.M. Rozali).

https://doi.org/10.1016/j.lwt.2018.09.061
Received 16 April 2018; Received in revised form 8 September 2018; Accepted 22 September 2018
Available online 24 September 2018
0023-6438/ © 2018 Elsevier Ltd. All rights reserved.

particles can lead to an increase in the shear viscosity of suspensions that exceeds the usual increase encountered for isometric particles. The increase in the viscosity with volume fraction for suspensions containing particles with different average aspect ratio is usually characterized based on the Krieger (Krieger, 1972) and Maron-Pierce (Maron & Pierce, 1956) relationships shown in Eqs. (2) and (3) respectively.

$$\eta_r = (1 - \varnothing/\varnothing_c)^{-[\eta]\varnothing_c} \quad (2)$$

$$\eta_r = (1 - \varnothing/\varnothing_c)^{-2} \quad (3)$$

in which $[\eta]$ is the intrinsic viscosity, $\varnothing$ is the volume fraction of suspensions and $\varnothing_c$ is the critical volume fraction. The Maron-Pierce relation is often considered as a special case of the Krieger relation, obtained by setting $[\eta]\varnothing_c = 2$. The intrinsic viscosity is a parameter that depends on the particle shape in the suspension, i.e. the particle aspect ratio.

Shear and extensional properties are rheological characteristics of a given material. Unlike shear rheology, which has been studied quite extensively, studies on the extensional rheology of fibre suspensions are very scarce. The different types of flow between shear and extensional fluids and their forms of deformations and resistances are clearly illustrated by (Steffe, 1996). In the presence of extensional flow, some liquids, such as fibre suspensions, can develop extra resistance or tension that cannot be quantified by shear rheology (Ooi & Sridhar, 2004). The extensional flow is present along with the shear flow in the cases where the flow undergoes a large contraction or expansion, such as in pipe contraction or a nozzle (Astarita & Greco, 1968). This extensional property or elasticity can influence the pressure drop and hence the atomization or sprayability of the liquids (Chhabra, 2006; Keshavarz et al., 2015; Li, 2006; Mansour & Chigier, 1995; Thompson & Rothstein, 2007). Thus, it is important to understand both shear and extensional rheology of fibre suspensions before incorporating pomace fibres as a drying aid in the spray drying.

Precise measurements of extensional properties such as fluid relaxation time are essential for a quantitative study of these effects. Relaxation time is the characteristic time scale for viscoelastic stress growth in a uniaxial elongational flow (Rodd, Scott, Cooper-White, & McKinley, 2004). There are few well-known methods that can be used to quantify the extensional effects which are Filament Stretching Extensional Rheometer, FiSER™ (Cambridge Polymer Group, Boston), Capillary Breakup Extensional Rheometer, CaBER™ (Cambridge Polymer Group, Boston and Haake) and Cambridge Trimaster (Hallmark et al., 2016). These devices measure the necking of an extensionally-strained fluid filament as a function of time. The CaBER was first developed by McKinley and co-workers at MIT in conjunction with the Cambridge Polymer Group. The CaBER can provide information on elasticity, relaxation time and filament breakup time. Conventional extensional rheometers are heavy, delicate and expensive. There is, therefore, a need for a portable device for measuring the extensional behaviour. The first lightweight portable extensional rheometer was built by Collett et al. (2015). The portable rheometer works very similarly to the CaBER, by monitoring the dynamics of the breakup of fluid filament following a short, rapid, extensional deformation. One can obtain information about the relaxation time, the extent of non-Newtonian behaviour and the breakup time for the fluid. The latter parameter is an important value in atomization applications.

The filament breakup dynamics of Newtonian liquids are very simple. The mid-plane diameter $D(t)$ of sufficiently viscous Newtonian liquids decays linearly with time until breakup (Hallmark et al., 2016). For different fluid systems all three effects of inertia, viscous and elastic stresses may be in balance with the capillary pressure for some part of the thinning and breakup process. For example, in the initial stage of the thinning, the flow in the filament will be dominated by inertia; and the mid-plane diameter will thin down with a timescale set by an inertia-capillary balance (also known as the Rayleigh timescale, τ_R). Immediately following the inertial regime there is visco-capillary regime, where the capillary forces are balanced by the shear viscosity of the fluid. In this regime, the mid-plane diameter of the filament decreases linearly with time (Clasen, Phillips, & Palangetic, 2012; McKinley & Tripathi, 2000). The linear viscous thinning regime is followed by an exponential filament thinning process at which the capillary pressure arising from the surface tension is balanced purely by the stress arising from the fluid elasticity. This is referred to as an elasto-capillary balance. Under the conditions of elasto-capillary balance, the mid-plane diameter $D(t)$ decays exponentially, and is given by Eq. (4) (Jaishankar, Wee, Matia-Merino, Goh, & McKinley, 2015; Keshavarz et al., 2015):

$$D(t)/D_0 = (GD_0/2\sigma)^{1/3} \exp[-t/(3\tau)] \quad (4)$$

in which D_0 is the initial filament diameter, G is the elastic modulus (Pa), σ is the surface tension (N/m) and τ is the relaxation time (s) in the Oldroyd-B model or also known as Upper Convected Maxwell model. Therefore, the experiments performed using a portable extensional rheometer yields a measure of the characteristic relaxation time of the liquid, τ in elongation. Deborah number, $De = \tau/\tau_R$ is usually used to balance the elastic and inertial forces. High De, usually more than 1, means that the flow is dominated by elasticity (Clasen et al., 2012).

The main objective of this research was to study the shear and extensional rheological properties of fibre suspensions. The results from this study can be compared to previous rheological studies of fibre suspensions which are often conducted under pure shear flow, neglecting extensional flow. The shear viscosity properties were measured using an available commercial rotary rheometer while the extensional viscosity properties were quantified using a portable capillary breakup extensional rheometer.

2. Experimental

2.1. Materials preparation and characterization

The commercial apple fibres (Apple Fibre 400-30) and wheat fibres (Wheat Fibre 101 & Wheat Fibre 600) used were supplied by IMCD New Zealand Limited and the citrus fibres were supplied by Hawkins Watt New Zealand; all were used as received. The fibres have different aspect ratios as tabulated in Table 1. Different concentration fibres suspensions were prepared by mixing the fibre powders into 60 °Brix concentrated apple juice, supplied by ENZA Food New Zealand, at 20 °C and continuously stirred until complete dispersion was achieved. All mixtures were prepared immediately before conducting a test.

The density of fibres, measured by helium pycnometry (AccuPyc II 1340, Micromeritics, Norcross, USA) at Fonterra New Zealand, were $1.47 \pm 0.001\ g/mL$, $1.56 \pm 0.002\ g/mL$, $1.57 \pm 0.002\ g/mL$ and $1.51 \pm 0.002\ g/mL$ for Apple Fibre 400-30, Wheat Fibre 101, Wheat Fibre 600 and citrus fibre respectively.

Table 1
Summary of fibre lengths and its corresponding aspect ratio.

Types of fibres	Supplier	Average fibre length (μm)	Aspect ratio
Apple Fibre 400-30	IMCD New Zealand Limited	30	2–3
Wheat Fibre 101	IMCD New Zealand Limited	50	2–3
Wheat Fibre 600	IMCD New Zealand Limited	100	8–10
citrus fibre	Hawkins Watt	200	8–10

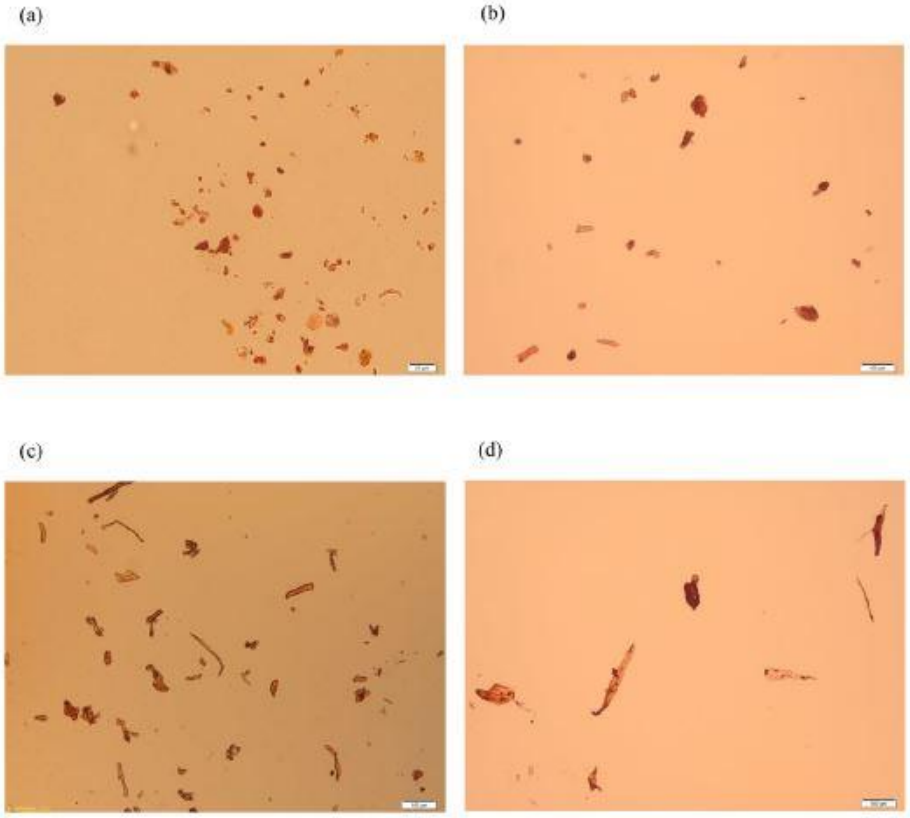

Fig. 1. Light microscope images of (a) Apple Fibre 400-30 (b) Wheat Fibre 101 (c) Wheat Fibre 600 (d) citrus fibre after staining with safranin. The length of the scale bar is 20 μm in (a) and 100 μm in (b–d).

2.2. Size characterization of fibres

A light microscopic technique was employed to determine the length distribution of all fibres. All fibre particles were stained with safranin and washed with MilliQ water afterwards. The stained fibres were resuspended in water to ensure a good separation between particles under the microscope. All fibre suspensions were photographed at a suitable magnification using Olympus BX53 microscope (Tokyo, Japan). Image analysis software, ImageJ, was used to measure the length and diameter of each fibre. An average of 30 images was analysed for each fibre type.

Microscope images of all fibres are shown in Fig. 1. Apple Fibre 400-30 and Wheat Fibre 101 fibres have average lengths of 30 and 50 μm, respectively. The aspect ratio is between 2 and 3 for both fibres. Wheat Fibre 600 and citrus fibres have an average length of 100 μm and 200 μm respectively with aspect ratios ranging from 8 to 10 as tabulated in Table 1. The fibre length distribution is plotted in Fig. 2.

2.3. Shear rheology

Shear rheology tests were performed using MCR 301 rheometer with a coaxial cylinder (Anton Paar GmbH) at 20 °C. The gap between the cup and bob of the coaxial cylinder was varied in the range 0.30–2.0 mm. During the shear flow tests, the shear rate was increased step-by-step from 0 to 1000/s and the change of viscosity was observed at the rate of 0.25 min/viscosity point. Small amplitude oscillatory shear measurements at a strain amplitude of 0.1% were conducted in order to obtain the linear viscoelastic properties of the fibre suspensions studied as a function of frequency between 1 and 100 rad/s.

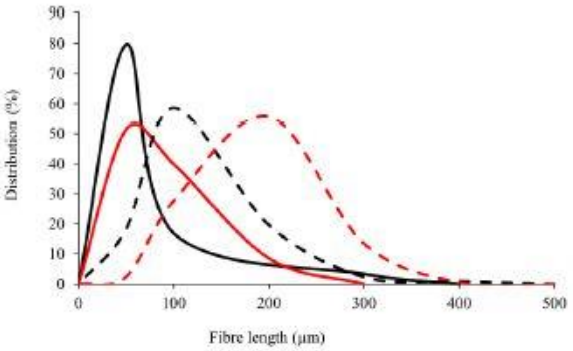

Fig. 2. Fibre length distribution measured using the combination of Olympus BX53 microscope and ImageJ. Black full line represents Apple Fibre 400-30, red full line represents Wheat Fibre 101, black dashed line represents Wheat Fibre 600 and red dashed line represents citrus fibre. (For interpretation of the references to colour in this figure legend, the reader is referred to the Web version of this article.)

2.4. Extensional rheology

Extensional rheology tests were carried out using a portable capillary breakup extensional rheometer, equipped with a battery-powered

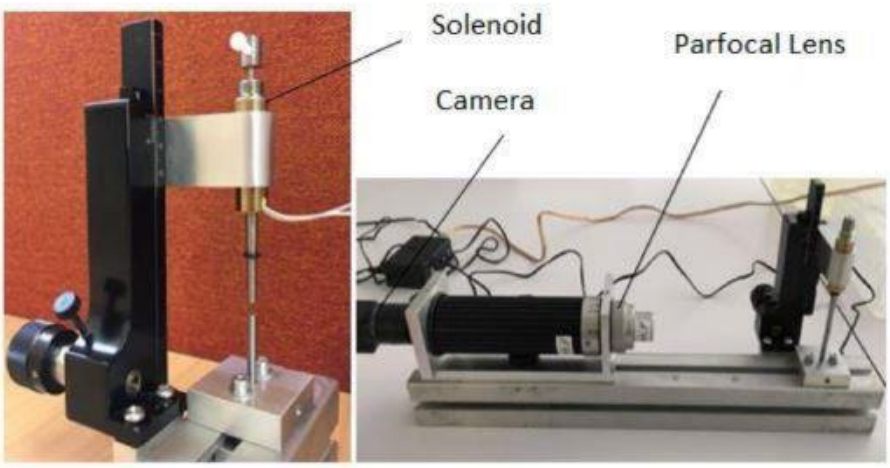

Fig. 3. (left) Close-up view of the portable extensional rheometer. (right) Photograph of the whole setup including camera, lens and the portable extensional rheometer.

solenoid that is capable of applying an abrupt stretch to a sample of liquid placed between two 4 *mm* pistons thus creating an extensional field. The rheometer was built in-house at Massey University based on the previous work by Bart et al. (2016). The setup is shown in Fig. 3. Fluid samples were carefully loaded between the pistons using a pipette. The upper piston was abruptly raised to a pre-set height to create a filament and a high-speed camera was used to capture images throughout the stretching process and these were used as a means of measuring the change in the diameter of the filament. MATLAB software was programmed to digitally analyse the measurement of the diameter in each frame.

3. Results and discussion

3.1. Steady shear properties

The viscosity of clear apple juice was measured for a range of shear rate from 0.1 to 1000/*s*. This is shown in Fig. 4. A closer observation on Fig. 4 shows that the viscosity is constant at 0.34 Pa.s from 0.2 to 500/*s* demonstrating that the apple juice follows Newtonian behaviour. At

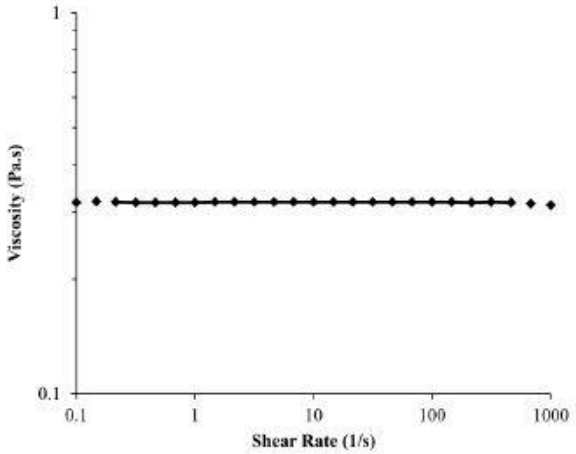

Fig. 4. Flow curve for clear apple juice. Raw experimental data (◆) and suggested reliable working range of 0.2/s-500/s (—) using MCR 301 rheometer.

shear rates above 500/*s*, it is suggested that viscous heating has started to become significant, which is evident from the slight decrease in viscosity value. Hence, all measurements on MCR 301 rheometer were restricted to the range between 0.2 to 500/*s*.

In contrast, all fibre suspensions when submitted to steady shear, show a shear thinning behaviour as seen in Fig. 5 and Table 2. This is the result of the breakdown of the macromolecular structures in the fibre suspension as the shear rate changes. The structures may be contributed by the non-hydrodynamic adhesive interactions between fibres, mechanical contacts between the fibres as well as floc or network formation, and all were destroyed by imposing greater shear rates (Bounoua, Lemaire, Férec, Ausias, & Kuzhir, 2016; Djalili-Moghaddam & Toll, 2006).

Fig. 5 shows that the shear viscosity increased with increasing fibre fraction since higher fibre fraction allows for more entanglements, which then provide greater resistance for the suspensions to flow. The results agree with previous studies done on microfibrillated cellulose (Lauri, Koponen, Haavisto, Czajkowski, & Fabritius, 2017). Entanglements are susceptible to occur due to the use of flexible fibres. Natural or plant-based fibres often have relatively low Young's modulus compared to other fibres (Facca, Kortschot, & Yan, 2006). Based on Eq. (1), a low Young's modulus contributes to a low stiffness of fibres, thus greater flexibility.

A fluid with non-Newtonian behaviour in which the strain rate experienced by the fluid is related to the stress in a non-linear way: $\tau = k\dot{\gamma}^n$ where τ is the shear stress (Pa), k is the consistency index ($Pa \times s^n$) and n is the flow index is known as a power-law fluid. Fig. 5 shows how the power-law model provides a reasonable description of the experimental data of 4.5 and 9.0 mL/100 mL fibre suspensions. Table 2 lists the values of the fit parameters, k and n, based on the power-law model. The degree of shear thinning is measured by the flow index, which decreases when pseudoplasticity increases. Higher values of n were observed at the lower concentration of 4.5 mL/100 mL fibre suspensions while lower values of n were observed at a greater concentration of 9.0 mL/100 mL fibre suspensions, which indicates that non-Newtonian behaviour increases with the increased volume of fibres in the suspensions. The same relation was found by Grigelmo-Miguel, Ibarz-Ribas, and Martín-Belloso (1999) in peach dietary fibre suspensions, by Bhattacharya, Bal, Mukherjee, and Bhattacharya (1991) in tamarind kernel suspensions and by Mahmoud and Fugitt (1996) in a nutritional supplement containing oat fibre.

Fig. 6 shows the effect of fibres aspect ratio on suspension

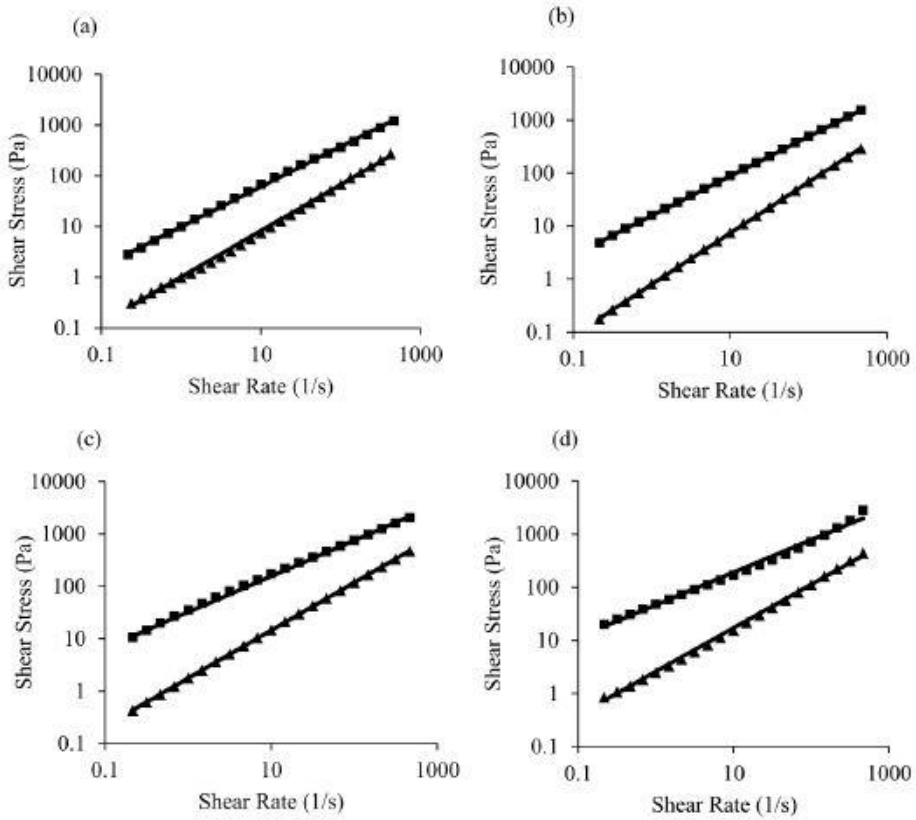

Fig. 5. (▲) 4.5 mL/100 mL and (■) 9.0 mL/100 mL fibre suspensions with power-law model fitting (—). (a) Apple Fibre 400-30 (b) Wheat Fibre 101 (c) Wheat Fibre 600 (d) citrus fibre suspensions.

Table 2
Fit parameters, k and n, based on power-law model for 4.5 mL/100 mL and 9.0 mL/100 mL fibre suspensions.

Fibre suspensions	Consistency index, k	Flow index, n	Consistency index, k	Flow index, n
	4.5 mL/100 mL		9.0 mL/100 mL	
Apple Fibre 400-30	1.01	0.91	9.86	0.79
Wheat Fibre 101	0.80	0.96	15.75	0.75
Wheat Fibre 600	1.76	0.91	32.11	0.68
citrus fibre	2.59	0.82	46.63	0.61

viscosities. At 4.5 mL/100 mL concentration, Wheat Fibre 600 and citrus fibre suspensions with an aspect ratio of 8–10, exhibit higher viscosity compared to the Apple Fibre 400-30 and Wheat Fibre 101 which have aspect ratios of 2–3. This behaviour can be related to the formation of a network-like structure. A higher aspect ratio of fibres allows for a greater probability of interaction between the fibres or fibre contacts. This clearly has a strong effect on the suspension's viscosity. Apple Fibre 400-30 and Wheat Fibre 101 can be said to exhibit similar shear viscosity throughout the runs since both fibres have identical aspect ratios. This also applies to Wheat Fibre 600 and citrus fibre. These results agree with previous studies by Djalili-Moghaddam and Toll (2006). From Figs. 5 and 6, it is evident that during shearing of a fibre suspension, both fibre fractions and aspect ratio play a dominant role in affecting suspension shear viscosity.

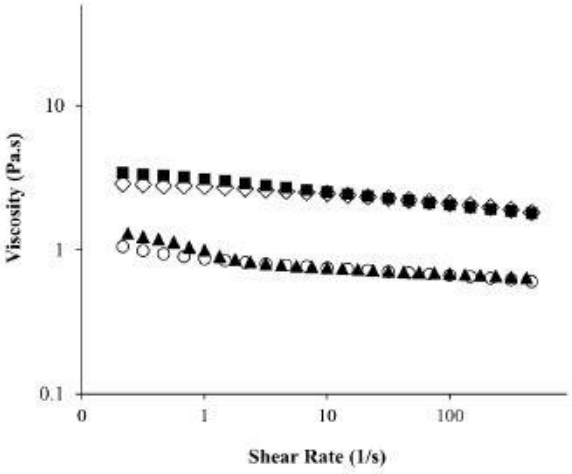

Fig. 6. Shear behaviour of different 4.5 mL/100 mL fibre suspensions as a function of aspect ratios. (▲) Apple Fibre 400-30 and (○) Wheat Fibre 101 at aspect ratio 2–3 (◊) Wheat Fibre 600 and (■) Citrus fibre at aspect ratio 8–10.

Fig. 7 shows the measured relative viscosities, η_r, together with fit curves obtained by non-linear regression via Eq. (2) (Krieger fit, dashed lines) and 3 (Maron-Pierce fit, full lines). The vertical asymptotics

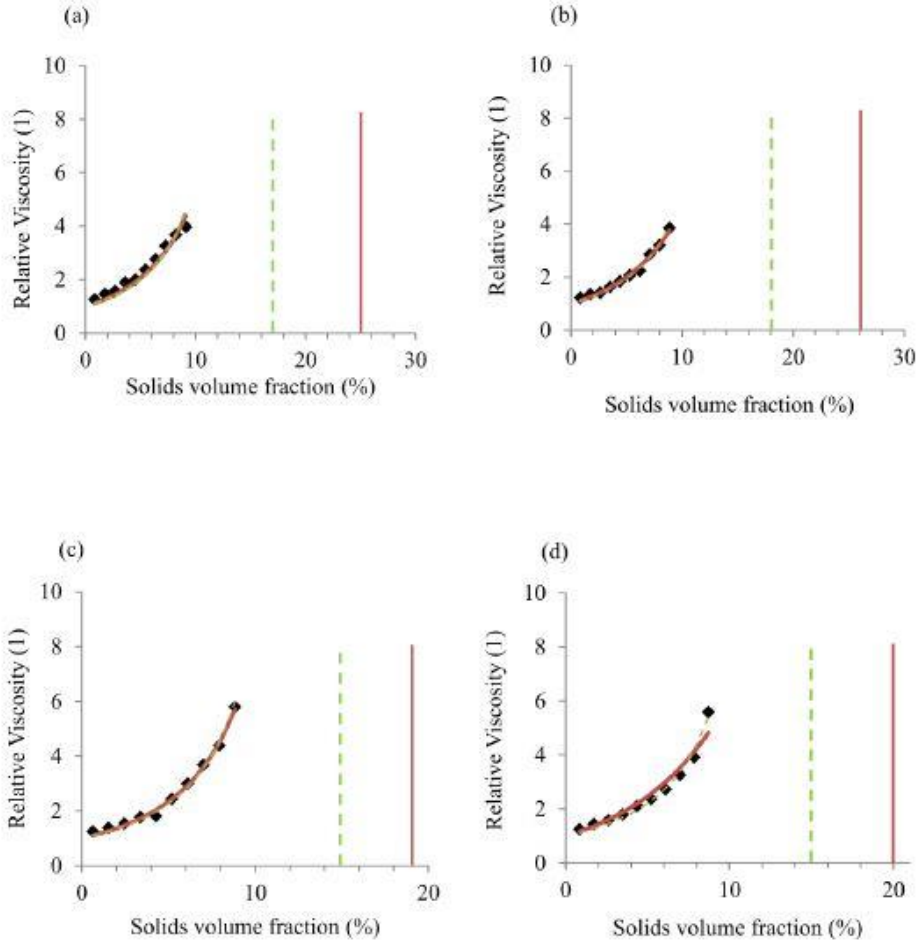

Fig. 7. Concentration dependence of the relative viscosity of (a) Apple Fibre 400-30 (b) Wheat Fibre 101 (c) Wheat Fibre 600 (d) citrus fibre. Red full line represents Krieger fit and green dashed line represents Maron-Pierce fit. The corresponding critical volume fraction obtained by fitting are indicated as vertical asymptotics. (For interpretation of the references to colour in this figure legend, the reader is referred to the Web version of this article.)

Table 3
Fit parameters, $\varnothing_c$ and $[\eta]$, for the concentration dependence of the relative viscosity of suspensions with different fibres obtained with the Krieger relation.

Fibre suspensions	$\varnothing_c$ (%)	$[\eta]$	C
Apple Fibre 400-30	25	13.00	0.97
Wheat Fibre 101	26	12.73	0.97
Wheat Fibre 600	19	14.61	0.95
Citrus Fibre	20	15.00	0.96

Table 4
Fit parameters, $\varnothing_c$, for the concentration dependence of the relative viscosity of suspensions with different fibres obtained with the Maron-Pierce relation.

Fibre suspensions	$\varnothing_c$ (%)	C
Apple Fibre 400-30	17	0.96
Wheat Fibre 101	18	0.96
Wheat Fibre 600	15	0.94
Citrus Fibre	15	0.95

indicate the corresponding critical volume fraction, $\varnothing_c$, obtained by fitting. Tables 3 and 4 list the values of the fit parameters, $[\eta]$ and $\varnothing_c$, together with the correlation coefficients, C, as a measure of the quality of the fit, determined using the Krieger and Maron-Pierce relations respectively. Mere visual inspection shows that both Krieger and Maron-Pierce fits are excellent for all types of fibre suspensions. In particular, the intrinsic viscosity based on Krieger relation of Wheat Fibre 600 suspension is very similar to that of citrus fibre suspension. The intrinsic viscosity of low aspect ratio Wheat Fibre 101 and Apple Fibre 400-30 is lower than Wheat Fibre 600 and citrus fibre suspensions.

A similar conclusion can be drawn with respect to the critical volume fractions determined from Krieger and Maron-Pierce relations. The critical volume fraction of Wheat Fibre 600 determined by both relations, is very similar to the value of citrus fibre. The critical volume fraction of Wheat Fibre 600 and citrus fibre suspensions are also lower than the critical volume fraction of Apple Fibre 400-30 and Wheat Fibre 101. The critical volume fraction is defined as the concentration at which blocking of the flowability occurs.

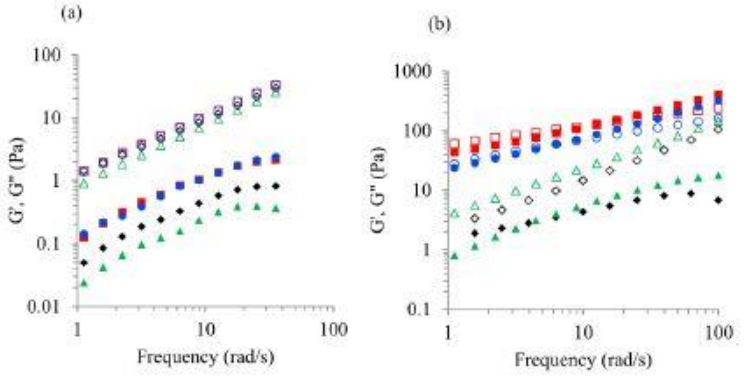

Fig. 8. Elastic (G′, filled symbols) and viscous (G″, open symbols) moduli evolution with frequency for (a) 4.5 mL/100 mL and (b) 9.0 mL/100 mL of (◆) Apple Fibre 400-30 (▲) Wheat Fibre 101 (■) Wheat Fibre 600 and (●) citrus fibre suspensions.

3.2. Small amplitude oscillatory shear properties

Fig. 8 shows the storage modulus, G' (elastic response) and loss modulus, G" (viscous response) from 1 to 100 rad/s for 4.5 and 9.0 mL/100 mL fibre suspensions. G′ and G″ represents the solid-like and fluid-like behaviours of the suspensions, respectively. The fluid-like behaviour prevails over the solid-like behaviour for the whole range of frequencies studied for 4.5 mL/100 mL fibre suspensions as shown in Fig. 8(a), which suggests the presence of weak entanglement networks (Piermaría, Bengoechea, Abraham, & Guerrero, 2016). G' and G" values of Apple Fibre 400-30 and Wheat Fibre 101 suspensions are lower than Wheat Fibre 600 and citrus fibre suspensions. For 9.0 mL/100 mL fibre suspensions, the fluid-like behaviour is dominant at lower frequencies until reaching a crossover where solid-like behaviour starts to be dominant. This behaviour is true for the higher aspect ratio suspensions of Wheat Fibre 600 and citrus fibre while no crossover appears within the tested frequency for the shorter aspect ratio of Apple Fibre 400-30 and Wheat Fibre 101. Fig. 8 also shows the effect of concentration on the mechanical properties of the fibre suspensions. The increase in fibre concentration results in an increase in the storage modulus of the suspensions. Elastic behaviour increases strongly with concentration, as the entanglements are favoured. This behaviour agrees with Damani, Powell, and Hagen (1993) and Xu, Chatterjee, Koelling, Wang, and Bechtel (2005). These results suggest that the fibre suspensions are not purely viscous and show significant elastic behaviour, depending on the concentration of fibres.

3.3. Extensional properties

Fig. 9 displays the profile of mid-filament diameter, D_{mid}, versus time of fibre suspensions measured on the portable extensional rheometer. To keep the initial filament configuration close to cylindrical with insignificant bulging effects, the capillary breakup tests employed axial separations so that $h_0/R_0 \leq 1/\sqrt{Bo}$ (Rodd et al., 2004). h_0 is the initial separation between upper and lower piston while R_0 is the initial sample radius. h_0 of 1.5 mm and R_0 of 2 mm were used in the experiment. The Bond number, Bo, is equivalent to $Bo = \rho g R_0^2/4\sigma$ where ρ is the density of the solution (kg/m^3) and g is the gravitational constant (m/s^2). Surface tensions of the solutions was measured beforehand using a Wilhelmy plate technique and were in the range of $0.065 - 0.069\ N/m$.

Theoretically, the breakup of Newtonian liquids follows a linear diameter profile where the liquids break after stretching (stretch-breaking stages only). It means that the dependence of thinning diameter on time is linear. This behaviour is shown by the apple juice in Fig. 9(a). Liquids with significant elastic properties display an exponential profile where the filament passes through stretch-relaxation-breaking stages, as shown in Fig. 9(a) with the suspensions with added

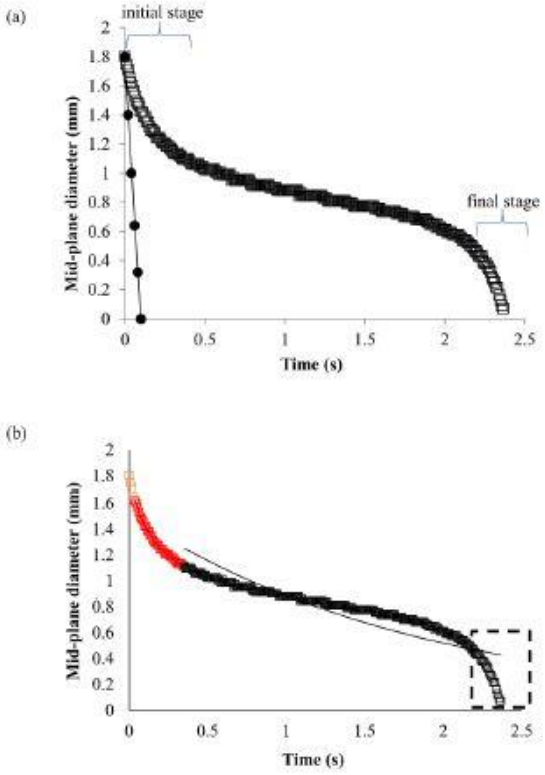

Fig. 9. (a) Filament diameter profile of (●) apple juice and (□) 6.0 mL/100 mL Wheat Fibre 600 suspensions (b) Filament diameter profile of the 6.0 mL/100 mL Wheat Fibre 600 suspensions showing the identified different regimes (□) inertia-capillary regime (□) visco-capillary regime (□) elasto-capillary regime (–) exponential fit.

fibre. Such exponential decay with time is a characteristic of a pure extensional flow which has been previously observed in various literature (Hallmark et al., 2016; Jaishankar et al., 2015; Piermaría et al., 2016).

Based on Fig. 9(a), the fibre suspension initially starts to thin by a similar mechanism as the Newtonian apple juice, as can be seen from the linear decrease in mid-plane diameter. The similar thinning dynamics or mechanism implies that the role of fibres is absent during this stage. It is suggested that the fibre particles remain in their equilibrium

conformation and thus are not influencing the thinning dynamics. However, after the linear decrease, the thinning dynamics start to diverge. The start of the divergence point is what is referred to as the onset of necking. At the onset of necking, the fibres are suggested to orientate, stretch and elongate suddenly due to the pure extensional flow created inside the filament. The idea of re-orientation of elongated particles along extensional flow direction has been discussed by Batchelor (1970) and Batchelor (1971). This creates high extensional viscosity that can resist the deformation of the thinning process of the filament and lead to the formation of a stable filament. This process then contributes to the delay in the breakup of the filament. This behaviour of fibre suspensions is similar to the behaviour of most polymer solutions (Piermaría et al., 2016). During the last stage, the thinning dynamics diverge back into a linear decrease. It is suggested that in this regime, the fibres have reached the maximum elongation such that the extensional viscosity could not resist the thinning anymore. This leads to a quick decay in mid-plane diameter until finally break up.

The exponential filament diameter profile of the fibre suspensions was divided into different regimes according to the thinning mechanisms explained above. The relaxation time, τ, for different fibre suspensions were obtained and compared. The data of 6.0 mL/100 mL Wheat Fibre 600 from Fig. 9(a) was plotted again in Fig. 9(b) according to the different regimes. The shape of the filament diameter profile helps in determining the onset of the elasto-capillary regime, in which Eq. (4) hold. At very early times, the liquid bridge has just been formed and the thinning filament was dominated by inertia and the mid-plane diameter thinned down with a timescale set by an inertia-capillary balance (plotted in orange bullets). Following this inertial regime, there is a visco-capillary regime characterized by the linear decrease in mid-plane diameter profile (plotted in red bullets). At this regime, capillary forces were balanced by the shear viscosity of the fibre suspension. The linear viscous thinning regime is followed by an exponential elasto-capillary regime in which the filament diameter decays as in Eq. (4) (plotted in black bullets). Regression of Eq. (4) enables the measurement of relaxation time, τ for the 6.0 mL/100 mL Wheat Fibre 600 suspension. In this case, the τ, of 6.0 mL/100 mL Wheat Fibre 600 suspension is 0.625 s. The deviation of the experimental value to the predicted value of mid-plane diameter at every single second was calculated using Root Mean Square Error (RMSE) method. The obtained RMSE values for every curve at every single point are all below 0.2 except for the data in the dashed rectangular region in Fig. 9 (b). The exponential decay in this region can be said to not fit the data anymore. This is suspected to be due to the fibres reaching their maximum stretching or extensibility limits such that they cannot extend anymore. This means that the fibres contribution to the extensional viscosity is saturated. After the finite extensibility of the fibres, the mid-plane diameter then sharply falls to zero in a linear manner. This reasoning can be supported by the fact that the exponential decay of Eq. (4) from Oldroyd-B model is originally predicted on infinite extensibility of a polymer chain and as a consequence, the thinning filament will never breakup which is physically impossible (Bazilevsky, Entov, & Rozhkov, 1990). Regression of Eq. (4) was performed on all $D_{mid}(t)$ vs. t data of different fibre suspensions to determine the relaxation time, τ. The relaxation time of all fibre suspensions are tabulated in Table 5. The ratio of the relaxation time, τ, to Rayleigh timescale, τ_R, of all fibre suspensions is more than 1, which indicates that the flow is dominated by elasticity. It is suggested that future works should be done looking at using a modified constitutive equation, instead of Eq. (4), that can better describe the complex flow phenomenon of fibre suspensions in extensional flow field.

Based on Fig. 10, it is apparent that the relaxation phase of Apple Fibre 400-30 and Wheat Fibre 101 is less obvious compared to the Wheat Fibre 600 and citrus fibre at both 4.5 and 6.0 mL/100 mL. This is probably due to the Wheat Fibre 600 and citrus fibre having longer fibres than Apple Fibre 400-30 and Wheat Fibre 101, which corresponds to a higher aspect ratio. It is suggested that for the same strength

Table 5
Relaxation time for 4.5 and 6.0 mL/100 mL of different fibre suspensions measured using the portable extensional rheometer.

Fibre suspensions	Fibre fraction (mL/100 mL)	Relaxation time, τ
Apple Fibre 400-30	4.5	0.120
	6.0	0.253
Wheat Fibre 101	4.5	0.161
	6.0	0.236
Wheat Fibre 600	4.5	0.338
	6.0	0.646
Citrus Fibre	4.5	0.333
	6.0	0.723

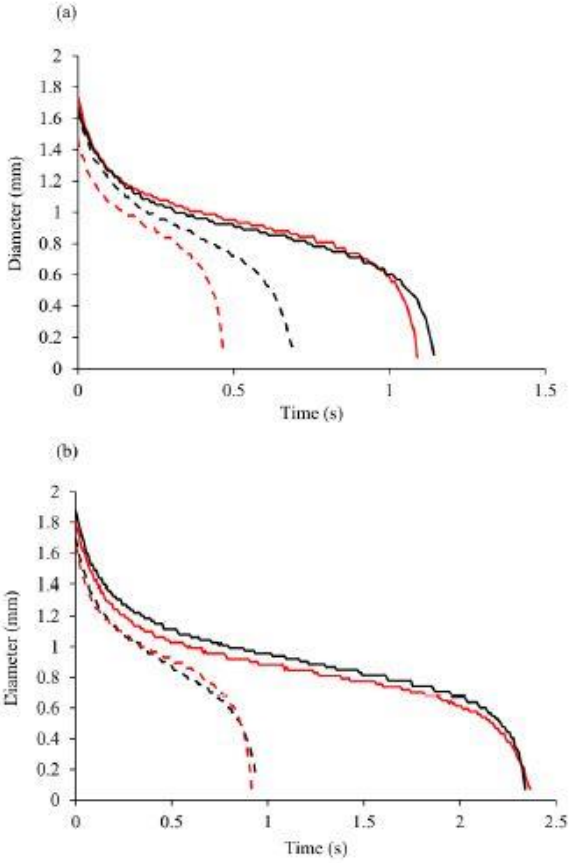

Fig. 10. Filament diameter profile of (a) 4.5 mL/100 mL and (b) 6.0 mL/100 mL of Apple Fibre 400-30 (red dashed line), Wheat Fibre 101 (black dashed line), Wheat Fibre 600 (red full line) and citrus fibre (black full line) suspensions. (For interpretation of the references to colour in this figure legend, the reader is referred to the Web version of this article.)

of extensional flow or deformation, individual fibre particles unravel and evolve with different rates and thus contribute to different steady-state extensions. Longer fibres require more time to unravel, stretch and elongate before reaching the critical condition where the filaments finally break. That explains the longer relaxation phase of Wheat Fibre 600 and citrus fibre suspensions compared to Apple Fibre 400-30 and Wheat Fibre 101 suspensions which are relatively short. In addition to the contribution by the individual fibres, fibre aggregates are also present during the flow. Higher aspect ratio induces greater probability of fibres interaction which then forms stronger fibre aggregates. During

the extensional flow, stronger fibre aggregates are suggested to require a longer time to deform and break compared to looser aggregates formed by lower aspect ratio fibres.

4. Concluding remarks

This study has shown the shear and extensional behaviour of fibre suspensions. Under shear deformation, all types of fibre suspensions show shear thinning behaviour. The magnitude of the viscosity or resistance depends on the fibre fraction and aspect ratio. Meanwhile, under extensional deformation, fibre suspensions show significant extensional behaviour, which is evidenced by the exponential thinning profile that is absent in Newtonian liquid flow. The fibre suspensions still underwent breakup but the breakup time is longer compared to a Newtonian liquid. The extensional behaviour is strongly dependent on fibre fraction and fibre aspect ratio. Further investigations using numerical computations to validate the claimed underlying mechanisms of fibre orientations are recommended in future studies.

The results from this study will assist in the designation of spray drying or atomization with fibre as the drying aid. Both the shear and extensional properties of fibre suspensions will influence the efficiency of the atomization process. An early hypothesis suggests that the shear thinning properties of fibre suspension will favour atomization as less energy is needed to overcome the shear resistance of fibre suspensions. Meanwhile, the extensional properties will limit the process by requiring more energy during atomization (Mansour & Chigier, 1995). Studies on the determination of the more dominant factor between shear and extensional flow during atomization and the method to optimize the atomization process in the case of fibre suspensions are currently ongoing.

Acknowledgements

The authors would like to thank the Ministry for Business, Innovation and Employment (MBIE) New Zealand for the funding provided through Food Industry Enabling Technologies (FIET) program that has enabled this project to proceed.

References

Anderson, J. W., & Chen, W. L. (1979). Plant fibre. Carbohydrate and lipid metabolism. *The American Journal of Clinical Nutrition, 32*, 346–363.
Astarita, G., & Greco, G. (1968). Excess pressure drop in laminar flow through sudden contraction. Newtonian liquids. *Industrial & Engineering Chemistry Fundamentals, 7*, 27–31.
Bart, H., Matthew, B., Ed, B., Simon, B., Tom, H., Ole, M., & Wilson, D. I. (2016). A portable and affordable extensional rheometer for field testing. *Measurement Science and Technology, 27*, 125302.
Batchelor, G. (1970). Slender-body theory for particles of arbitrary cross-section in Stokes flow. *Journal of Fluid Mechanics, 44*, 419–440.
Batchelor, G. (1971). The stress generated in a non-dilute suspension of elongated particles by pure straining motion. *Journal of Fluid Mechanics, 46*, 813–829.
Bazilevsky, A., Entov, V., & Rozhkov, A. (1990). Liquid filament microrheometer and some of its applications. *Paper presented at the third European rheology conference and golden jubilee meeting of the British society of rheology*.
Bhattacharya, S., Bal, S., Mukherjee, R. K., & Bhattacharya, S. (1991). Rheological behaviour of tamarind (Tamarindus indica) kernel powder (TKP) suspension. *Journal of Food Engineering, 13*, 151–158.
Bibbó, M. A. (1987). *Rheology of semiconcentrated fibre suspensions*. Massachusetts Institute of Technology.
Bounoua, S., Lemaire, E., Férec, J., Ausias, G., & Kuzhir, P. (2016). Shear-thinning in concentrated rigid fibre suspensions: Aggregation induced by adhesive interactions. *Journal of Rheology, 60*, 1279–1300.
Boyer, J., & Liu, R. H. (2004). Apple phytochemicals and their health benefits. *Nutrition Journal, 3*, 1–15.
Camerlingo, C., Zenone, F., Delfino, I., Diano, N., Mita, D. G., & Lepore, M. (2007). Investigation on clarified fruit juice composition by using visible light micro-Raman spectroscopy. *Sensors, 7*, 2049–2061.
Chhabra, R. P. (2006). *Bubbles, drops, and particles in non-Newtonian fluids*. CRC press.
Clasen, C., Phillips, P. M., & Palangetic, L. (2012). Dispensing of rheologically complex fluids: The map of misery. *AIChE Journal, 58*, 3242–3255.
Collett, C., Ardron, A., Bauer, U., Chapman, G., Chaudan, E., Hallmark, B., ... Wilson, D. I. (2015). A portable extensional rheometer for measuring the viscoelasticity of pitcher plant and other sticky liquids in the field. *Plant Methods, 11*, 16.
Coudray, C., Bellanger, J., Castiglia-Delavaud, C., Remesy, C., Vermorel, M., & Rayssignuier, Y. (1997). Effect of soluble or partly soluble dietary fibres supplementation on absorption and balance of calcium, magnesium, iron and zinc in healthy young men. *European Journal of Clinical Nutrition, 51*, 375.
Crowson, R., Folkes, M., & Bright, P. (1980). Rheology of short glass fibre-reinforced thermoplastics and its application to injection molding I. Fiber motion and viscosity measurement. *Polymer Engineering & Science, 20*, 925–933.
Damani, R., Powell, R. L., & Hagen, N. (1993). Viscoelastic characterization of medium consistency pulp suspensions. *The Canadian Journal of Chemical Engineering, 71*, 676–684.
Djalili-Moghaddam, M., & Toll, S. (2006). Fibre suspension rheology: Effect of concentration, aspect ratio and fibre size. *Rheologica Acta, 45*, 315–320.
Facca, A. G., Kortschot, M. T., & Yan, N. (2006). Predicting the elastic modulus of natural fibre reinforced thermoplastics. *Composites Part A: Applied Science and Manufacturing, 37*(10), 1660–1671.
Farahnaky, A., Abbasi, A., Jamalian, J., & Mesbahi, G. (2008). The use of tomato pulp powder as a thickening agent in the formulation of tomato ketchup. *Journal of Texture Studies, 39*, 169–182.
Ganani, E., & Powell, R. (1985). Suspensions of rodlike particles: Literature review and data correlations. *Journal of Composite Materials, 19*, 194–215.
Grigelmo-Miguel, N., Ibarz-Ribas, A., & Martín-Belloso, O. (1999). Rheology of peach dietary fibre suspensions. *Journal of Food Engineering, 39*, 91–99.
Hallmark, B., Bryan, M., Bosson, E., Butler, S., Hoier, T., Magens, O., & Wibberley, S. (2016). A portable and affordable extensional rheometer for field testing. *Measurement Science and Technology, 27*, 125302.
Hobani, A. I. (1998). Rheological behaviour of date-water concentrates. *Journal of Food Engineering, 36*, 349–357.
Jaishankar, A., Wee, M., Matia-Merino, L., Goh, K. K., & McKinley, G. H. (2015). Probing hydrogen bond interactions in a shear thickening polysaccharide using nonlinear shear and extensional rheology. *Carbohydrate Polymers, 123*, 136–145.
Juszczak, L., & Fortuna, T. (2003). Viscosity of concentrated strawberry juice. Effect of temperature and soluble solids content. *Electronic Journal of Polish Agricultural Universities, 6*(2).
Keshavarz, B., Sharma, V., Houze, E. C., Koerner, M. R., Moore, J. R., Cotts, P. M., ... McKinley, G. H. (2015). Studying the effects of elongational properties on atomization of weakly viscoelastic solutions using Rayleigh Ohnesorge Jetting Extensional Rheometry (ROJER). *Journal of Non-Newtonian Fluid Mechanics, 222*, 171–189.
Keshtkar, M., Heuzey, M. C., & Carreau, P. J. (2009). Rheological behaviour of fibre-filled model suspensions: Effect of fibre flexibility. *Journal of Rheology, 53*, 631–650.
Kitano, T., & Kataoka, T. (1981). The rheology of suspensions of vinylon fibres in polymer liquids. I. Suspensions in silicone oil. *Rheologica Acta, 20*, 390–402.
Kitano, T., Kataoka, T., & Nagatsuka, Y. (1984). Dynamic flow properties of vinylon fibre and glass fibre reinforced polyethylene melts. *Rheologica Acta, 23*, 408–416.
Kotsilkova, R. (1992). Dynamic rheological properties of glass fibre suspensions. *Proceedings of XIth international congress on rheology* (pp. 856–858). Brussels, Belgium: Elsevier Science.
Krieger, I. M. (1972). Rheology of monodisperse latices. *Advanced in Colloid and Interface Science, 3*, 111–136.
Laun, H. (1984). Orientation effects and rheology of short glass fibre-reinforced thermoplastics. *Colloid and Polymer Science, 262*, 257–269.
Lauri, J., Koponen, A., Haavisto, S., Czajkowski, J., & Fabritius, T. (2017). Analysis of rheology and wall depletion of microfibrillated cellulose suspension using optical coherence tomography. *Cellulose, 24*, 4715–4728.
Li, L. K. B. (2006). *An experimental study on air-blast atomization of viscoelastic liquids*. University of British Columbia.
Mahmoud, M. L., & Fugitt, M. (1996). Rheological properties of a calorically dense nutritional supplement as a function of nitrogen source and dietary fibre. *1996 IFT annual meeting, book of abstracts* 80A-26.
Mansour, A., & Chigier, N. (1995). Air-blast atomization of non-Newtonian liquids. *Journal of Non-Newtonian Fluid Mechanics, 58*, 161–194.
Maron, S. H., & Pierce, P. E. J. (1956). Application of ree-eyring generalized flow theory to suspensions of spherical particles. *Journal of Colloid Science, 11*, 80–95.
McKinley, G. H., & Tripathi, A. (2000). How to extract the Newtonian viscosity from capillary breakup measurements in a filament rheometer. *Journal of Rheology, 44*, 653–670.
Montagne, L., Pluske, J. R., & Hampson, D. J. (2003). A review of interactions between dietary fibre and the intestinal mucosa, and their consequences on digestive health in young non-ruminant animals. *Animal Feed Science and Technology, 108*, 95–117.
Ooi, Y. W., & Sridhar, T. (2004). Resistance to uniaxial extensional flow of fibre suspensions. *Rheologica Acta, 43*, 223–231.
Pabst, W., Gregorová, E., & Berthold, C. (2006). Particle shape and suspension rheology of short-fibre systems. *Journal of the European Ceramic Society, 26*, 149–160.
Piermaria, J., Bengoechea, C., Abraham, A. G., & Guerrero, A. (2016). Shear and extensional properties of kefiran. *Carbohydrate Polymers, 152*, 97–104.
Rodd, L. E., Scott, T. P., Cooper-White, J. J., & McKinley, G. H. (2004). Capillary break-up rheometry of low-viscosity elastic fluids. *Applied Rheology* HMI. Report Number 04-P-04.
Soszynski, R. M., & Kerekes, R. J. (1988). Elastic interlocking of nylon fibres suspended in liquid. Part 1. Nature of cohesion among fibres. *Nordic Pulp and Paper Research Journal, 3*, 172–184.
Steffe, J. F. (1996). *Rheological methods in food process engineering*. Freeman press.
Sudha, M. L., Baskaran, V., & Leelavathi, K. (2007). Apple pomace as a source of dietary fibre and polyphenols and its effect on the rheological characteristics and cake making. *Food Chemistry, 104*, 686–692.
Switzer, L. H., III, & Klingenberg, D. J. (2003). Rheology of sheared flexible fibre

2) Rozali, S. N., Paterson, A. H., Hindmarsh, J. P., & Huffman, L. M. (2019). Atomization behaviour of juice-fibre suspensions in a two-fluid nozzle. *Journal of Food Engineering, 256*, 53-60.

MASSEY UNIVERSITY
GRADUATE RESEARCH SCHOOL

STATEMENT OF CONTRIBUTION
DOCTORATE WITH PUBLICATIONS/MANUSCRIPTS

We, the candidate and the candidate's Primary Supervisor, certify that all co-authors have consented to their work being included in the thesis and they have accepted the candidate's contribution as indicated below in the *Statement of Originality*.

Name of candidate:	Siti Nadjiha Mohd Rozali
Name/title of Primary Supervisor:	Prof Tony Paterson
Name of Research Output and full reference:	
Rozali, S. N., Paterson, A. H., Hindmarsh, J. P., & Huffman, L. M. (2019). Atomization behaviour of juice-fibre suspensions in a two-fluid nozzle. Journal of Food Engineering, 256, 53-60.	
In which Chapter is the Manuscript /Published work:	Chapter 6
Please indicate:	
• The percentage of the manuscript/Published Work that was contributed by the candidate:	100%
and	
• Describe the contribution that the candidate has made to the Manuscript/Published Work:	
The candidate carried out all laboratory work and data analysis. The candidate drafted the manuscript and did the amendments during manuscript revision.	
For manuscripts intended for publication please indicate target journal:	
Candidate's Signature:	
Date:	28/05/2019
Primary Supervisor's Signature:	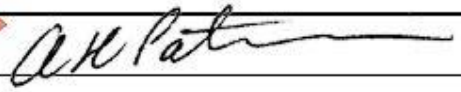
Date: May 2019	

Contents lists available at ScienceDirect

Journal of Food Engineering

journal homepage: www.elsevier.com/locate/jfoodeng

Atomization behaviour of juice-fibre suspensions in a two-fluid nozzle

Siti N.M. Rozali[a,*], Anthony H.J. Paterson[a], Jason P. Hindmarsh[a], Lee M. Huffman[b]

[a] School of Food and Advanced Technology, Massey University, New Zealand
[b] The New Zealand Institute for Plant and Food Research Limited, New Zealand

ARTICLE INFO

Keywords:
Atomization
Extensional rheology
Fiber suspensions
Shear thinning
Viscoelastic liquids

ABSTRACT

Atomization of non-Newtonian viscoelastic liquids was carried out using a two-fluid nozzle. Juice-fibre suspension is a shear thinning liquid that exhibits significant extensional resistance when forced through an extensional flow-field. Two types of fibres were used with aspect ratios of 2–3 and 8–10. The atomization behaviour of the suspensions discharging in the air was photographed using a backlit setup to visualise the atomization pattern of viscoelastic fibre suspensions. The effect of the extensional resistance is to delay the droplet formation by forming filamentary structures that link successive droplets together. As a consequence, droplets of viscoelastic fibre suspensions are usually bigger than Newtonian droplets. Using a two-fluid nozzle, at an atomizing air velocity of 150 m/s, the average droplet size of fibre suspension with aspect ratio 2–3 was 450 μm while the average droplet size of fibre suspension with aspect ratio 8–10 was 530 μm. Increasing the atomizing air velocity in the two-fluid nozzle yielded better atomization by forming smaller droplets as proved by the droplet size analysis. At the highest tested atomizing air velocity of 240 m/s, both average droplet sizes were reduced to approximately 200–250 μm.

1. Introduction

Atomization of liquids plays a major role in many industrial processes such as spray drying, internal combustion engines and painting. In spray drying, the inherent advantages of efficient or good atomization prior to the drying stage have been known and proved many times. In fruit juices applications, the spray drying process requires incorporation of a drying aid to assist with the drying step. Maltodextrin is a commercially used drying aid that has been in practice for the previous decades (Verma and Singh, 2015).

Atomization is the process of breaking up or disrupting a bulk liquid jet into droplets. This phenomenon occurs due to the competition between two opposing forces; disruptive and cohesive. Atomization occurs when the former force overcome the latter. The disruptive forces include kinetic energy, friction, gravity, interface shearing and pressure fluctuation. Meanwhile, the cohesive forces include shear viscosity and surface tension of liquids that stabilize the liquid jet from breaking up. Many studies have tried to explain and propose atomization mechanisms based on these forces. Early works usually relate the atomization with shear viscosity and surface tension of the liquid as the main forces that opposed the atomization. From there, various correlations, atomization maps and atomization mechanisms were developed to predict the performance of Newtonian liquid atomization (Faeth et al., 1995; Hinze, 1955; Lasheras et al., 1998; Lefebvre and McDonell, 2017; Wierzba, 1990). The maps and atomization mechanisms are usually explained based on Reynolds number, *Re* and Weber number, *We* (Reitz and Bracco, 1986). *Re*, as in Eq. (1), determines the state of jets flow, either laminar or turbulent while *We*, as in Eq. (2), is the ratio between aerodynamic disruptive forces exerted on the liquid and the restoring surface tension forces.

$$Re = \rho_L U_L D_J + \mu \quad (1)$$

$$We = \rho_L (U_L - U_G)^2 D_J / \sigma \quad (2)$$

where ρ_L, μ and σ are the density (kg/m^3), shear viscosity (Pa.s) and surface tension (N/m) of the liquid respectively. D_J is the jet diameter (m) and U_L and U_G are the velocity (m/s) of the liquid and air respectively. Various authors suggested different critical values of *We*, between 4 and 99.6, above which the atomization occurs (Derby, 2010; Hanson et al., 1963; Wierzba, 1990).

Most liquids of commercial and industrial relevance have complex behaviours that do not necessarily follow Newtonian behaviour. There are many applications in which these non-Newtonian liquids experience atomization such as inkjet printing and spray drying of foods. Previous work has shown that some non-Newtonian liquids behave in a different manner compared to Newtonian liquids. Specifically, some non-Newtonian liquids such as fibre suspensions can develop extensional

* Corresponding author.
E-mail address: S.Mohd-Rozali@massey.ac.nz (S.N.M. Rozali).

https://doi.org/10.1016/j.jfoodeng.2019.03.017
Received 4 December 2018; Received in revised form 18 March 2019; Accepted 19 March 2019
Available online 22 March 2019
0260-8774/ © 2019 Elsevier Ltd. All rights reserved.

resistances or elasticity that cannot be quantified by shear rheology when forced through an extensional flow-field (Christanti and Walker, 2006; Ooi and Sridhar, 2004; Rozali et al., 2019; Steffe, 1996; Thompson and Rothstein, 2007). The different types of flow field between shear and extensional and their forms of deformations and resistances are clearly illustrated by Steffe (1996). This has motivated many researchers to focus on the extensional rheological properties of liquids in order to better understand the effect of viscoelastic liquids on atomization performance (Christanti and Walker, 2006; Thompson and Rothstein, 2007). There are a few well-known methods that can be used to quantify the extensional rheology of liquids such as Filament Stretching Extensional Rheometer (FiSER™), Capillary Breakup Extensional Rheometer (CaBER™) and Cambridge Trimaster. Previous work has characterised and quantified both shear and extensional rheology of fibre suspensions that were used in the current atomization study (Rozali et al., 2019).

The importance of incorporating the extensional rheology, along with the shear rheology in explaining atomization mechanisms, has gained more recognition recently. The addition of viscoelasticity can lead to significant changes in both jet breakup and final droplet size. Chao et al. (1984) and Owens et al. (2011) show that the addition of elasticity may inhibit the sprayability of a liquid. The extensional resistance also impairs atomization by inducing ligaments stretching prior to the formation of droplets, which at the end hinders the atomization or increases the final droplet size (Mansour and Chigier, 1995).

To better understand the complex effects of fluid rheology on atomization, Marmottant and Villermaux (2004) successfully explained the key fluid mechanical features of a spray. They show that by using a two-fluid nozzle and working with a Newtonian liquid, the overall breakup process can be described by a sequence of instabilities. The liquid jet first experiences a high shear rate at its surface, induced by the surrounding high-velocity flow of air. This leads to the generation of waves on the jet surface. As the waves grow, the acceleration of the high-velocity air elongates ligaments of the liquid into the air stream. These stretched ligaments thin down in the neck region and ultimately detach from the jet. After this, the detached ligaments fragment and stabilize into smaller droplets.

The objective of this study was to spray dry concentrated fruit juices by using fibres as a drying aid. Prior to the drying stage of the concentrated fruit juices, this study aimed to identify and prove the possible nozzle to be used during the drying stage. Identification of the nozzle involved the understanding of the rheology of the fruit juice with fibres. The understanding of the juice-fibre suspensions behaviour was carried out prior to the atomization (Rozali et al., 2019). This paper focuses on investigating the atomization performance of the juice-fibre suspensions based on a two-fluid nozzle. Juice-fibre suspensions have been shown to exhibit significant extensional resistance (Rozali et al., 2019), hence, the two-fluid nozzle was chosen due to its ability to supply high atomizing air velocity as a means to stretch the ligaments of the fibre suspensions. Very few have tried to atomize viscoelastic liquids (Brenn et al., 2002; Hoyt et al., 1974; Thompson and Rothstein, 2007). These studies all used a pressure nozzle with a different configuration such as a plain, flat-fan, hollow-cone and swirl type. Keshavarz and co-workers (2015) tried to atomize a viscoelastic polymer solution using a two-fluid nozzle. To the author's knowledge, no studies have been carried out on the atomization of viscoelastic liquid based on a mixture of fruit juices and fibre.

2. Experimental

2.1. Test liquid construction

The commercial fibres used in this study were supplied by IMCD New Zealand Limited (Auckland, New Zealand). Two different types of fibres with different aspect ratio were used; Wheat Fibre 101 with an aspect ratio of 2–3 and Wheat Fibre 600 with an aspect ratio of 8–10.

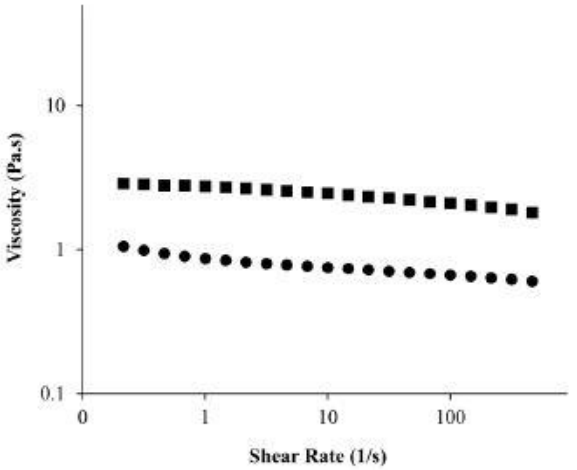

Fig. 1. Shear behaviour of different 5 g/100 g fibre suspensions as a function of aspect ratios. (●) Wheat Fibre 101 with an aspect ratio of 2–3 (■) Wheat Fibre 600 with an aspect ratio of 8–10. The figure is reproduced from Rozali et al. (2019).

Size analysis of the fibres has been explained thoroughly in previous work (Rozali et al., 2019). The 5 g/100 g fibre suspensions were prepared by mixing the fibre powders into 60 °Brix concentrated apple juice, supplied by Cedenco Foods New Zealand Limited (Hastings, New Zealand), at 20 °C and continuously stirred until complete dispersion was achieved.

2.2. Shear and extensional rheology of fibre suspensions

Shear and extensional rheology tests were carried out prior to the atomization studies. A detailed explanation of the methods and findings have been documented in previous work (Rozali et al., 2019). Shear rheology tests were performed using a commercial rotary rheometer, MCR 301 (Anton Paar GmbH, Graz, Austria). The 5 g/100 g fibre suspensions showed a shear thinning behaviour with a magnitude dependent on the fibre aspect ratio. As shown in Fig. 1, the longer fibre (higher aspect ratio) of the Wheat Fibre 600 suspension exhibited greater viscosity compared to the shorter fibres of the Wheat Fibre 101 suspension.

Capillary tube viscometer was used to obtain viscosity data at a higher shear rate of more than 1000/s. Large, medium and small diameter capillary tubes were operated in the range of shear rates $500/s < 8V/D < 2000/s$, $3000/s < 8V/D < 11000/s$ and $11000 < 8V/D < 20000/s$ respectively, where D is the tube diameter (m) and V is the average velocity inside the tube (m/s). The large, medium and small tube diameters were 9.2 mm, 5.0 mm and 3.2 mm respectively. A differential pressure transmitter (Endress + Hauser, Reinach, Switzerland) was used to obtain the pressure drop across two points on each capillary tube, while a volumetric flow meter transmitter (Endress + Hauser, Reinach, Switzerland) was used to obtain the volumetric flow rate. Details on the calculation of viscosity from the pressure drop data can be found in Mansour and Chigier (1995).

Extensional rheology tests were performed using a portable capillary breakup extensional rheometer. This method is based on the observation of a thinning profile of filamentary structures. Using the decay profile, precise measurements of fluid relaxation time can be made for a quantitative study of the extensional rheology. When subjected to an extensional flow field, the 5 g/100 g fibre suspensions displayed a significant extensional resistance compared to the Newtonian pure apple juice. As shown in Fig. 2, the thinning dynamic of the apple juice followed a linear diameter profile. It means that after

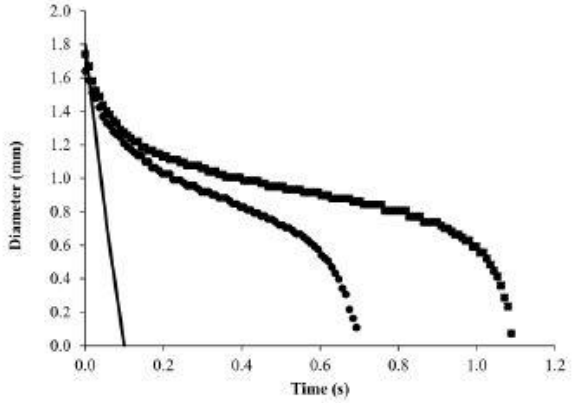

Fig. 2. Filament diameter profile of (—) apple juice (●) 5 g/100 g Wheat Fibre 101 and (■) 5 g/100 g Wheat Fibre 600 suspensions. The figure is reproduced from Rozali et al. (2019).

applying an extensional deformation towards the apple juice, the filament reacted by directly thinning down and finally breaking up in a short timescale. Meanwhile, 5 g/100 g fibre suspensions displayed an exponential profile with Wheat Fibre 600 breaking up later than Wheat Fibre 101 suspensions. During the extensional deformation, the fibres orientate, stretch and elongate inside the filament. This creates high extensional resistance that resists the thinning process of the filament and leads to the formation of a stable filament. This process then contributes to the delay in the breakup of the filament. Similar to shear resistance, longer fibres of Wheat Fibre 600 suspension induced greater resistance towards the extensional deformation compared to Wheat Fibre 101 suspension. For the same strength of extensional flow or deformation, the longer fibre (higher aspect ratio) of Wheat Fibre 600 and its aggregates required more time to deform, unravel, stretch and elongate before it reached the critical condition where the filaments finally broke. This explains the longer relaxation phase and time of Wheat Fibre 600 suspension compared to Wheat Fibre 101 suspension, as shown in Fig. 2. A more detailed discussion is provided by Rozali et al. (2019).

2.3. Atomisation

The two-fluid nozzle used in this study was of external-mix and plain jet design from Spraying System New Zealand Limited (Auckland, New Zealand). The diameter of the round liquid orifice (D_J) was 1.5 mm. The nozzle used had an annular air orifice of inner diameter (D_i) and outer diameter (D_o) of 2.54 mm and 3.00 mm respectively. The liquid flow was supplied by a gear pump and measured using a graduated cylinder and stopwatch. The air flow rate was monitored using a pressure regulator and a rotameter. Spray tests were conducted at room temperature of 20 ± 1 °C and in atmospheric air.

The experiments were conducted at a liquid flow rate of 90 mL/min, which produced a velocity of $U_L = 0.85$ m/s inside the liquid orifice. The liquid velocity was maintained constant while the atomizing air velocity was varied between 42 m/s and 240 m/s. Corresponding Reynolds number of the liquid (Re_L) was maintained at 6. Meanwhile, the Weber number (We) was varied between 4.5×10^4 and 1.2×10^6. The characteristic shear viscosity used in calculating the Re_L was chosen based on the wall shear rate, $\dot{\gamma}$ (1/s) experienced inside the liquid orifice. For a non-Newtonian liquid with a power-law index, n, the shear rate is given as in Eq. (3), where Q_L (mL/min) is the liquid flow rate (Fredrickson, 1964). The calculated shear viscosity based on the instantaneous wall shear rate should only be taken as an approximation. Based on Eq. (3), the shear rate inside the liquid orifice is calculated to be approximately 6000/s.

$$\dot{\gamma} = (3n + 1/n)(Q_L/\pi(D_J/2)^3) \quad (3)$$

Extension or strain rates inside the liquid orifice can be estimated based on Eq. (4) (Lindstedt et al., 2005), where H is the orifice length (m). Based on Eq. (4), the bulk strain rate inside the orifice is calculated to be approximately 900/s.

$$S_b = 2(U_L/H) \quad (4)$$

2.4. Flash photography

A high-intensity light source and a MS85K high-speed camera (Mega Speed, Tennessee, U.S.) were used for imaging atomization behaviour. A typical backlit setup was used, in which the spray was situated between the light source and a camera such that liquid droplets and ligaments appeared dark on a bright background. The high-intensity light source with a short pulse duration (10 ns) was triggered using a PM 5712 pulse generator (Philips, Eindhoven, Netherlands) to illuminate and freeze droplets in mid-flight.

2.5. Digital SLR (DSLR) photography

A 60 mm micro lens and SB-910 speedlight were attached to a Nikon D90 camera. The DSLR was used to capture the image of a whole spray for spray angle identification.

2.6. Droplet size analysis

Captured images from the flash photography were processed using a MATLAB™ (2015b) image analysis through which the D-values of D (v, 10), D (v, 50) and D (v, 90) of the sprays were generated. The droplet size results obtained from the MATLAB image analysis were compared with the results generated by a Malvern Mastersizer S (Malvern Instruments Ltd., Worcestershire, U.K.). The D-values are the intercepts for 10%, 50% and 90% of the cumulative volume. For example, D (v,10) is the diameter at which 10% of the sample's volume is comprised of droplets with a diameter less than this value. D (v,50) is defined as the diameter where half of the sample's volume has droplets with a diameter less than this value. Similarly, D (v,90) is the diameter at which 90% of the sample's volume contains droplets with a diameter less than this value.

3. Results and discussion

3.1. Choice of a two-fluid nozzle

Using the commercial rotary rheometer, the maximum applied shear rate was 1000/s, as shown in previous work (Rozali et al., 2019). However, it is believed that a shear rate higher than 1000/s is expected in the atomization process (Schröder et al., 2011). This means that for the shear thinning fibre suspensions, the actual shear viscosity experienced during atomization is far lower than can be predicted through the rotary rheometer. Hede et al. (2008) proposed an equation to calculate the shear rate during atomization with an assumption that momentum is transferred between the liquid feed and atomizing gas in the mixing zone, and both leave the atomization zone at a constant average velocity, V_{av} (Hede et al., 2008). V_L is the velocity of the liquid feed within the nozzle before the exit. Based on Eq. (5), at atomizing air velocity of 42 m/s, the estimated shear rate during the atomization is ~25 000/s.

$$\dot{\gamma} = 2((V_{av} - V_L)/D_J) \quad (5)$$

At a very high shear rate encountered at the nozzle of more than 1000/s, the shear viscosity of 5 g/100 g Wheat Fibre 101 and 5 g/100 g Wheat Fibre 600 suspensions were reduced. This is shown in Fig. 3 where the viscosity of the fibre suspensions was measured using a

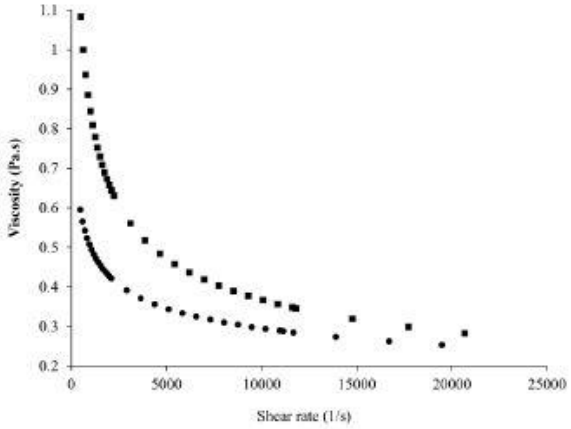

Fig. 3. Shear behaviour of different 5 g/100 g fibre suspensions as a function of aspect ratios at much greater shear rate of more than 1000/s. (●) Wheat Fibre 101 with an aspect ratio of 2–3 (■) Wheat Fibre 600 with an aspect ratio of 8–10.

capillary viscometer. Due to pumping limitation, only data up to 20 000/s is shown in Fig. 3. Based on Fig. 3, the viscosity of each fibre suspension can be said to approximately reach their own plateau limitation at a shear rate above 20 000/s. Therefore, the shear thinning of the fibre suspensions is almost finished where increasing the shear rate above a certain value might not reduce the shear viscosity anymore.

Fig. 3 subtly shows that the use of a conventional pressure nozzle to atomize fibre suspensions may not be efficient. The principal of the pressure nozzle is the conversion of pressure energy within the liquid into kinetic energy by applying high pumping pressure. However, as shown in Fig. 3, increasing the pumping energy, thus the shear rates after a certain point, may not result in any significant decrease in shear viscosity. There is no point in pumping more because, at that point, the shear viscosity may not be the dominant factor that resists atomization.

The rheology study shows that fibre suspensions exhibit extensional resistance along with shear resistance. The two-fluid nozzle was chosen due to its ability to supply high atomizing air velocity to stretch the ligaments of the fibre suspensions and thus overcome the extensional resistance.

3.2. Effect of shear rheology

Based on Fig. 4, the appearances of the atomization behaviour between 5 g/100 g Wheat Fibre 101 and 5 g/100 g Wheat Fibre 600 suspensions were very similar. Both liquids displayed a rope-like ligament pattern. Both types of fibre suspensions showed a pattern where the liquid streams or ligaments remained intact and underwent erratic excursions away from the centreline. This behaviour of liquid breakup is very similar to a Newtonian liquid breakup. Other than the similar breakup pattern and behaviour, the appearance of both sprays was marked by an extremely short jet breakup length. The images in Fig. 4 were taken at a position 10 mm below the nozzle which means that both types of fibre suspensions achieved a breakup length of, at most, 10 mm. The spray angle of both liquids appeared full at approximately 40°, which indicates that a fully developed spray was produced by both Wheat Fibre 101 and Wheat Fibre 600 suspensions. Fig. 5 shows the image of the spray angle for 5 g/100 g Wheat Fibre 101. The spray was captured using a DSLR camera.

If the fibre suspensions have negligible extensional resistance like Newtonian liquids, increasing the atomizing air velocity will disintegrate the ligaments by collapsing the ligaments into a multiplicity of small droplets immediately downstream of the atomizer (Chigier and Farago, 1992). This is because high air velocity provides a greater shear rate to the fibre suspensions. At that high-velocity high shear rate, the shear viscosity of the fibre suspensions is low and allows the formation of droplets immediately downstream from the atomizer. However, as shown in the rheology study, the behaviour of the fibre suspensions is also dominated by extensional resistance. Hence, although the fibre suspensions have low shear viscosity, the extensional resistance can prevent the formation of complete atomization immediately downstream from the atomizer.

3.3. Effect of extensional rheology

Unlike the breakup pattern dominated by shear viscosity, as shown in Fig. 4, the pattern with extensional resistance dominance is very different. The latter usually incorporates a pattern where the liquid stream is well-dispersed and does not remain intact. Based on Fig. 6, increasing the atomizing air velocity to 150 m/s did not result in the dispersion of ligaments into droplets right after the nozzle like in the case of Newtonian liquid atomization. Instead, the 5 g/100 g Wheat Fibre 101 and 5 g/100 g Wheat Fibre 600 suspensions which exhibited significant extensional properties displayed a pattern of filamentary structures, connecting successive droplets together. The presence of the filaments prevented the pinch-off of droplets between each other. A clear illustration of the situation is shown in Fig. 6 (a). Red circles in Fig. 6 (a) highlight the droplets, while the yellow arrows point to the pinch-off or necking region of a filament. Due to the significant extensional properties of fibre suspensions, as evidenced from the rheology study, the elastic filament induced additional tensile stresses in their cross-sections at the pinch-off that enhanced its stability against capillary forces and, thus, inhibited breakup (Rozali et al., 2019). This means that the breakup of the filaments was delayed and thus affected the final droplet formation. This breakup pattern is very similar to polymer solutions which also exhibit significant viscoelasticity (Chao et al., 1984; Hoyt et al., 1974).

Unlike viscoelastic liquids, a Newtonian liquid breakup does not show the presence of stretched filaments (Aliseda et al., 2008; Bailardi et al., 2010; Ochowiak et al., 2017). A Newtonian breakup also has a high stretching rate at high atomizing air velocity. However, the stretched ligaments thin down very quickly as a result of capillary force and are not resisted by the extensional resistance. This is clearly portrayed by the difference in the filament thinning profile between pure apple juice and fibre suspensions as shown in Fig. 2 (Rozali et al., 2019). While apple juice thinned linearly, the filament thinning of 5 g/100 g Wheat Fibre 101 and 5 g/100 g Wheat Fibre 600 suspensions occurred exponentially. Consequently, the filament of fibre suspensions broke up later compared to the apple juice. In other words, Newtonian liquids will undergo filament thinning that breaks during the visco-capillary regime, while 5 g/100 g fibre suspensions break up during the elasto-capillary regime (Rozali et al., 2019).

As shown in Fig. 6, the modification to the breakup pattern of viscoelastic liquid as compared to a Newtonian breakup occurred mainly when the fluid element reached a large strain and rapid deformation rate that was generated in the final breakup and pinch off stages. It is believed that shear resistance controls the early breakup stage while extensional resistance controls the final breakup stage. This can be explained by referring to the basic mechanism of two-fluid atomization. At first, the calm liquid jet was disturbed to create waves or instabilities on the liquid surface. These waves and instabilities were not generated through pulling or stretching of the thick liquid jet by the surrounding atomizing air. Rather, the air sheared the outer jet surface which then generated thin liquid elements. This is referred to as ligaments. Only after this did the air act to pull or stretch the thin liquid elements generated from the previous stage.

Based on Fig. 6, both 5 g/100 g Wheat Fibre 101 and 5 g/100 g Wheat Fibre 600 suspensions showed a similar atomization pattern where the droplets were connected to each other by filaments. The

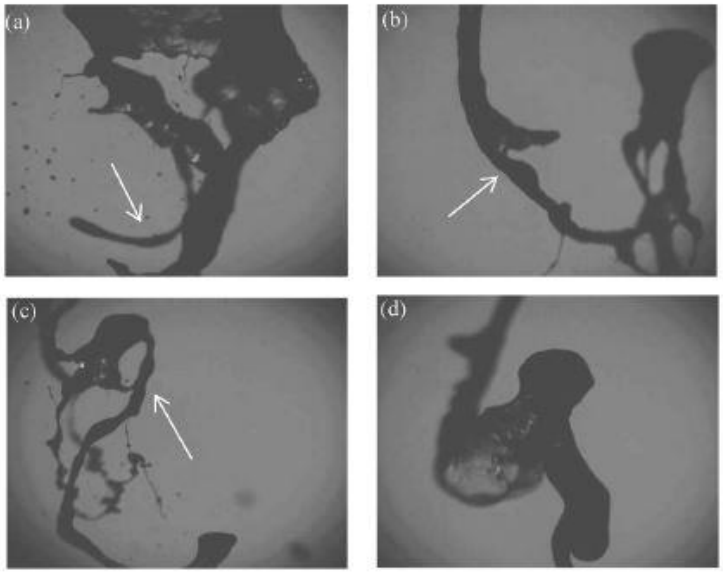

Fig. 4. Photographs of the breakup of (a & b) 5 g/100 g Wheat Fibre 101 (c & d) 5 g/100 g Wheat Fibre 600 suspensions at similar atomizing air velocity of 42 m/s. Images were obtained at a position 10 mm below the nozzle. Ligaments are pointed out by white arrows.

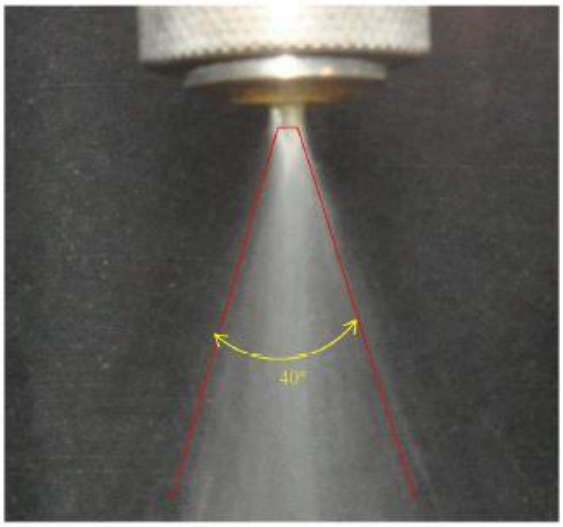

Fig. 5. Approximate boundary of the spray is highlighted by the red line. The spray angle is measured to be around 40°. (For interpretation of the references to colour in this figure legend, the reader is referred to the Web version of this article.)

filaments were seen to undergo a large stretching motion before they broke up, resulting in long threads of liquid attached to droplets. A white arrow in Fig. 6 (a) shows an example where the droplet at one end was suggested to have pinched off from the filament. Increasing atomizing air velocity, and thus extensional rates, was expected to break the filaments faster compared to at 150 m/s. This is simply because the disruptive forces were increased while the stabilizing forces remained the same. It is difficult to evaluate the efficiency of the atomization based on the images of ligaments and filaments only. Furthermore, the quality of the images was reduced at much higher atomizing air velocity. The images are not shown here but a mere observation of the atomization images at a greater atomizing air velocity of 195 m/s indicated that more filaments had already broken up at a position 10 mm below the nozzle. It means that more droplets were pinched off from the filaments compared to in Fig. 6. Most of the droplets have a similar appearance to the droplet with a white arrow in Fig. 6 (a) where a droplet appears to have pinched off and broken from the filament.

To better understand the effect of extensional resistance on atomization, atomization images were captured at a position 50 mm below the nozzle. This was carried out to see the effect of extensional resistance on final droplet formation. Fig. 7 (a) shows the droplet formation of 5 g/100 g Wheat Fibre 101. The image was converted into a binary image, as in Fig. 7 (b), to ease the analysis for droplet size measurements. Fig. 7 shows that the droplet formation of liquid with extensional resistance was very different from Newtonian droplets. Many previous works have shown the spherical and symmetrical droplets of Newtonian liquids. In contrast, the atomization of fibre suspensions which exhibit significant extensional properties results in the formation of non-spherical and non-symmetrical droplets at a position 50 mm below the nozzle. Specifically, the droplets are characterised by the presence of a bridge between them. The existence of bridges, unsymmetrical droplets and non-spherical droplets are all the consequence of a delay in the filament breakup at position 10 mm below the nozzle.

Based on the Newtonian breakup, the detachment of ligaments from the liquid jet is ultimately followed by the fragmentation of the ligaments into a cascade of droplets. Beyond that point, usually, the droplets will be dispersed into smaller droplets due to the equilibrium effect of surface tension (Lefebvre, 1988). However, in the case of 5 g/100 g fibre suspensions, the delay in the breakup of filamentary structures shown in Fig. 6 that connected successive droplets or chunk of ligaments together, prevented the fragmentation of the ligaments into individual droplets. This later inhibited the stabilization of the droplets into equilibrium size and shape at a position far below the nozzle. Droplets in Fig. 7 were characterised by the non-spherical shape and the presence of bridges. This must be due to the insufficient time it took for the droplets to reach the equilibrium condition because of the delay in

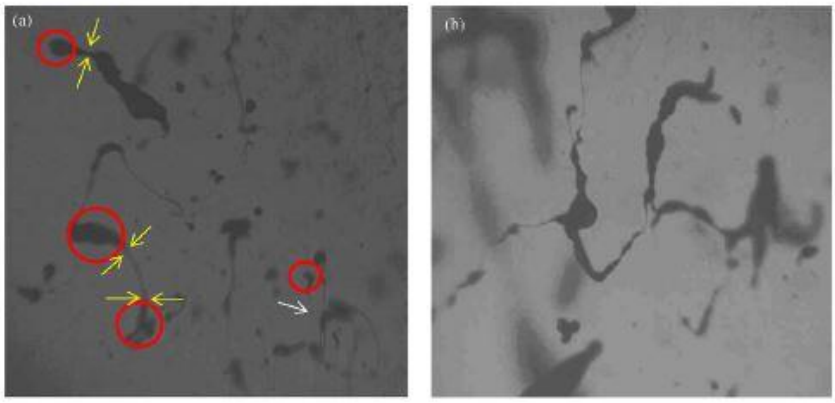

Fig. 6. Photographs of the breakup of (a) 5 g/100 g Wheat Fibre 101 (b) 5 g/100 g Wheat Fibre 600 suspensions at similar atomizing air velocity of 150 m/s. Images were obtained at a position 10 mm below the nozzle.

the filament breakup. It is also possible that the strain rates or disruptive forces applied were not sufficient to break the filaments at position 10 mm below the nozzle and, as a result, some droplets at position 50 mm below the nozzle were still connected by a bridge or filament.

As mentioned earlier, increasing atomizing air velocity gave enough or sufficient force to stretch and break the filaments as shown in Fig. 6. The breakup of the filaments then resulted in a better droplet formation at a position 50 mm below the nozzle. This is evidenced in Fig. 8. The atomizing air velocity was increased to 195 m/s. Fig. 8 shows a more spherical and symmetrical final droplets formation. The presence of bridges between droplets due to the insufficient forces to stretch and break the filaments beforehand was also reduced. The breakup of filaments or pinch-off of droplets at a position 10 mm below the nozzle at much higher atomizing air velocities provided sufficient time for all droplets to stabilize into symmetrical spherical droplets. Large unsymmetrical droplets were also able to disintegrate and stabilize into smaller droplets due to the surface tension effect.

3.4. Droplet size analysis

Evaluating the ability of atomization to perform through a qualitative comparison of several captured images alone may be misleading. Hence, it is necessary to perform a droplet size analysis on both 5 g/100 g Wheat Fibre 101 and 5 g/100 g Wheat Fibre 600 suspensions. MATLAB image analysis was performed on at least 1000 droplets at a position 50 mm below the nozzle. The results are shown in Tables 1 and 2. The diameter of each droplet was calculated based on the measured surface area of the particles. The results from the MATLAB were compared with the results generated by Malvern Mastersizer based on Passing-Bablok regression analysis. Passing-Bablok analysis is usually used for method comparison studies (Passing and Bablok, 1983). A null hypothesis was tested being that the relationship between two variables, which are the D-values generated by MATLAB and Malvern Mastersizer, is linear. A p-value of more than 0.05 was obtained for all D-values, as shown in Table 3, which indicates weak evidence against the null hypothesis, hence we fail to reject the null hypothesis. In short, it means a good correlation was obtained between the D-values generated by MATLAB image analysis and Malvern Mastersizer.

As seen in Fig. 9, increasing the atomizing air velocity from 150 m/s to 240 m/s reduced the droplet sizes of both 5 g/100 g Wheat Fibre 101 and 5 g/100 g Wheat Fibre 600 suspensions. Increasing the air velocity to 240 m/s provided greater strain rate and thus sufficient disruptive forces to stretch and break filaments at a position 10 mm below the nozzle. The breakup of the filaments and pinched-off of droplets right after the nozzle led to the formation of more symmetrical spherical droplets at a position 50 mm below the nozzle. In contrast, at 150 m/s atomizing air velocity, most of the droplets were not pinched-off from the filaments right after the nozzle. This later led to a breakup of filaments and the presence of unbroken filaments, non-spherical and non-symmetrical droplets at a position far below the nozzle. Consequently, these resulted in bigger droplet sizes as measured by the Malvern Mastersizer.

Based on Fig. 9, increasing the atomizing air velocity significantly reduced the D (v, 90) and gave the least effect on D (v, 10). A less significant reduction in D (v, 10) must be due to the atomization performance reaching its limit where the surface tension pressure that holds the spherical droplets and the aerodynamic pressure outside the droplets are in equilibrium with the droplets internal pressure (Lefebvre, 1988). The D (v,90) reduced considerably and significantly

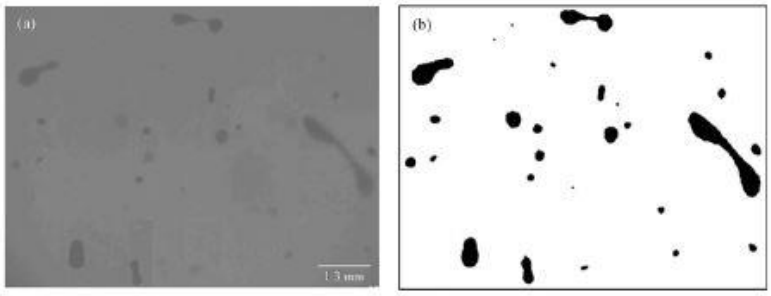

Fig. 7. Photograph of the droplets of 5 g/100 g WF 101 at position 50 mm below the nozzle and at atomizing air velocity of 150 m/s. (a) Raw image (b) Binary image.

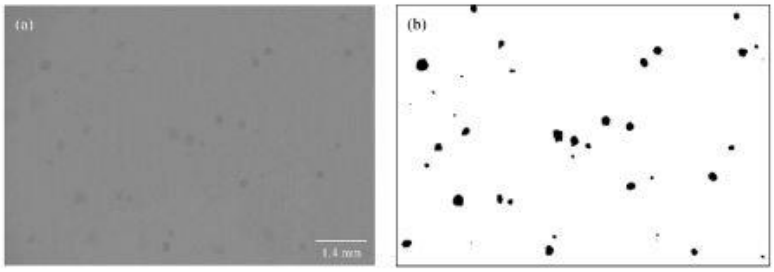

Fig. 8. Photograph of the droplets of 5 g/100 g WF 101 at position 50 mm below the nozzle and at atomizing air velocity of 195 m/s. (a) Raw image (b) Binary image.

Table 1
D-values of 5 g/100 g Wheat Fibre 101 suspension generated by MATLAB and Malvern Mastersizer.

Fibre suspensions	Atomizing air velocity (m/s)	D-values	Methods	Droplet sizes (um)
5 wt% Wheat Fibre 101	150	D (v,10)	MATLAB	210
			Malvern	200
		D (v,50)	MATLAB	465
			Malvern	450
		D (v,90)	MATLAB	790
			Malvern	740
	195	D (v,10)	MATLAB	165
			Malvern	160
		D (v,50)	MATLAB	355
			Malvern	390
		D (v,90)	MATLAB	620
			Malvern	630
	215	D (v,10)	MATLAB	150
			Malvern	145
		D (v,50)	MATLAB	265
			Malvern	290
		D (v,90)	MATLAB	400
			Malvern	420
	240	D (v,10)	MATLAB	130
			Malvern	110
		D (v,50)	MATLAB	240
			Malvern	200
		D (v,90)	MATLAB	350
			Malvern	360

Table 2
D-values of 5 g/100 g Wheat Fibre 600 suspension generated by MATLAB and Malvern Mastersizer.

Fibre suspensions	Atomizing air velocity (m/s)	D-values	Methods	Droplet sizes (um)
5 wt% Wheat Fibre 600	150	D (v,10)	MATLAB	305
			Malvern	215
		D (v,50)	MATLAB	680
			Malvern	530
		D (v,90)	MATLAB	965
			Malvern	1265
	195	D (v,10)	MATLAB	195
			Malvern	185
		D (v,50)	MATLAB	355
			Malvern	385
		D (v,90)	MATLAB	645
			Malvern	690
	215	D (v,10)	MATLAB	155
			Malvern	160
		D (v,50)	MATLAB	280
			Malvern	310
		D (v,90)	MATLAB	450
			Malvern	495
	240	D (v,10)	MATLAB	130
			Malvern	130
		D (v,50)	MATLAB	260
			Malvern	250
		D (v,90)	MATLAB	360
			Malvern	390

compared to the D (v,10) due to the absence of large and connecting droplets at much greater atomizing air velocity. In summary, it can be said that the smaller droplets represented by D (v,10) were controlled by the surface tension pressure limit. Meanwhile, the bigger droplets or D (v,90) were controlled by the atomizing air velocity.

Fig. 9 shows that the D-values of 5 g/100 g Wheat Fibre 101 suspension were lower than 5 g/100 g Wheat Fibre 600 suspension, especially at the lowest atomizing air velocity of 150 m/s. This is due to the greater extensional resistance exhibited by the 5 g/100 g Wheat Fibre 600 suspension due to the longer fibres and higher aspect ratio (Rozali et al., 2019). Increasing the atomizing air velocity reduced the difference between the D-values. Despite the difference in the droplet sizes between 5 g/100 g Wheat Fibre 101 and 5 g/100 g Wheat Fibre 600 suspensions, it is evident that the droplet sizes of viscoelastic liquids were bigger than Newtonian liquids. This is in agreement with previous studies (Christanti and Walker, 2006; Mansour and Chigier, 1995; Mun et al., 1999). They show that the addition of viscoelasticity can lead to significant changes in atomization performance, especially in the production of bigger average droplet sizes of the sprays.

In atomizing viscoelastic liquids, greater disruptive forces are required. This is evident from the *We* used in this study. Previous authors suggested a critical *We* of less than 100 (Derby, 2010; Hanson et al., 1963; Wierzba, 1990), however, throughout this study, the minimum *We* of 4.5×10^4 did not yield complete atomization, as shown in Fig. 4.

Table 3
p-value based on the comparison between D-values generated by MATLAB image analysis and Malvern Mastersizer.

D-value	D (v,10)	D (v,50)	D (v,90)
p-value	0.699	0.699	0.699

This is highly related to the parameter that is being considered as the stabilizing force in generating the *We* equation, as shown in Eq. (2). Based on Eq. (2), surface tension is regarded as the stabilizing force that opposed atomization. However, this is only true for Newtonian liquids as they exhibit insignificant extensional behaviour. In viscoelastic atomization or fibre suspensions atomization, the extensional behaviour of the liquid dominates the atomization resistance. A much greater disruptive force is required to overcome the extensional resistance as suggested by the *We* used in this study. Hence, it can be said that the critical *We* reported by previous authors is true only for Newtonian liquids or water. Future works should attempt to generate an atomization map that characterizes the performance of viscoelastic atomization. This includes suggesting a new critical *We*. Further investigations involving the prediction of actual shear and strain rates during atomization based on velocity data of filaments and droplets is also recommended.

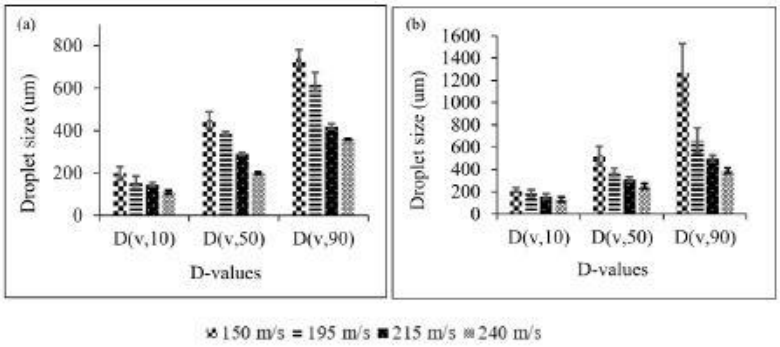

Fig. 9. Droplet size analysis based on droplets formation at position 50 mm below nozzle. The results were generated by Malvern Mastersizer. Different atomizing air velocity was supplied (a) 5 g/100 g Wheat Fibre 101 (b) 5 g/100 g Wheat Fibre 600.

4. Concluding remarks

Visualization studies of the atomization performance of fibre suspensions which exhibit both shear and extensional properties were carried out. The shear rheology of fibre suspensions did not suggest any significant difference in the atomization performance when compared to Newtonian atomization. However, when the atomizing air velocity was increased, the spray visualization showed that the extensional rheology of the fibre suspensions significantly affected the atomization behaviour, specifically at the final breakup stage. The final breakup pattern of the fibre suspensions showed filamentary structures connecting successive droplets together. This pattern is absent in Newtonian atomization. These filamentary structures contributed to the formation of big droplet sizes of viscoelastic fibre suspensions. Droplet size analysis showed that the final size of viscoelastic droplets was highly dependent on the aspect ratio of fibres used but this effect was reduced when much greater atomizing air velocity was applied during the atomization.

This study shows that the atomization of fibre suspensions which exhibit extensional properties can be achieved by using a two-fluid nozzle at high air velocity. At these conditions, smaller spherical droplets of fibre suspensions were produced that will assist the performance of drying in the spray drying process later.

Acknowledgement

The authors would like to thank the Ministry for Business, Innovation and Employment (MBIE) New Zealand for the funding provided through Food Industry Enabling Technologies (FIET) program that has enabled this project to proceed.

References

Aliseda, A., Hopfinger, E., Lasheras, J.C., Kremer, D., Berchielli, A., Connolly, E., 2008. Atomization of viscous and non-Newtonian liquids by a coaxial, high-speed gas jet. Experiments and droplet size modeling. Int. J. Multiph. Flow 34, 161–175.
Ballardi, G., Negri, M., Ciezki, H., 2010. Several aspects of the atomization behavior of various Newtonian fluids with a like-on-like impinging jet injector. In: Paper Presented at the Proceedings of the 23rd European Conference on Liquid Atomization and Spray Systems.
Brenn, G., Stelter, M., Durst, F., 2002. The influence of viscoelastic fluid properties on spray formation from flat-fan and pressure-swirl atomizers. Atomization Sprays 12, 299–327.
Chao, K., Child, C., Grens, E., Williams, M., 1984. Antimisting action of polymeric additives in jet fuels. AIChE J. 30, 111–120.
Chigier, N., Farago, Z., 1992. Morphological classification of disintegration of round liquid jets in a coaxial air stream. Atomization Sprays 2.
Christanti, Y., Walker, L.M., 2006. Quantifying air atomization of viscoelastic fluids through fluid relaxation times. Atomization Sprays 16.
Derby, B., 2010. Inkjet printing of functional and structural materials: fluid property requirements, feature stability, and resolution. Annu. Rev. Mater. Res. 40, 395–414.
Faeth, G., Hsiang, L.-P., Wu, P.K., 1995. Structure and breakup properties of sprays. Int. J. Multiph. Flow 21, 99–127.
Fredrickson, A.G., 1964. Principles and Applications of Rheology. Prentice-Hall.
Hanson, A., Domich, E., Adams, H., 1963. Shock tube investigation of the breakup of drops by air blasts. Phys. Fluid. 6, 1070–1080.
Hede, P.D., Bach, P., Jensen, A.D., 2008. Two-fluid spray atomisation and pneumatic nozzles for fluid bed coating/agglomeration purposes: a review. Chem. Eng. Sci. 63 (14), 3821–3842.
Hinze, J., 1955. Fundamentals of the hydrodynamic mechanism of splitting in dispersion processes. AIChE J. 1, 289–295.
Hoyt, J., Taylor, J., Runge, C.D., 1974. The structure of jets of water and polymer solution in air. J. Fluid Mech. 63, 635–640.
Keshavarz, B., Sharma, V., Houze, E.C., Koerner, M.R., Moore, J.R., Cotts, P.M., McKinley, G.H., 2015. Studying the effects of elongational properties on atomization of weakly viscoelastic solutions using Rayleigh Ohnesorge Jetting Extensional Rheometry (ROJER). J. Non-Newtonian Fluid Mech. 222, 171–189.
Lasheras, J., Villermaux, E., Hopfinger, E., 1998. Break-up and atomization of a round water jet by a high-speed annular air jet. J. Fluid Mech. 357, 351–379.
Lefebvre, A., 1988. Atomization and Sprays. CRC press.
Lefebvre, A.H., McDonell, V.G., 2017. Atomization and Sprays. CRC press.
Lindstedt, R.P., Luff, D.S., Whitelaw, J.H., 2005. Velocity and strain-rate characteristics of opposed isothermal flows. Flow, Turbul. Combust. 74 (2), 169–194.
Mansour, A., Chigier, N., 1995. Air-blast atomization of non-Newtonian liquids. J. Non-Newtonian Fluid Mech. 58, 161–194.
Marmottant, P., Villermaux, E., 2004. Fragmentation of stretched liquid ligaments. Phys. Fluids 16, 2732–2741.
Mun, R.P., Young, B.W., Boger, D.V., 1999. Atomisation of dilute polymer solutions in agricultural spray nozzles. J. Non-Newtonian Fluid Mech. 83, 163–178.
Ochowiak, M., Matuszak, M., Włodarczak, S., 2017. The analysis of pneumatic atomization of Newtonian and non-Newtonian fluids for different medical nebulizers. Drug Dev. Ind. Pharm. 43, 1999–2010.
Ooi, Y.W., Sridhar, T., 2004. Resistance to uniaxial extensional flow of fibre suspensions. Rheol. Acta 43, 223–231.
Owens, M.S., Vinjamur, M., Scriven, L., Macosko, C., 2011. Misting of non-Newtonian liquids in forward roll coating. J. Non-Newtonian Fluid Mech. 166, 1123–1128.
Passing, H., Bablok, W., 1983. A new biometrical procedure for testing the equality of measurements from two different analytical methods. Application of linear regression procedures for method comparison studies in clinical chemistry, Part I. Clin. Chem. Lab. Med. 21, 709–720.
Reitz, R., Bracco, F., 1986. Mechanisms of breakup of round liquid jets. Encyclopedia of Fluid Mechanics 3, 233–249.
Rozali, S.N., Paterson, A.H., Hindmarsh, J.P., Huffman, L.M., 2019. Understanding the shear and extensional properties of pomace-fibre suspensions prior to the spray drying process. LWT 99, 138–147.
Schröder, J., Lederer, M., Gaukel, V., Schuchmann, H., 2011. Effect of atomizer geometry and rheological properties on effervescent atomization of aqueous polyvinylpyrrolidone solutions. In: Paper Presented at the ILASS–Europe 24rd Annual Conference on Liquid Atomization and Spray Systems. Estoril, Portugal.
Steffe, J.F., 1996. Rheological Methods in Food Process Engineering. Freeman press.
Thompson, J.C., Rothstein, J.P., 2007. The atomization of viscoelastic fluids in flat-fan and hollow-cone spray nozzles. J. Non-Newtonian Fluid Mech. 147, 11–22.
Verma, A., Singh, S.V., 2015. Spray drying of fruit and vegetable juices - a review. Crit. Rev. Food Sci. Nutr. 55, 701–719.
Wierzba, A., 1990. Deformation and breakup of liquid drops in a gas stream at nearly critical Weber numbers. Exp. Fluid 9, 59–64.

3) Rozali, S. N., Paterson, A. H., Hindmarsh, J. P., & Huffman, L. M. (2019). Theoretical prediction of atomization performance of fibre suspensions and the effect of feed temperature and air velocity. *Journal of Food Engineering*, *269*.

MASSEY UNIVERSITY
GRADUATE RESEARCH SCHOOL

STATEMENT OF CONTRIBUTION
DOCTORATE WITH PUBLICATIONS/MANUSCRIPTS

We, the candidate and the candidate's Primary Supervisor, certify that all co-authors have consented to their work being included in the thesis and they have accepted the candidate's contribution as indicated below in the *Statement of Originality*.

Name of candidate:	Siti Nadjiha Mohd Rozali
Name/title of Primary Supervisor:	Prof Tony Paterson
Name of Research Output and full reference:	
Rozali, S. N., Paterson, A. H., Hindmarsh, J. P., & Huffman, L. M. (2019). Theoretical prediction of atomization performance of fibre suspensions and the effect of feed temperature and air velocity. Journal of Food Engineering, 269.	
In which Chapter is the Manuscript /Published work:	Chapter 6
Please indicate:	
• The percentage of the manuscript/Published Work that was contributed by the candidate:	100%
and	
• Describe the contribution that the candidate has made to the Manuscript/Published Work:	
The candidate carried out all laboratory work and data analysis. The candidate drafted the manuscript and did the amendments during manuscript revision.	
For manuscripts intended for publication please indicate target journal:	
Candidate's Signature:	
Date:	November 2019
Primary Supervisor's Signature:	
Date:	November 2019

Journal of Food Engineering 269 (2020) 109742

Contents lists available at ScienceDirect

Journal of Food Engineering

journal homepage: http://www.elsevier.com/locate/jfoodeng

Theoretical prediction of atomization performance of fibre suspensions and the effect of feed temperature and air velocity

Siti N.M. Rozali [a,*], Anthony H.J. Paterson [a], Jason P. Hindmarsh [a], Lee M. Huffman [b]

[a] School of Food and Advanced Technology, Massey University, New Zealand
[b] The New Zealand Institute for Plant and Food Research Limited, New Zealand

ARTICLE INFO

Keywords:
Droplet sizes
Extensional rheology
Relaxation time
Two-fluid nozzle
Viscoelastic liquids

ABSTRACT

Atomization performances of juice-fibre suspensions, which are non-Newtonian extensional liquids, inside a two-fluid nozzle were predicted theoretically by using two different relationships, in which one of the relationships does not incorporate the extensional rheological properties in its prediction. A good correlation was obtained between the theoretical and experimental droplet sizes of fibre suspensions when the theoretical droplet sizes were predicted by considering the extensional rheological property which is the relaxation time of the fibre suspensions. This finding confirms that the atomization of fibre suspensions, which the fibre suspensions exhibit significant extensional properties, are dominantly controlled by extensional resistance with minor effects of shear resistance and surface tension. It also implies that the relatively bigger droplet sizes of the fibre suspensions, when compared to Newtonian droplets, were due to the extensional resistance of the suspensions, with little effect by shear viscosity and surface tension. The atomization performance was observed at elevated temperatures ranging between 20 and 70 °C. By using a two-fluid nozzle at a low atomizing air velocity of 150 m/s, the D(v,90) significantly reduced from >1000 μm to 650 μm when the temperature was increased from 20 to 70 °C. Meanwhile, at a high atomizing air velocity of 240 m/s, the D(v,90) can be said to remain constant between 350 and 400 μm.

1. Introduction

Nowadays most of the commercial and industrial relevance liquids have complex behaviours which mean they are not simply following Newtonian behaviour. These liquids are termed non-Newtonian liquids and some non-Newtonian liquids exhibit viscoelastic properties in which they contribute or exhibit both solid (Hooke's law of elasticity) and liquid (Newton's law of viscosity) characteristics (Chhabra, 2006; Collett et al., 2015). An example of viscoelastic liquid which exhibits significant extensional properties is a concentrated fruit juice containing fibres as a drying aid, which is also called juice-fibre suspension (Rozali et al., 2019b). The literature on extensional rheology is limited when compared to shear rheology. As a result, the effect of the viscoelasticity and extensional rheology on atomization performance is rarely explored. A previous study by Rozali et al. (2019a) has explained in depth about the atomization behaviour of fibre suspensions when using a two-fluid nozzle, which it shows experimentally the atomization pattern and droplet sizes of the fibre suspensions affected by the extensional properties of the fibre suspensions.

Atomization is the process of disrupting liquid sheets into droplets due to disruptive and stabilizing forces. The disruptive forces include kinetic energy, friction, gravity, interface shearing and pressure fluctuation. Meanwhile, the cohesive forces include shear resistance, surface tension of liquids and extensional resistance that stabilise the liquid jet from breaking up. By identifying the forces involved, previous works have developed different correlation equations in attempts to predict the atomization performance, specifically the droplet sizes inside a two-fluid nozzle (Aliseda et al., 2008; Masters, 1979; Rajan and Pandit, 2001; Varga et al., 2003). However, as the importance of extensional rheology in influencing the atomization of non-Newtonian liquids was not studied, all the models do not include the effect of extensional properties such as the extensional viscosity or relaxation time of the liquids. The current study is aimed to show the difference in the droplet sizes of fibre suspensions theoretically predicted using two different theoretical equations, those are proposed by Aliseda et al. (2008) and Keshavarz et al. (2015). Aliseda et al. (2008) developed a theoretical equation to predict the droplet sizes inside a two-fluid nozzle based on shear rheology of a liquid and Keshavarz et al. (2015) extended the equation to

* Corresponding author.
E-mail address: S.Mohd-Rozali@massey.ac.nz (S.N.M. Rozali).

https://doi.org/10.1016/j.jfoodeng.2019.109742
Received 22 July 2019; Received in revised form 24 September 2019; Accepted 25 September 2019
Available online 27 September 2019
0260-8774/© 2019 Elsevier Ltd. All rights reserved.

include the properties of extensional rheology in their prediction. The theoretical prediction of the droplet sizes of fibre suspensions was then directly compared to the experimental results from Rozali et al. (2019a). Eq. (1) shows the Newtonian equation developed by Aliseda et al. (2008) while Eq. (2) shows the extended equation developed by Keshavarz et al. (2015), which includes the effect of additional extensional resistance. d_{VE} (μm) is the average droplet size, specifically D(n,50) for viscoelastic liquids, D_J (mm) is the jet diameter which is similar to the orifice diameter, U_A (m/s) is the atomizing air velocity, σ (mN/m) is the surface tension and ρ is the density (kg/m^3). *We* and *Oh* are the Weber number and Ohnesorge number respectively based on the jet shearing, while De_{R_l} and Oh_{R_l} are the Deborah number and Ohnesorge number based on the ligament stretching.

$$\frac{d_l}{D_J} \cong 1.2\left(\frac{\sigma}{\rho U_A^2 D_J}\right)^{\frac{1}{4}}\left[1+We^{\frac{1}{4}}Oh^{\frac{1}{2}}\right] \tag{1}$$

$$\frac{\langle d\rangle_{VE}}{D_J} \cong 1.2\left(\frac{\sigma}{\rho U_A^2 D_J}\right)^{\frac{1}{4}}\left[1+We^{\frac{1}{4}}Oh^{\frac{1}{2}}\right] \times \left[\frac{\left(\frac{\sqrt{8}c}{6}\right)Oh_{R_l}^{-1}}{\left(\frac{\sqrt{8}c}{6}\right)Oh_{R_l}^{-1}+Oh_{R_l}^{2}-ln\left(1+\frac{cDe_{R_l}}{3Oh_{R_l}}\right)}\right] \tag{2}$$

1st term 2nd term

By referring to Eq. (2), the first term on the right-hand side of the equation represents the competing effect of shear viscosity and surface tension on the average droplet size, first predicted by Aliseda et al. (2008). That explains the calculation of *Oh* and *We* number based on the jet diameter. The final overall form of Eq. (2) includes all of the competing effects of shear viscosity, surface tension and elasticity on overall mean droplet sizes as proposed by Keshavarz et al. (2015). The second term on the right-hand side of Eq. (2) represents the effect of extensional resistance in influencing the average droplet size. The calculation of Oh_{R_l} and De_{R_l} is based on the data extracted from capillary breakup extensional rheometer. The extraction of extensional properties data from capillary breakup extensional rheometer was explained in depth in Rozali et al. (2019b). The De_{R_l} equation contains the fluid relaxation time which represents the extensional rheological property.

Industrially, spray drying of fruit juices usually proceeds at a temperature greater than the room temperature (Brennan et al., 1971; Goula et al., 2008; Mani et al., 2002). Specifically, the feed inlet is usually preheated to temperatures as high as 80 °C (Mani et al., 2002; Verma and Singh, 2015). Pre-heating the feed inlet to a temperature greater than the room temperature before the spray drying process improves the overall economic value of the spray drying process, as less energy needs to be supplied in terms of the hot gas to dry the liquid into dry powder and reduced shear viscosity to reduce pumping requirements. A study by Shu et al. (2006) shows that increasing the feed inlet temperature from 35 to 55 °C resulted in a better atomization effect when spray drying because it led to a lower shear viscosity of the feed. By increasing the temperature of the juice-fibre suspensions prior to the atomization, this study seeks to see if the atomization performance can be improved, or if smaller droplet sizes can be produced by using a two-fluid nozzle.

Overall, the objective of this study was to experiment and analyse the atomization performance of juice-fibre suspensions inside a two-fluid nozzle. Rozali et al. (2019a) have previously explained the atomization mechanism of the juice-fibre suspensions in depth. The current study focused on the theoretical prediction of droplet sizes based on shear, surface tension and extensional properties of the fibre suspensions and the improvement to the atomization performance at higher feed temperatures. The study done by Rozali et al. (2019a) serves as a background or platform that thoroughly explained the atomization mechanisms of the fibre suspensions, which these mechanisms assisted and contributed in explaining the findings in the current study.

2. Experimental

2.1. Test liquid construction

Commercial fibres used in this study consist of four types of insoluble food fibres available in New Zealand. Apple Fibre 400-30, Wheat Fibre 101, Wheat Fibre 600 were supplied by IMCD New Zealand Limited (Auckland, New Zealand) and Citrus Fibre was supplied by Hawkins Watt (Auckland, New Zealand). These fibres were made up of different aspect ratios; Apple Fibre 400-30 and Wheat Fibre 101 with aspect ratio of 2–3 and Wheat Fibre 600 and Citrus Fibre with aspect ratio of 8–10. Size analysis of the fibres has been explained thoroughly in previous work (Rozali et al., 2019b). The 5 g/100 g fibre suspensions (based on wet basis) were prepared by mixing the fibre powders into 60 °Brix concentrated apple juice, supplied by Cedenco Foods New Zealand Limited (Hastings, New Zealand), at 20 °C and continuously stirred until complete dispersion was achieved.

2.2. Rheology and surface tension of fibre suspensions

Shear rheology test was performed using a stress-controlled rheometer, model MCR 301 (Anton Paar GmbH, Graz, Austria), equipped with a coaxial cylinder. This MCR series rheometer was used in two different modes. Rotational mode was set during the steady shear rheology test while oscillatory mode was used to examine the small amplitude oscillatory shear properties. Cup and bob geometry were utilized throughout the study. During the rotational mode, the shear rate was increased step-by-step from 0 to 1000/s and the change of shear viscosity was observed at the rate of 0.25 min/viscosity point. Shear viscosity measurements were carried out at temperatures ranging between 20 and 40 °C. The main purpose of conducting the oscillatory test was to obtain the linear viscoelastic properties of the fibre suspensions. During the small amplitude oscillatory test, the angular frequency was increased from 0.1 rad/s to 100 rad/s at a constant 0.1% strain. Oscillatory tests were carried out at temperatures ranging between 20 and 70 °C and the elastic modulus, G' was observed.

Surface tension measurement was performed using Wilhelmy plate method that employed a commercial apparatus Krüss K12 Tensiometer (Krüss GmbH, Hamburg, Germany). This method used a vertical platinum plate. Surface tension measurements were performed at temperatures ranging between 20 and 70 °C.

2.3. Atomization

Two-fluid nozzle used in this study is of external-mix and plain jet design from Spraying System New Zealand Limited (Auckland, New Zealand). Diameter of the round liquid orifice (D_J)of nozzle is 1.5 mm. This nozzle has an annular air orifice of inner diameter (D_I) and outer diameter (D_O) of 2.54 and 3.00 mm, respectively. Liquid flow was supplied by a gear pump and measured using a graduated cylinder and stopwatch. Air flow rate was monitored using a pressure regulator and a rotameter. Spray tests were conducted at room temperature (20±1 °C) using atmospheric air. Experiments were conducted at a liquid flow rate of 90 mL/min, which produced a velocity of U_L = 0.85 m/s inside the liquid orifice. The liquid velocity was maintained constant while the atomizing air velocity, U_A was varied between 150 and 240 m/s.

Some of the tests required the atomization to occur at temperatures greater than 20 °C and up until a maximum of 70 °C. A 5.0 m long heating tape was attached along the pipeline between the liquid tank and the inlet of the two-fluid nozzle. The heating tape (HTS/Amptek Co., Texas, USA) and a temperature sensor were connected to a temperature controller. The temperature sensor probe was inserted into the pipeline near the two-fluid nozzle by making a hole so that the temperature sensor can accurately measure the temperature of the liquid inside the pipeline.

2.4. Droplet size analysis

A Malvern Mastersizer (Model S, Malvern Instruments Limited, Malvern, Worcestershire, UK) unit was used throughout the experiments when the feed temperature was increased above the room temperature. The spray was positioned so that the laser beam was directed through the centre of the spray at a longitudinal axis of approximately 50 mm below the nozzle. D(v,10), D(v,50), D(v,90) and droplet size distribution were generated for each atomization run. The D-values are the intercepts for 10%, 50% and 90% of the cumulative volume. Specifically, D(v,10) is the diameter at which 10% of the sample's volume is comprised of droplets with a diameter less than this value. D(v,50) is defined as the diameter where half of the sample's volume has droplets with a diameter less than this value. Similarly, D(v,90) is the diameter at which 90% of the sample's volume contains droplets with a diameter less than this value.

2.5. Spraying into liquid nitrogen

To see the actual droplets of the fibre suspensions after the atomization without drying the droplets, the fibre suspensions were sprayed into liquid nitrogen to freeze the droplets. Liquid nitrogen was filled in a chilly bin and the spraying was directed into the bin. The frozen droplets were then picked up and put on glass slides. The glass slides used for the microscope observation were first frost inside a container filled with dry ice. The frozen droplets were then examined under a microscope (Olympus, Japan) equipped with a temperature-controlled mechanism. Specifically, the microscope area, which was the area where the droplets were put for observation, can be lowered to −20 °C by using liquid nitrogen. Dry ice was also scattered on the microscope area. All these acts were carried out to keep the temperature as low as possible to prevent the frozen droplets from melting once put under the microscope.

3. Results and discussion

3.1. Theoretical prediction of droplet sizes in a two-fluid nozzle

During atomization, the enhanced resistance of the fibre suspensions to stretching coming from the extensional properties of the fibre suspensions which plays a key role in controlling the dynamics of the filament breakup (Rozali et al., 2019a). Based on the experimental work done by Rozali et al. (2019a), the atomization pattern of the fibre suspensions showed filamentary structures connecting successive droplets together and this pattern was absent in Newtonian atomization. Fig. 1 shows the examples of how the additional extensional resistance led to the appearance of elongated filaments connecting successive droplets to each other. These filamentary structures, in the end, contributed to the formation of big droplet sizes of viscoelastic fibre suspensions when compared to the Newtonian droplet sizes. Droplet size analysis showed that the final size of the viscoelastic droplets was highly dependent on the aspect ratio of fibres used but this effect was reduced when much greater atomizing air velocity was applied during the atomization (Rozali et al., 2019a). Overall, Rozali et al. (2019a) concluded that during the atomization of viscoelastic fibre suspensions, the extensional behaviour of the liquid dominates the atomization resistance, with minimum effect by shear viscosity and surface tension.

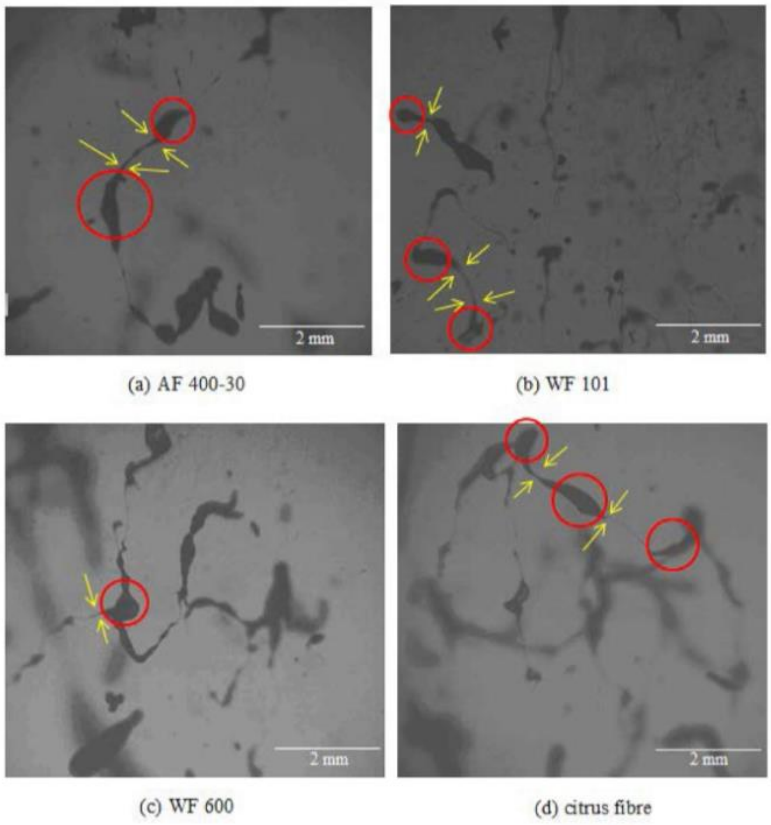

Fig. 1. Photographs of the breakup of 5 g/100 g fibre suspensions at an atomizing air velocity of 150 m/s. (a) Apple Fibre 400-30 (b) Wheat Fibre 101 (c) Wheat Fibre 600 and (d) Citrus Fibre. Images were captured at a position 10 mm below the nozzle exit. Red circles highlight the droplets, while the yellow arrows point to the pinch-off or necking region of a filament. Some of the images are reproduced from Rozali et al. (2019a). (For interpretation of the references to colour in this figure legend, the reader is referred to the Web version of this article.)

Keshavarz et al. (2015) developed a theoretical equation to explore the effect of viscoelasticity on the average droplet size during the two-fluid atomization. Specifically, the equation relates the effect of liquid relaxation time, τ (*De* number in Eq. (2) contains the τ parameter) to the average droplet diameter, d_{VE}. Relaxation time, τ is one of the extensional properties of fibre suspensions that has been discussed in depth in Rozali et al. (2019b). Fig. 2 shows the theoretically predicted average droplet sizes, d_{VE} or D(n,50), based on the Keshavarz et al. (2015) equation for 5 g/100 g Apple Fibre 400-30, Wheat Fibre 101, Wheat Fibre 600 and Citrus Fibre suspensions obtained via non-linear regression of Eq. (2). *c* in Eq. (2) is a single fitting constant and the values are 2.02, 2.73, 4.38 and 4.10 for 5 g/100 g fibre suspension of Apple Fibre 400-30, Wheat Fibre 101, Wheat Fibre 600 and Citrus Fibre, respectively. As shown in Fig. 2, for all types of fibre suspensions, good correlations were obtained between the experimental and theoretical values of droplet sizes. A maximum of 12.0% deviation of experimental value from the theoretical value was obtained and corresponds to the D (n,50) of 5 g/100 g Wheat Fibre 600 suspension at 150 m/s. Other than that, most of the deviations vary between 2 and 7%. Some of the experimental values from Fig. 2 were taken from Rozali et al. (2019a), except that D(n) values were used instead of D(v) values. D(v) is based on the total volume of droplets in the spray while D(n) is based on the total number of droplets in the spray. As shown in Fig. 2, increasing the atomizing air velocity reduced the droplet size of the fibre suspensions. This has been shown experimentally in Rozali et al. (2019a). Besides that, based on Fig. 2, the high aspect ratio of the fibre suspensions made of 5 g/100 g WF 600 and Citrus Fibre exhibited greater average droplet size compared to the low aspect ratio fibre suspensions made of 5 g/100 g AF 400-30 and WF 101.

The good correlations between the experimental values and the predicted values of droplet size in Fig. 2 prove the atomization of fibre suspensions was dominated by the extensional properties of the fibre suspensions, with the shear properties and surface tension only having minor roles. This demonstrates the importance of incorporating the extensional properties during the atomization of fibre suspensions or other complex non-Newtonian liquids, especially if the atomization performances or droplet sizes are forecasted theoretically without experimental observation. The consequence of excluding the extensional resistance and thus relying on the shear resistance and surface tension as the sole sources of stabilizing forces is discussed in Fig. 3.

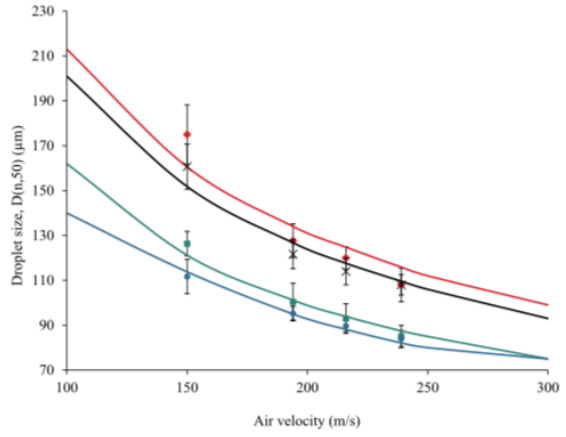

Fig. 2. Relationships between the droplet sizes obtained experimentally and predicted theoretically based on Keshavarz et al. (2015), Eq. (2). (○) 5 g/100 g Apple Fibre 400-30, (□) 5 g/100 g Wheat Fibre 101, (◇) 5 g/100 g Wheat Fibre 600 and (×) 5 g/100 g Citrus Fibre suspensions are the average droplet size of fibre suspensions obtained experimentally, while the theoretical prediction for each fibre suspension is represented by the full line.

Fig. 3 shows the theoretical mean droplet size of 5 g/100 g Wheat Fibre 600 suspension when predicted using a correlation generated by Aliseda et al. (2008), which it does not include the extensional properties. Excluding the extensional resistance means that during the prediction of droplet size, only shear resistance and surface tension are considered. In Aliseda et al. (2008) correlation, only shear viscosity and surface tension parameters exist, while extensional rheology parameter (such as relaxation time, Deborah number *De* or extensional viscosity) is absent. As shown in Fig. 3, the mean droplet sizes of the 5 g/100 g Wheat Fibre 600 suspension predicted using Aliseda et al. (2008) correlation were very different from the experimental observations. Droplet sizes of 5 g/100 g Apple Fibre 400-30, Wheat Fibre 101 and Citrus Fibre suspensions predicted using Aliseda et al. (2008) equation are not shown in Fig. 3 because the values were very similar to the predicted values shown by the 5 g/100 g Wheat Fibre 600 fibre suspension. This is because, using Aliseda et al. (2008) correlation, it implies that only shear viscosity and surface tension affect the atomization performance or the droplet sizes. The shear viscosity of the different 5 g/100 g fibre suspensions were all very similar at all atomizing air velocities. This is due to the very high shear rates of greater than 20 000/s were achieved at all the atomizing air velocities, and the shear viscosities of the different aspect ratio fibre suspensions were all relatively similar at that high shear rates (Rozali et al., 2019a). For the 5 g/100 g Wheat Fibre 600 suspension shown in Fig. 3, the predicted droplet sizes based on Aliseda et al. (2008) relationship were very small, ranging between 10 and 30 μm, whereas, the mean droplet sizes from the experimental observation were very large exceeding 100 μm at all atomizing air velocities. This indicates the use of simple Newtonian correlations, such as Aliseda et al. (2008) equation, is not accurate and reliable in predicting the atomization performance of non-Newtonian fibre suspensions. It also implies that the relatively bigger droplet sizes of the fibre suspensions were probably due to the extensional resistance of the suspensions, with little effect by shear viscosity and surface tension. The predicted droplet size of the Newtonian concentrated apple juice based on the Aliseda et al. (2008) relationship yielded a good and better correlation to the experimental observation compared to the non-Newtonian

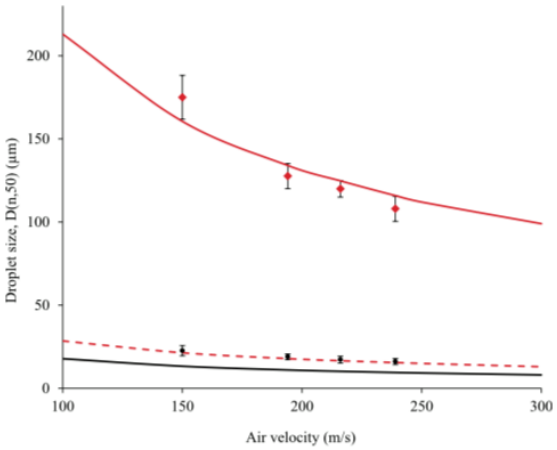

Fig. 3. Relationships between the mean droplet sizes obtained experimentally and predicted theoretically based on Keshavarz et al. (2015) and Aliseda et al. (2008) relationships. (•) Droplet size of concentrated apple juice obtained experimentally, (——) theoretical droplet size of concentrated apple juice based on Aliseda et al. (2008), (◇) droplet size of 5 g/100 g Wheat Fibre 600 suspension obtained experimentally, (- - - -) theoretical droplet size of 5 g/100 g Wheat Fibre 600 suspension based on Aliseda et al. (2008) and (——) theoretical droplet size of 5 g/100 g Wheat Fibre 600 suspension based on Keshavarz et al. (2015) equation.

viscoelastic fibre suspension.

3.2. Improving the atomization performance of the two-fluid nozzle by increasing the feed temperature

Atomization of fibre suspensions has shown to yield bigger droplets compared to the atomization of simple Newtonian liquids. The Newtonian fluid (apple juice) atomization usually produced droplets with an average size, D(v) of less than 150 μm (Aliseda et al., 2008; Buckner and Sojka, 1991) while the atomization of fibre suspensions produced droplets ranging between 200 and 250 μm at a high atomizing air velocity of 240 m/s. This section attempts to change or modify the parameter involved to improve the atomization performance of the fibre suspensions. Improving the atomization performance means producing smaller droplets to prepare for the drying stage inside a spray dryer.

The atomization of 5 g/100 g Wheat Fibre 600 suspension was performed by varying the temperature of the fibre suspension between 20 and 70 °C. The atomization of the fibre suspension at greater inlet temperatures was evaluated using the Malvern Mastersizer. As shown in Fig. 4(a), increasing the inlet temperature from 20 to 70 °C produced smaller droplet sizes especially regarding D(v,50) and D(v,90). At an atomizing air velocity of 150 m/s, increasing the inlet temperature reduced the D(v,90) from more than 1000 μm to around 650 μm while the D(v,50) reduced from approximately 550 μm to around 390 μm. In contrast, D(v,10) underwent insignificant changes. The effect of the inlet temperature on atomization performance was investigated at greater atomizing air velocities. As shown in Fig. 4(b), increasing the inlet temperature from 20 to 70 °C at an atomizing air velocity of 195 m/s significantly reduced the D(v,90), although the reduction is less compared to at 150 m/s atomizing air velocity. Meanwhile, the D(v,50) and D(v,10) seem to undergo very minor reduction compared to the D(v,90). When the atomizing air velocity was further increased to 215 m/s and 240 m/s, the D(v,90) underwent an insignificant reduction, this was similar to the D(v,50) and D(v,10). This can be seen in Fig. 4(c–d). Overall, it means increasing the inlet temperature did not reduce the D(v,10) at all atomizing air velocities and slightly reduced the D(v,50). Whereas, in case of the D(v,90), increasing the inlet temperature considerably reduced the droplet sizes at the lowest atomizing air velocity of 150 m/s. At atomizing air velocities beyond 195 m/s, less or no significant reduction was observed for all the D-values. This is highly suspected to be due to the individual effect of shear rheology, surface tension and extensional rheology when the temperature of the feed was increased. Based on Fig. 5 and Fig. 6, the surface tension and shear viscosity of the 5 g/100 g Wheat Fibre 600 suspension, respectively, significantly reduced when the temperature was increased. Meanwhile, the viscoelasticity of 5 g/100 g Wheat Fibre 600 suspension, represented by the elastic modulus (G') in Fig. 7, insignificantly reduced when the temperature was increased. It is possible to say that the G' generally decreased as the temperature was increased from 20 to 70 °C, but the reduction was insignificant or very weak. The G' can be said to be fairly constant between 20 and 70 °C. G' represents the solid-like behaviour contributed by the fibres. Weak temperature-dependence of G' indicates that the fibres were not significantly thermally activated within the range tested; 20 and 70 °C. Thus, when the temperature was increased to 70 °C, while the fibre-solvent interactions became weaker, thus lowering the shear viscosity, the fibre-fibre interactions stayed the same. ANOVA

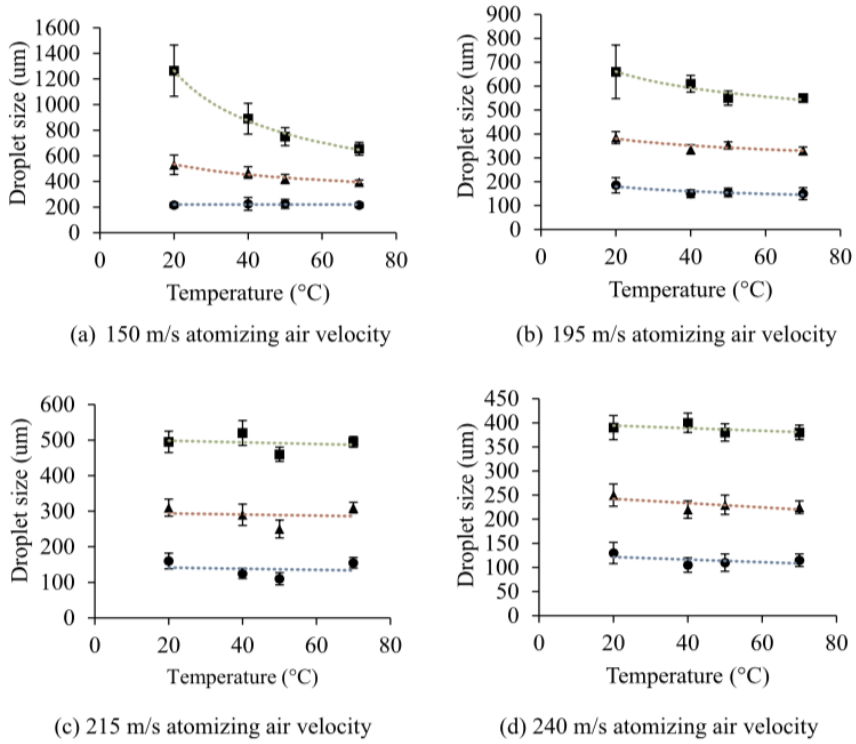

Fig. 4. The D-values against the increasing feed temperature of the 5 g/100 g Wheat Fibre 600 suspension at an atomizing air velocity of (a) 150 m/s, (b) 195 m/s, (c) 215 m/s and (d) 240 m/s. The D-values shown were obtained using the Malvern Mastersizer method. (●) D(v,10), (▲) D(v,50) and (■) D(v,90).

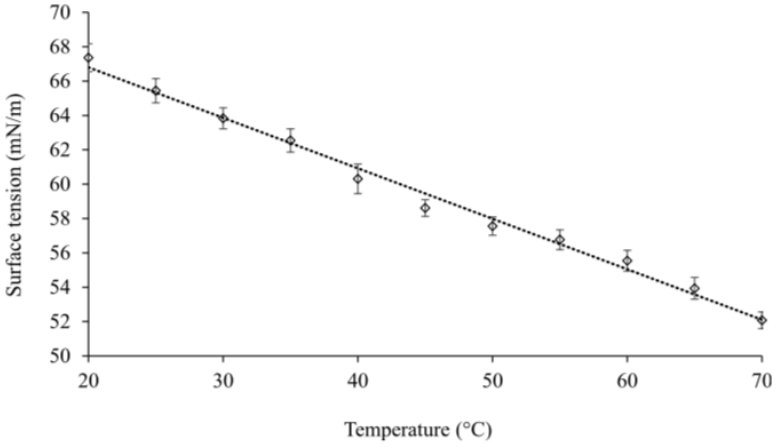

Fig. 5. Surface tension of 5 g/100 g Wheat Fibre 600 suspension as a function of temperature.

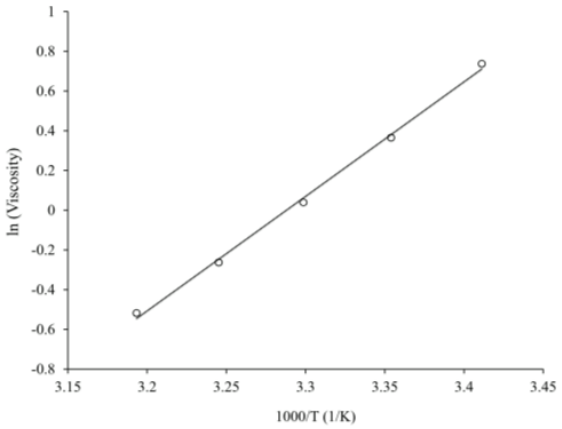

Fig. 6. Arrhenius plot of the viscosity versus 1/T for 5 g/100 g Wheat Fibre 600 suspension.

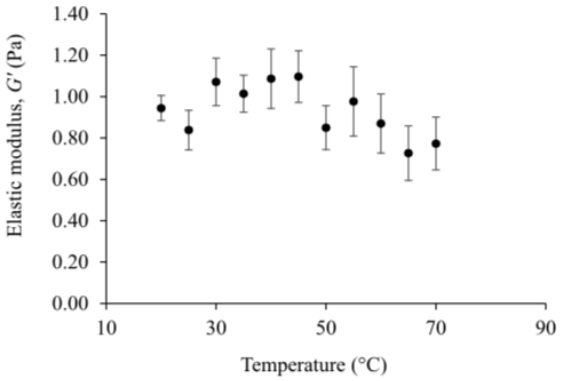

Fig. 7. The effect of temperature on the elastic modulus, G′ of 5 g/100 g Wheat Fibre 600 suspension.

tests were performed to check whether there are any significant differences between the G' as the temperature was increased. The result shows that the p-value was more than 0.05, which means that the G' at different temperatures were all equal, thus the effect of temperature on G' was insignificant. The previous study by Chindam et al. (2014) showed the indistinct trend of the G' of microfibres film as the temperature was increased at least to 70 °C. Other studies by Pothan et al. (2003) and Moberg et al. (2016) reported that the G' of banana fibre and cellulose nanofibrils composites insignificantly decreased when the temperature was increased to 60–70 °C. Overall, while the shear rheology of fibre suspensions was strongly affected by temperature, the dependence of extensional rheology and viscoelasticity of fibre suspensions on temperature was relatively weak, at least within the temperature range of 20–70 °C. Atomization performance is hugely influenced by the shear and extensional resistance. This indicates that as the temperature increases, the energic requirements of atomization may become dominated by the extensional resistance, as the shear resistance at increasing temperatures decreases.

At the lowest atomizing air velocity of 150 m/s, the effect of surface tension and shear viscosity still existed, along with the extensional viscosity. Increasing the inlet temperature allowed the jet to be disrupted and sheared better or more intensely as the surface tension and especially the shear viscosity, were reduced. Besides that, increasing the inlet temperature of the fibre suspensions yielded a better breakup due to shearing of the liquid jet at a much lower shear viscosity. This then proceeded with the stretching of the ligaments into droplets. This means, at the lowest atomizing air velocity of 150 m/s, the reductions of the surface tension and shear viscosity at elevated temperatures affect the overall performance of the fibre suspension atomization. However, at much greater atomizing air velocity of more than 150 m/s, the effect of shear viscosity on atomization performance was minimal which means the atomization was dominated by the extensional resistance. Extensional resistance insignificantly reduced with increasing temperature, as represented by the viscoelasticity or the G'. This explains the insignificant reduction in droplet sizes when the atomization proceeded at greater inlet feed temperatures.

Another explanation can be gained by comparing the competing effect of temperature and atomizing air velocity. Increasing the inlet temperature and atomizing air velocity both change the conditions of atomization. Increasing the atomizing air velocity provides greater disruptive forces during the atomization and increasing the inlet temperature lessens the stabilizing forces during the atomization. At atomizing air velocity of 150 m/s, both the temperature and atomizing air velocity significantly influenced the atomization performance (droplet size distribution). However, at an atomizing air velocity of

195 m/s and beyond, it is suggested that the rate of disruption due to very high velocity of air exceeded the rate of reduction in the stabilizing forces, and thus the atomizing air velocity dominated and controlled the whole atomization performance. Lowering the stabilizing forces gave no significant effect on the atomization performance. It means that the extensional resistance and viscoelasticity of the fibre suspensions that negatively impact the drop size and produced a wider distribution when compared to other Newtonian liquids, were overwhelmed and affected by the high atomizing air velocity but not the high temperature. As shown in Fig. 8(a), at an atomizing air velocity of 150 m/s, increasing the inlet temperature from 40 to 70 °C shifted the drop size distribution to smaller droplet sizes and produced a narrower distribution. In contrast, at a greater atomizing air velocity of 240 m/s, increasing the inlet temperature did not significantly change the drop size distribution when compared to the change that occurred at 150 m/s atomizing air velocity.

Figs. 4 and 8 suggest that the atomization of viscoelastic fibre suspensions at 150 m/s atomizing air velocity should undertake at a higher inlet temperature as this approach resulted in smaller droplet sizes and thus better atomization. In contrast, the atomization of the viscoelastic fibre suspensions at 195 m/s atomizing air velocity and beyond, does not necessarily need to occur at high temperatures as there were insignificant changes in the droplet sizes and atomization performances.

3.3. Morphology of frozen droplets as a representative of dried powders

Atomization of fibre suspensions from a liquid into droplets will be followed by the drying into a powder. Although the drying of the droplets was not of interest in the current study, however, it is important to prove that the fibres can act as a drying aid during the drying inside a spray dryer. Drying of concentrated apple juice without drying aid produces a sticky powder. At first, it was unknown how the fibres placed themselves after the atomization, either they accumulate inside the droplets or they are sticking out from the droplets. It is also essential to demonstrate the fibres are not separated from the droplets during the atomization. Complete separation of the fibres from the droplets means that the fibres will not be effective in assisting the drying of the sticky apple juice droplets. Most importantly, in the case of atomization, the separation could result in a bimodal or multimodal drop size or particle size distribution. This is because the size distribution of the fibres and size distribution of the droplets could possibly establish bimodal distribution with two different peaks. In this analysis, the visualization of the actual droplets supports the no separation hypothesis. The frozen droplets were produced by spraying the fibre suspension into liquid nitrogen.

Fig. 9 shows the frozen droplets of 5 g/100 g Wheat Fibre 600 suspension when atomization occurred at 195 m/s atomizing air velocity.

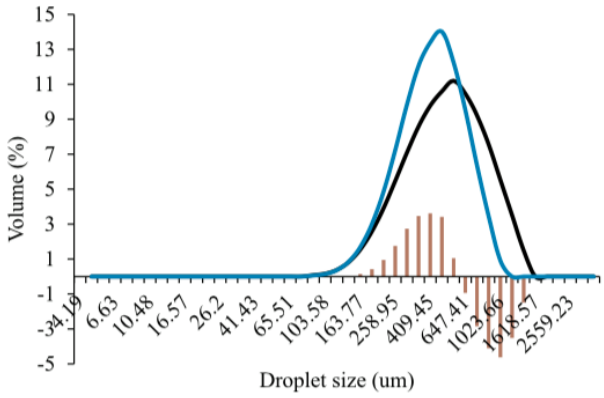

(a) Increasing the temperature from 40 °C to 70 °C at a constant atomizing air velocity of 150 m/s.

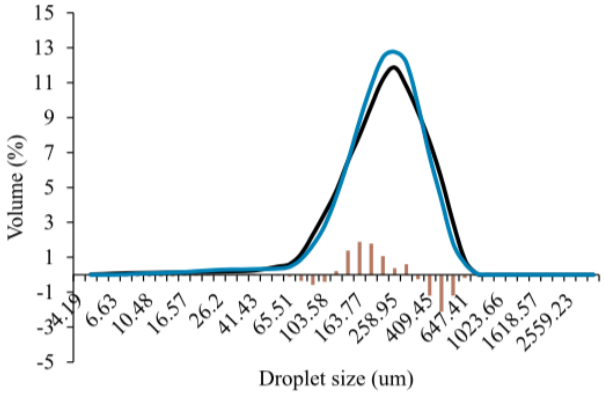

(b) Increasing the temperature from 40 °C to 70 °C at a constant atomizing air velocity of 240 m/s.

Fig. 8. The change in the drop size distributions of the 5 g/100 g Wheat Fibre 600 suspension when the feed temperature was increased from 40 to 70 °C. (a) At an atomizing air velocity of 150 m/s and (b) at an atomizing air velocity of 240 m/s. (▬) At an inlet temperature of 40 °C, (▬) at an inlet temperature of 70 °C and (red bar) reduction that occurred when subtracting the distribution curve at 70 °C with the curve at 40 °C. (For interpretation of the references to colour in this figure legend, the reader is referred to the Web version of this article.)

Most of the droplets had a spherical shape. First observation on Fig. 9 reveals that the droplets all stick together. This is expected since during the spraying into the liquid nitrogen, the droplets freeze rapidly to ice, and when two or more ice spheres meet each other, they stick due to the adhesion effect of the ice (Ryzhkin and Petrenko, 1997).

Fig. 10 shows the images of the frozen droplets at a higher magnification. The fibres appear to be enclosed in the droplets. The images suggest there was no separation during the atomization of fibre suspensions using a two-fluid nozzle at high atomizing air velocity. This indicates that the two-fluid nozzle is reliable in producing droplets with the fibres remaining enclosed in the drops, the fibres can assist the drying of the wet droplets and normal drop size distributions were attained during the atomization.

As shown in Fig. 10, there were air bubbles trapped inside the droplets. These air bubbles most likely caused by dissolved air in the solution. Other than the air bubbles, some of the frozen droplets in

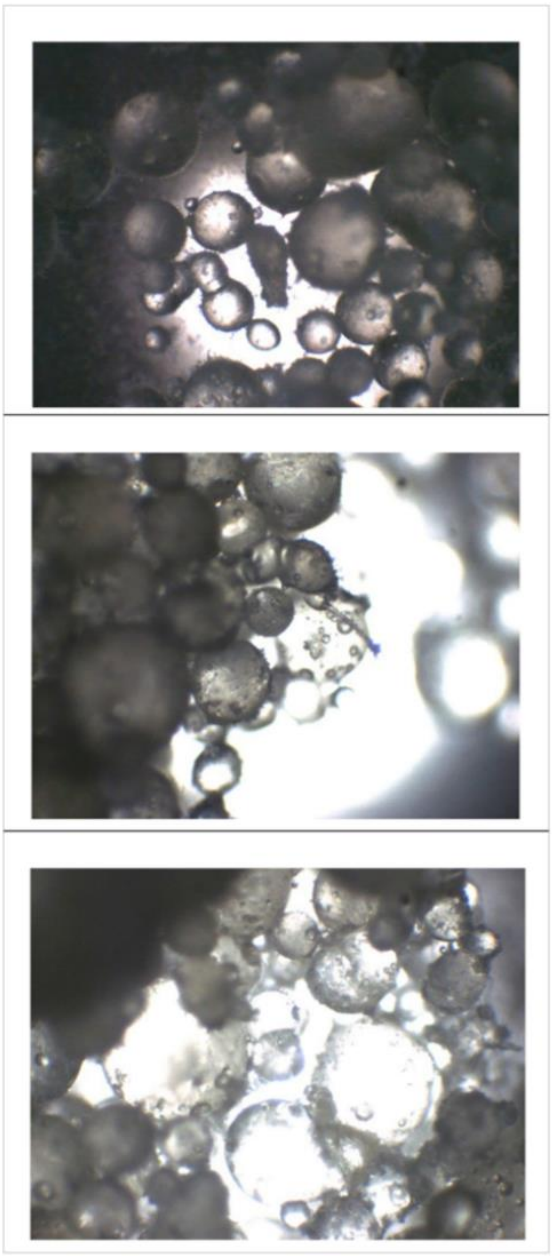

Fig. 9. Frozen droplets of 5 g/100 g Wheat Fibre 600 suspension stick together after the spraying of the fibre suspension into a container filled with liquid nitrogen. The images correspond to 4× magnification.

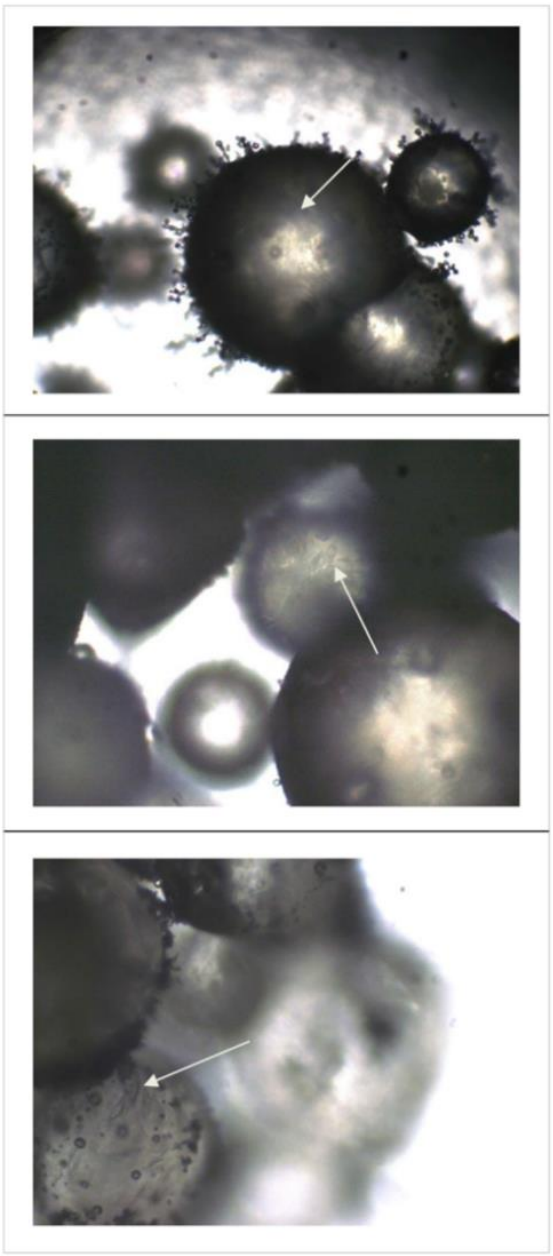

Fig. 10. Zoomed-in images of the frozen droplets of 5 g/100 g Wheat Fibre 600 suspension showing the fibres inside the frozen droplets. Fibres are pointed out by the white arrows. The images correspond to 10× magnification.

Figs. 9 and 10 appear bigger with the size exceeding 800 μm and a maximum of 1000 μm. Based on the experimental results of the exact similar fibre suspension explained in the previous study when using MATLAB and Malvern Mastersizer methods, the D(v,90) of 5 g/100 g Wheat Fibre 600 suspension at atomizing air velocity of 195 m/s was approximately 700 μm (Rozali et al., 2019a). The relatively big frost droplets resulted from spraying into the liquid nitrogen may be due to the coalescence of droplets. When two or more drops float or levitate on the surface of liquid nitrogen, the drops first do not interact, but they move closer to each other. When the curvatures of liquid nitrogen under the drops meet each other, drop coalescence occurs (Kim et al., 2011). Drop coalescences of the 5 g/100 g Wheat Fibre 600 suspension could possibly result in the bigger drop sizes compared to the results by MATLAB and Malvern Mastersizer methods. The spraying into the liquid nitrogen proceeded for 10 s. Thus, it is also possible that during the spraying into the liquid nitrogen, the later sprayed liquid drop met with the prior sprayed liquid drop that had already turned into a solid ice sphere. The liquid drop then surrounded the solid ice sphere and a spherically concentric liquid shell was formed around the solid ice sphere. This contributed to the bigger final drop size.

4. Concluding remarks

Atomization performances of fibre suspensions were theoretically predicted by using two different relationships, one of which excludes the effect of extensional property of the fibre suspensions. The results show that the predicted droplet sizes of fibre suspensions were very different from the experimental droplet sizes when extensional property called relaxation time was ignored. Perfect correlations were obtained between the predicted and experimental droplet sizes when the relaxation time was incorporated during the theoretical prediction of droplet size. Overall, this finding strengthens the conclusion made from the previous study by Rozali et al. (2019a) that the atomization performance of non-Newtonian liquid with significant extensional rheology such as fibre suspensions, is highly affected by the extensional resistance with minor roles by shear viscosity and surface tension.

This study further shows that the atomization performance of the fibre suspensions that was controlled and dominated by extensional resistance was not significantly changed when the feed temperature was increased. This is a novel finding as previous studies mostly show the significant reduction in droplet sizes or a better atomization performance when the feed temperature was increased, where all of these studies only dealt with shear viscosity and surface tension as the dominant resistance during the atomization.

Overall, this study shows valuable insights into the atomization performance of fibre suspensions which are categorized as non-Newtonian viscoelastic liquids.

Acknowledgement

The authors would like to thank the Ministry for Business, Innovation and Employment (MBIE) New Zealand for the funding provided through Food Industry Enabling Technologies (FIET) program that has enabled this project to proceed.

References

Aliseda, A., Hopfinger, E., Lasheras, J.C., Kremer, D., Berchielli, A., Connolly, E., 2008. Atomization of viscous and non-Newtonian liquids by a coaxial, high-speed gas jet. Experiments and droplet size modeling. Int. J. Multiph. Flow 34, 161–175.
Brennan, J., Herrera, J., Jowitt, R., 1971. A study of some of the factors affecting the spray drying of concentrated orange juice, on a laboratory scale. Int. J. Food Sci. Technol. 6, 295–307.
Buckner, H.N., Sojka, P.E., 1991. Effervescent atomization of high-viscosity fluids: Part I. Newtonian liquids. Atomization Sprays 1 (3).
Chhabra, R.P., 2006. Bubbles, Drops, and Particles in Non-newtonian Fluids. CRC press.
Chindam, C., Lakhtakia, A., Brown, N.R., Orfali, W., Awadelkarim, O.O., 2014. Frequency-and temperature-dependent storage and loss moduli of microfibrous thin films of Parylene C. Mater. Lett. 116, 296–298.
Collett, C., Ardron, A., Bauer, U., Chapman, G., Chaudan, E., Hallmark, B., Wilson, D.I., 2015. A portable extensional rheometer for measuring the viscoelasticity of pitcher plant and other sticky liquids in the field. Plant Methods 11, 16.
Goula, A.M., Karapantsios, T.D., Achilias, D.S., Adamopoulos, K.G., 2008. Water sorption isotherms and glass transition temperature of spray dried tomato pulp. J. Food Eng. 85, 73–83.
Keshavarz, B., Sharma, V., Houze, E.C., Koerner, M.R., Moore, J.R., Cotts, P.M., McKinley, G.H., 2015. Studying the effects of elongational properties on atomization of weakly viscoelastic solutions using Rayleigh Ohnesorge Jetting Extensional Rheometry (ROJER). J. Non-Newtonian Fluid Mech. 222, 171–189.
Kim, H., Lee, Y., Cho, H., 2011. Levitation time measurement of water drops on the surface of liquid nitrogen. J. Korean Phys. Soc. 58 (6), 1628–1632.
Mani, S., Jaya, S., Das, H., 2002, September. Sticky issues on spray drying of fruit juices. Paper presented at the. In: ASAE/CSAE North-Central Intersectional Meeting.
Masters, K., 1979. Spray Drying Handbook. Spray Drying Handbook, third ed.
Moberg, T., Tang, H., Zhou, Q., Rigdahl, M., 2016. Preparation and viscoelastic properties of composite fibres containing cellulose nanofibrils. J. Nanomater. 30, 2016.
Pothan, L.A., Oommen, Z., Thomas, S., 2003. Dynamic mechanical analysis of banana fiber reinforced polyester composites. Compos. Sci. Technol. 63, 283–293.
Rajan, R., Pandit, A., 2001. Correlations to predict droplet size in ultrasonic atomisation. Ultrasonics 39, 235–255.
Rozali, S.N.M., Paterson, A.H.J., Hindmarsh, J.P., Huffman, L.M., 2019. Atomization behaviour of juice-fibre suspensions in a two-fluid nozzle. J. Food Eng. 256, 53–60.
Rozali, S.N.M., Paterson, A.H.J., Hindmarsh, J.P., Huffman, L.M., 2019. Understanding the shear and extensional properties of pomace-fibre suspensions prior to the spray drying process. Lebensm. Wiss. Technol. 99, 138–147.
Ryzhkin, I.A., Petrenko, V.F., 1997. Physical mechanisms responsible for ice adhesion. J. Phys. Chem. B 101, 6267–6270.
Shu, B., Yu, W., Zhao, Y., Liu, X., 2006. Study on microencapsulation of lycopene by spray-drying. J. Food Eng. 76, 664–669.
Varga, C.M., Lasheras, J.C., Hopfinger, E.J., 2003. Initial breakup of a small-diameter liquid jet by a high-speed gas stream. J. Fluid Mech. 497, 405–434.
Verma, A., Singh, S.V., 2015. Spray drying of fruit and vegetable juices—a review. Crit. Rev. Food Sci. Nutr. 55, 701–719.

References

Keshavarz, B., Sharma, V., Houze, E. C., Koerner, M. R., Moore, J. R., Cotts, P. M., . . . McKinley, G. H. (2015). Studying the effects of elongational properties on atomization of weakly viscoelastic solutions using Rayleigh Ohnesorge Jetting Extensional Rheometry (ROJER). *Journal of Non-Newtonian Fluid Mechanics, 222*, 171-189.

McKinley, G. H., & Tripathi, A. (2000). How to extract the Newtonian viscosity from capillary breakup measurements in a filament rheometer. *Journal of Rheology, 44*(3), 653-670.

Vargaftik, N., Volkov, B., & Voljak, L. (1983). International tables of the surface tension of water. *Journal of Physical and Chemical Reference Data, 12*(3), 817-820.